ISBN 978-82-326-4653-1 (printed version)
ISBN 978-82-326-4652-4 (electronic version)
ISSN 1503-8181

Doctoral theses at NTNU, 2020:152

Senthuran Ravinthrakumar

Numerical and Experimental Studies of Resonant Flow in Moonpools in Operational Conditions

Doctoral Thesis

Senthuran Ravinthrakumar

Doctoral theses at NTNU, 2020:152

NTNU

Norwegian University of Science and Technology

NTNU
Norwegian University of
Science and Technology
Faculty of Engineering
Department of MarineTechnology

NTNU

Norwegian University of
Science and Technology

Senthuran Ravinthrakumar

Numerical and Experimental Studies of Resonant Flow in Moonpools in Operational Conditions

Thesis for the degree of Philosophiae Doctor

Trondheim, June 2020

Norwegian University of Science and Technology
Faculty of Engineering
Department of MarineTechnology

NTNU
Norwegian University of
Science and Technology

NTNU
Norwegian University of Science and Technology

Thesis for the degree of Philosophiae Doctor

Faculty of Engineering
Department of MarineTechnology

ISBN 978-82-326-4653-1 (printed version)
ISBN 978-82-326-4652-4 (electronic version)
ISSN 1503-8181

Doctoral theses at NTNU, 2020:152

Printed by Skipnes Kommunikasjon as

Acknowledgements

This work has been carried out under the supervision of Professor Trygve Kristiansen at the Department of Marine Technology, Norwegian University of Science and Technology (NTNU). The PhD is funded by the department. Grants from the Norwegian Shipowners' Association and Equinor to attend conferences and to buy equipment for the model tests are highly appreciated.

The continuous support, guidance, and the deep understanding of hydrodynamics of my supervisor, Trygve Kristiansen, is highly appreciated. This work would not been possible without his support. More than the aforementioned points, I would like to thank him for being a friend and supportive when needed. Since I am one of his first PhD students, I would like to mention the following to the coming PhD students; you are lucky! He is a proper teacher and a person that really cares. If you are able to take in even 10 % of what he is trying to teach you, you will come good.

The support and guidance of my co-supervisor, Dr. Babak Ommani, is invaluable. During these years, we have had several meetings and discussions, which have been crucial for the PhD work, especially for the numerical simulations carried out in the present work.

I would also like to thank Professor Bernard Molin and Professor Odd M. Faltinsen for their input and guidance. I have had several meetings with them, which I believe has raised the quality of the work. Discussing sloshing with the both has been important for this thesis work. I would like to thank Professor Molin for the help he provided with developing the present Domain Decomposition method. In practice, one might say that they have acted as my co-supervisors.

During the model tests, I got a lot of help from Trond Innset (Rhino calculations),

Ole-Erik Vinje, Torgeir Wahl and Terje Rosten. I would like to thank them for coping with my demands without losing motivation. They have worked overtime for several hours in order to ensure that the experiments were finished in time, which I highly appreciate. I would also like to thank Henning Borgen for several conversations regarding the design of ships with moonpools.

My colleagues and friends at the department have contributed with many interesting and helpful discussions, which I am grateful for. A special thanks to my dear friend, Fredrik Mentzoni, for proof reading parts of the thesis, and for the support during the last 3.5 years. The PhD journey has been like a rollercoaster ride at times, where his support during the lows has been immense.

Finally, I would like to thank my lovely mother, father, sister and fiancèe for their support and encouragement during my studies.

Abstract

The present work is relevant for ships with moonpools. A moonpool is a vertical opening through the ship hull, typically used to descend objects into the sea. Model tests and numerical simulations are carried out to investigate the hydrodynamic interaction between ship and moonpool responses. The studies are performed in forced motion and in freely floating conditions. We investigate ships with small, moderate, and large moonpools.

Four sets of model tests are carried out. In the first round, moonpools with recess are investigated in forced heave in a two-dimensional setting. The same set-up is investigated in freely floating conditions with incident waves in the second round. In the third round, moonpools without recess are investigated in both forced heave and freely floating conditions. The first three rounds of model tests are carried out in a wave flume at NTNU. These tests serve as a basis for the final and fourth round of experiments, which are carried out in the Ocean Basin at Sintef Ocean. The model tests in the Ocean Basin are the main part of the present work, where we investigate the hydrodynamic interaction between ship and moonpool responses in a three-dimensional setting. The experiments in the Ocean Basin are carried out with a ship model that resembles a real ship, with three different moonpool sizes. By that, we investigate the importance of the moonpool-to-ship-volume-ratio on the hydrodynamic interaction between ship and moonpool responses, both in regular and irregular waves.

Two numerical solvers are implemented in the present thesis work; a two-dimensional time-domain boundary element method (BEM) code solving the linearized potential flow problem and a two-dimensional hybrid solver combining Navier–Stokes and potential flow solvers. These solvers are used to estimate the moonpool and ship responses, and the numerical simulations are compared against the model

tests that are carried out in an idealized two-dimensional setting. WAMIT and an existing hybrid Navier–Stokes solver (PVC3D) are used to perform numerical simulations in 3D.

Based on the model tests and numerical simulations, we see that the moonpool and ship responses are strongly coupled for ships with moderate and large moonpools. For small moonpools, the hydrodynamic interaction between ship and moonpool responses is almost negligible. The importance of damping due to flow separation at the moonpool entrance is discussed, both at the piston and sloshing modes. Several nonlinear free-surface effects are discussed, such as Duffing-type moonpool responses, swirling and secondary resonance, where most of them occur in a relevant wave period range with respect to ocean waves in the North Sea.

Contents

Nomenclature

B_t	Tank width
BEM	Boundary element method
COG	Center of gravity
D	Ship draft
ϵ_{mp}	Phase angle between moonpool response and forced motion
FDM	Finite difference method
FEM	Finite element method
FVM	Finite volume method
g	Gravitational constant
GM	Metacentric height
H	Wave height
h	Tank depth
H_r	Recess height
HPC	Harmonic polynomial in cell method
I	Moment of inertia
L	Ship length
L_*	Distance between the two sinks, as discussed by Molin (2001)
L_m	Moonpool length
L_r	Recess length
L_t	Tank length
λ	Wave length
NWT	Numerical wave tank
ω	Wave or forced oscillation circular frequency
p	Fluid pressure
ϕ	Velocity potential

PM	Pierson-Moskowitz spectrum
PNWW	Pink noise for water waves
PVC3D	Potential viscous code in 3D
RAO	Response amplitude operator
Re	Reynolds number
S_ζ	Irregular wave spectrum
T	Wave or forced oscillation period
T_n	nth moonpool resonance mode
$\boldsymbol{U}$	Body velocity vector
$\boldsymbol{u}$	Fluid velocity vector
V_S	Submerged ship volume
V_{MP}	Moonpool volume
VOF	Volume of fluid method
x	Longitudinal direction
y	Transverse direction
z	Vertical direction
ζ	Free surface elevation
ζ_{mp}	Moonpool response

Part I

Literature Review and Theory

Chapter 1

Introduction

A moonpool is a vertical opening through the ship structure, often used to descend objects through into the sea. An alternative to this is to offload the object off to the side of the ship (cf. Figure 1.1(a)). The positives with a moonpool is that it partially shelters the object from environmental loads, such as wind and waves. Example of such objects are remotely operated vehicles and diving bells. Other applications for a moonpool is on drillships, where the moonpool is used to lower risers into the sea. The problem with a moonpool is that the moonpool exhibits resonant oscillations at certain periods (an example from a real vessel is illustrated in Figure 1.1(b)). The water oscillations in the moonpool can be significant, which is of concern with respect to the objects being lowered through the moonpool, hence, the operability of the moonpool. Large moonpool responses are also a concern with regard to the on board crew and water on deck. Therefore, it is important to understand the dominant physics when resonant moonpool oscillations occur, such that we can estimate the moonpool responses as accurately as possible. In terms of resonant moonpool responses, we distinguish between; the piston mode and the sloshing modes. The former is, generally, associated with vertical near-uniform oscillations of the moonpool, while the latter is associated with standing waves in the moonpool. The aim of the present work is to investigate the coupled ship and moonpool responses, and to identify dominant physical effects at moonpool resonance by performing dedicated experiments. We also discuss how accurately different state-of-the-art numerical methods are able to predict the moonpool responses.

In the present work, moonpools with and without recess are investigated. The latter is referred to as clean moonpools in this thesis, and is the most common moonpool type. A moonpool with recess is illustrated in Figure 1.2, and is typically found

(a) Object lowered off to the side of the vessel, an alternative to lowering an object through the moonpool (https://www.youtube.com/watch?v=wYcS6shEUwo)

(b) Snapshots from video recordings illustrating violent moonpool responses on a drill ship (https://www.youtube.com/watch?v=PKvkFOkD6uQ)

Figure 1.1: Objects can be descended through a moonpool, or as an alternative, off to the side of the vessel. The moonpool partially shelters the object from environmental loads, but can exhibit large resonant oscillations at certain periods, which is of concern with respect to the operability of the moonpool.

on drillships. The term recess refers to the upper part of the sub-compartment in Figure 1.2, which is the water in the "extension" of the moonpool. We use the term recess floor to describe lower sub-compartment, which is a part of the ship hull. Moonpools with recess are typically used to transport an object into the moonpool, and assemble it, prior to descending it into the sea (Son et al. 2008).

The different models that are investigated in the present work are summarized in Figure 1.3. We study the moonpool responses in both forced motion and in freely floating conditions. The studies are carried out in both two-dimensional (2D) and three-dimensional (3D) settings. Numerical simulations are carried out to further investigate the dominant physical effects at moonpool resonance.

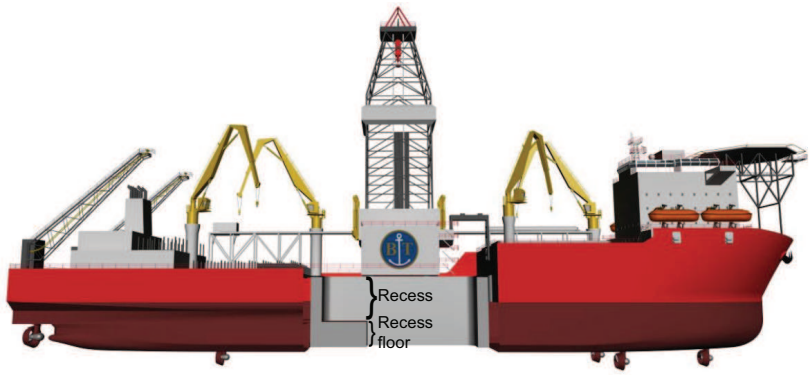

Figure 1.2: Moonpool with recess on a drillship. Figure taken from Törnblom and Hammargren (2012) and modified for illustration purposes. The recess and the recess floor are indicated.

1.1 Previous studies versus present work

Kuo (1978) was one of the first to discuss the moonpool resonance problem, and the importance of damping at the piston mode. He performed experiments with a fixed barge with a moonpool in incident regular waves in a wave flume. Although their experimental results suggest that the moonpool responses are affected by reflected waves, the Response Amplitude Operators (RAOs) indicate that he observed piston mode resonance. He also proposed that introducing appendages, such as stiffeners along the moonpool walls, would increase the damping of the water oscillations, although it was not proved by means of theory, numerical simulations or experiments.

Several authors have discussed resonance in moonpools in recent years. Molin (2001) developed theory to predict the natural periods and corresponding modes

Figure 1.3: Photos of models with moonpools from the present model tests. The model tests are performed in two-dimensional and three-dimensional settings.

in a clean moonpool. He extended his theoretical model to estimate the natural periods for moonpool with recess in Molin (2017), where the flow in the moonpool is assumed to be two-dimensional, while the flow outside the moonpool is three-dimensional in infinite water depth. In this thesis, we extend his theory by assuming that the flow outside the moonpool is two-dimensional in finite water depth, such that it is suitable for the presently investigated configurations.

Faltinsen et al. (2007) developed a theoretical model in 2D to predict the moonpool responses based on linear potential flow theory. They developed a domain decomposition method, where they used four subdomains to obtain the velocity potential. Later, Faltinsen and Timokha (2015) developed theory to include the effect of damping due to flow separation in a 2D potential flow solver. We implement their theory in the presently developed 2D potential flow solver.

Aalbers (1984) developed simplified theory by means of using the equation of motion for the moonpool response, and compared the results with model tests. He showed that damping due to viscous effects was important at the piston mode. Later, several authors have discussed that the dominant viscous damping arises due to flow separation at the moonpool entrance (see e.g. Kristiansen and Faltinsen (2008; 2012)). Kristiansen and Faltinsen (2008) performed forced heave experiments of a model with moonpool in a two-dimensional setting, and identified that the dominant damping in the proximity of the piston mode was due to flow separation at the moonpool inlet. In the present study, we investigate this effect for moonpools with recess in a similar setting. Bonfiglio and Brizzolara (2018) performed numerical simulations using VOF to determine the added mass and damping coefficients of a twin hull around moonpool resonance in a two-dimensional setting. They concluded that linear potential flow theory failed to predict the added mass and damping coefficients accurately around resonance, due to that the moonpool responses are over-estimated by linear potential flow theory. They also discussed that the piston mode period is amplitude-dependent.

Wang and Wu (2008) investigated a two-dimensional moonpool setup numerically with a potential flow solver. Their focus was on the sloshing responses in forced heave and forced surge. Their study is one of few that focuses on the sloshing responses in moonpools. They showed with numerical simulations that the first sloshing mode responses were nonlinearly excited, due to activation of higher modes. They extended their work in Wang et al. (2011), and used a fully nonlinear potential flow theory solver, where they observed significant second harmonic moonpool responses. In the present work, we investigate the main sources of damping in the proximity of the sloshing modes. As mentioned above, the main source of damping at the piston mode is widely discussed in the literature, while the sources of damping at the sloshing modes are not clearly addressed. We do so

by performing model tests, and numerical simulations with linear potential flow and hybrid Navier–Stokes solvers.

In freely floating conditions, the resonant moonpool responses are different from those in forced motion tests. The piston mode period is different due to coupling between the moonpool and ship responses. This is due to that poles in the radiation and diffraction potentials cancel out each other at the piston mode period as predicted in e.g. forced heave (McIver 2005). This was investigated further by Fredriksen et al. (2015), where they performed experiments with a freely floating body in incident regular waves in a two-dimensional setting. They showed that the piston mode period was considerably different from the one predicted in forced heave. The importance of damping due to flow separation at the piston mode was emphasized. The coupling between the heave and piston mode responses was significant for the model investigated therein. In their study, the moonpool volume, V_{MP}, was large compared to the ship volume, V_S. In the present work, we investigate whether the V_{MP}/V_S-ratio is important on the hydrodynamic interaction between ship and moonpool responses. van't Veer and Tholen (2008) presented an overview over existing ships with moonpools. Based on their overview, it can be shown that the typical V_{MP}/V_S-ratio is in the range 0.01-0.07. We investigate the hydrodynamic interaction between ship and moonpool responses with V_{MP}/V_S-ratios in the range 0.01-0.43, both experimentally and numerically.

Guo et al. (2017) performed experimental studies in an offshore basin, and investigated the resonant moonpool responses in a large moonpool with recess in regular waves. They reported some higher harmonic moonpool responses when sloshing occurred with $V_{MP}/V_S \approx 0.1$, where the moonpool length was 25 % of the overall ship length. The largest moonpool length in this work is 50 % of the overall ship length.

Yang et al. (2013) studied ships with and without moonpool to investigate the hydrodynamic interaction between the moonpool and ship responses. They performed numerical simulations, and observed some influence of the piston mode on the heave responses. Maisondieu and Le Boulluec (2001) studied a Wellhead barge floating unit in 3D, where the moonpool length was approximately 45 % of the overall length. The concept was dedicated to oil productions in deep waters. Their experiments indicated significant coupling between the heave and moonpool responses. In the present study, we investigate the hydrodynamic interaction between the moonpool and ship responses in surge, sway, heave, pitch and roll.

The aforementioned studies were conducted for ships with moonpool in operational conditions. Several authors have discussed the moonpool responses and increased ship resistance for ships with moonpool in transit. van't Veer and Tholen

(2008) investigated a ship with moonpool in forward speed in calm water by means of model tests, and observed an increase in the ship resistance due to large moonpool oscillations. They reported that the increased resistance due to the moonpool oscillations could be as large as 100 % relative to the measured resistance for a similar vessel without moonpool at certain forward speeds. Son et al. (2008) performed similar studies for moonpools with recess in forward speed, where they observed a reduction in the resistance relative to the resistance for a ship with a clean moonpool. They proposed designs for various devices in the moonpool to further reduce the moonpool-caused resistance by reducing the moonpool oscillations at the piston mode. Fredriksen et al. (2014) performed experimental and numerical studies to investigate the moonpool responses at low forward speed, while the model was forced to heave sinusoidally. They observed that the moonpool responses at the piston mode decreased slightly with forward speed, relative to the moonpool responses in forced heave without forward speed. In the present work, the effect of forward speed is not investigated. We focus on the ship and moonpool responses in operational conditions.

Several authors have studied configurations that are closely related to ships with moonpools. Sun et al. (2010) and Sun et al. (2015) investigated the resonant free-surface motions between two closely spaced rectangular barges in fixed and freely floating conditions. They performed numerical studies with incident waves to investigate the gap and barge responses. Their studies showed that the hydrodynamic interaction between the barge and gap responses, in particular between the gap and heave responses, were significant. Moreover, they observed excitation of higher gap modes due to secondary resonance by solving the first and second order potentials. We discuss secondary resonance for moonpools from the model tests performed in the Ocean Basin. Sphaier et al. (2007) studied a monocolumn platform with a moonpool both experimentally and numerically. The purpose of their study was to investigate whether the platform could be equipped with a moonpool to reduced the heave motion of the platform. They concluded that the monocolumn with moonpool was able to reduce the heave motion of the platform.

1.2 Applicable numerical methods

There exists many numerical methods, each suitable for various flow problems. The Navier–Stokes equations are traditionally solved numerically for viscous flows, and are generally solved numerically by means of the Finite Volume Method (FVM), Finite Difference Method (FDM) or Finite Element Method (FEM) (Ferziger and Perić 2002). The Navier–Stokes solvers are, in general, computationally demanding compared to potential flow solvers. There exists methods which capture fully nonlinear free-surface effects. Such methods are for instance Volume of Fluid

(VOF) or level-set techniques, which are used to capture the free-surface. Ommani et al. (2016) used VOF to predict the moonpool responses in a moonpool with an object, where it showed good agreement with their experiments.

Commonly applied potential flow theory methods are the Boundary Element Method (BEM) and Harmonic Polynomial in Cell (HPC). Shao and Faltinsen (2014) studied the efficiency and accuracy of HPC versus various field methods (such as FVM and FEM) and BEM. Their results show that HPC provides improvements in terms of CPU time over all of the aforementioned methods. There exists many versions of BEM, each with slightly different formulations. In this thesis, BEM is referred to as one method. BEM is widely discussed in the literature, and full detailed derivation can be found in many textbooks, such as Katz and Plotkin (2001) and Faltinsen and Timokha (2009). The benefit with BEM is that only the boundaries enclosing the computational domain need to be modeled. The methods can be simplified further by choosing a Green's function that satisfies the free-surface, bottom wall, and radiation conditions, which is used by e.g. WAMIT (Lee and Newman 2006).

Kristiansen and Faltinsen (2008) used a vortex tracking method to model the damping due to flow separation at the moonpool inlet in a 2D potential flow solver. They observed good agreement between their numerical simulations and model tests.

Grilli (2008) developed a hybrid numerical method by combining BEM with a Navier–Stokes solver in 3D. In the far-field, potential flow theory was assumed. He used nonlinear BEM in the numerical wave tank (NWT), coupled with a Navier–Stokes solver in the proximity of the seabed, to model the complex seabed dynamics.

Greco et al. (2013) developed a 3D domain-decomposition strategy to couple a potential flow solver with a Navier–Stokes solver. In the potential flow domain, they used BEM, while a level-set technique was used to capture complex flow such as slamming on objects due to water on deck. The problem with combining a surface capturing method with BEM, is that the free-surface is a sharp transition from air to water in BEM, while that is not true with surface capturing methods such as VOF or level-set. This requires that the air problem must be solved for by BEM, in addition to other remedies discussed in Greco et al. (2013) and other related papers by the authors.

Kristiansen and Faltinsen (2012) developed a hybrid Navier–Stokes solver in 2D, where they solved for the acceleration potential in the inviscid domain, and the Navier–Stokes equations in the viscous domain. This work was further extended in Kristiansen et al. (2013), where the hybrid method was incorporated into the open

source software OpenFOAM, and they referred to the hybrid solver as Potential Viscous Code in 3D (PVC3D). Fredriksen (2015), and other related articles by the same author, coupled HPC in the inviscid domain with a Navier–Stokes solver in the viscous domain.

In the present work, we want to simulate the water flow for ships with moonpools. There are a few obvious aspects that must be considered while choosing the numerical methods for the present work; first, there is a moving body. Secondly, there is an interface between air and water which must be considered. Finally, based on previous studies, flow separation at the moonpool entrance must be accounted for, which is a viscous effect. Therefore, a hybrid Navier–Stokes solver in 2D, similar to the one developed by Kristiansen and Faltinsen (2012), is implemented in the present work. At the free-surface, linear potential flow theory is assumed, and is referred to as the inviscid domain. In the remaining domain, the Navier–Stokes equations are solved, and is referred to as the viscous domain. The solutions in the two domains are coupled by the pressure. A 2D time-domain BEM assuming linearized potential flow theory is also developed, such that potential flow effects are clearly isolated. Numerical simulations in 3D are carried out using WAMIT and PVC3D.

1.3 Main contributions

Main findings in previous works include addressing the importance of flow separation damping at the piston mode for clean moonpools. The main findings in the present work are summarized as:

- Main source of damping in the proximity of piston and first sloshing modes for moonpools with recess.
- Main source of damping in the vicinity of sloshing modes for clean moonpools.
- Importance of V_{MP}/V_S-ratio on the hydrodynamic interaction between ship and moonpool responses.
- Dominant nonlinear effects at moonpool resonance, such as Duffing-type responses, swirling, and secondary resonance.

The first is investigated in a two-dimensional setting, where both experiments and numerical studies are carried out. The studies are carried out for moonpools with recess. This is motivated by findings in Molin (2017), where he showed that the piston mode shape changed due to the presence of the recess.

The main sources of damping at the piston mode for clean moonpools is widely discussed in the literature, as mentioned earlier. The main source of damping at the piston and sloshing modes is investigated in this thesis work by performing model tests and numerical simulations in both forced heave and in freely floating conditions.

The importance of the V_{MP}/V_S-ratio on the hydrodynamic interaction between ship and moonpool responses is investigated by performing model tests in the Ocean Basin at Sintef Ocean, Norway. The model tests are carried out in a three-dimensional setting with a realistic moonpool vessel. Prior to the model tests in the Ocean Basin, model tests in a wave flume with four different V_{MP}/V_S-ratios are conducted, as preliminary tests to the ones in the Ocean Basin. The findings from the model tests in the wave flume serve as a basis to the model tests in the Ocean Basin.

The following scientific articles were published as a result of the present work: Ravinthrakumar et al. (2019b), Ravinthrakumar et al. (2019a), Ravinthrakumar et al. (2020b) and Ravinthrakumar et al. (2020a).

1.4 Structure of the thesis

The thesis is divided in three parts. In Part I, the theoretical background needed to develop the present numerical methods, and important physics at moonpool resonance, are discussed. The dominant physical aspects to consider for ships with moonpool are discussed in Chapter 2. The mathematical formulations forming the basis for the numerical methods in the present work are presented in Chapter 3.

The model tests and the numerical methods are presented in Part II. The experimental setup in the wave flume at NTNU is presented and discussed in Chapter 4. The experimental setup in the Ocean Basin at Sintef Ocean is presented and discussed in Chapter 5. The numerical methods used in the present work are presented in Chapter 6.

Results, discussions and conclusions are presented in Part III. The results are discussed in Chapters 7 - 9. In Chapter 7, the experimental and numerical results from the forced motion studies are presented. In Chapter 8, the results from the freely floating tests in the wave flume are presented with numerical simulations. The results from the Ocean Basin tests are presented in Chapter 9 with WAMIT simulations. Conclusions and recommendations for further work are presented in Chapter 10.

All variables in the present work are presented in SI units, unless otherwise stated. The results from the model tests and numerical simulations are presented in model

scale. The results are, in general, presented as amplitude-dependent RAOs as function of the period, T, in seconds. The period can be the wave period or forced oscillation period, depending on the conditions the ship model is exposed to. Often non-dimensional periods, e.g. $T^* = T\sqrt{g/D}$, are used to present the results, where g and D are the gravitational acceleration constant and ship draft, respectively. However, the author prefers to present the results in terms of dimensional periods, since it is more relatable in the author's opinion. The same applies for the choice of using T instead of the circular frequency, $\omega = 2\pi/T$.

Chapter 2

Moonpool responses

There are infinitely many resonant modes in a moonpool. Methods to predict the resonant periods in moonpools are briefly presented in §2.1. In §2.2, the coupling between ship and moonpool responses is discussed. Once the natural periods are determined, it is important to estimate the moonpool responses as accurately as possible. This requires that dominant physics in the proximity of the resonant modes are understood. Dominant physics at the piston mode is briefly discussed in §2.3. Finally, beating in the proximity of moonpool resonance is discussed in §2.4.

2.1 Prediction of natural periods

As discussed in §1.1, there exist various methods to predict the natural periods of the resonant modes in a moonpool. In the following sections, some of these methods are presented. In early design stages of ships with moonpool, it is important to determine the natural periods. There exists infinite many natural periods and corresponding modes that can be excited in a moonpool. The zeroth mode is commonly referred to as the piston mode. The piston mode is, in general, associated with a near-uniform mode shape. The term sloshing modes is used to refer to standing waves in the moonpool. The piston and first sloshing mode responses in a two-dimensional setting are illustrated in Figure 2.1. The piston mode is not uniform for long moonpools in freely floating conditions, which we discuss in detail in §9.7.

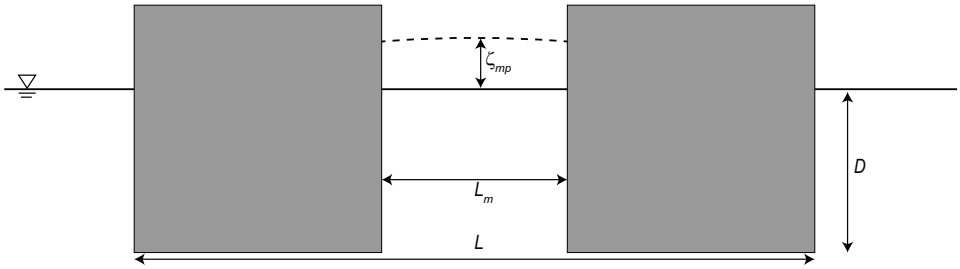

(a) Piston mode

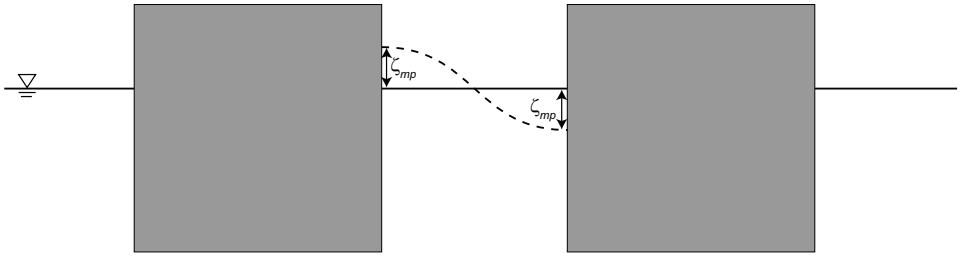

(b) First sloshing mode

Figure 2.1: Sketch illustrating the piston and first sloshing modes in a clean moonpool in a two-dimensional setting. The piston mode oscillates nearly uniformly in the vertical direction. The first sloshing mode is a standing wave with its largest amplitude, typically, at the moonpool ends. ζ_{mp} is used to denote the moonpool response. L_m, L, and D are the length of the moonpool, length of the ship, and draft, respectively.

2.1.1 Clean moonpools

Several authors have presented methods to determine the natural periods and corresponding modes for clean moonpools. By assuming that the moonpool oscillates uniformly in the vertical direction, Faltinsen (1993) showed that the piston mode period can be estimated as

$$T_0 = 2\pi\sqrt{\frac{D}{g}}, \tag{2.1}$$

where D is the draft, and g is the gravitational acceleration. If we imagine that the piston mode response is represented as a mass-spring system, D and g can be interpreted as mass and stiffness, respectively. (2.1) provides a basis to discuss the methods presented in the following.

Molin (2001) presented a method to predict the natural periods and corresponding modes by using domain-decomposition, assuming linear potential flow theory. Two domains were used in the derivation, which results in an eigenvalue problem. Molin (2001) further simplified the eigenvalue problem, such that the natural periods are determined by means of simple expressions. The piston mode period in the two-dimensional case is be obtained as

$$T_0 = 2\pi\sqrt{\frac{D + \underbrace{\frac{L_m}{\pi}\left(\frac{3}{2} + \ln\left(\frac{L_*}{2L_m}\right)\right)}_{①}}{g}}, \tag{2.2}$$

where L_m is the length of the moonpool, and $L_* > L$ is the distance at which the sinks are located to avoid that the potential becomes singular at infinity (details are given by Molin (2001)). (2.2) can be compared with (2.1), where the difference is the additional term in the numerator. ① can therefore be interpreted as an added mass term. Imagine that the moonpool is a rigid body, and oscillates uniformly in the vertical direction. Fluid is displaced due to the motion of the rigid body, and yields an added mass force, which demonstrates why ① can be interpreted as an added mass term.

The nth sloshing mode period using the single mode approximation as presented by Molin (2001) is estimated in 2D as

$$T_n = 2\pi\sqrt{\frac{J_n + \tanh(\lambda_n h)}{g\lambda_n(J_n + \tanh(\lambda_n h))}}, \tag{2.3}$$

where $J_n = -2n/\pi^2 I_{nn}$, I_{nn} is given in Molin (2001, Appendix 1), and $\lambda_n = n\pi/L_m$.

According to DNV (2010), the piston mode period in 3D can be estimated as

$$T_0 = 2\pi\sqrt{\frac{D + \kappa\sqrt{A}}{g}}, \tag{2.4}$$

where A is the cross-sectional area of the moonpool, and κ is a factor which depends on the cross-sectional shape ($\kappa = 0.46$ for a rectangle and $\kappa = 0.473$ for a square). The $\kappa\sqrt{A}$ term is similar to ① in (2.2) in the sense that it can be interpreted as an added mass term. In general, the piston mode periods as predicted using theory by Molin (2001) in 3D and (2.4) yield similar results. In the present

work, methods presented by Molin (2001) are used to estimate the natural periods for clean moonpools.

2.1.2 Moonpools with recess

A domain-decomposition (DD) method to determine the natural frequencies of the resonant modes in a two-dimensional moonpool with recess in finite water depth is developed. The method is a continuation of the method described in Molin (2017), where the flow in the moonpool was two-dimensional, while the flow outside the moonpool was three-dimensional. He assumed that the water depth was infinite and used two subdomains. A fully two-dimensional DD method for the purpose of predicting the natural periods and corresponding modes in a moonpool with recess in finite water depth is needed for the studies in the present work, and is presented in the following. The present DD method was presented in Ravinthrakumar et al. (2019a). Note that the origin of the coordinate system is located at the moonpool inlet in this subsection (cf. Figure 2.2), as done by Molin (2017). Elsewhere in the thesis, the origin is always located at the centre of the vessel at the still waterline.

Linear potential flow theory is assumed. Based on matched eigen-function expansions, the fluid domain is divided into three subdomains. We require that the normal velocities and velocity potentials match at the boundaries of the domains. The main geometric parameters used in the present DD method are indicated in Figure 2.2. In this thesis, the terms moonpool entrance and moonpool inlet are used to refer to the moonpool opening, i.e. in the range $0 < x < a$ at $z = 0$ (cf. Figure 2.2).

The present formulation allows for two recesses. Analytical expressions for the velocity potentials that satisfy the Laplace equation and homogeneous Neumann conditions for ϕ at the walls read

$$\phi_1(x,z) = C_0 + D_0\frac{z-d}{h} + \sum_{n=1}^{\infty}\left[C_n\cosh(\lambda_n(z-d)) + D_n\sinh(\lambda_n(z-d))\right]\cos(\lambda_n(x+b)), \tag{2.5a}$$

$$\phi_2(x,z) = A_0 + B_0\frac{z}{d} + \sum_{n=1}^{\infty}\left[A_n\cosh(\kappa_n z) + B_n\sinh(\kappa_n z)\right]\cos(\kappa_n x), \tag{2.5b}$$

$$\phi_3(x,z) = \sum_{n=1}^{\infty}\left(E_n\frac{\cosh(\mu_n(z+H))}{\cosh(\mu_n H)}\right)\sin(\mu_n(x+B)), \tag{2.5c}$$

with $\lambda_n = \frac{n\pi}{a+b+c}$, $\kappa_n = \frac{n\pi}{a}$ and $\mu_n = \frac{n\pi}{a+B+C}$. The subscripts 1,2, and 3 correspond to the three domains illustrated in Figure 2.2. ϕ_1 and ϕ_2 are similar to that derived by Molin (2017), and ϕ_3 is fairly similar to that derived by Zhang et al. (2019).

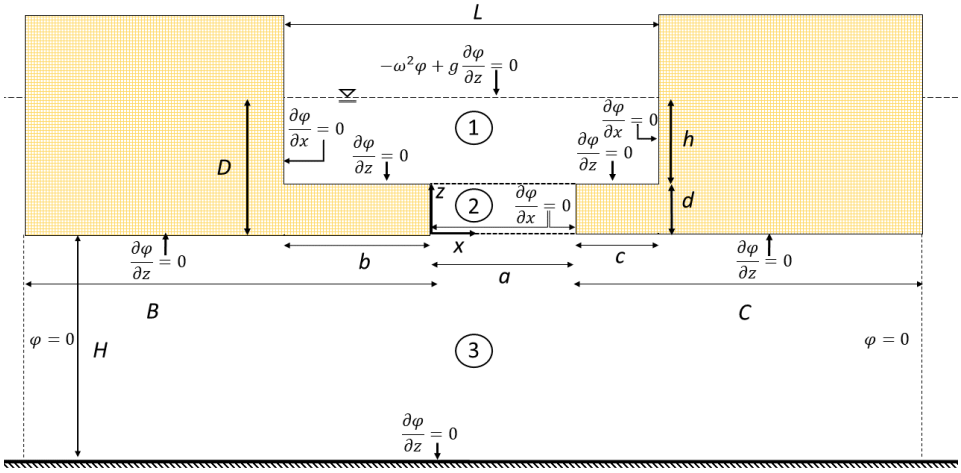

Figure 2.2: Boundary value problem for the present DD method with three subdomains. Main geometric parameters are indicated.

In the two-dimensional case, some remedy must be applied to obtain the piston mode periods, as discussed by Molin (2001). If not, the velocity potential becomes infinite. To remedy this, Molin (2001) placed two sinks outside the ship in the two-dimensional case. An alternative option is to apply homogeneous Dirichlet condition at $x = a + C$ and $x = -B$, as done by Molin et al. (2018) and Zhang et al. (2019). The homogeneous Dirichlet condition, that is $\phi = 0$, is applied in the present DD method, and satisfied in (2.5c). This is equivalent to stating that there are no radiated waves.

At $z = d$, the velocity potentials ϕ_1 and ϕ_2, and their vertical derivatives, are matched such that a vectorial equation system is obtained. First, each side is integrated over the moonpool entrance. Then, multiplying both sides with $\cos(\kappa_n x)$ and integrating over the moonpool inlet, the relationship

$$\vec{A} + \boldsymbol{D_B}\vec{B} = \boldsymbol{M_C}\vec{C} \tag{2.6}$$

is obtained for the matching of ϕ_1 and ϕ_2. $\boldsymbol{D_B} = [1, \tanh(\kappa_n d)]$ is a diagonal matrix, $\boldsymbol{M_C}$ is a full matrix, $\vec{A} = [A_0, \ldots, A_n]$ and $\vec{B} = [B_0, \ldots, B_n]$.

Matching the vertical derivatives of the potentials in domain ① and ②, and performing the two-steps of integration as earlier, gives

$$\vec{D} = \boldsymbol{M_{DA}}\vec{A} + \boldsymbol{M_{DB}}\vec{B}, \tag{2.7}$$

where $\vec{D} = [D_0, \ldots, D_n]$.

The combined free-surface condition reads $-\omega^2\phi_1 + g\frac{\partial\phi_1}{\partial z} = 0$. Inserting for ϕ_1 gives

$$\boldsymbol{D_1}\vec{C} + \boldsymbol{D_2}\vec{D} = \omega^2\left(\vec{C} + \boldsymbol{D_4}\vec{D}\right), \tag{2.8}$$

where $\boldsymbol{D_1} = [0, g\lambda_n \tanh(\lambda_n h)]$, $\boldsymbol{D_2} = [g/h, g\lambda_n]$ and $\boldsymbol{D_4} = [1, \tanh(\lambda_n h)]$ are diagonal matrices as given by Molin (2017).

Performing matching of the velocity potentials ϕ_2 and ϕ_3, and their vertical derivatives, at $z = 0$, we obtain

$$\vec{A} = \boldsymbol{M_{EA}}\vec{E}, \tag{2.9a}$$
$$\vec{E} = \boldsymbol{M_{BE}}\vec{B}. \tag{2.9b}$$

Combining (2.6) to (2.9) gives the eigenvalue problem

$$\begin{aligned}&\left\{\boldsymbol{D_1} + \boldsymbol{D_2}\left[\boldsymbol{M_{DA}}\boldsymbol{M_C} + (\boldsymbol{M_{DB}} - \boldsymbol{M_{DA}}\boldsymbol{D_B})(\boldsymbol{M_{EA}}\boldsymbol{M_{BE}} + \boldsymbol{D_B})^{-1}\boldsymbol{M_C}\right]\right\}\vec{C}\\ -\omega^2&\left[\boldsymbol{I} + \boldsymbol{D_4}\boldsymbol{M_{DA}}\boldsymbol{M_C} + \boldsymbol{D_4}(\boldsymbol{M_{DB}} - \boldsymbol{M_{DA}}\boldsymbol{D_B})(\boldsymbol{M_{EA}}\boldsymbol{M_{BE}} + \boldsymbol{D_B})^{-1}\boldsymbol{M_C}\right]\vec{C} = 0.\end{aligned} \tag{2.10}$$

The natural frequencies $\omega_n = 2\pi/T_n$, with $n = 0, 1, \ldots, \infty$, are the solutions to (2.10). The natural frequencies are predicted with a precision of four significant digits with $N = 25$, where N is the number of terms in the series in (2.5). Hence, $N = 25$ is used in the present work. This is discussed in Appendix C.1.1.

2.2 Freely floating ship with moonpool

In reality, the ship is freely floating where it responds in six degrees of freedom (DOF). The ship motions are coupled for a freely floating rigid body (Faltinsen 1993). For instance, it is well-understood that the heave and pitch motions are coupled for a ship with no fore-aft-symmetry. Similarly, the moonpool response is "coupled" with the ship responses, as discussed by e.g. Fredriksen et al. (2015). We use the term *hydrodynamic interaction* to discuss that the ship motions may be affected by the moonpool, and vice versa, in this thesis. Strictly speaking, this is not hydrodynamic interaction. Hydrodynamic interaction can be observed

for e.g. two ships operating side-by-side, which is not the case for the presently investigated ship models with moonpools, since there is only one body.

For the sake of explaining the coupling between ship and moonpool responses, it is imagined that the heave and moonpool responses are represented as a coupled two DOF system. The damping is neglected in the present discussion. The rigid body modes surge, sway, heave, roll, pitch and yaw are denoted by η_i in this thesis, where $i = 1, 2, \ldots, 6$, following the definitions by Faltinsen (1993). In this section, the moonpool response is denoted as η_7, and is assumed to oscillate as a rigid body, as done by Molin (2001) with the frozen approximation. The coupled two DOF system reads

$$(M + A_{33})\ddot{\eta}_3 + A_{37}\ddot{\eta}_7 + C_{33}\eta_3 = F_{3,exc}, \tag{2.11a}$$
$$(m + A_{77})\ddot{\eta}_7 + A_{73}\ddot{\eta}_3 + C_{77}\eta_7 = F_{7,exc}, \tag{2.11b}$$

where A_{ij} and C_{ij} are the added mass and restoring coefficients in i-direction due to motion in the j-direction. $F_{i,exc}$ is the excitation force in the i-direction, which is set equal to zero when determining the natural periods. m and M are the mass of the moonpool and the vessel, respectively. The homogeneous problem of (2.11) is written in matrix form as

$$\left(-\omega^2(\boldsymbol{M} + \boldsymbol{A}) + \boldsymbol{C}\right)\boldsymbol{\eta} = \boldsymbol{0}, \tag{2.12}$$

where $\boldsymbol{M}$, $\boldsymbol{A}$ and $\boldsymbol{C}$ are the mass, added mass and restoring matrices, and $\boldsymbol{\eta} = [\eta_3, \eta_7]$. The trivial solution of the two DOF system is that $\boldsymbol{\eta} = \boldsymbol{0}$. The determinant of the coefficients of $\boldsymbol{\eta}$ must be zero, i.e. $\det\left(-\omega^2(\boldsymbol{M} + \boldsymbol{A}) + \boldsymbol{C}\right) = \boldsymbol{0}$, to determine the non-trivial solution.

The equations above are a simplification of the reality. However, they can be used to illustrate how the moonpool response is coupled with the ship motions, and vice versa. The off-diagonal terms in the added mass matrix provide the coupling between the ship and moonpool responses, which results in a shift in the natural period relative to the one found using the methods presented in §2.1. The shift depends on how strong the coupling is, which is discussed in more detail in Chapter 9. For clean moonpools, A_{77} can be determined using ① in the single mode approximation in (2.2). The coupled added mass term, A_{37}, can then be treated as an unknown. We present such a simplified analysis in §9.1.

2.3 Sources of damping

When resonant moonpool oscillations occur, damping plays a dominant role. Several authors have discussed damping of the moonpool response at the piston mode, see e.g. Kristiansen and Faltinsen (2012), Fredriksen et al. (2015) and Faltinsen and Timokha (2015). There are two main sources of damping of the moonpool response; wave radiation damping and viscous damping. The former is associated with wave radiation due to communication between the moonpool response and the outer domain, as illustrated on the left in Figure 2.3. The latter is associated with damping due to flow separation at the moonpool inlets, as illustrated on the right in Figure 2.3. Damping due to flow separation is dominant at the piston mode. The damping due to flow separation is amplitude-dependent, which means that the moonpool RAOs are amplitude-dependent at the piston mode.

In reality, separated vortical structures (wake flows) quickly become turbulent. Kristiansen and Faltinsen (2008) discussed that the primary vortices provide the main contribution to damping of the moonpool response. They also showed that the vortices travelled away from the moonpool in pairs, as illustrated in Figure 2.3 (i.e. the vortex pairs (A) are not of major importance with respect to the moonpool response). This means that a laminar Navier–Stokes solver is, in general, adequate to predict the moonpool responses.

Kristiansen and Faltinsen (2008) showed that the damping due to the boundary layer close to the walls in the moonpool is negligible. This implies that the moonpool responses can be determined with a Navier–Stokes solver without a fine mesh close to the moonpool walls to resolve the boundary layer. Similar observations were made recently by Chua et al. (2018), where they investigated the viscous energy dissipation due to skin friction and vortex shedding for two fixed and closely spaced barges in incident waves. They showed that the damping due to flow separation was approximately five orders of magnitude larger than skin friction damping. Kristiansen (2009) presented results for the moonpool response from nonlinear BEM simulations, and compared them against experiments and linear BEM simulations. Their study showed that damping due to nonlinear free-surface effects are negligible for all practical purposes for small moonpools, and that linear theory is adequate at the piston mode for the configurations studied therein.

Typically, moonpools on real ships are equipped with appendages and/or damping grids to increase the damping of the moonpool oscillations. A photo taken on a real moonpool with damping grids is presented in Figure 2.4. In the present work, we investigate the moonpool responses in naked moonpools, i.e. without supplements to damp the moonpool oscillations, while acknowledging that the additional damping can be introduced by the damping grids. However, preliminary model

tests performed by Trygve Kristiansen (personal conversations, 2019) indicated low damping effect of such vertical perforated plates near the walls.

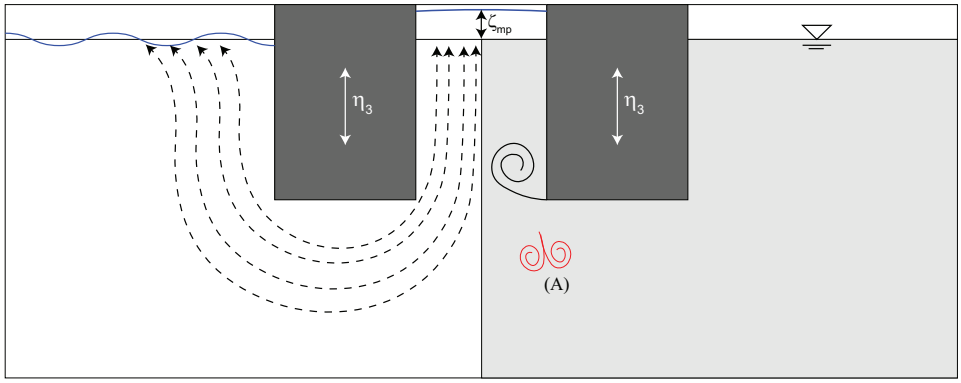

Figure 2.3: Model in forced heave, η_3. Two main sources of damping on the moonpool response; wave radiation damping and viscous damping due to flow separation. The latter is illustrated on the grey part (right side), and the former is illustrated on the left side. Vortex pairs (A) are indicated with red color, and are of minor importance with respect to the moonpool response.

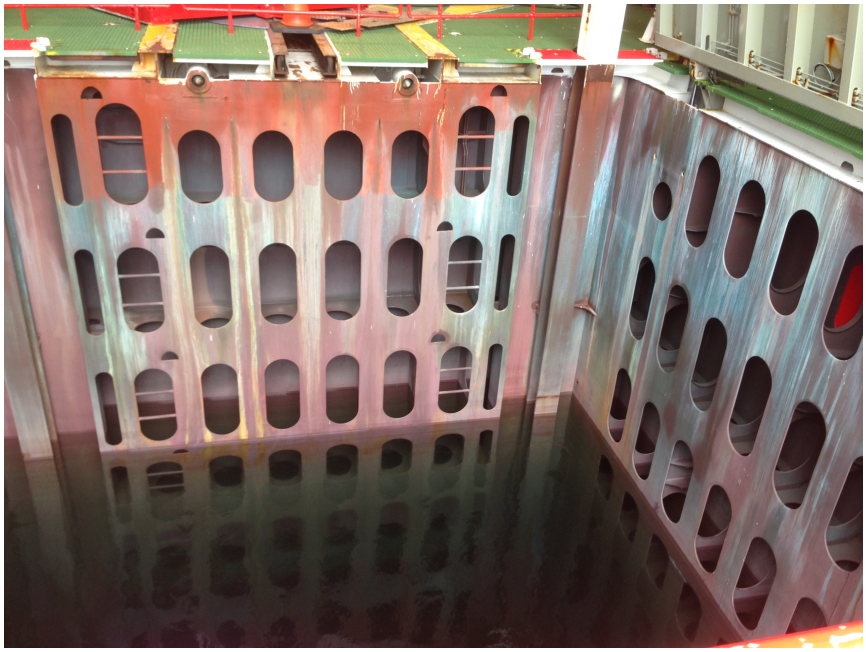

Figure 2.4: An offshore service vessel with moonpool. The moonpool is equipped with damping grids (perforated plates) to damp the moonpool oscillations. Photo taken by Babak Ommani.

2.4 Beating

In the present work, we are interested in the steady-state responses. If the system is lightly damped, a significant amount of time is required to reach steady-state in the proximity of a resonant mode, due to beating. In order to explain the beating phenomenon, a one DOF mass-damper-spring system is imagined on the form

$$m\ddot{x} + b\dot{x} + kx = F_a \sin(\omega t), \tag{2.13}$$

where m, b, k and F_a are the mass, damping, stiffness and excitation force coefficients. Here, x is the motion of the mass. The steady-state solution of (2.13) can be found in many textbooks (e.g. Kreyszig (2011)), and is $x(t) = A\sin(\omega t + \epsilon)$, where ϵ is the phase angle between the force and response, and A is the amplitude of the response. The steady-state solution is independent of the initial conditions, as one requires that the initial transients have died out, and the mass oscillates at the driving frequency ω.

Besides the steady-state (particular) solution, there exists a homogeneous solution to (2.13). The transient part of the solution is, in general, damped out quickly. However, if the system is lightly damped, the transient response will persist for a significant amount of time. In the undamped case, the transient solution persists as $t \to \infty$, and the total solution takes the form

$$x(t) = C\left(\frac{1}{\omega_n^2 - \omega^2}\right)\sin\left(\frac{(\omega_n - \omega)t}{2}\right)\sin\left(\frac{(\omega_n + \omega)t}{2}\right) \tag{2.14}$$

where C is the amplitude of the response. ω_n and ω are the natural and driving frequencies, respectively. If the system is lightly damped, the response will contain beats, as illustrated in Figure 2.5(a). This is a practical problem in the present BEM simulations, where the radiation damping in the proximity of the sloshing modes is small. Consequently, a significant amount of simulation time is needed to damp out the transient response. To remedy this, artificial damping is applied, and linearly released after the transient response is damped out. The implementation of the artificial damping is presented in §6.1.1. An example of the moonpool response, where artificial damping is applied, is illustrated in Figure 2.5(b).

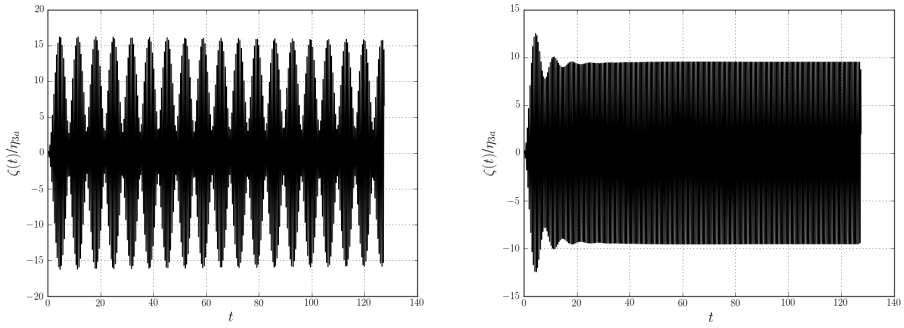

(a) No artificial damping applied **(b)** With artificial damping

Figure 2.5: Example time-series from forced heave simulations with the presently developed 2D linear time-domain BEM, illustrating the importance of artificial damping in the proximity of the first sloshing mode. The artificial damping is linearly released. Here, ζ is the free-surface elevation in the moonpool, and η_{3a} is the forced heave amplitude.

Chapter 3

Mathematical formulations

Mathematical formulations forming the basis for the presently developed viscous and potential flow solvers are presented in this chapter. Although the presently developed codes are two-dimensional solvers, the mathematical formulations are formulated in 3D. Finally, wavemaker theory is presented, since it is used throughout the thesis.

3.1 Incompressible Newtonian fluid

The pressure and velocities in a fluid domain are determined from the Navier–Stokes equations. Incompressible Newtonian fluid properties are assumed. Detailed derivations of the Navier–Stokes equations can be found in many textbooks, such as Schlichting (1979). The momentum equation for an incompressible fluid is

$$\underbrace{\rho\frac{\partial \boldsymbol{u}}{\partial t}}_{①} + \underbrace{\rho \boldsymbol{u}\nabla \boldsymbol{u}}_{②} = \underbrace{-\nabla p}_{③} + \underbrace{\mu\nabla^2 \boldsymbol{u}}_{④} + \underbrace{\boldsymbol{X}}_{⑤}, \tag{3.1}$$

where $\boldsymbol{u} = [u, v, w]$ is a vector containing velocity components of the fluid particles in x-, y- and z-direction. $\boldsymbol{X}$ is a vector accounting for gravity forces, p is the pressure, ρ is the density of the fluid, μ is the dynamic viscosity coefficient, and $\nabla = \left[\frac{\partial}{\partial x}, \frac{\partial}{\partial y}, \frac{\partial}{\partial z}\right]$. (3.1) is valid when the flow is laminar, since the disregarded turbulent stress components might be important at large Reynolds numbers (Schlichting 1979). The governing equations consist of the momentum equation (3.1) and the continuity equation

$$\nabla \cdot \boldsymbol{u} = 0. \tag{3.2}$$

Physically, ① in (3.1) is the term due to acceleration of the fluid particles. ② is the advection acceleration term, due to an Eulerian description of the flow. ③ is the term due to pressure forces, where the pressure gradient accelerates the fluid. ④ is the diffusive term, which is due to shear forces between the fluid particles. ⑤ is the contribution from gravity, which is $\boldsymbol{X} = [0, 0, -\rho g]$ in an Earth-fixed coordinate system with z positive upwards.

3.2 Potential flow

In the present work, numerical simulations with BEM assuming linear potential flow theory are carried out to clearly distinguish between potential flow and viscous effects in the moonpool responses. In addition, we apply linear potential flow theory in the inviscid domain in the present hybrid Navier–Stokes solver.

We assume that the fluid is incompressible and inviscid, and that the flow is irrotational. The consequence of assuming potential flow theory is that the flow can be represented in terms of a velocity potential, ϕ, which can be used to determine the fluid velocities and pressure (see e.g. Faltinsen (1993)). We assume that there exists a velocity potential such that $\boldsymbol{u} = \boldsymbol{\nabla}\phi$, and the continuity equation (3.2) is expressed as

$$\nabla^2 \phi = 0. \tag{3.3}$$

Numerical simulations with the linear potential flow solver (BEM) are carried out by solving ϕ in the computational domain. The velocities and pressure are determined given the velocity potential.

In the hybrid Navier–Stokes solver, the Navier–Stokes equations are solved in the viscous domain. In the inviscid domain, linear potential flow theory is assumed (cf. §6.5), where we solve for the pressure as $\nabla^2 p = 0$, using that $p = -\rho \frac{\partial \phi}{\partial t}$. ② and ④ in (3.1) are neglected in the inviscid domain. We require that the pressure and velocities are continuous at the intersection of the viscous and inviscid domains. This implies that separated vortical structures shall not travel into the inviscid domain. We attempt to satisfy this by ensuring that the vortices do not travel into the viscous domain. The potential flow domain allows for circulation, but not vorticity. An alternative, which is not applied in the present work, is to apply a numerical scheme to damp out the vortices travelling into the inviscid domain.

3.3 Boundary conditions

Boundary conditions are needed to determine the fluid motions. We distinguish between two types of boundary conditions; Neumann and Dirichlet boundary conditions. Neumann boundary conditions are applied on boundaries where the derivative of a solution is known. Dirichlet boundary conditions are imposed on boundaries where the value of the solution is known. Figure 3.1 illustrates a numerical wave tank (NWT) with a surface-piercing body, where different types of boundaries are illustrated.

In the present study, linearized body-boundary and linearized free-surface conditions are applied. This implies that the mesh remains undeformed throughout the simulation, and the boundary conditions are applied at the mean position of the moving boundary. Consequently, computational time related to re-meshing is saved. Linearized body-boundary conditions are justified if the relative flow is dominated by the water motions. Linearized free-surface conditions are, naturally, justified if nonlinear free-surface motions are negligible.

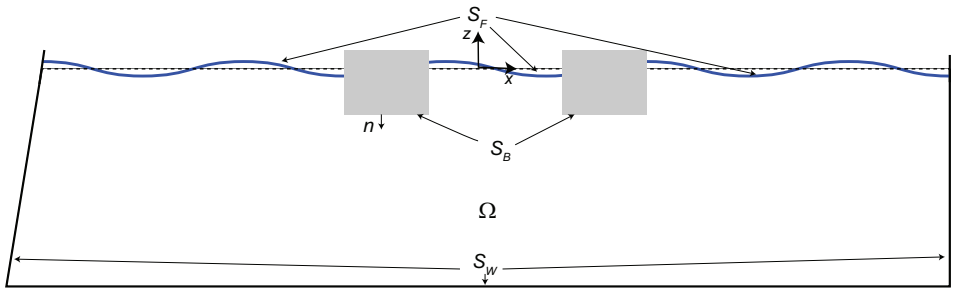

Figure 3.1: Sketch of numerical wave tank (NWT) with a flap-type wavemaker to the left. S_B, S_W and S_F are the surfaces of the body, walls and free-surface, respectively. $\boldsymbol{n}$ is the normal vector, pointing into the fluid. Ω is the computational domain.

3.3.1 Rigid body surfaces

Linearized body-boundary conditions are applied on the tank walls of the NWT and the body (S_W and S_B in Figure 3.1, respectively). It is assumed that the boundaries are rigid. We require that the normal flow velocity on the boundary is equal to the normal velocity of the body, i.e. $\boldsymbol{u} \cdot \boldsymbol{n} = \boldsymbol{U} \cdot \boldsymbol{n}$. Here, $\boldsymbol{U}$ and $\boldsymbol{n}$ are the body velocity and normal vectors. In addition, no-slip condition are needed to solve the Navier–Stokes equations, and are imposed as $\boldsymbol{u} \cdot \boldsymbol{s} = \boldsymbol{U} \cdot \boldsymbol{s}$, where $\boldsymbol{s}$ is the tangential vector.

The Navier–Stokes equations require a boundary condition for the pressure, which is derived by neglecting the advection and diffusion terms in (3.1) as

$$\frac{\partial p}{\partial n} = -\rho \boldsymbol{a} \cdot \boldsymbol{n}. \tag{3.4}$$

Here, $\boldsymbol{a} = [a_x, a_y, a_z]$ is the body acceleration vector in the x- y-, and z-directions.

3.3.2 Free surface

Since the interface between air and water is free to move, the velocity on the free-surface boundary (S_F in Figure 3.1) is unknown a priori. There are two unknowns on the free-surface; the free-surface elevation and the pressure. To estimate these, we require that a particle on the free-surface remains on the free-surface, and that the pressure is atmospheric at $z = \zeta$, where ζ is the free-surface elevation.

Requiring that a particle on the free-surface remains on the free-surface, the kinematic free-surface condition is obtained as

$$\frac{D(z-\zeta)}{Dt} = 0 \qquad \Rightarrow \qquad \frac{\partial \phi}{\partial z} = \frac{\partial \zeta}{\partial t} + \nabla\phi \cdot \nabla\zeta, \tag{3.5}$$

where the material derivative is defined as $\frac{D}{Dt} = \frac{\partial}{\partial t} + \nabla\phi \cdot \nabla$. The pressure at the interface between the air and water is required to be atmospheric. This serves as a dynamic condition on the free-surface, and is expressed by using Bernoulli's equation as

$$p - p_a = \rho g\zeta + \rho\frac{\partial \phi}{\partial t} + \rho\left|\nabla\phi\right|^2 = 0 \qquad \Rightarrow \qquad g\zeta = -\frac{\partial \phi}{\partial t} - \left|\nabla\phi\right|^2. \tag{3.6}$$

Thus, (3.5) and (3.6) form the two equations needed to determine the two unknowns on the free-surface, namely ζ and ϕ. Since linearized free-surface conditions are applied, (3.5) and (3.6) become

$$\frac{\partial \zeta}{\partial t} = \frac{\partial \phi}{\partial z} \qquad \text{at } z = 0, \tag{3.7a}$$

$$\frac{\partial \phi}{\partial t} = -g\zeta \qquad \text{at } z = 0. \tag{3.7b}$$

In the present hybrid Navier–Stokes solver, the uppermost cell layer constitutes the inviscid domain. Thus, the linearized free-surface conditions are applied to the Navier–Stokes solver by using that $w = \frac{\partial \phi}{\partial z}$ and $p = -\rho\frac{\partial \phi}{\partial t}$. This yields a differential evolution equation for the free-surface elevation as $\frac{\partial \zeta}{\partial t} = w$, and a boundary condition $p = \rho g\zeta$, at $z = 0$.

3.4 Wavemaker theory

Experiments and numerical simulations with a freely floating model in a wave tank with incident regular waves are presented in this thesis. Consequently, there is a need for analytical solutions of the relationship between the wavemaker motion and the resulting far-field wave height. Such analytical expressions between the stroke amplitude of the wavemaker, S, and generated wave height, H, can be found in many textbooks, see e.g. Dean and Dalrymple (1991, p. 177). They present the full derivation for the RAOs, H/S, for both *piston-type* and *flap-type* wave generators, assuming linear potential flow theory. A wave tank with a hinged flap-type wave generator on the left-hand side is illustrated in Figure 3.2.

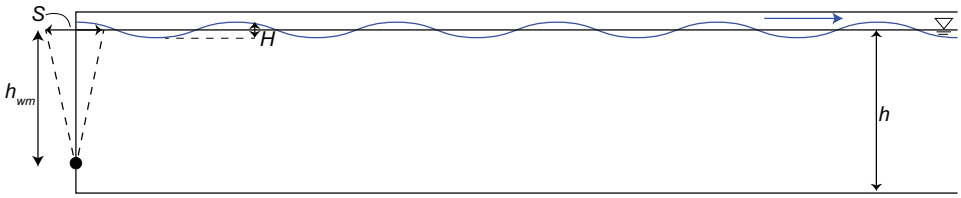

Figure 3.2: Wave tank with a hinged flap-type wavemaker with stroke, S, generating waves with wave height H. The water depth in the wave tank is h. h_{wm} is the height of the hinged flap-type wavemaker.

The relationship between the steady-state far-field wave height and wave generator stroke is

$$\frac{H}{S} = \left(\frac{2\cosh(2kh) - 1}{\sinh(2kh) + 2kh} \right), \qquad \text{(piston)} \tag{3.8a}$$

$$\frac{H}{S} = \left(\frac{4\sinh(kh)}{\sinh 2kh + 2kh} \right) \left(\sinh(kh) + \frac{\cosh(kh - kh_{wm}) - \cosh(kh)}{kh_{wm}} \right), \qquad \text{(hinged flap)} \tag{3.8b}$$

$$\frac{H}{S} = \left(\frac{4\sinh(kh)}{\sinh(2kh) + 2kh} \right) \left(\frac{kh\sinh(kh) - \cosh(kh) + 1}{kh} \right), \qquad \text{(flap)} \tag{3.8c}$$

where H is the steady-state wave height far away from the wave generator. h and k are the water depth and wave number, respectively. h_{wm} is the height of the hinged flap. The hinged flap-type wavemaker is used in the experiments, which is illustrated in Figure 3.2. (3.8c) is simply a special case of (3.8b), where $h_{wm} = h$, which is used in the present numerical simulations.

Part II

Experiments and Numerical Methods

Chapter 4

Experiments in 2D wave flume

Model tests were carried out in a wave flume at the Marine Technology Centre in Trondheim, Norway. In the period August-October 2017, forced heave experiments were carried out for moonpools with recess in a two-dimensional setting. The same configurations were tested in freely floating conditions in April 2018. In July 2018, models with clean moonpools were tested in a quasi three-dimensional setting. The term quasi three-dimensional will become clear to the reader after reading this chapter.

An illustration of the models is provided in Figure 4.1. Different types of boxes were used to represent the moonpool configurations. In the two-dimensional set-up for moonpools with recess, boxes A and C constituted the model, while boxes A and B were used to create the clean moonpools tested in a quasi three-dimensional setting.

The tank is 13 m long, 0.6 m wide, and a water depth of 1.0 m was used. The tank is equipped with a wavemaker and an oscillator. Details of the wave flume and experimental setups are provided in the following. First, the characteristics of the wave flume are given in §4.1 - §4.3. This is followed by error analysis in §4.4. Finally, detailed description of each setup in the wave flume is given in §4.5 and §4.6. The measured data was sampled with a frequency of 200 Hz, while the input to the wavemaker and oscillator were given with sample frequency of 50 Hz.

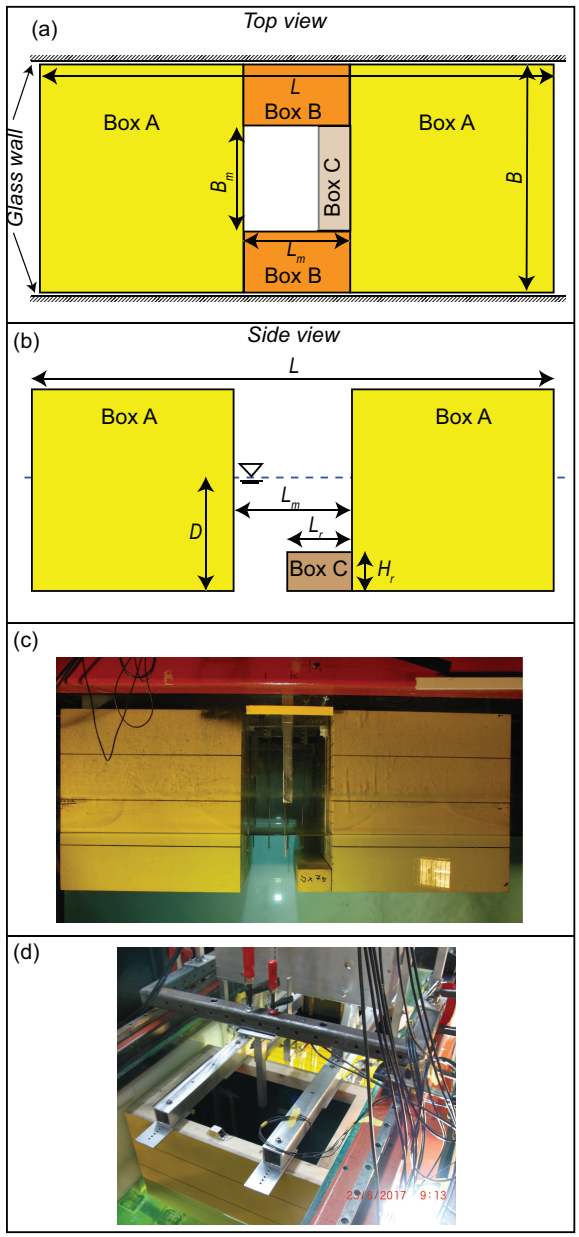

Figure 4.1: Experimental set-up in the wave flume. Three box-types were used; Box A was used in all of the tests. Box B was only used in the quasi three-dimensional model tests. Box C was only used in the configurations in a two-dimensional setting, where moonpools with recess were tested. L and B are the model length and width. L_m and B_m are the moonpool length and width. L_r and H_r are the recess length and height. (a) bird's eye view of the set-up, (b) side view of the set-up, (c) and (d) photos from the model tests.

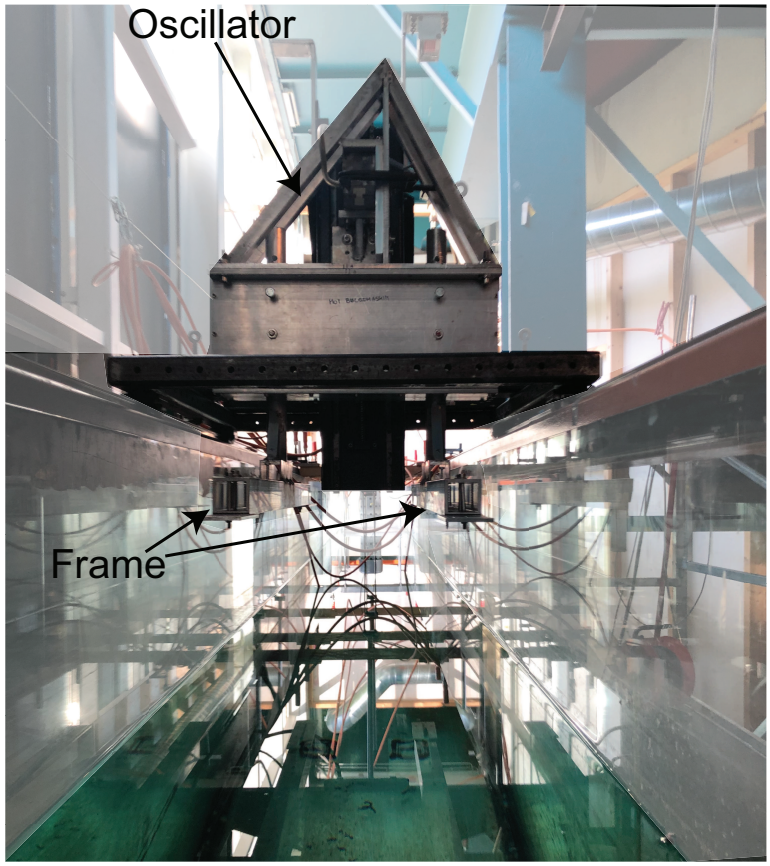

Figure 4.2: Photo of the wave flume seen from the wavemaker. The oscillator was located at the middle of the wave flume. Oscillator was fixed to a carriage. Carriage fixed to the rails in the wave flume. Tank width 0.60 m. The model width was 0.59 m. Models were fitted rigidly to the frame.

4.1 Oscillator

The oscillator in the wave flume was used to perform model tests in forced heave. The model was fastened to the oscillator with a frame mounted on top of the model (the oscillator and the frame are illustrated in Figure 4.2). Model tests in both regular and irregular forced heave motions were conducted.

4.1.1 Regular forced heave motion

The regular forced heave oscillations of the model were specified in terms of long time series (typically 20-24 hours). Waiting time of three minutes was used for the free-surface to calm down. The duration of each test was $60T$, where T is the forced heave period. Linear ramp up and ramp down, as discussed in §6.3, were applied at the start and end of each test (the duration of the linear ramps were $5T$). An example of a long time-series from the forced heave experiments is presented in Figure 4.3.

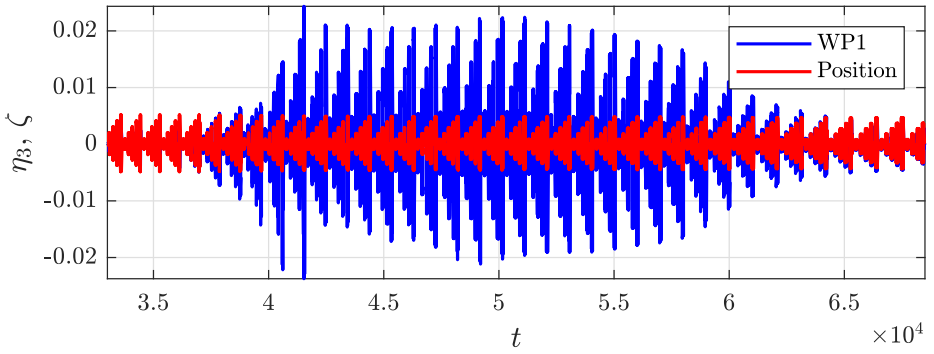

Figure 4.3: t is the time in seconds. An example time-series from the forced heave experiments in the wave flume (approximately the last half of the time-series is presented for the sake of clarity). The forced heave motion of the model, η_3, and the free-surface elevation in the moonpool at WP1 (located at the opposite wall end of the recess, cf. Figure 4.13), ζ, are presented.

It was observed that the oscillator delivered somewhat lower forced heave amplitudes, primarily for low forced heave periods, than specified. In order to account for this, a mechanical transfer function between the specified and measured forced heave amplitude, κ, was used, as presented in Figure 4.4. Thus, the sinusoidal motion of the oscillator was defined as

$$\eta_3(t) = r(t)\kappa(T)\eta_{3a}\sin(\omega t), \tag{4.1}$$

where $\omega = 2\pi/T$ and η_{3a} is the forced heave amplitude. $r(t)$ is the ramp function

as defined in §6.3.

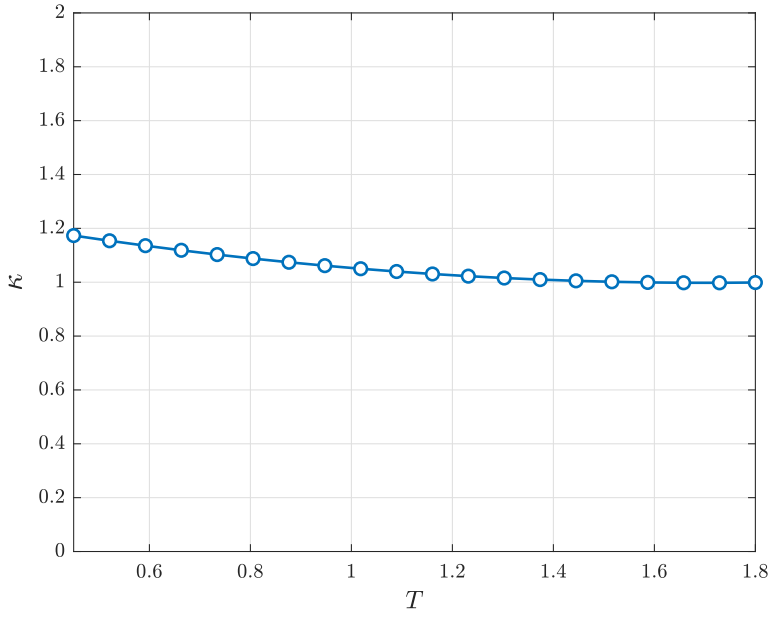

Figure 4.4: Transfer function between specified and measured forced heave amplitude. For low forced heave periods ($T \approx 0.5$ s), the oscillator delivered approximately 20 % lower forced heave amplitudes than specified.

4.1.2 Irregular forced heave motions

The 3DQ configurations, which are presented in §4.5, were tested in irregular forced heave motion in an attempt to achieve moonpool RAOs faster than by performing regular forced heave tests. The duration of each test was 15 minutes, with linear ramp ups and ramp downs of ten seconds. Waiting time of seven minutes was used for the free-surface to calm down.

Pink noise spectra were used to define the irregular forced heave motion. We define the magnitude of the pink noise spectra such that we obtain $\eta_{3S} = 1$ mm, 2 mm, 3 mm, 4 mm and 5 mm. η_{3S} is the average of the third largest peaks of the irregular forced heave motion.

The specified and measured pink noise spectra are presented in Figure 4.5. Fair agreement between the specified and measured spectra are observed, although some discrepancies for $T < 0.7$ s are illustrated. The differences between the specified and measured spectra are up to approximately 25 % in this forced heave period range. We believe this is due to that the mechanical transfer function κ is not included in defining the pink noise spectra.

The irregular forced heave motion is realized as

$$\eta_3(t) = \sum_{i=1}^{N} \sqrt{2S_{\eta_3}(\omega_i)\Delta\omega}\sin(\omega_i t + \epsilon_i) \tag{4.2}$$

where ϵ_i is a uniformly distributed random variable between 0 and 2π. $\Delta\omega = 2\pi/T_{dur}$, where T_{dur} is the total duration of the test.

The moonpool RAOs, ζ_{mp}/η_{3a}, are determined in the usual sense as

$$\frac{\zeta_{mp}}{\eta_{3a}} = \sqrt{\frac{S_{\zeta_{mp}}}{S_{\eta_3}}}, \tag{4.3}$$

where $S_{\zeta_{mp}}$ and S_{η_3} are the measured moonpool response and forced heave spectra. We assume that the spectra represent stationary processes and that here is a linear relationship between the forced heave and moonpool response spectra. A moving average approach is used to smooth the measured spectra from the model tests.

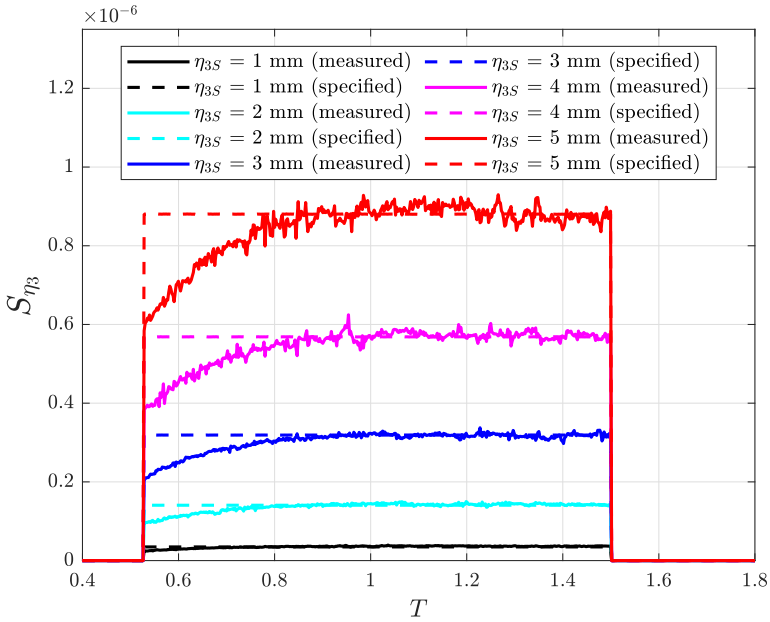

Figure 4.5: Specified and measured forced heave spectra from the irregular forced heave motion tests.

4.2 Wavemaker

The wave flume is equipped with a hinged flap-type wavemaker. The wavemaker was hinged 0.1 m from the bottom of the wave flume. As for the oscillator, the input of the flap motion was given as long time-series. Given the water depth, wave period and wave steepness, the stroke of the flap was calculated using (3.8b).

The duration of the wavemaker motion was chosen such that it stopped when re-reflected waves reached the model, that is, the tests were stopped when $t = \frac{3L_e}{c_g}$, where L_e is the distance from the wavemaker to the model, and c_g is the group velocity as predicted by linear wave theory. Each test was followed by a waiting time of three minutes for the free-surface to calm down. Linear ramp up and ramp down were applied at the start and end of each test, where the duration of the linear ramps were $2T$. Here, T is the wave period.

In order to obtain the specified wave height in the experiments, two transfer functions were established; a transfer function between the specified and measured stroke amplitude, $\alpha(T)$, and a transfer function between the specified and measured wave height, $\beta(T)$. The transfer functions α and β are presented in Figure 4.6 with three different wave steepnesses, H/λ. First the transfer function α was established. Subsequently, the transfer function β was established given the correction on the flap motion using α. β was established by measuring the wave height with a wave probe located at the center of the wave flume. The sinusoidal flap motion, σ, was defined as

$$\sigma(t) = \frac{1}{\alpha(T)\beta(T)} r(t) \frac{S}{2} \sin(\omega t). \tag{4.4}$$

4.3 Undesired resonant modes in the wave flume and the moon-pool

Resonant fluid motion in the wave flume can be excited at certain periods. The natural periods in the wave flume, T_{nf}, are determined as

$$T_{nf\ i,j} = 2\pi \sqrt{\frac{1}{g k_{i,j} \tanh(k_{i,j} h)}}, \tag{4.5}$$

as derived by Faltinsen and Timokha (2009, p. 131). Here, $k_{i,j} = \pi \sqrt{(i/L_t)^2 + (j/B_t)^2}$. L_t, B_t and h are the length, width and water height of the wave flume. i and j are indices of the resonant sloshing modes in the longitudinal and transverse tank directions, respectively.

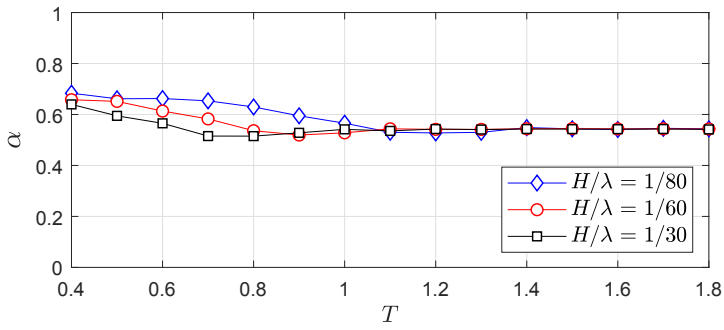

(a) Transfer function between specified and measured flap stroke.

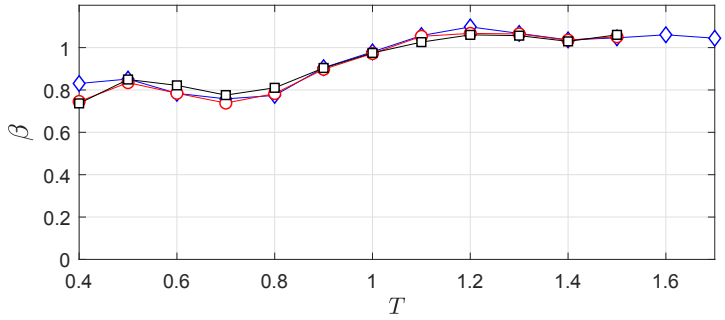

(b) Transfer function between specified and measured wave height.

Figure 4.6: Transfer functions α and β for the wavemaker in the wave flume.

The first longitudinal sloshing mode of the wave flume (seiching mode) is approximately 8.7 s, which is far outside the tested range in the present work. The first transverse sloshing mode is approximately 0.88 s, which is in the tested range. The second and third transverse sloshing modes in the tank are 0.62 s and 0.5 s, respectively.

Transverse sloshing was detected using paired wave probes inside and outside the moonpool. For the present configurations, the first transverse sloshing mode in the moonpool was excited in the model tests that were carried out in a two-dimensional setting. However, the second and third sloshing modes were not detected during any of the model tests. Tests containing transverse sloshing are removed from the moonpool RAOs.

An example time-series where transverse sloshing occurred from the forced heave tests are presented in Figure 4.7. Transverse sloshing occurred at $T = 0.82$ s for Case 3, and not $T = 0.88$ s as discussed above, due to that the presence of the recess. The phases between the measured free-surface elevations in the moonpool indicated that transverse sloshing occurred in the moonpool. An interesting note was that when transverse sloshing occurred, it occurred almost immediately. We expected that transverse sloshing would develop over a longer time span.

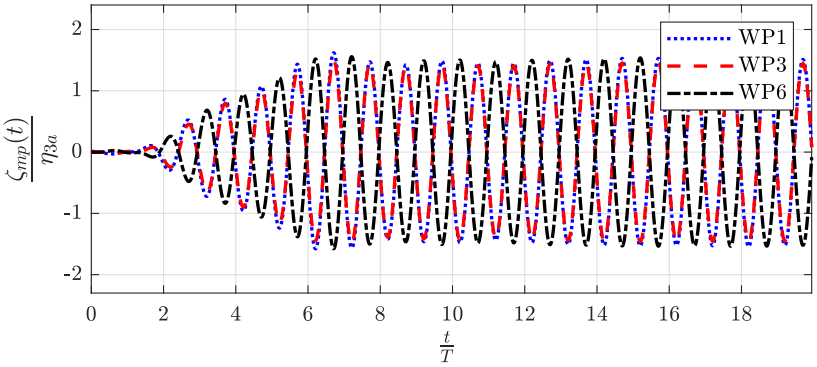

Figure 4.7: Transverse sloshing in the moonpool for Case 3 are presented (cf. Table 4.1). $T = 0.82$ s and η_{3a} = 3 mm. The wave probe (WP) numbering is illustrated in Figure 4.13.

4.4 Error analysis

The experiments were carried out carefully in order to minimize potential error sources. In this section, some of the potential error sources are addressed and discussed (besides those discussed in §4.1 - 4.3), in order to assess the quality of the experimental results.

4.4.1 Parabolic beaches

The tank was equipped with two parabolic beaches; one on each end of the tank to avoid wave reflection. The parabolic beaches were adjusted prior to each test such that the uppermost point of the beaches was located approximately 2 mm below the free-surface, which was found in Kristiansen and Faltinsen (2012) to be efficient for waves with small wave steepness. With a parabolic beach, however, it is not always possible to avoid reflection for all wave periods and wave steepnesses. For long waves ($T \gtrsim 1.4$ s), some reflection was expected, based on previous studies and the wavelength-to-beach length ratio. In the case with incident waves, only one parabolic beach at the opposite end of the wavemaker was used.

4.4.2 Wave probes

Wave probes are sensitive to large temperature variations in the surroundings. The temperature variations in the wave flume were small during the testing period (within 1 degree Celsius between each time the wave probes were calibrated). Still a drift in the zero value was observed. This offset was accounted for by daily zero-setting, and during post-processing. The paired wave probes in the moonpool gave similar results, except when transverse sloshing occurred (as discussed in §4.3).

4.4.3 Distance between glass walls and model

A distance of 5 mm was kept between the model and the glass walls of the tank, in order to avoid contact. This introduces a 3D effect. The gap is, however, not more than 1.67 % of the total width of the tank, so the mass flux of water in and out of the gap between the glass wall and the model is small, although it represents a source of error, in particular damping of resonant ship motions in freely floating conditions. A quantitative analysis of this error was not performed. Similar studies earlier concluded this error was small (see e.g. Kristiansen and Faltinsen (2012)).

4.4.4 Repeatability

Selected periods with selected configurations were repeated eight times for forced heave amplitudes $\eta_{3a} = 1$ mm, 3 mm and 5 mm. The RAOs and time-series correspond well; in the piston mode period range (0.9 s $< T <$ 1.5 s), the largest standard deviation in the RAO was less than 1 % relative to the mean value. In the range of the first sloshing mode (0.45 s $< T <$ 0.6 s), the largest standard deviation in the RAO was less than 3.5 % relative to the mean value, as presented in Figure 4.8 from the forced heave tests. The somewhat larger discrepancy around the first sloshing mode is likely to be related to the fact that the free-surface motion in the moonpool was larger, and to some extent nonlinear (cf. §7.1.3), in this range of T.

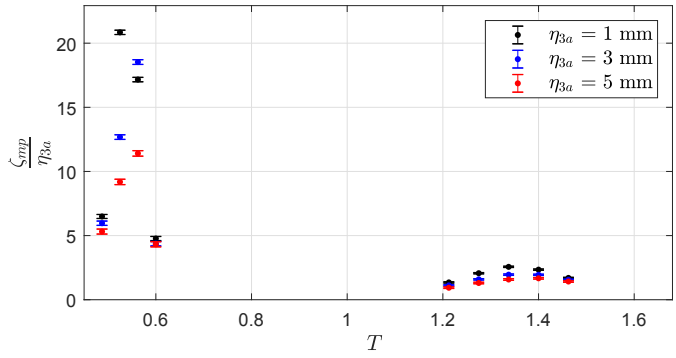

Figure 4.8: Repetition tests from the forced heave tests in the wave flume (WP1). Selected forced heave periods were repeated eight times with three different forced heave amplitudes. Repetition tests for Case 3 are presented (cf. Table 4.1).

4.4.5 Accelerometers versus position sensor

The vertical motion of the model was measured with a draw-wire sensor and accelerometers in the forced heave experiments. The accelerometers and the draw-wire sensor were in good agreement. In general, differences less than 1.5% were observed. This is illustrated in Figure 4.9. On some occasions, however, the displacement sensor failed for unknown reasons. Consequently, the accelerometers are used to determine the heave motion, η_3, in the present study.

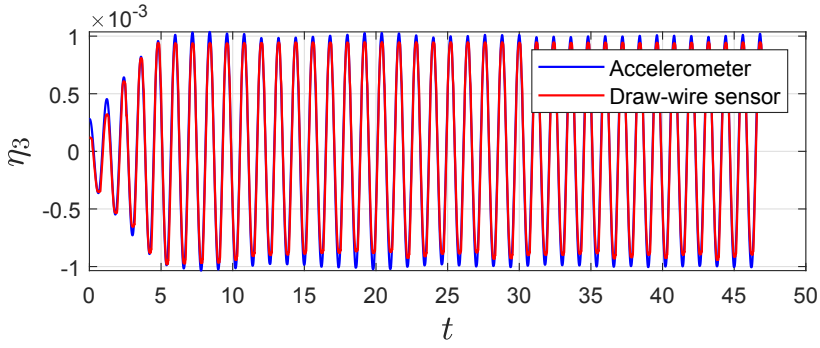

Figure 4.9: The draw-wire sensor measurements and the acceleration integrated twice in time are presented for Case 3 (cf. Table 4.1) with $T = 1.2$ s and $\eta_{3a} = 1$ mm.

4.5 Forced heave experiments

Moonpools with recess were investigated in forced heave in a two-dimensional setting (2DMR), and models with clean moonpools were studied in a quasi three-dimensional setting (3DQ). We use the term "quasi" due to that the set-up is equi-

valent to an infinitely long barge with infinite many moonpools. The configurations are presented in Figures 4.10 and 4.11. A side view of the setup in the wave flume is presented in Figure 4.12.

The model tests for the 2DMR cases were performed with two boxes, and different recess floors attached to the boxes, which constitute a model with moonpool with recess. Several configurations were tested. Due to unexpected circumstances, some of the sensors failed during the testing period for the 2DMR configurations. This was especially a problem for configurations with twice the moonpool length to those presented in Table 4.1, were almost all of the wave probes failed to measure the responses. These tests are briefly discussed in Appendix C.2. Three representative cases from the 2DMR studies are presented in this thesis. Three configurations were tested in the 3DQ experiments. The main dimensions are listed in Table 4.1. The free-surface elevation outside the model was measured with six wave probes, as illustrated in Figure 4.12. In addition, wave probes inside the moonpool were used to measure the moonpool responses, as illustrated in Figures 4.13 and 4.14.

Table 4.1: Main dimensions for the 2DMR and 3DQ configurations. L_r and H_r are the length and height of the recess floor, respectively. L_m and B_m are the length and width of the moonpool. D is the draft. L and B are the model length and width.

Case	L_m	B_m	L_r	H_r	D	L	Configuration type
Case 1	0.2 m	0.59 m	0.05 m	0.05 m	0.11 m	1.0 m	2DMR
Case 2	0.2 m	0.59 m	0.075 m	0.05 m	0.11 m	1.0 m	2DMR
Case 3	0.2 m	0.59 m	0.1 m	0.05 m	0.11 m	1.0 m	2DMR
Case 4	0.1 m	0.1 m	-	-	0.15 m	0.8 m	3DQ
Case 5	0.2 m	0.1 m	-	-	0.15 m	0.8 m	3DQ
Case 6	0.2 m	0.2 m	-	-	0.15 m	0.8 m	3DQ

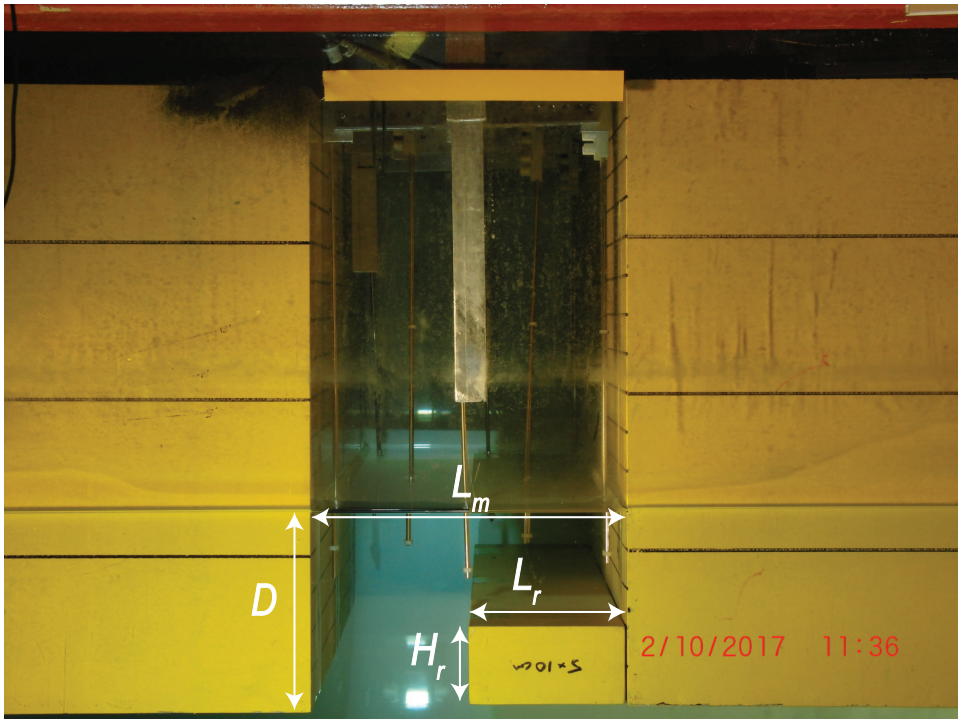

Figure 4.10: Moonpool with recess configuration in a two-dimensional setting (called 2DMR in this thesis). The model was equipped with rails along the walls in the moonpool such that different recess sizes could be tested. L_m = 0.2 m, B_m = 0.59 m, L_r = 0.1 m, H_r = 0.05 m and D = 0.11 m.

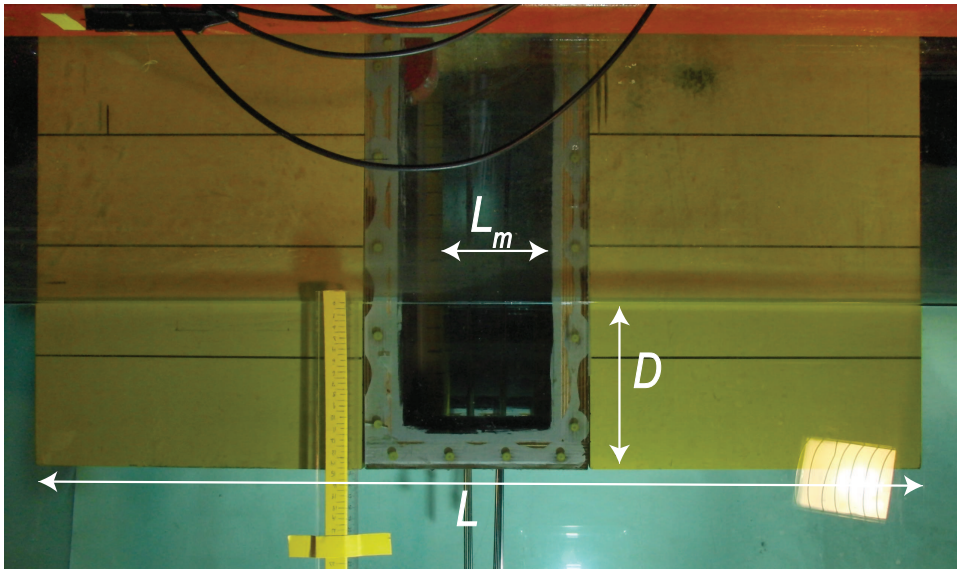

Figure 4.11: Clean moonpool configuration in a quasi three-dimensional setting (called 3DQ in this thesis). L_m = 0.1 m, B_m = 0.1 m and D = 0.2 m.

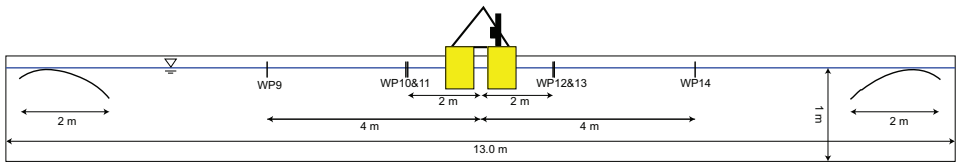

Figure 4.12: Side view of the wave flume with oscillator and model. The location of the parabolic beaches and the wave probes outside the model are indicated.

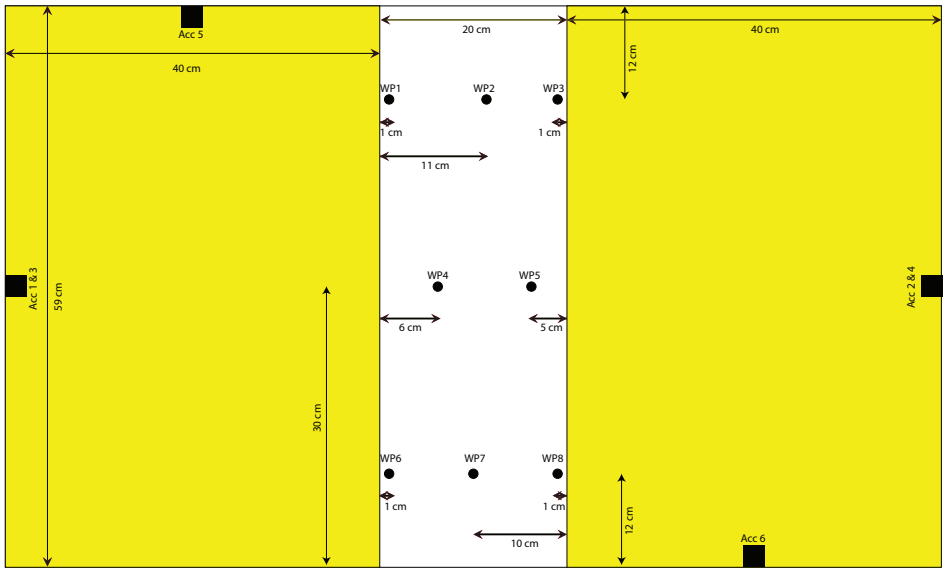

Figure 4.13: Bird's eye view, illustrating the locations of wave probes (WP) in the moonpool for the 2DMR cases. The moonpool responses were measured in an Earth-fixed coordinate system. $L = 1.0$ m was the length of the model.

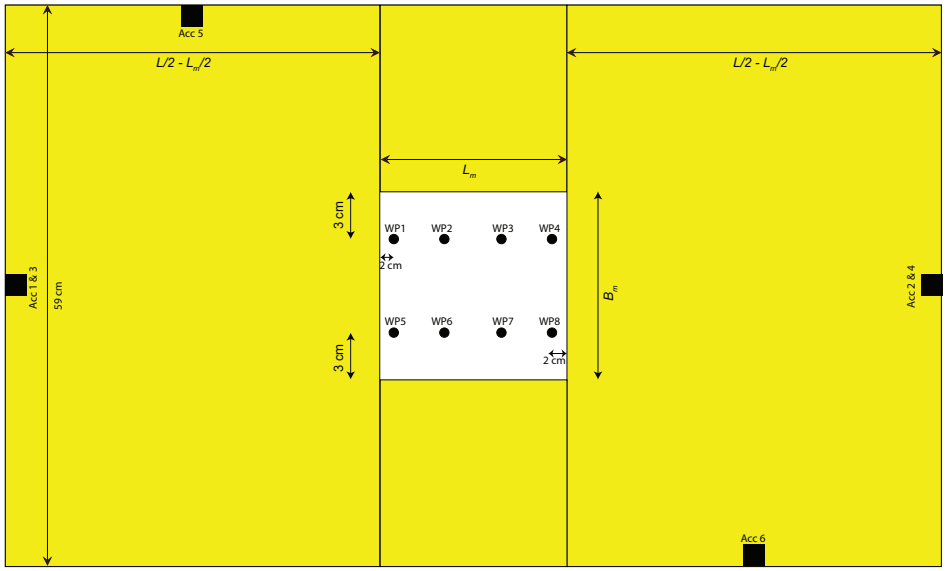

Figure 4.14: Bird's eye view, illustrating the locations of wave probes (WP) in the moonpool for the 3DQ cases. WP3, WP4, WP7 and WP8 were not used in Case 4. The moonpool responses were measured in an body-fixed coordinate system. $L = 0.8$ m was the length of the model.

4.6 Freely floating experiments

Some of the configurations presented in Table 4.1 were also studied in freely floating conditions. The models were moored with four horizontal springs, as illustrated in Figure 4.15. Each spring had a spring stiffness of 22.5 N/m. The pretension in each spring was approximately 5.6 N. The tests were performed with the 2DMR and 3DQ configurations in incident regular waves.

The wave probe setup with the 2DMR configurations was changed, and is illustrated in Figure 4.16. The moonpool responses were measured in a body-fixed coordinate system. Ten body-fixed wave probes were used in the moonpool, where four of them were conductive aluminum tapes attached to the model and six of them were traditional capacitance type wave gauges. For the 3DQ configurations, the wave probe setup was the same as in forced heave (cf. Figure 4.14). Acceleration in x-, y- and z- directions were measured with six body-fixed accelerometers. Motions in each direction was obtained by integrating twice in time using a standard Fourier transform-based integration method. The accelerometers measuring in the z-direction were used to determine the pitch motion of the model. The accelerometers measuring the surge acceleration failed due to unknown reasons. Hence, the surge responses for the configurations presented in Table 4.2 are not presented in this thesis. A photo of the experimental set-up is provided in Figure 4.17.

One representative case from the 2DMR configurations, and three from the 3DQ configurations, were selected for the purpose of studying the effect of the hydrodynamic interaction between ship and moonpool responses in freely floating conditions, with a main focus on the role of V_{MP}/V_S-ratios, where V_{MP} and V_S are the moonpool and submerged ship volumes (cf. Table 4.2). The radius of gyration in pitch, r_{55}, and center of gravity, COG, were determined with the CAD software Rhino. The mass of the models was measured prior to the tests. Weights were placed in the model such that the desired draft and zero trim were obtained. These model tests were performed as preliminary to the experiments in the Ocean Basin (cf. Chapter 5), in order to investigate whether it was worthwhile studying models with different moonpool sizes.

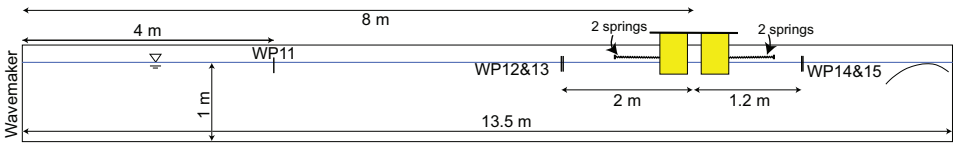

Figure 4.15: Side view of the wave flume with oscillator and model. The location of the wave probes outside the model are indicated.

Table 4.2: Main properties of the models tested in freely floating conditions. The center of gravity is measured relative to the origin of the coordinate system, which is located at the waterline $L/2$ from the aft of the model, and L is the length of the model. See Table 4.1 for main dimensions of the cases listed below.

Case 2 (V_{MP}/V_S = 0.203)	
Ship mass (m)	54.9 kg
Center of gravity ($\mathrm{COG}_x, \mathrm{COG}_y, \mathrm{COG}_z$)	(0.025 m, 0 m, -0.055 m)
Radius of gyration (r_{55})	0.277 m
Case 4 (V_{MP}/V_S = 0.022)	
Ship mass (m)	66.9 kg
Center of gravity ($\mathrm{COG}_x, \mathrm{COG}_y, \mathrm{COG}_z$)	(0.0 m, 0 m, -0.077 m)
Radius of gyration (r_{55})	0.224 m
Case 5 (V_{MP}/V_S = 0.045)	
Ship mass (m)	65.5 kg
Center of gravity ($\mathrm{COG}_x, \mathrm{COG}_y, \mathrm{COG}_z$)	(0.0 m, 0 m, -0.076 m)
Radius of gyration (r_{55})	0.242 m
Case 6 (V_{MP}/V_S = 0.094)	
Ship mass (m)	62.7 kg
Center of gravity ($\mathrm{COG}_x, \mathrm{COG}_y, \mathrm{COG}_z$)	(0.0 m, 0 m, -0.072 m)
Radius of gyration (r_{55})	0.248 m

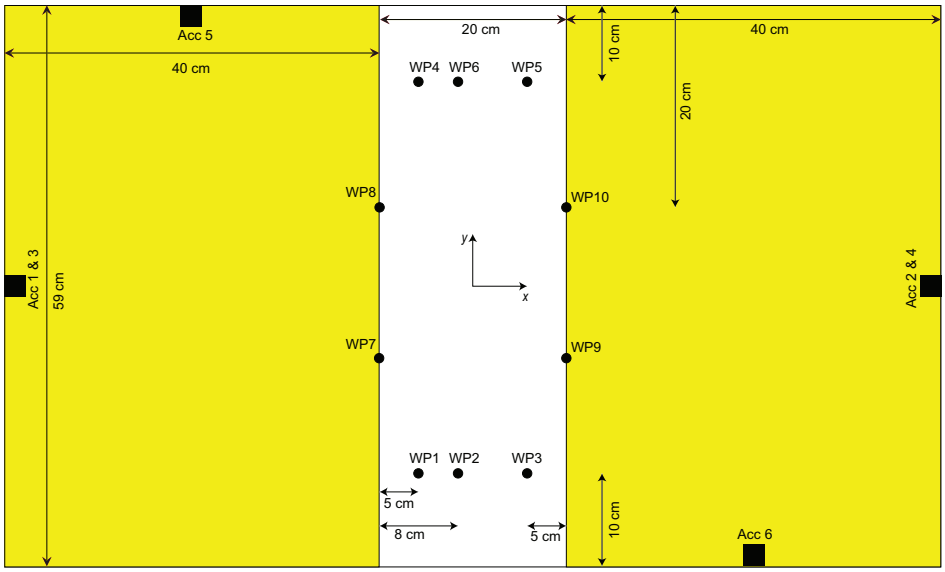

Figure 4.16: Locations of wave probes (WP) in the moonpool for the 2DMR configurations in freely floating conditions (bird's eye view). The 3DQ setup in freely floating conditions was the same as in Figure 4.14. The moonpool responses were measured in a body-fixed coordinate system.

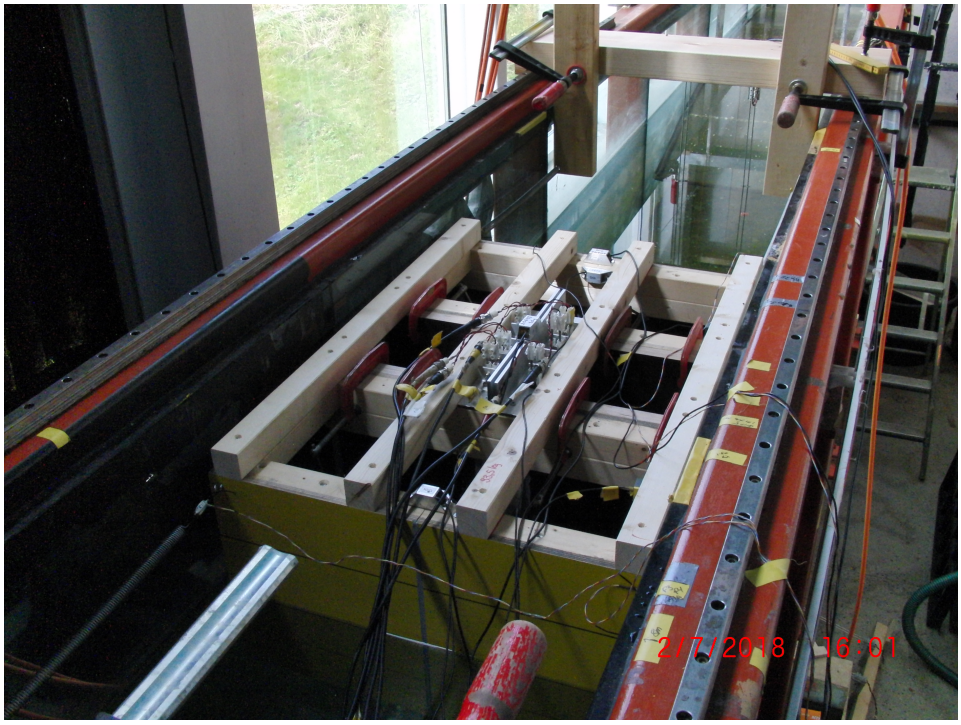

Figure 4.17: A photo from the freely floating model tests in the wave flume with the 3DQ set-up (Case 4).

Chapter 5

Model tests in the Ocean Basin

After the model tests in the wave flume with four different V_{MP}/V_S-ratios in freely floating conditions were conducted, we concluded that it was of interest to investigate the hydrodynamic interaction between ship and moonpool responses with different moonpool sizes in detail in the Ocean Basin.

Dedicated experimental studies were carried out in the Ocean Basin at Sintef Ocean in Trondheim, Norway, in December 2018 - January 2019. The basin is 80 m long, 50 m wide and the water depth was 5 m. The basin is equipped with a hinged double-flap wavemaker (see BM2 in Figure 5.1). The vessel and moonpool responses were investigated in long-crested waves with a model that resembles a realistic ship.

The experiments were carried out with the model freely floating in incident waves. The tests were conducted in both regular and irregular waves. The duration of the former was three minutes, with a waiting time of six minutes between each test for the basin to calm down. The irregular waves consisted of time-series of 15 minutes, with a waiting time of 15 minutes between each test. The first three minutes of the irregular wave tests are disregarded during post-processing, such that a time-window where all of the wave components have reached the model is analyzed.

In §5.1, the details of the ship models are provided. The cradle, incline and free decay tests are discussed in §5.2, §5.3 and §5.4, respectively. In §5.5 and §5.6, the irregular and regular waves are discussed. Finally, possible error sources are addressed in §5.7.

5.1 Ship models

The model length was 4 m, and a scale of 1:34.5 was imagined. Other main particulars of the ship model are summarized in Table 5.1. The model was designed such that different moonpool sizes could be tested. Photo of the model is presented in Figure 5.2. The hull had vertical walls and horizontal bottom. The model was not equipped with bilge keels.

Models with three different moonpool sizes were tested, referred to as MP1, MP2 and MP3 (cf. Table 5.1). Cradle tests were conducted to determine the radius of gyration in pitch and center of mass of the fully equipped models with weights (cf. §5.2 and Appendix A). Weights in the model were placed such that zero trim and heel angles were obtained in calm water. The origin of the coordinate system is placed in the center of the model at the mean waterline (i.e. $L/2$ from the aft of the model). All results in this thesis are presented in model scale, unless otherwise stated.

The model particulars were based on a real moonpool vessel that was investigated by Sintef Ocean in 2018. The moonpool size for MP2 is based on the moonpool dimensions of the example vessel. Some modifications were made. For instance, the hull shape of the present models do not have double-curvature, which the example vessel had, such as to simplify matters in relation to mesh generation for the numerical simulations. The hull form of the models is presented in Appendix A.1.

The model was equipped with body-fixed wave probes evenly and pairwise distributed in the moonpool, with four, six and twelve wave probes for MP1, MP2 and MP3, respectively (cf. Figure 5.3). In addition, six Earth-fixed wave probes were used outside the model, as illustrated in Figure 5.1. Oqus position system was used to measure the motion in six directions. The model was equipped with three body-fixed accelerometers, each measuring accelerations in x-, y- and z-directions.

The vessel was moored with four horizontal mooring lines, each with a stiffness of 90 N/m (cf. Figure 5.4). The pre-tension in the mooring line was prescribed to be 45 N. The pre-tension was checked during the model tests with the force transducers, and the measurements showed that the prescribed pre-tension was achieved with a difference less than 3 %. The model was equipped with four force rings, one in each mooring line, and two force transducers (one on each end of the model, cf. Figure 5.4). The force measurements are not presented herein.

Table 5.1: Main properties of the present ship model. A model scale of 1:34.5 is imagined. The moonpool center is measured relative to the origin of the coordinate system.

	Model scale	Full scale
Length (L)	4.0 m	138 m
Beam (B)	0.8 m	27.6 m
Draft (D)	0.2 m	6.9 m
Dimensions with MP1 (V_{MP}/V_S = 0.015)		
Moonpool length (L_m)	0.2 m	6.9 m
Moonpool width (B_m)	0.2 m	6.9 m
Moonpool center ((c_x, c_y, c_z))	(0.65 m, 0 m, 0 m)	(22.4 m, 0 m, 0 m)
Ship mass (m)	526.7 kg	21627.8 t
Center of gravity (COG)	(-0.11 m, 0 m, 0.055 m)	(-3.8 m, 0 m, 1.9 m)
Radius of gyration ((r_{44}, r_{55}, r_{66}))	(0.28 m, 1.02 m, 0.76 m)	(9.7 m, 35.2 m, 26.2 m)
Dimensions with MP2 (V_{MP}/V_S = 0.064)		
Moonpool length (L_m)	0.4 m	13.8 m
Moonpool width (B_m)	0.4 m	13.8 m
Moonpool center ((c_x, c_y, c_z))	(0.65 m, 0 m, 0 m)	(22.4 m, 0 m, 0 m)
Ship mass (m)	502.69 kg	20642.3 t
Center of gravity (COG)	(-0.15 m, 0 m, 0.057 m)	(-5.2 m, 0 m, 2.0 m)
Radius of gyration ((r_{44}, r_{55}, r_{66}))	(0.29 m, 1.024 m, 0.75 m)	(10.0 m, 35.2 m, 25.9 m)
Dimensions with MP3 (V_{MP}/V_S = 0.427)		
Moonpool length (L_m)	2.0 m	69 m
Moonpool width (B_m)	0.4 m	13.8 m
Moonpool center ((c_x, c_y, c_z))	(-0.15 m, 0 m, 0 m)	(-5.2 m, 0 m, 0 m)
Ship mass (m)	374.69 kg	15386.1 t
Center of gravity (COG)	(-0.08 m, 0 m, 0.083 m)	(-2.76 m, 0 m, 2.9 m)
Radius of gyration ((r_{44}, r_{55}, r_{66}))	(0.30 m, 1.11 m, 1.13 m)	(10.4 m, 38.3 m, 39.0 m)

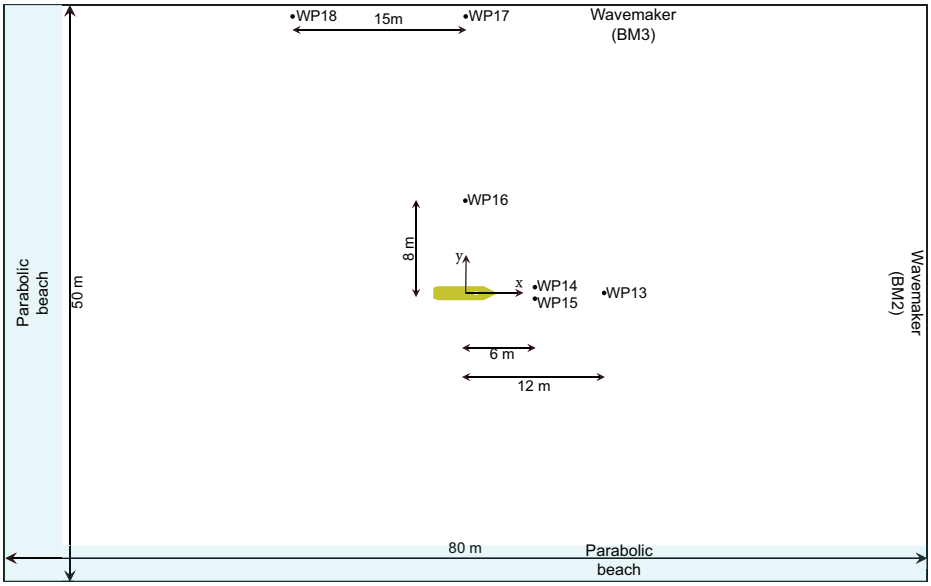

Figure 5.1: Bird's eye view of the Ocean Basin illustrating the location of the wave probes outside the moonpool. BM2 is the wave generator that was used in the present work. BM3 is a multi-flap wavemaker that was not used. Coordinate system with origin in vessel center.

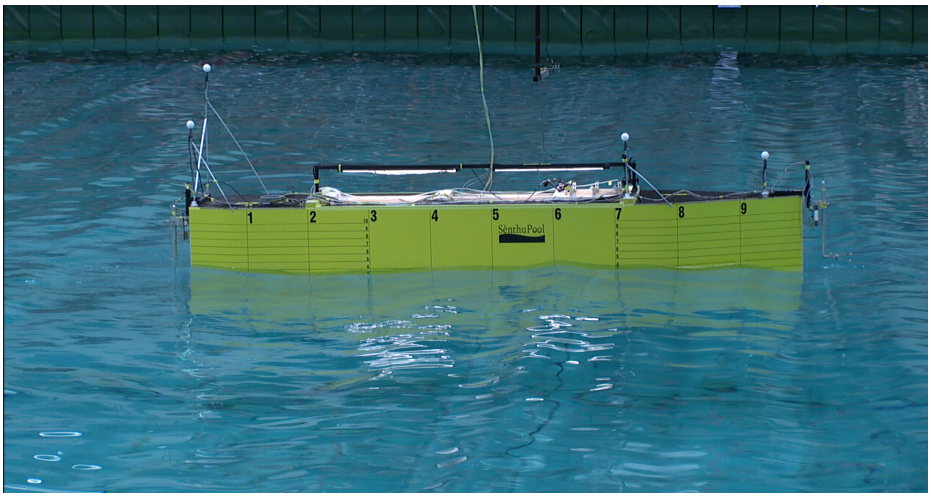

Figure 5.2: Model in the Ocean Basin at Sintef Ocean, Trondheim, Norway. The model is equipped with four marker spheres to measure six degree-of-freedom motions using Oqus, three accelerometers, four force rings and two force transducers, and two cameras in the moonpool. The model is moored with four horizontal mooring lines.

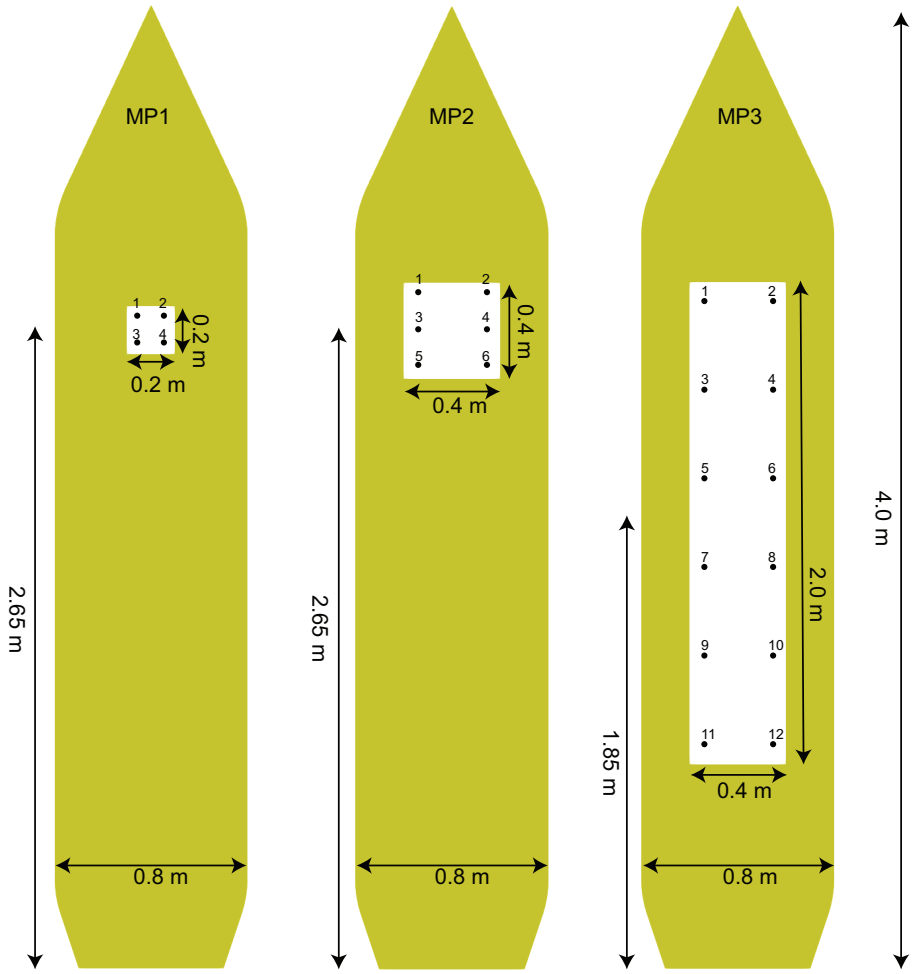

Figure 5.3: Bird's eye view of the wave probes (WP) in the moonpool for the configurations tested in the Ocean Basin. The model dimensions are indicated. The wave probes are evenly and pairwise distributed in the moonpool, with a distance of 5 cm from the walls. The distance from aft to the center of the moonpool is indicated.

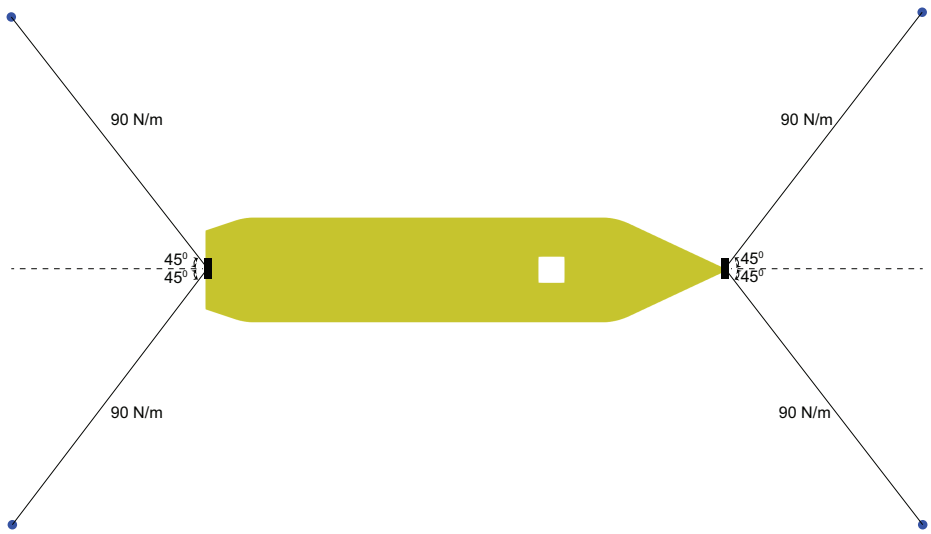

Figure 5.4: Bird's eye view of a model illustrating the horizontal mooring lines. Each mooring line has a stiffness of 90 N/m, and with a pre-tension of 45 N. The locations of the force transducers are indicated by the black rectangles.

5.2 Cradle test

Cradle tests of the naked MP3 model, fully equipped MP1 model and the fully equipped MP3 model were conducted. The results for the naked model are not presented herein. The cradle tests were carried out to determine the radius of gyration in pitch, and the center of gravity, COG. The total mass of the model was also measured during the process.

First, the empty platform was oscillated at three different heights (cf. Figure 5.5), such that the moment of inertia in pitch and COG of the platform itself was determined. The model was then placed such that the COG in the x-direction of the model and platform coincide.

The platform and model were swinging freely until at least 15 oscillations were obtained. Subsequently, the average of the oscillations periods was used. Given the oscillation period, τ, from the cradle tests, the moment of inertia about the COG, I, and the distance from keel to the COG, COG_z, were determined using that (Mabie and Ocvirk 1957, p. 320)

$$I = mgL_{o,i}\left[\frac{\tau^2}{4\pi^2} - \frac{L_{o,i}}{g}\right] \tag{5.1}$$

where m is the total dry mass and $L_{o,i}$ is the distance from knife number i to the COG, as indicated in Figure 5.5(b). The vertical distance from keel to the center of gravity, COG_z, is determined given $L_{o,i}$, with $i = 1, 2, 3$.

In theory, the cradle tests need to be conducted at two different heights. The two unknowns (COG_z and I) are determined given τ at two different heights. In the present cradle tests, the procedure as recommended by Sintef Ocean was followed, where the cradle tests were conducted at three different heights. Thus, three values for I and three values for COG_z were obtained. The average of the obtained results were used in the present study. The standard deviation in the measured I and COG_z relative to the mean values were approximately 0.6 %. The calculations are performed with an in-house program developed by Sintef Ocean. The cradle tests were performed in pitch only, since the model was too long to perform cradle tests in roll. The calculated moment of inertia, dry mass and COG were in good agreement with the calculations in Rhino, with differences less than 3 %, as presented in Table 5.2. Thus, the moment of inertia in roll, pitch and yaw as calculated by Rhino are used in the present work.

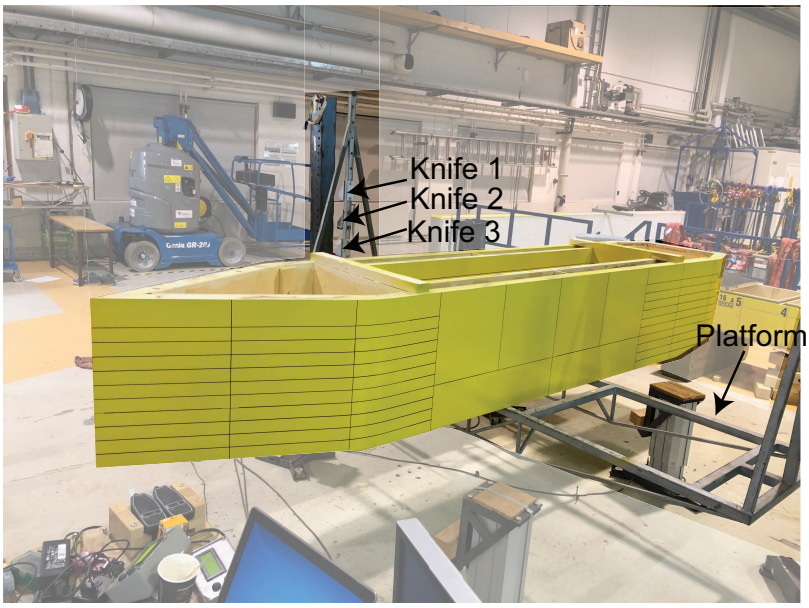

(a) Naked model

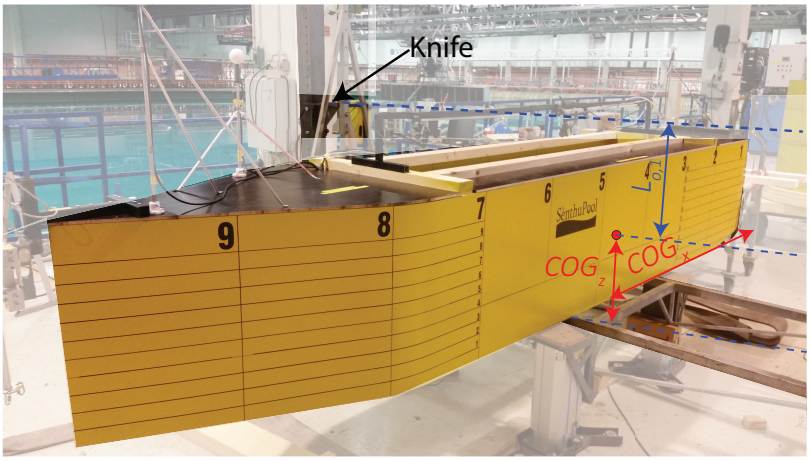

(b) Fully equipped model

Figure 5.5: Cradle tests with MP3 to determine the radius of gyration in pitch and center of gravity.

Table 5.2: KG and r_{55}/L as predicted from cradle tests and with Rhino. Cradle tests were not performed with MP2.

Model	KG (Cradle test)	KG (Rhino)	r_{55}/L (Cradle test)	r_{55}/L (Rhino)
MP1	0.248 m	0.255 m	0.261	0.258
MP2	-	0.257 m	-	0.256
MP3	0.276 m	0.283 m	0.292	0.286

5.3 Inclining test

Prior to the model tests, it was important to ensure that the models were stable in roll. The metacentric height, GM, can be determined using the known hydrostatic properties of the models. However, inclining tests were conducted with MP1 and MP3 to determine the stability properties as accurately as possible. The procedure involves causing the fully equipped ship model to heel by placing weights on both sides of the model, as illustrated in Figure 5.6. GM was calculated as

$$\mathrm{GM} = \frac{Mr}{m \sin \Theta} \tag{5.2}$$

where M and m are the mass of the weight and model. r is the distance between the weights placed at port and starboard. Θ is the difference in the angles obtained when the weight is placed port and starboard. The angle Θ was calculated using two different methods; with a digital leveler and with a cord. The weights, the distance r, and the measured angle Θ are given as input to an in-house program developed by Sintef Ocean, which in return outputs GM.

Given the hydrostatic properties of the model, GM is calculated theoretically as

$$\mathrm{GM} = \mathrm{KB} + \mathrm{BM} - \mathrm{COG}_z \tag{5.3}$$

where KB, $\mathrm{BM} = I/V$ and COG_z are the distances from keel to the center of buoyancy, center of buoyancy to the metacenter and keel to center of gravity, respectively. I is the second moment of inertia of the waterplane, and V is the displaced volume. KB and V are determined by WAMIT. Rhino was used to determine COG_z. GM as predicted from the incline tests and using (5.3) are presented in Table 5.3. Fair agreement between the incline tests and the calculations are illustrated. The largest differences are observed for MP1, with approximately 4 % difference between the values determined from the incline test and (5.3).

Table 5.3: GM as predicted from incline tests and with (5.3). Incline tests were not performed with MP2.

Model	Incline test	Calculated using (5.3)
MP1	0.1053 m	0.1092 m
MP2	-	0.1151 m
MP3	0.1472 m	0.1433 m

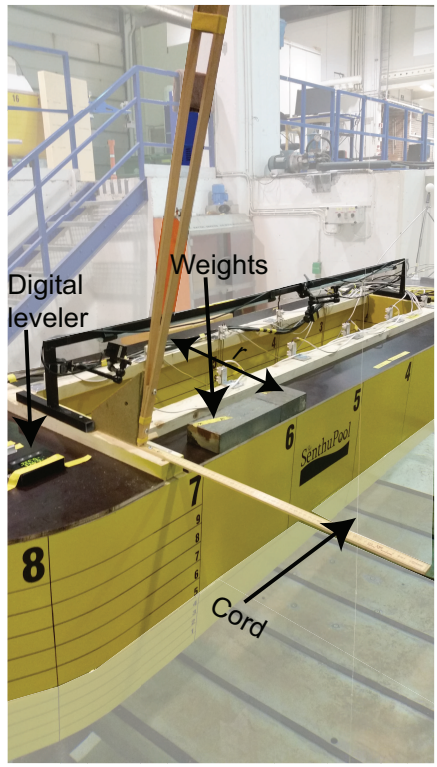

Figure 5.6: Inclining tests with MP3. The weights, digital leveler and cord are indicated. The distance between the masses when placed starboard and port, r, is indicated.

5.4 Free decay tests

Free decay tests of the fully equipped models were conducted with MP1 and MP3, as illustrated by measured roll time-series in Figure 5.7. Free decay tests for MP2 were not conducted since the configuration was fairly similar to MP1. Free decay tests were attempted in all the degrees of freedom. In heave and pitch, it was difficult to obtain reasonable results, since the motions were damped out quickly (cf. Figure 5.8). The free decay tests were carried out carefully in an attempt to achieve motions purely in one degree of freedom. This is, in general, difficult to achieve. However, the motion measurements from the free decay tests indicate that the motions were, in practice, in one degree of freedom.

The natural periods as predicted from the free decay tests and by WAMIT are presented in Table 5.4. Fair agreement between the free decay tests and WAMIT calculations is illustrated. The natural periods from WAMIT are determined using (2.12) for the 6 DOF coupled system including horizontal mooring. Added mass and hydrostatic restoring coefficients as calculated by WAMIT are used.

Table 5.4: Natural periods as predicted by WAMIT and from free decay tests. Decay tests were conducted for MP1 and MP3. In heave and pitch, it was not possible to perform free decay tests of the model, and the natural periods were therefore not determined (ND) from free decay tests.

Mode (method)	MP1	MP2	MP3
η_1 (WAMIT)	13.32 s	13.22 s	11.72 s
η_1 (Decay test)	13.51 s	ND	11.67 s
η_2 (WAMIT)	17.00 s	16.95 s	16.14 s
η_2 (Decay test)	16.46 s	ND	16.07 s
η_3 (WAMIT)	1.43 s	1.41 s	1.32 s
η_3 (Decay test)	ND	ND	ND
η_4 (WAMIT)	2.15 s	2.03	1.82 s
η_4 (Decay test)	2.18 s	ND	1.86 s
η_5 (WAMIT)	1.54 s	1.55 s	1.45 s
η_5 (Decay test)	ND	ND	ND
η_6 (WAMIT)	9.22 s	8.74 s	7.1 s
η_6 (Decay test)	8.53 s	ND	6.8 s

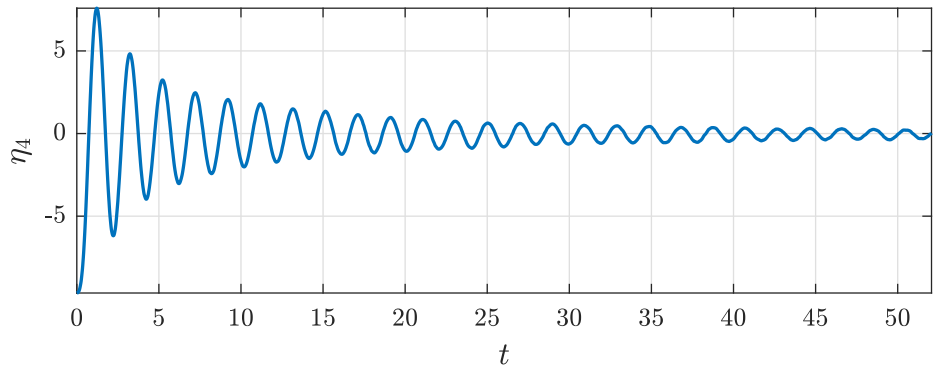

(a) MP1

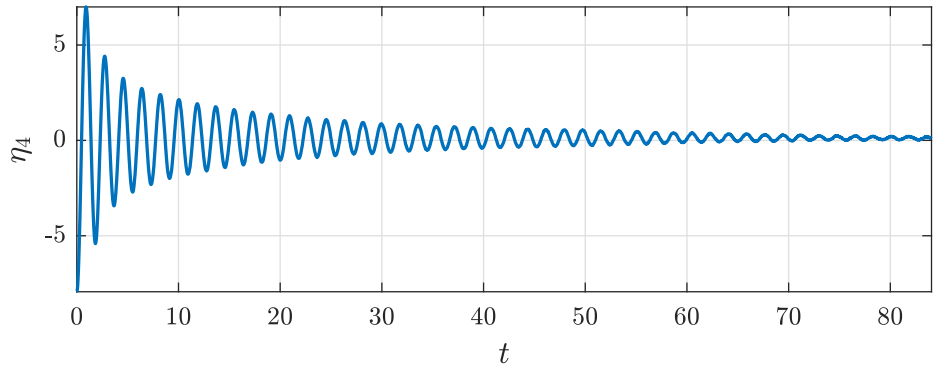

(b) MP3

Figure 5.7: Decay tests in the Ocean Basin in roll with MP1 and MP3. The roll motion, η_4, is presented.

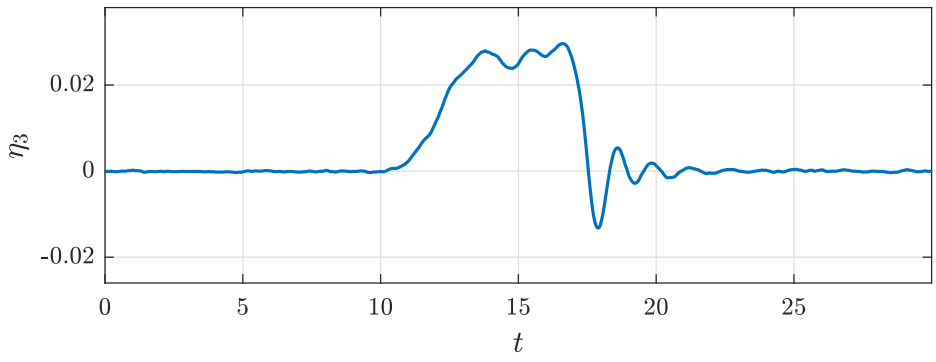

Figure 5.8: Decay tests in heave, η_3. We were not able to obtain reasonable free decay motion in heave and pitch due to that the motions were quickly damped out. It was also difficult to displace the model in these degrees of freedom.

5.5 Irregular waves

We tested the model irregular waves in an attempt to be able to directly compare the RAOs from the irregular wave tests with RAOs from the regular wave tests. We established a formulation for the wave spectrum, S_ζ, based on the spectrum value for a regular wave given wave steepness and wave period. A regular wave given the wave steepness, H/λ, and wave period, T, is

$$\zeta(x,t) = \frac{H}{2}\sin(\omega t - kx), \tag{5.4}$$

where k is the wave number, $\lambda = 2\pi/k$ is the wavelength, $\omega = 2\pi/T$ is the circular frequency and H is the wave height. Subsequently, the spectrum value for a given wave circular frequency, $S_\zeta(\omega)$, was determined by performing Fast Fourier Transform (FFT) of (5.4) for a given wave steepness and wave period. We refer to this wave spectrum as Pink Noise for Water Waves (PNWW) spectrum in this thesis. The specified and measured wave spectra are compared in Figure 5.9. We found satisfactory agreement between the desired and measured wave spectra, although we observe discrepancies, up to 15 %, in particular for wave periods close to 2 s.

We also performed model tests in irregular waves with the Pierson-Moskowitz (PM) spectrum (DNV 2011)

$$S_\zeta(\omega) = \frac{5}{16}H_s^2\omega_p^4\omega^{-5}\exp\left(-\frac{5}{4}\left(\frac{\omega}{\omega_p}\right)^{-4}\right), \tag{5.5}$$

where H_s and $w_p = 2\pi/T_p$ are the significant wave height and angular spectral peak frequency, respectively. Three different wave spectra, which are relevant with respect to realistic sea states in the North Sea, were tested as presented in Table 5.5. The measured and desired wave spectra are presented in Figure 5.10. We present the "desired" wave spectra, and not the "specified", since the input to the wave-maker is generated by a software tool developed by Sintef Ocean. Thus, the specified wave spectra are unavailable. We observe satisfactory agreement between the desired and measured wave spectra, although there are some discrepancies, up to approximately 15 %, around the spectral peak periods. Model tests with the PM spectra were only conducted with the MP3 configuration (cf. Table 5.1).

Note the differences in the asymptotic behavior of the PNWW and PM spectra. As $\omega \to \infty$ the PM spectrum $S_\zeta \propto 1/\omega^5$. By contrast, the PNWW spectrum is $S_\zeta \propto 1/\omega^4$. To show this, we use that $S_\zeta \Delta\omega = 0.5\zeta_a^2$. Assuming infinite water depth the dispersion relation for water waves is $\omega^2 = gk$. Hence, for a given

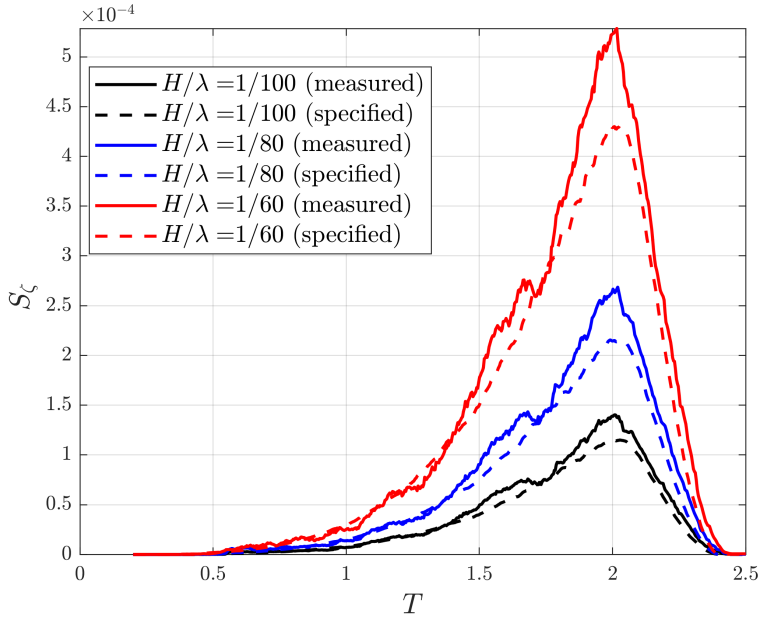

Figure 5.9: Measured and specified pink noise for water waves spectra with three different wave steepnesses.

Table 5.5: Tested irregular waves with PNWW and PM spectra. The measured and specified significant wave heights, H_s, are also presented.

Spectrum type	H/λ	H_s specified	H_s achieved
PNWW	$1/100$	0.034 m	0.035 m
PNWW	$1/80$	0.046 m	0.049 m
PNWW	$1/60$	0.092 m	0.103 m
PM spectrum with $T_p = 1.02$ s	-	0.072 m	0.069 m
PM spectrum with $T_p = 1.36$ s	-	0.101 m	0.113 m
PM spectrum with $T_p = 1.70$ s	-	0.130 m	0.122 m

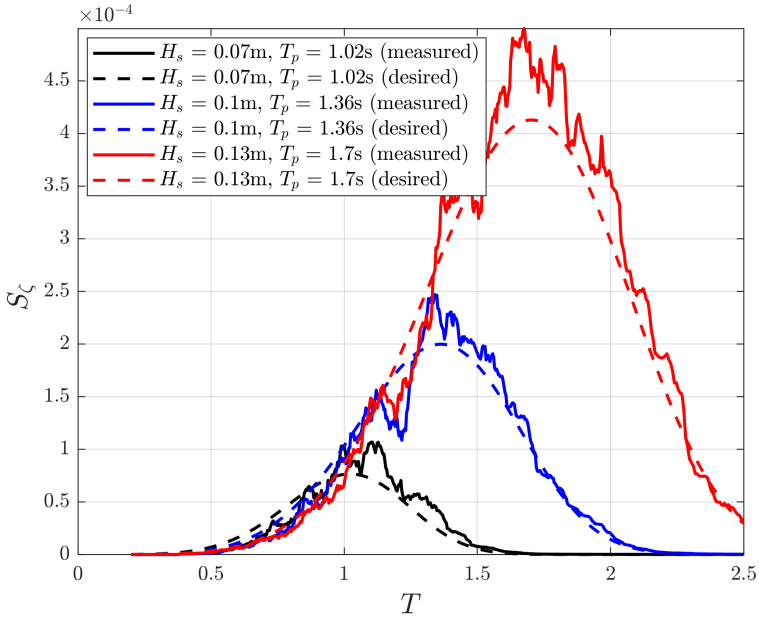

Figure 5.10: Measured and desired PM spectra. We present the desired PM spectra as calculated using (5.5), since the specified spectra are unavailable.

wave steepness, H/λ, we show that $S_\zeta \Delta\omega = \frac{1}{2}\frac{(H/\lambda)^2(\pi g)^2}{\omega^4}$, which implies that the present PNWW spectrum's behavior for large ω is $S_\zeta \propto 1/\omega^4$.

The RAO of a variable R is defined in the usual sense as

$$H_R(T) = \sqrt{\frac{S_R(T)}{S_\zeta(T)}} \tag{5.6}$$

where H_R and S_R are the RAO and spectrum of the variable R, respectively. Here, we assume that the spectra represent a stationary process and that there is a linear relationship between the wave and response spectra. A moving average approach is used to smooth the measured spectra from the model tests.

5.6 Regular waves

A wavemaker software tool developed by Sintef Ocean was used to generate regular waves, where the wave period and height were given as input. The wave height is determined as $H = \frac{H}{\lambda}\frac{2\pi}{k}$ for a given wave steepness (H/λ) and wave period. This information is converted by the software to motion of the dual-flap wavemaker. Some discrepancies in desired and measured wave amplitudes were expected, although Sintef Ocean's software uses a mechanical transfer function to keep the discrepancies to a minimum.

The measured and specified wave heights in regular waves are presented in Figure 5.11. Satisfactory agreement between specified and measured wave heights was observed. The maximum difference in the desired and measured wave amplitude was 7 %. Throughout the rest of the thesis, we refer to the measured wave height, $H = 2\zeta_a$. The duration of each regular wave test was three minutes, with a linear ramp up of ten seconds at the start of each test.

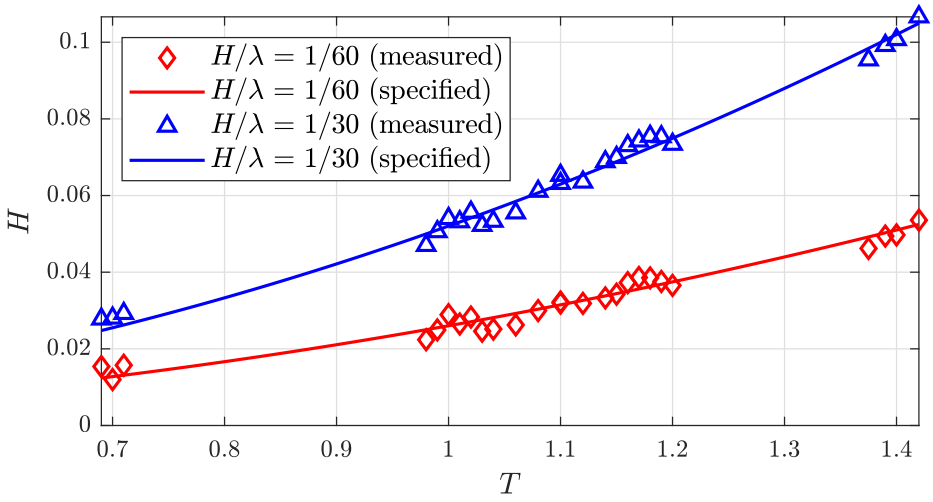

Figure 5.11: Measured wave height versus specified wave height for two different wave steepnesses.

5.7 Error discussions

The model tests in the Ocean Basin were conducted carefully to minimize inaccuracies and errors in measurements. Possible bias and random errors are assessed to discuss the quality of the experimental results in the following sections.

5.7.1 Wave probes

The wave probes used in the experiments in the Ocean Basin, as the wave probes used in the wave flume, are sensitive to large temperature variations. The temperature variations were, however, small during the testing period (cf. Figure 5.12). The wave probes were calibrated four times during the testing period, where we found negligible differences in the calibration factor. The paired wave probes gave similar measurements when it was expected (for instance when the piston mode was excited).

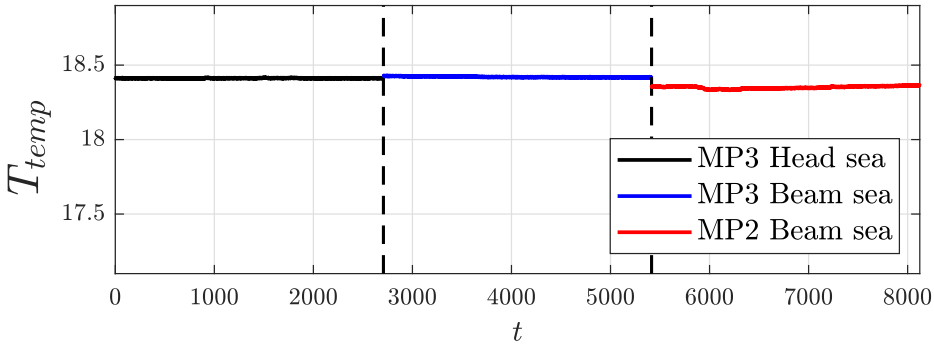

Figure 5.12: Water temperature (in degrees Celsius), T_{temp}, variations in the Ocean Basin. The tests with MP3 in head sea, MP3 beam sea and MP2 in beam sea were performed 22.01.2019, 24.01.2019, and 25.01.2019, respectively. The dashed lines indicate a day change.

5.7.2 Reflection from walls

The basin is equipped with a parabolic beach at the opposite side of the wavemakers (cf. Figure 5.1). For the range of periods and wave steepnesses tested in the present study, some re-reflection was expected from the beach (typically 5 % of the incident wave was expected to be reflected by the beach).

Reflection from the side walls were small, in general. In a certain wave period range in head sea, re-reflection from the side walls affected the model tests in irregular waves. In regular waves, we use a time-window prior to re-reflection. This is discussed in §9.3.

Re-reflections from the wavemaker were observed, especially in beam sea condi-

tions. Time-series exemplifying this is provided in Figure 5.13. This was accounted for during post-processing by using a time-window prior to re-reflection from the wavemaker.

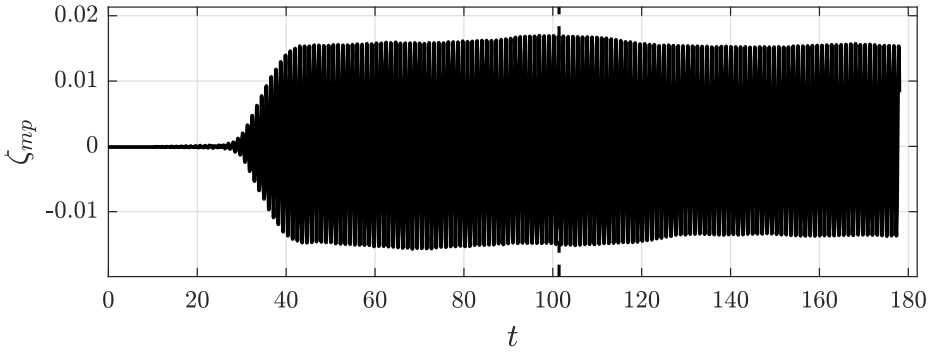

(a) MP1 head sea

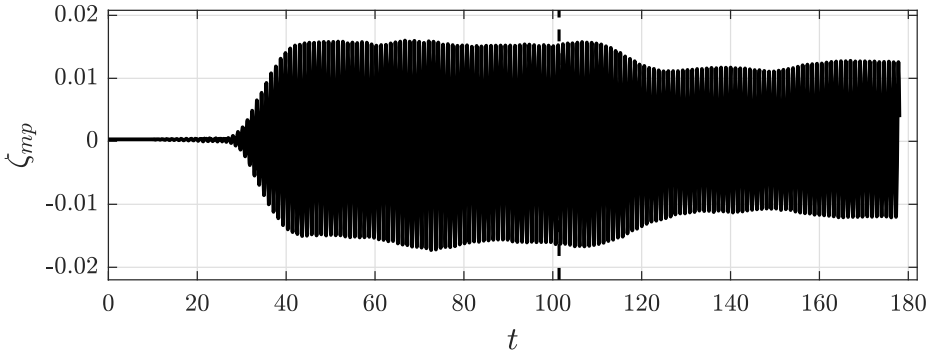

(b) MP1 beam sea

Figure 5.13: Time-series of the moonpool response at WP1 in head and beam sea conditions, and $T = 1.08$ s (MP1). In beam sea conditions, the results are clearly affected by re-reflected waves from the wavemaker. The dashed line indicate the time of re-reflection as predicted by theory.

5.7.3 Oqus and accelerometers

The rigid body motions as measured by the Oqus positioning system were compared to acceleration measurements by integrating twice in time using standard Fourier transformation using an in-house code developed by Sintef Ocean. The results showed satisfactory agreement, with negligible differences for all practical purposes. The model was equipped with four spherical Oqus markers to ensure redundancy in case one marker was not detected by the cameras during the tests. We did not observe any failure in marker detection during the tests, which was as expected, since the model tests were carried out without forward speed.

5.7.4 Repetition tests

Repetition tests were carried out in both irregular and regular waves for the MP2 and MP3 configurations. The same irregular wave with the PNWW spectrum was repeated five times with wave steepnesses $H/\lambda = 1/80$ and $H/\lambda = 1/60$ (cf. Figure 5.14). Here, the response and wave spectra from the irregular wave tests were calculated at 1000 discrete periods by interpolating the spectra obtained from the Fourier transform. Subsequently, we compared the standard deviation in the obtained RAOs from the repetition tests at these points. In general, the standard deviation was less than 1 % relative to the mean value. At narrow peaks close to the first sloshing mode for MP2 in beam sea, the standard deviation of the free-surface motion in the moonpool was approximately 4 % relative to the mean value. In regular waves, the same trend was observed, where the standard deviation in the repetition tests was less than 1 % relative to the mean value, in general, but approximately 4.5 % at the first sloshing mode with MP2. We believe that this is related to the fact that swirling occurred in beam sea for MP2, which is discussed in §9.4. In regular waves, the same wave was repeated eight times for selected wave periods.

5.7.5 Video recordings

Videos of the free-surface motion in the moonpool was recorded from two different angles. In addition, side- and under-water view video recordings of the model were also stored (cf. Figure 5.15). All of the video recordings were saved for each test automatically, where the video recordings started and ended at the same time as the other measurements. The video recordings served as a tool to interpret the model test results, such as swirling inside the moonpool. Snapshots from the video recordings are presented in Chapter 9.

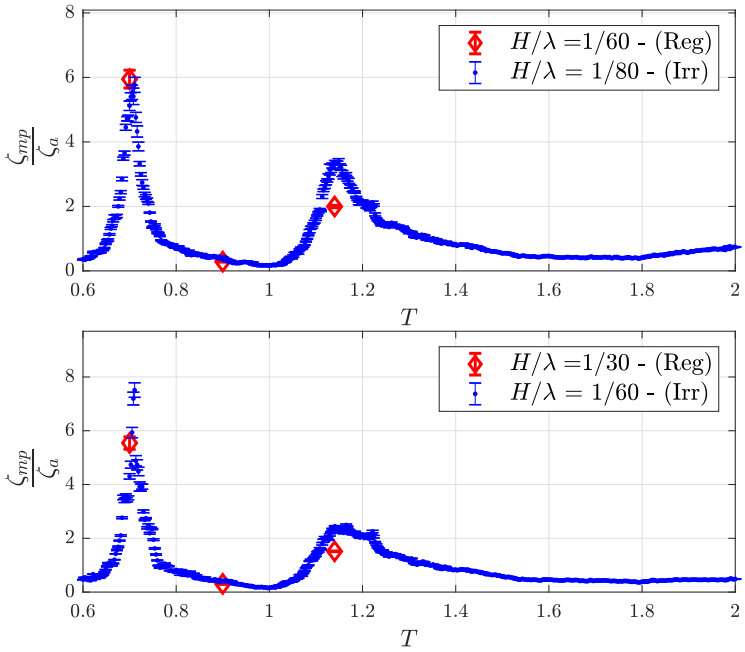

Figure 5.14: Mean values and standard deviations of WP1 (inside moonpool) from irregular wave tests with PNWW spectra. Repetition tests for MP2 in beam sea conditions with two wave steepnesses. The piston mode and first longitudinal/transverse sloshing mode periods for MP2 are $T_0 = 1.15$ s and $T_1 = 0.71$ s, respectively, cf. Table 9.1.

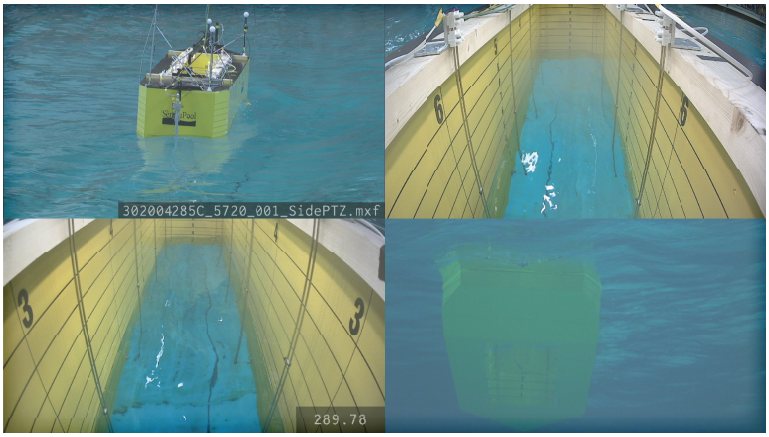

Figure 5.15: Video recordings from the model tests in the Ocean Basin in irregular sea (MP3). Side view (top left), under water (bottom right) and two views in the moonpool (top right and bottom left) were stored for each test.

Chapter 6

Numerical methods

Two-dimensional potential and viscous flow solvers are developed to investigate the moonpool responses in both forced motion and in freely floating conditions. The linear potential flow solver is referred to as BEM. CFD is an abbreviation for computational fluid dynamics (Faltinsen and Timokha 2009), which implies that it could refer to any numerical flow solver, for instance also a potential flow solver. In this thesis, however, the term CFD is used to refer to the presently developed hybrid 2D Navier–Stokes solver.

The presently developed two-dimensional linear BEM is discussed in §6.1 and §6.2. WAMIT is used to conduct simulations assuming linear potential flow theory in 3D, and the software is briefly discussed in §6.4. Two viscous solvers are presented; the presently developed hybrid 2D Navier–Stokes solver in §6.5 and PVC3D in §6.6. Mesh convergence is discussed after each numerical code is presented. Verification and validation simulations of the 2D BEM and hybrid Navier–Stokes solvers are presented in §6.9.

6.1 Boundary element method

A two-dimensional time-domain lowest order linear BEM code is implemented. The basis for BEM follows from Green's second identity

$$\int\limits_{S+\Sigma} \left[\psi \frac{\partial \phi}{\partial n} - \phi \frac{\partial \psi}{\partial n}\right] dS = \int\limits_{\Omega} \left[\cancelto{0}{\phi \nabla^2 \psi} - \cancelto{0}{\psi \nabla^2 \phi}\right] d\Omega = 0. \tag{6.1}$$

where S is the surface enclosing the computational domain, and Ω is the computational domain. The last equality in (6.1) is satisfied by choosing ψ such that it is

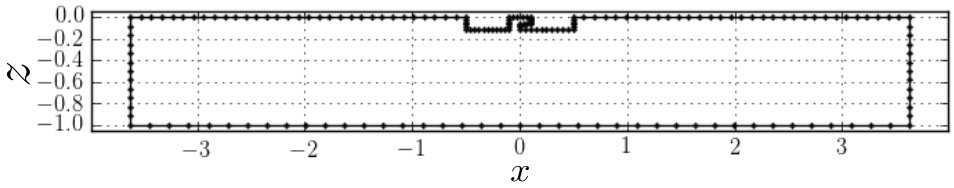

Figure 6.1: An example mesh of a model with moonpool and recess. A coarse mesh is presented for the sake of clarity, with approximately N = 200, where N is the number of panels.

harmonic, thus satisfying Laplace's equation. ψ is chosen as $\psi = \log(R)$, where $R = \sqrt{(x-\eta)^2 + (z-\xi)^2}$. Here, x and z are the field points, and η and ξ are the location of the singularity, and the origin of the coordinate system Oxz is located at the center of the model with $z = 0$ at the mean waterline.

The integration must be performed over an additional surface, Σ, due to the singularity at the collocation points. Thus, we obtain

$$\alpha\phi = -\int\!\!\!\!\!\!-_S \phi \frac{\partial \psi}{\partial n} dS + \int_S \psi \frac{\partial \phi}{\partial n} dS. \tag{6.2}$$

α is the internal angle (2π for a point inside the computational domain which is not a part of a surface, or π when the point is a part of a flat surface). (6.2) is a distribution of sources and dipoles on the surfaces enclosing the computational domain. A lowest-order method is applied, which implies that the source and dipole strengths over the panel are assumed to be constant.

We solve for the velocity potential, ϕ, with a piecewise representation of the surfaces enclosing the computational domain, as illustrated in Figure 6.1. The surfaces enclosing the computational domain consist of different types of surfaces, where either Neumann or Dirichlet boundary conditions are imposed. Thus, (6.2) is re-arranged and written on matrix form as

$$\underbrace{\begin{bmatrix} k_{1,1} & k_{1,2} & \dots & k_{1,N} \\ \vdots & \ddots & & \vdots \\ \dots & \dots & \dots & k_{N,N} \end{bmatrix}}_{\boldsymbol{K}} \underbrace{\begin{bmatrix} b_1 \\ \vdots \\ b_N \end{bmatrix}}_{\vec{b}} = \underbrace{\begin{bmatrix} u_{1,1} & u_{1,2} & \dots & u_{1,N} \\ \vdots & \ddots & & \vdots \\ \dots & \dots & \dots & u_{N,N} \end{bmatrix}}_{\boldsymbol{U}} \underbrace{\begin{bmatrix} \chi_1 \\ \vdots \\ \chi_N \end{bmatrix}}_{\vec{\chi}}, \tag{6.3}$$

where $\boldsymbol{K}$ and $\boldsymbol{U}$ are matrices containing integrals of ψ or $\frac{\partial \psi}{\partial n}$, depending on whether panel number i is part of a Neumann or Dirichlet boundary, where $i =$

$1, \ldots, N$ is the panel number, and N is the total number of panels. $\vec{b}$ is a vector containing the known velocities and velocity potential on the panels, while $\vec{\chi}$ is a vector containing the unknown velocity potential and velocities.

The coefficients in the matrices and vectors in (6.3) are determined as

$$k_{i,j} = \begin{cases} \left(\int \psi dS\right)_{i,j} & \text{if Neumann boundary,} \\ \left(\int \frac{\partial \psi}{\partial n} dS\right)_{i,j} & \text{if Dirichlet boundary,} \end{cases} \tag{6.4a}$$

$$u_{i,j} = \begin{cases} \left(\int \frac{\partial \psi}{\partial n} dS\right)_{i,j} & \text{if Neumann boundary,} \\ \left(\int \psi dS\right)_{i,j} & \text{if Dirichlet boundary,} \end{cases} \tag{6.4b}$$

$$b_i = \begin{cases} \left(\frac{\partial \phi}{\partial n}\right)_i & \text{if Neumann boundary,} \\ (\phi)_i & \text{if Dirichlet boundary,} \end{cases} \tag{6.4c}$$

$$\chi_i = \begin{cases} (\phi)_i & \text{if Neumann boundary,} \\ \left(\frac{\partial \phi}{\partial n}\right)_i & \text{if Dirichlet boundary.} \end{cases} \tag{6.4d}$$

The integrations in (6.4a) and (6.4b) are performed over the panels. i and j are the panel indices. Analytical expressions of the integrals in (6.4) can be found in many textbooks, such as Katz and Plotkin (2001). (6.3) is simplified further as a linear matrix system as

$$\boldsymbol{A}\vec{b} = \vec{\chi}, \tag{6.5}$$

where $\boldsymbol{A} = \boldsymbol{U}^{-1}\boldsymbol{K}$. The solution is time-stepped using an explicit fourth-order Runge–Kutta method by solving for $\vec{\chi}$ at each time step. $\vec{b}$ is updated at each time step according to the boundary conditions. Since linearized boundary conditions are applied, $\boldsymbol{A}^{-1}$ is only established once during a simulation to save computational time. The fact that $\boldsymbol{A}$ is a dense matrix makes BEM computationally demanding when the number of panels increases.

6.1.1 Artificial damping

Artificial damping is applied to the simulations in order to avoid representing unwanted physics. This can be done either in a spatial or temporal sense, depending on the purpose of the artificial damping. The strength and length over which the artificial damping is applied must be carefully chosen. If the strength is small, it will not serve its purpose. If the strength is too large, it will affect the results in the entire domain, leading to unphysical numerical simulations. The strengths and

extent of the artificial damping in the present work are chosen carefully by trial and error.

Numerical beach

Numerical beaches are modelled at the ends of the numerical wave tank to avoid reflected waves in the simulations. The artificial damping is constant in time, while it follows a third order polynomial in space, similar to that by Kristiansen (2009). The damping is applied to the kinematic and dynamic free-surface conditions as

$$\frac{\partial \phi}{\partial t} = -g\zeta + \nu_1(x)\phi, \tag{6.6a}$$

$$\frac{\partial \zeta}{\partial t} = \frac{\partial \phi}{\partial z} + \nu_2(x)\zeta, \tag{6.6b}$$

where $\nu_1(x)$ and $\nu_2(x)$ are

$$\nu_i(x) = \begin{cases} 0 & \text{if } |x| < L_t/2 - L_b \\ \nu_{0,i}\left(3\tilde{x}^2 - 2\tilde{x}^3\right) & \text{if } |x| \geq L_t/2 - L_b \end{cases} \tag{6.7}$$

where i = 1,2 and $\tilde{x} = \frac{|x|-(L_t/2-L_b)}{L_b}$. $\nu_{0,i}$ and L_b are the strength and length of the numerical beach. L_t is the length of the numerical wave tank. For the configurations in the present study, it was found that the beach length should be $L_b = 3\lambda$, where λ is the wavelength. The distance from the model to the numerical beach is 4λ. The strengths of the beach at the tank ends are chosen as $v_{0,1} = 0.85$ s^{-1} and $v_{0,2} = 0.425$ s^{-1}, and is found to work sufficiently for the configurations in the present study.

Removal of beats

In some cases, it might be convenient to apply artificial damping over a certain amount of time. An example of such an application is when the transient responses must be removed, since the system is lightly damped, and only the steady-state response is of interest, cf. §2.4. We observed that beating occurs in the BEM simulations in the proximity of the first sloshing mode in forced heave for the presently investigated 2DMR cases. Therefore, artificial damping is imposed as

$$\frac{\partial \phi}{\partial t} = -g\zeta + \mu_1(t)\phi \tag{6.8a}$$

$$\frac{\partial \zeta}{\partial t} = \frac{\partial \phi}{\partial z} + \mu_2(t)\zeta \tag{6.8b}$$

$$\mu_i(t) = \begin{cases} 0 & \text{if } t \geq T_e \\ \mu_{0,i}\left(1 - \tilde{t}\right) & \text{if } t < T_e \end{cases} \tag{6.8c}$$

where T_e is the time when the artificial damping is completely released, and $\tilde{t} = \frac{t}{T_e}$.

In the present work, (6.8) is applied to the free-surface in the moonpool. It was necessary in the proximity of sloshing resonance, where beating can occur since the wave radiation damping is small. The strength and duration of the damping is empirically determined by trial and error. The strength is set to $\mu_{0,i} = \nu_{0,i}$. The duration of the artificial damping for removal of beats is $T_e = 100T$, where T is the period. The damping is applied uniformly on the free-surface in the moonpool, while the free-surface conditions remain the same as in (3.7) outside the moonpool. In the present work, this type of artificial damping is only applied in the proximity of the first sloshing mode for Cases 1-3, cf. Table 4.1, and the total duration of the simulations is $200T$.

6.1.2 Mesh convergence

The meshes for the BEM simulations are created by defining two variables; Δx and Δx_f. The former is the panel size on the body, and the latter is the mesh size on the free-surface. The number of panels per wavelength, $N_{per,BEM}$, is used to define $\Delta x_f = \lambda / N_{per,BEM}$. λ is the wavelength. Mesh sensitivity analysis is carried out by varying Δx and $N_{per,BEM}$. The mesh convergence studies for Case 3 are presented in Figure 6.2. The moonpool RAOs in the proximity of the piston and first sloshing modes are presented separately.

Satisfactory agreement between the presently adopted mesh, where $\Delta x = 0.004$ m and $N_{per,BEM} = 80$, and the finest mesh, where $\Delta x = 0.001$ m and $N_{per,BEM} = 120$, is illustrated. In general, converged results are obtained with $\Delta x = 0.01$ m and $N_{per,BEM} = 40$. However, with that mesh, the peak at the first sloshing mode is approximately 5 % lower than predicted with the presently adopted and finest meshes.

6.2 Viscous BEM

Since linear potential flow theory is often used for engineering applications, it is of interest to model the damping due to flow separation at the moonpool entrance empirically in a potential flow solver. The two main sources of damping of the moonpool response are wave radiation damping and damping due to flow separation at the moonpool entrance. With BEM, the latter is not captured. Faltinsen and Timokha (2015) developed theory to model this viscous effect for clean moon-

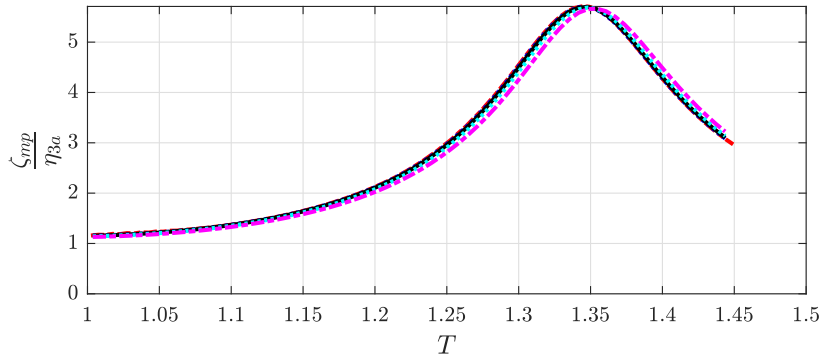

(a) Piston mode

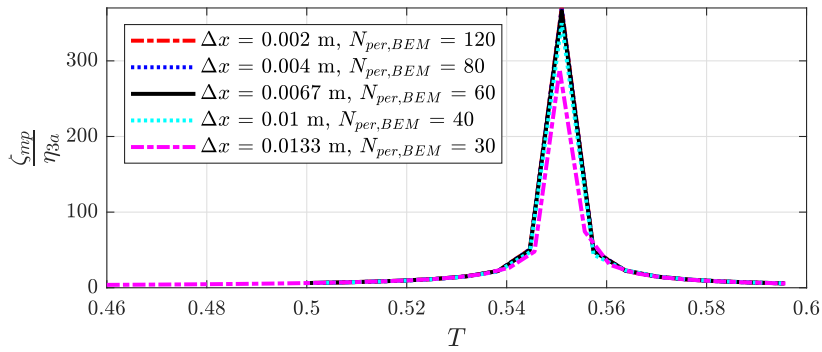

(b) First sloshing mode

Figure 6.2: Mesh convergence studies in the proximity of the piston and first sloshing modes for Case 3 (cf. Table 4.1). $\Delta x_f = \lambda / N_{per,BEM}$ is the panel size on the free-surface, where λ is the wavelength and $N_{per,BEM}$ is the number of panels per wavelength.

pools in a potential flow solver, which is briefly presented in the following. Their model is implemented in the present BEM code, and is referred to as viscous BEM (VBEM). Note that this is not a viscous solver, but that viscous effects are empirically modelled.

The flow separation at the moonpool entrance is associated with a pressure drop relative to the pressure as predicted by potential flow theory. Faltinsen and Timokha (2015) mirror the moonpool setup, and assume that the mirrored moonpool configuration resembles a slat screen. They mirrored the moonpool about the sources as placed by Molin (2001) for a moonpool in 2D and showed that the streamlines for the mirrored moonpool setup resembled that for a slat screen. The pressure drop for a slat screen, Δp, is expressed as

$$\Delta p = \frac{1}{2}\rho K W|W| \tag{6.9}$$

where W is the ambient cross-flow velocity. The pressure drop coefficient, K, is a function of the solidity ratio, Sn, and is determined from empirical formulas based on experimental studies. In Faltinsen and Timokha (2015), and the present work, it is assumed that the pressure drop coefficient is independent of the KC number, and is calculated as

$$K(\mathrm{Sn}) = \left(\frac{1}{C_0(1-\mathrm{Sn})} - 1\right)^2, \qquad C_0 = 0.405\exp\{-\pi\mathrm{Sn}\} + 0.595 \tag{6.10}$$

where C_0 is the so-called contraction coefficient. The solidity ratio is defined as $\mathrm{Sn} = \frac{L_* - L_m}{L_*}$, where $L_* > L$ is the distance between the sources placed somewhere outside the model to determine the piston mode period according to the theory presented by Molin (2001). L and L_m are the ship and moonpool lengths, respectively.

In order to determine L_*, the piston mode period must be known a priori. Given the piston mode period, L_* is determined using (2.2). In the present VBEM code, the piston mode period is determined from the DD method presented in §2.1.2.

In reality, the pressure drop due to flow separation occurs at the moonpool entrance. Faltinsen and Timokha (2015) transformed the pressure drop from the moonpool inlet to the free-surface, assuming that the drop in pressure is constant vertically through the moonpool. We add a quadratic pressure loss term in the dynamic free-surface condition in our BEM,

$$\frac{\partial \phi}{\partial t} = \begin{cases} -g\zeta - \nu_2(x)\phi - \frac{1}{4\gamma^2} K\overline{w}|\overline{w}| & \text{on } S_{F,moon} \\ -g\zeta - \nu_2(x)\phi & \text{on } S_{F,out}. \end{cases} \tag{6.11}$$

where $S_{F,moon}$ and $S_{F,out}$ are the free-surfaces inside and outside the moonpool, respectively. An illustration is presented in Figure 6.3. $W = \overline{w}/\gamma$, where $\overline{w}$ is the averaged vertical fluid velocity at the moonpool entrance, is used, with $\gamma = L_*/L_m$, as by Faltinsen and Timokha (2015). The kinematic free-surface condition remains the same as in (6.6b).

In the present work, the VBEM is used for moonpools with recess. By using the VBEM for moonpools with recess, the validity of the theory presented by Faltinsen and Timokha (2015) is pushed. However, we believe that if the method is applicable for moonpools with recess in practical use, it might serve as an engineering tool for fast estimates of the moonpool responses, where damping due to flow separation is accounted for.

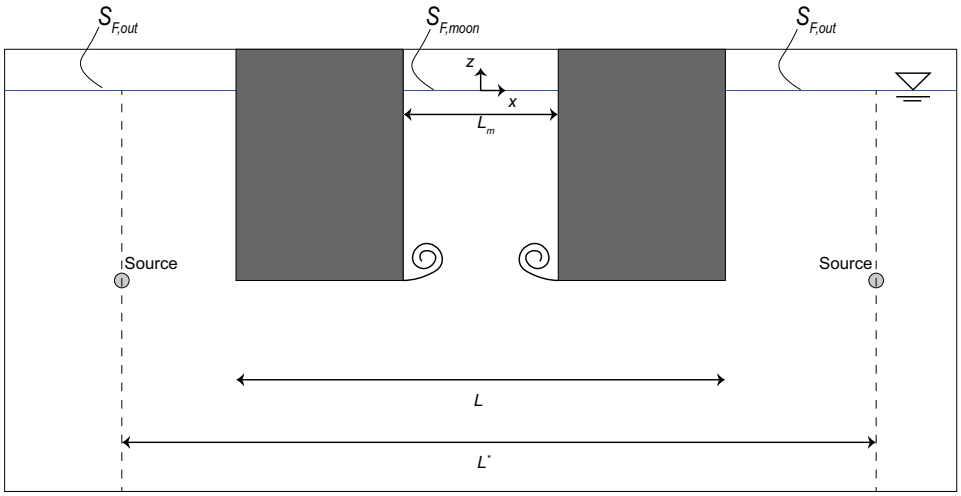

Figure 6.3: Sketch of moonpool configuration simplified as a slat screen. The sources are placed outside the body, and the distance L_* is determined using the single mode approximation by Molin (2001).

6.3 Ramp function

The motion of the moving object (wavemaker or oscillating body) is linearly increased from zero to the desired harmonic oscillations of the object as

$$r(t) = \begin{cases} 1 & \text{if } t > T_{tot} \;\&\; t < T_{end} - T_{tot} \\ \frac{t}{T_{tot}} & \text{if } t \leq T_{tot} \\ \frac{T_{end}-t}{T_{tot}} & \text{if } t \geq T_{end} - T_{tot} \end{cases} \tag{6.12}$$

where $T_{tot} = 5T$. T_{end} is the time at the end of the simulation. r is the factor which is multiplied with the sinusoidal motion of the moving body, e.g. $\eta_3 = r(t)\eta_{3a}\sin(\omega t)$, where η_3 and η_{3a} are the forced heave motion and amplitude of the oscillating body. Similar ramp up is applied in the experiments, as discussed in §4.1 and §4.2.

6.4 WAMIT

The model tests in the Ocean Basin were conducted in a three-dimensional setting. The presently developed codes are two-dimensional flow solvers. WAMIT v6.4 was chosen to perform simulations in 3D. WAMIT solves the radiation and diffraction problem, and the body motions, assuming linear potential flow theory in frequency domain (i.e. harmonic time dependence is adopted). Several authors have performed simulations with empirical damping by means of a massless lid on the free-surface in the moonpool to account for damping due to flow separation at the moonpool entrance (see e.g. Newman (2004)). No such empirical damping is applied in the present WAMIT simulations.

A major strength of WAMIT is that only the wetted body boundary needs to be meshed, since the Green's function used in WAMIT satisfies the free-surface conditions, radiation condition due to far-field waves, and wall conditions (i.e. all the boundary conditions except on the wetted body are satisfied). The drawback is that there are infinite many unphysical resonant modes that can be excited, often referred to as irregular frequencies (Lee and Newman 2006). WAMIT provides a remedy to solve this problem by meshing the inner free-surface. Another drawback is that only one wall can be simulated in WAMIT. With two walls we could have simulated the 3DQ configurations with WAMIT.

In the present simulations, we have applied empirical damping in roll to avoid unphysically large roll motions by following Ikeda et al. (1993), giving the empirical expression for the damping in roll for a rectangular barge with sharp corners as

$$B_{44} = \frac{2}{\pi}\rho L D^4 \left(H_o^2 + 1 - \frac{OG}{D}\right)\left(H_o^2 + \left(1 - \frac{OG}{D}\right)^2\right)\eta_{4a}\omega \tag{6.13}$$

where $H_o = B/(2D)$, B and D are the ship beam and draft, OG is the distance from the mean waterline to the center of gravity, ρ is the density of water and

η_{4a} is the roll amplitude. In the present simulations, η_{4a} is chosen such that the roll RAOs with WAMIT at roll resonance are approximately the same as in the experiments with wave steepness $H/\lambda = 1/100$. Without the additional damping, clearly unrealistically large roll motions were predicted, also affecting sway motions.

The outputs from WAMIT are given in an Earth-fixed coordinate system. The moonpool response is in some cases, however, presented in a body-fixed coordinate system. The free-surface elevation in the moonpool is converted from an Earth-fixed coordinate system to a body-fixed coordinate system by using

$$\zeta_{mp}(t) = \zeta_{ea}\sin(\omega t + \epsilon_{mp}) - (\eta_{3a}\sin(\omega t + \epsilon_3) + y_{wp}\eta_{4a}\sin(\omega t + \epsilon_4) - x_{wp}\eta_{5a}\sin(\omega t + \epsilon_5)), \quad (6.14)$$

where ζ_{ea} is the moonpool response amplitude in an Earth-fixed coordinate system. ϵ_i is the phase angle. η_{ia} with $i = 1, 2, \ldots, 6$ is the motion amplitude in the i-direction. x_{wp} and y_{wp} are the distances from the origin to the location of the wave probes in the x- and y-directions, respectively. Numerical wave probes as used in the experiments are used in the simulations (cf. Figure 5.3).

6.4.1 Mesh

The meshes of the geometries tested in the Ocean Basin are created using a presently developed code. The code also generates all of the relevant input files needed to run a WAMIT simulation. Examples of meshes used in the present study are illustrated in Figure 6.4. The mesh of the inner free-surface for removal of irregular frequencies is also created by the present code. Lower order geometries are used.

The total mass of the structure is calculated using the Gauss' divergence theorem as

$$m = \rho V = -\iint_{S_b} n_1 x dS = -\iint_{S_b} n_2 y dS = -\iint_{S_b} n_3 z dS \quad (6.15)$$

where m is the mass of the ship model. S_b is the mean wetted surface of the model. V is the submerged volume of the model. n_i, with $i = 1, 2, 3$, are the normal vectors in x-, y- and z-directions, respectively. The mass is calculated using all three forms, and an average of the three forms is used to evaluate the total mass.

Mesh convergence studies were carried out for all four geometries. The results for MP1 and MP3 are presented in Figure 6.5. In general, the results converge faster

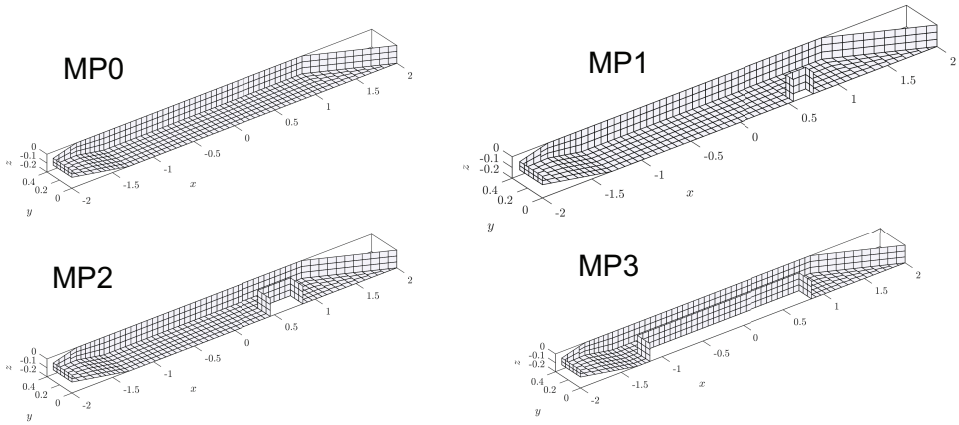

Figure 6.4: Example meshes for MP0-3 (cf. Table 5.1). A coarse mesh is illustrated for the sake of clarity, where the half-body is presented. MP0 has no moonpool.

for large wave periods, as expected. For the coarsest meshes and small periods, some unphysical peaks are observed in the RAOs. Satisfactory convergence is obtained for $N \gtrsim 2000$, where the difference relative to the finest mesh is less than 1 % (N is the number of panels over the half-body). In the present study, a mesh with approximately 5000 panels over the half-body is adopted.

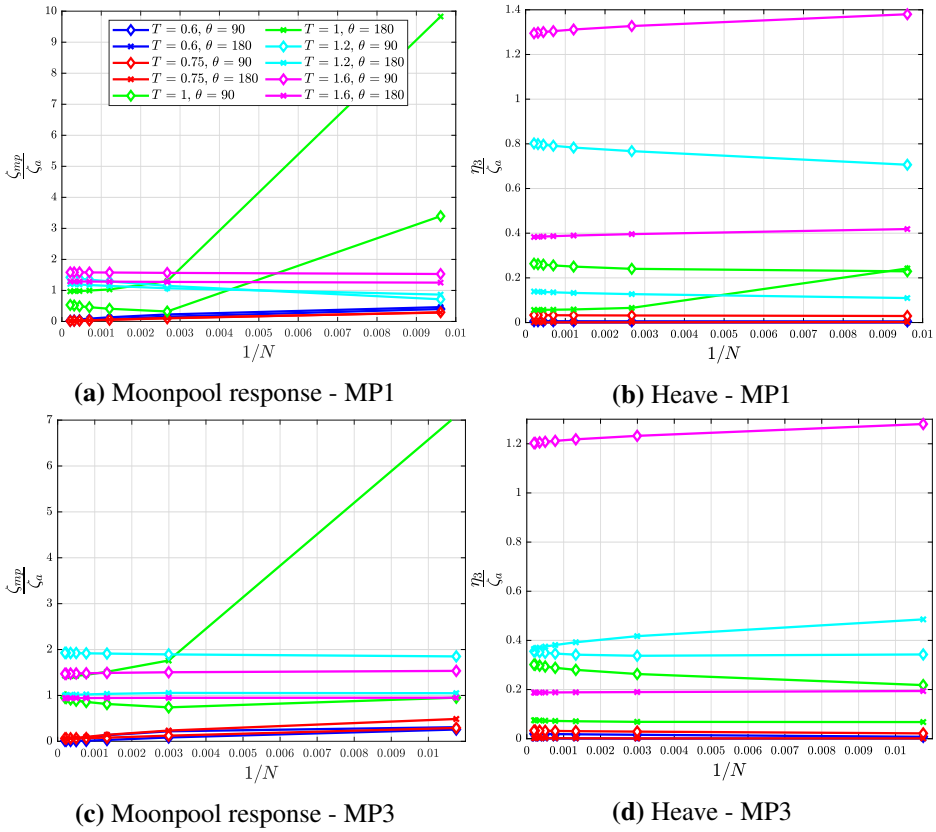

(a) Moonpool response - MP1

(b) Heave - MP1

(c) Moonpool response - MP3

(d) Heave - MP3

Figure 6.5: Mesh sensitivity analysis of moonpool and heave responses for MP1 and MP3 for selected wave periods and two wave headings. In general, converged results are observed for $N \gtrsim 2000$. Similar results were obtained for MP0 and MP2. θ is the heading angle, and is defined such that $\theta = 180°$ is head sea conditions. Here, ζ_{mp} is the moonpool response at the WP1 (cf. Figure 5.3). The moonpool resonance modes are summarized in Table 9.1.

6.5 Two-dimensional hybrid Navier–Stokes solver

A Navier–Stokes (NS) solver is implemented in order to capture viscous effects related to flow separation. The solver is referred to as CFD. The present hybrid method is based on previous work by Kristiansen and Faltinsen (2012). A difference is that the inviscid domain only constitutes the uppermost cell layer in the present CFD. The motivation for only the upper layer being inviscid is based on previous studies carried out by Professor Trygve Kristiansen (personal conversations, 2018), where they observed that circulation developed over time when they used a step-wise transition from the inviscid domain to the viscous domain (see e.g. Kristiansen et al. (2013)). Moreover, expanding the inviscid domain does not necessarily yield lower computational time, since majority of the required CPU time is dedicated to solving the Poisson's equation for the pressure (the Poisson's equation for the pressure is discussed later in this section).

The flow is solved using the Finite Volume Method (FVM). The Navier–Stokes equations are time-marched using an explicit fourth order Runge–Kutta scheme. For simplicity, the present derivation is given for the explicit forward Euler method. The governing equations and the assumptions in the present method are described in the following.

The Navier–Stokes and the continuity equations,

$$\underbrace{\rho\frac{\partial \boldsymbol{u}}{\partial t}}_{\text{FD}} + \underbrace{\rho\boldsymbol{u}\cdot\boldsymbol{\nabla}\boldsymbol{u}}_{\text{BD}} = \underbrace{-\boldsymbol{\nabla}p}_{\text{CD}} + \underbrace{\mu\boldsymbol{\nabla}^2\boldsymbol{u}}_{\text{CD}} + \kappa(x)\boldsymbol{u}, \tag{6.16a}$$

$$\frac{\partial u}{\partial x} + \frac{\partial w}{\partial z} = 0, \tag{6.16b}$$

are solved in the viscous domain. The advection and diffusion terms are neglected in the potential flow domain. In this way, the irrotationality of the flow is satisfied in the potential flow domain. Here FD, BD and CD are abbreviations for *forward difference*, *backward difference* and *central difference* differential schemes, respectively. The choices for the differential schemes are based on theory presented by Ferziger and Perić (2002) and Barba and Forsyth (2018). Numerical stability is considered while choosing the differential schemes. The discretization schemes take into account that the cells are stretched. The first-order upwind scheme is used to discretize the advection terms (Ⓑ in (6.16a)). The second-order central difference schemes are used to discretize Ⓒ in (6.16a) and for the pressure in (6.17).

Numerical beaches are modeled by introducing a source term proportional to the velocity ($\kappa(x)\boldsymbol{u}$) in the Navier–Stokes equations. $\kappa(x)$ is a third order polynomial,

with a magnitude such that $\kappa(\pm L_t/2)/\rho = 1.0\,\mathrm{s}^{-1}$ at the tank ends, where L_t is the length of the numerical wave tank. The third order polynomial is equivalent to that discussed in §6.1.1. The length of the numerical beaches is $L_b = \lambda$. Note that the numerical beach in the CFD is shorter than in the BEM (cf. §6.1.1). On contrary to the numerical beach in the BEM, the beach in the CFD dissipates energy more efficiently since the whole water column contributes, while in BEM, naturally, only the panels on the free-surface contribute.

The Navier–Stokes equations are solved using Chorin's projection method (Chorin 1967). This implies solving for an auxiliary velocity field in an intermediate substep * without accounting for the pressure. In general, the velocity field in substep * is not divergence free. Consequently, a Poisson's equation for the pressure in the viscous domain is obtained as

$$\nabla^2 p^{n+1} = \frac{\rho}{\Delta t}\boldsymbol{\nabla}\boldsymbol{u}^*, \tag{6.17}$$

where n is the time step number. (6.17) is a consequence of requiring that continuity is satisfied in the next time step, but not necessarily in the intermediate step. In the inviscid domain, the pressure is a harmonic function and thus satisfies the Laplace equation

$$\nabla^2 p^{n+1} = 0, \tag{6.18}$$

and is derived from (3.3) and using that $p = -\rho\partial\phi/\partial t$. (6.18) is consistent with (6.17), since $\boldsymbol{u}^* = \boldsymbol{u}^n$ in the inviscid domain, and $\nabla\boldsymbol{u}^n = 0$.

Given the pressure and $\boldsymbol{u}^*$, the velocity components in x- and z-direction are determined as

$$\boldsymbol{u}^{n+1} = \boldsymbol{u}^* - \frac{\Delta t}{\rho}\boldsymbol{\nabla} p^{n+1}. \tag{6.19}$$

Linearized body-boundary and free-surface conditions are applied. This is justified if the water motions are dominant relative to the body velocities, and if nonlinear free-surface effects are negligible, as discussed in §3.3. Close to moonpool resonance, the water motion is, in general, considerably larger than the body motion.

6.5.1 Staggered grid

In the present CFD code, a *forward staggered grid* is adopted. It has the positive aspects that it links the velocities and pressure well. However, it involves somewhat comprehensive links to be accounted for, since it involves using three

different grid systems for u, w and p. The pressure is located at the center of a cell. The u-component is located at the middle of the east face of the cell. The w-component is located at the middle of the north face. An illustration is provided in Figure 6.6. The present hybrid NS solver can be used to simulate sharp cornered box-shaped geometries in 2D.

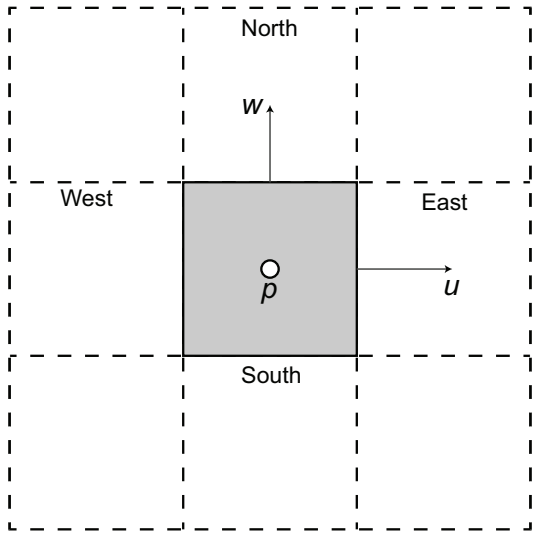

Figure 6.6: Sketch of the forward staggered grid system adopted in the presently developed NS solver.

A cartesian grid system is adopted to perform the numerical simulations. Since an increase in the number of cells results in an increase in computational time, the mesh sizes are stretched until the maximum limits of Δx_{max} and Δz_{max} are reached in the x- and z- directions, respectively, as illustrated in Figure 6.7. The mesh is kept constant to Δx and Δz within the "fine mesh" region. Outside this region, the mesh is stretched as a geometric series, until the maximum limits are reached. The cell size in the x-direction for cell number i is

$$\Delta x_i = \begin{cases} \Delta x & x_L < x < x_R \\ \Delta x \cdot r^m & \text{if } \Delta x \cdot r^m < \Delta x_{max} \text{ and } \{\ x < x_L \text{ or } x > x_R\} \\ \Delta x_{max} & \text{if } \Delta x \cdot r^m \geq \Delta x_{max} \text{ and } \{\ x < x_L \text{ or } x > x_R\} \end{cases} \tag{6.20}$$

where r is the stretching factor. x_L and x_R are illustrated in Figure 6.7(a). Similar treatment of the cell size in the z-direction, Δz, is applied. m is the number of cells from the "fine mesh" region to the cell i, as illustrated in Figure 6.7(b). $r = 1.07$ was chosen during the early stages by trial and error. The length of the fine mesh region is chosen as $2L$, where L is the length of the model.

In the present code, rectangular boxes as illustrated in Figure 6.7, are pre-defined, and represent the bodies in the computational domain. Firstly, a mesh is generated without accounting for any bodies in the computational domain (i.e. only the numerical wave tank is meshed). Finally, cells within the rectangular boxes are removed from the mesh. An example of the resulting mesh for the presently investigated models is provided in Figure 6.8.

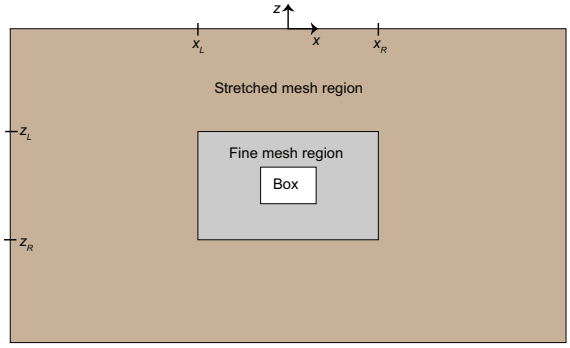

(a) The white region illustrates the body. Cells inside this region are removed from the mesh.

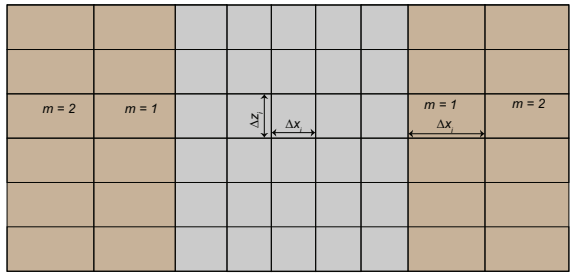

(b) Cell size stretching is illustrated in the x-direction, while the cell size is constant in the z-direction. m in (6.20) is indicated.

Figure 6.7: Sketches illustrating the concept of grid generation in the present code. In the brown region, the cell size is stretched. The grey region is the fine mesh region, where the mesh size is kept constant.

6.5.2 Mesh convergence

We performed mesh convergence studies for Case 3 (cf. Table 4.1) with the present CFD code in Ravinthrakumar et al. (2019a). The results for Case 3 are presented in the following. The results in the proximity of the piston and first sloshing modes are presented separately in Figure 6.9. We observe satisfactory convergence with the presently adopted cell sizes, which are $\Delta x = \Delta z = 0.01$ m. In the proximity

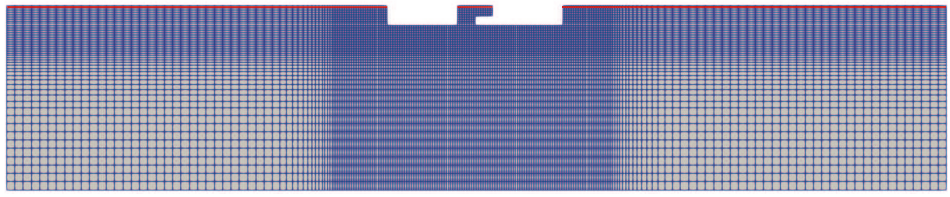

(a) Entire computational domain

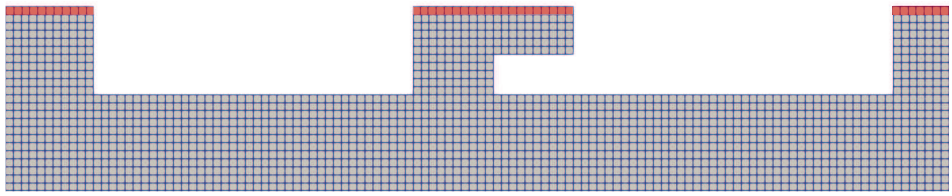

(b) Zoomed in around model with moonpool

Figure 6.8: Example mesh for Case 3 (cf. Table 4.1). The grey region indicates the viscous domain, while the red indicates the inviscid domain. Cells are stretched until the maximum limits are reached.

of the first sloshing mode, we observe that the responses increase somewhat with $\Delta x = \Delta z = 0.005$ m, which diverges away from the experimental results (cf. §7.1.3).

The present mesh densities do not solve the details of the boundary layer, since it is assumed that viscous stresses in the boundary layer are of secondary importance, cf. discussion in §2.3.

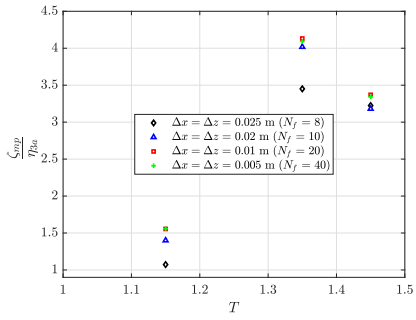

(a) Piston mode

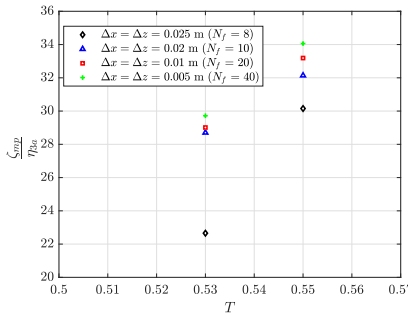

(b) Sloshing mode

Figure 6.9: Mesh convergence studies in the proximity of the piston and first sloshing modes for Case 3 (cf. Table 4.1). $N_f = L_m/\Delta x$ is the number of cells along the moonpool length at the mean waterline, L_m. Δx is the mesh size in the x-direction.

6.6 Potential viscous code in 3D

OpenFOAM is an open source code that is used to solve the Navier–Stokes equations numerically. A hybrid method was developed by Kristiansen et al. (2013), where a potential flow solver was combined with a NS solver, similar to the presently developed NS solver as discussed in §6.5, to perform simulations in forced motions. They referred to the method as Potential Viscous Code in 3D (PVC3D). The method is based on a set of C++ libraries called by the solver in OpenFOAM. The details of PVC3D are not presented herein. In the following, PVC3D simulations with MP1-3 are discussed, cf. Table 5.1. PVC3D simulations with the 3DQ configurations are also presented in this thesis, and are discussed in Appendix B.3.

Example meshes from the present PVC3D simulations are presented in Figure 6.10. The simulations are carried out with boundary conditions on the NWT as indicated in Figure 6.11. Symmetry conditions at the xz-plane at $y = 0$ are applied. At the other ends and bottom of the NWT, wall conditions are applied. Numerical beaches are not implemented. Thus, the length and width of the domain are such that waves are not reflected back to the model during the simulation time, which is $40T$, and T is the forced oscillation period. The water depth is set as 5 m, i.e. the same as in the experiments in the Ocean Basin. Linearized body-boundary on the oscillating body, and linearized free-surface conditions, are applied. This is similar to the presently developed hybrid 2D NS solver. Numerical wave probes, as used in the experiments, are used in the simulations (cf. Figure 5.3).

A code to generate the necessary input files to run PVC3D is developed. The code automatically generates the input files for generating the meshes using the module SnappyHexMesh. First, a mesh using BlockMesh is created. This mesh is then used by the SnappyHexMesh module, where the mesh size is refined towards the ship by defining boxes. Within each box, the mesh sizes are decreased by a factor of two. The module also removes any cells within the body, and re-defines the mesh shapes in the proximity of the body such that the mesh conforms the body surface. Detailed description of the BlockMesh and SnappyHexMesh modules is given by Greenshields (2015).

The mesh sizes are defined such that the number of cells per wavelength, $N_{per,of}$, is defined in the coarsest region. $\Delta x_{far} = \lambda/N_{per,of}$ is the mesh size in the coarsest mesh region. The mesh sizes are defined such that the cells are cube-shaped (at least away from the near proximity of the ship). The mesh sizes are refined towards the ship. Three refinement regions are defined in the presently adopted meshes. The extent of these regions and more details about the meshes are provided in Appendix B.2. The numerical simulations with PVC3D are performed with $N_{per,of} = 15$.

With the presently adopted approach to generate the meshes, the number of cells, and the mesh sizes in the vicinity of the ship, vary with the oscillation period. For instance, with $T = 0.7$ s, the mesh size close to the body is approximately 0.006 m, which gives a total of approximately 6,100,000 cells. The required CPU time with this mesh is approximately 75 hours for 40 oscillations. By contrast, with $T = 1.0$ s, the mesh size is approximately 0.01 m close to the body, giving a total of approximately 2,350,000 cells and total CPU time of approximately 27 hours for 40 oscillations.

The presently adopted approach for mesh generation is based on previous experiences (see e.g. Kristiansen et al. (2013)), where we saw that the mesh size in the proximity of the piston mode should be such that we obtain approximately 20 cells across the moonpool length and width. With the present meshes, we obtain approximately 18 cells across the moonpool for MP1 at the piston mode, while we obtain approximately 34 for MP2 at the piston mode. At the sloshing modes, we obtain finer meshes. This is fair, since the moonpool response shapes are non-uniform at the sloshing modes, in contrast to the near-uniform piston mode. In the proximity of the first longitudinal sloshing mode for MP2, we obtain approximately 65 cells across the moonpool length.

6.6.1 Mesh convergence

Mesh sensitivity analysis for MP1, MP2 and MP3 in forced heave is performed. The results are presented in Figure 6.12 in terms of amplitude-dependent moonpool RAOs. The mesh sensitivity analysis is carried out by varying $N_{per,of}$. More results are presented in §9.2. The total number of cells is approximately 2,450,000 with $T = 1.0$ s and the presently adopted mesh sizes. By contrast, the finest mesh presented in Figure 6.12 consists approximately 9,500,000 cells at $T = 1.0$ s. The simulations with the finest mesh are simulated for $25T$.

The convergence study, presented in Figure 6.12, suggests that satisfactory mesh convergence is obtained with the presently adopted meshes (i.e. with $N_{per,of} = 15$). Close to resonance, the responses with $N_{per,of} = 15$ compare well with the two finer meshes. In general, the differences between the presently adopted mesh and the finest mesh are less than 2.5 %. The agreement between WAMIT and PVC3D simulations outside resonance is acceptable.

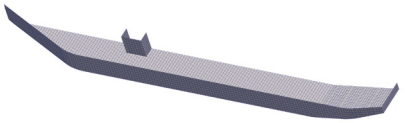

(a) Mesh around the vessel

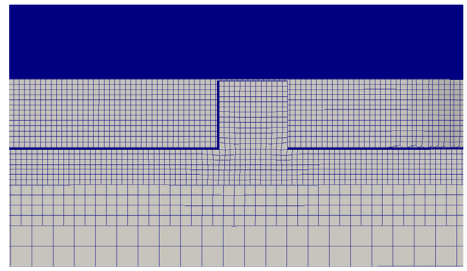

(b) Side view - zoomed in around the moonpool

(c) View from top - zoomed in along the edges of the ship

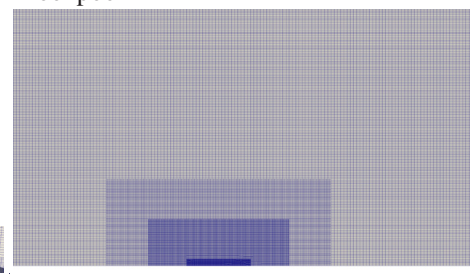

(d) View from top - the entire computational domain

Figure 6.10: Example meshes from the PVC3D simulations. Here, a relatively coarse mesh is presented for the sake of clarity. The mesh size is refined towards the ship.

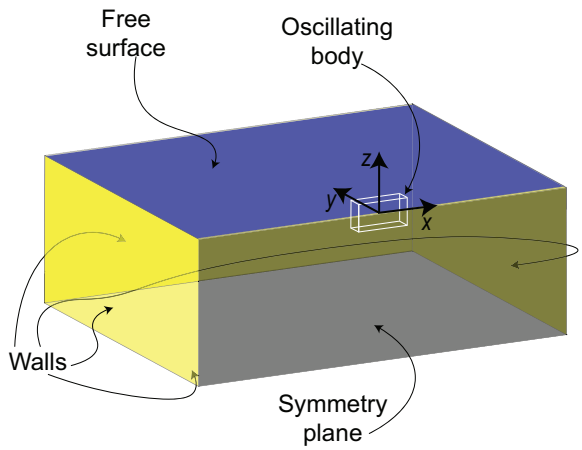

Figure 6.11: Sketch illustrating the boundary conditions applied in the present simulations with PVC3D. The arrows indicate the different boundary conditions applied in the present simulations. The boundary conditions for the 3DQ configurations are discussed in Appendix B.3.

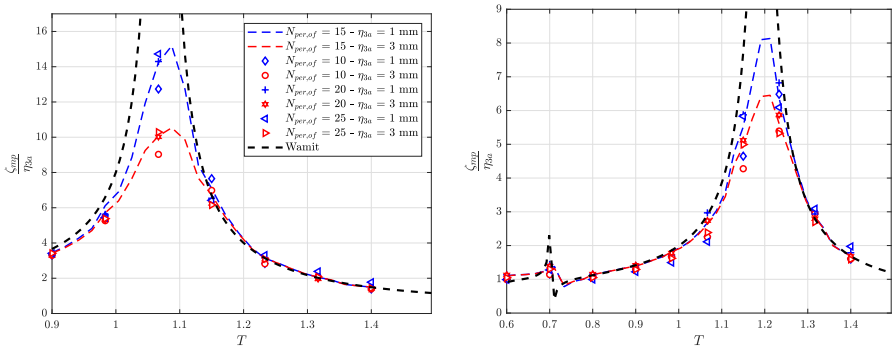

(a) MP1 **(b)** MP2

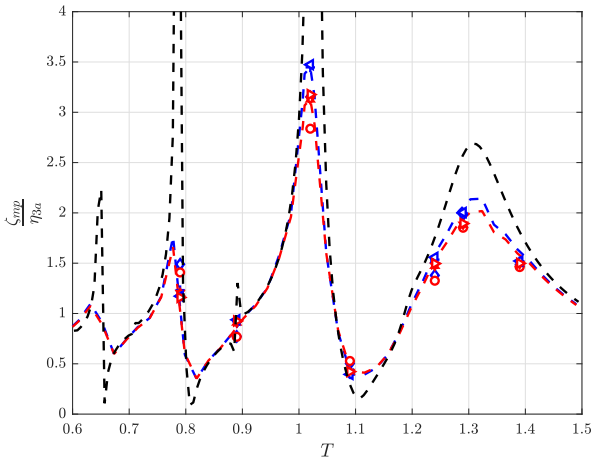

(c) MP3

Figure 6.12: Mesh sensitivity analysis in forced heave simulations with PVC3D. Simulations with different $N_{per,of}$ are compared. WAMIT simulations are also presented.

6.7 Freely floating body in 2D

Performing numerical simulations for a freely floating body requires solving a generalized version Newton's second law for a rigid body at each time step. The body floats freely with incident waves. The hydrodynamic force in the i-direction is determined as

$$F_i = -\int_{S_B} p n_i dS \tag{6.21}$$

where S_B is the mean wetted surface of the freely floating body, and n_i is the normal vector in i-direction pointing into the fluid. The equation of motion in the i-direction reads

$$M\ddot{\eta}_i = F_i - C_{i1}\eta_1 - C_{i3}\eta_3 - C_{i5}\eta_5, \tag{6.22}$$

where $C_{ij} = C^*_{ij} + C^{**}_{ij}$. C^*_{ij} is the hydrostatic restoring coefficient in the i direction due to motion in the j direction. C^{**}_{ij} is the restoring coefficient due to the mooring system. In the present 2D simulations, we use that $C^{**}_{11} = k_s$, $C^{**}_{55} = LF_{pre}$ (where L is the length of the vessel) and $C^{**}_{15} = C^{**}_{51} = -k_s z_s$ (Fredriksen 2015). k_s is the spring stiffness, z_s is the vertical distance from the center of gravity to the spring connections, and F_{pre} is the pre-tension in the springs.

An artificial added mass force $\tilde{A}_{ii}\ddot{\eta}_i$ is added on both sides of (6.22), in order to make the time marching scheme stable. If this term is excluded, the scheme becomes unconditionally unstable. $\tilde{A}_{ii}$ can be chosen freely, as long as it counteracts the added mass force contribution in F_i. However, if $\tilde{A}_{ii}$ is set too large, the numerical result will lag in time relative to the exact solution. This was discussed by e.g. Kristiansen (2009). He found that with $\tilde{A}_{ii} = 5m$, the time lag in the simulations was negligible, and the simulations were stable. To further explain the unstability that appears by neglecting the artifical added mass force, we consider a linear system of ODE on the form $d\boldsymbol{g}/dt = G(g)$, where $\boldsymbol{g}$ is a vector of unknowns, and G is a linear operator. The eigenvalues of G must lie within the stability region for the time-integration scheme to be stable. If we have a system on the form $d\boldsymbol{g}/dt = G(\boldsymbol{g}, d\boldsymbol{g}/dt)$, the explicit time-integration scheme is always unstable (personal conversations with Professor Harry B. Bingham, 2020). The unstability appears due to the presence of the acceleration term on the right hand side (the hydrodynamic added mass force, in our case). Hence, an artificial added mass term on the right hand side to cancel the hydrodynamic added mass force in F_i is required to make the time-marching scheme stable.

The acceleration in the i direction is determined as

$$\ddot{\eta}_i^{n+1} = \frac{F_i - C_{i1}\eta_1^n - C_{i3}\eta_3^n - C_{i5}\eta_5^n + \tilde{A}_{ii}\ddot{\eta}_i^n}{m + \tilde{A}_{ii}}, \tag{6.23}$$

where $\tilde{A}_{ii} = 5m$ is used in the present simulations. n is the time step number. Note that m is the dry mass in translational degrees of freedom, while it is the moment of inertia in rotational degrees of freedom. The velocities and positions are determined by splitting (6.23) into two sets of differential equations.

6.8 Time marching methods

The CFD and BEM simulations involve time stepping differential equations. There exists many time marching methods. The choice of the numerical schemes for time marching are often a trade-off between accuracy and time consumption. In this work, the explicit fourth order Runge–Kutta (RK) method is used to time-march the governing equations. The choice is based on its known capability to evolve the free-surface conditions in time, as discussed by e.g. Fredriksen (2015). The Crank–Nicolson method is used to integrate (6.23) in time. The overall accuracy of the simulations in freely floating conditions is therefore second order in time.

The free-surface conditions in the PVC3D simulations are time-marched by means of the implicit Euler method. The Navier–Stokes equations are integrated in time with the explicit Euler method.

The numerical time marching schemes applied in the present work are summarized in Table 6.1. Details of the numerical schemes are discussed in detail in many textbooks, such as Kreyszig (2011).

Table 6.1: Numerical time marching schemes adopted in the presently developed BEM and CFD solvers, and PVC3D.

	BEM	CFD	PVC3D
Free-surface conditions	4th order RK	4th order RK	Implicit Euler
Equation of motion (6.23)	Crank–Nicolson	Crank–Nicolson	-
Navier–Stokes equations	-	4th order RK	Euler

6.8.1 Time step size

The Courant–Friedrichs–Lewy (CFL) is used as an upper limit to the time-step size to achieve stable solutions, given the mesh sizes, Δx, Δy, and Δz (Ferziger and Perić 2002). In the one-dimensional case,

$$\mathrm{CFL} = \frac{u\Delta t}{\Delta x}, \tag{6.24}$$

where u is the fluid velocity in the x-direction. Δx and Δt are mesh and time step sizes, respectively. Similar treatment can be applied in the y- and z-directions. In the present work, $\mathrm{CFL} < 0.7$ is used as a criterion. The criterion is determined by trial and error.

Dommermuth and Yue (1987) presented another stability criteria to solve the free-surface conditions by performing a von Neumann stability analysis for the fourth order Runge–Kutta scheme with linearized free-surface conditions. They obtained the condition

$$\Delta t^2 \leq \frac{8\Delta x}{g\pi}, \tag{6.25}$$

where g is the gravitational constant. In general, these criteria imply that $\Delta t \approx T/200$ to $\Delta t \approx T/80$, depending on the period, T, and forced heave amplitude, η_{3a}, or the wave steepness, H/λ, for the presently adopted meshes.

If the aforementioned criteria are exceeded in the CFD simulations, a warning message appears, such that the simulations can be re-run with a smaller Δt.

6.9 Verification and validation

Verification and *validation* are important when developing numerical tools. Verification is a check on whether the equations are solved right, while validation is a check whether the right equations are solved Faltinsen and Timokha (2009). Numerical codes are verified by comparing the simulations with theory. Validation is, for instance, comparisons with benchmark model tests.

In the present work, two numerical codes are developed; BEM and CFD. The present BEM and CFD codes are verified against wavemaker theory. Verifying a NS solver is not straightforward, since it is difficult to find analytical solutions of the Navier–Stokes equations. There exist many benchmark numerical simulations with very fine meshes, which can be used to validate the present NS solver. A commonly adopted configuration for validation is the *cavity flow*, which is discussed in the following. Finally, a rectangular section in heave decay is simulated with

the BEM and CFD codes.

6.9.1 Lid-driven cavity flow

A common approach to verify a Navier–Stokes solver is by simulating a lid-driven cavity. A non-zero horizontal velocity is applied at the top of the cavity. Various Reynolds numbers– defined as $\mathrm{Re} = \frac{UD}{\nu}$, where U is the velocity of the lid, D is the length of the square cavity, and ν is the kinematic viscosity –are tested. In the following simulations, $D = 1$ m and $U = 1\frac{m}{s}$. ν is varied to obtain different Reynolds numbers. The present simulations are compared against results presented by Ghia et al. (1982) and AbdelMigid et al. (2017). They performed cavity flow simulations with 2D solvers. AbdelMigid et al. (2017) used a mesh with approximately 360,000 cells, while Ghia et al. (1982) performed their simulations with approximately 65,000 cells. The simulations with the present CFD are carried out with 6,400, 10,000, and 40,000 cells. No stretching is applied. Since there is no free-surface and oscillating body in the computational domain, these simulations are fully nonlinear.

Vortices are created in the cavity, as illustrated in Figure 6.13. We distinguish between the primary vortex and the secondary vortices, where the location of the vortices are dependent on the Reynolds number. Results in terms of the location of the primary vortex are presented in the following. The secondary vortices are typically located at the top left, bottom left and/or bottom right of the cavity. No clear evidence of the top left vortex was observed in the presently tested range of Reynolds numbers with the present NS solver, which is consistent with the benchmark numerical simulations. The results from the present simulations are saved every 1000 time step, and the simulations are carried out until the location of the primary vortex has converged with differences less than 0.5 %.

The cavity flow problem is simulated at three Reynolds numbers, $\mathrm{Re} = 100, 400$ and 1000. The results with 10,000 cells are presented in Figure 6.14. The location of the primary vortex as determined with the present CFD code is compared to the benchmark simulations by Ghia et al. (1982) and AbdelMigid et al. (2017) in Table 6.2. The results with the present CFD are acceptable compared with the previous studies.

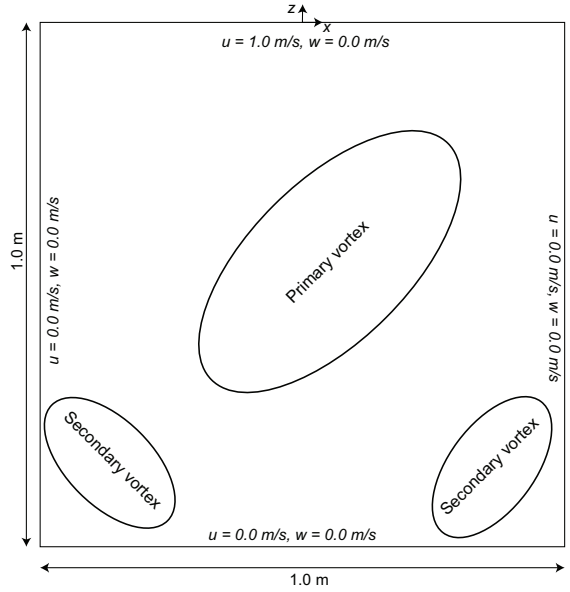

Figure 6.13: Cavity flow problem, with boundary conditions. The regions where the primary and secondary vortices are typically located are indicated.

Table 6.2: Location of primary vortex as predicted by the presently developed NS solver compared with results as presented by Ghia et al. (1982) and AbdelMigid et al. (2017). The origin of the coordinate system is defined in Figure 6.13.

Case	$\mathrm{Re} = 100$	$\mathrm{Re} = 400$	$\mathrm{Re} = 1000$
Mesh with 6,400 cells	[0.126 , -0.256]	[0.066 , -0.376]	[0.036 ,-0.416]
Mesh with 10,000 cells	[0.125 , -0.255]	[0.060 , -0.385]	[0.035 ,-0.425]
Mesh with 40,000 cells	[0.121 , -0.265]	[0.057 , -0.390]	[0.034 ,-0.430]
Ghia et al. (1982)	[0.117 , -0.266]	[0.055 , -0.395]	[0.031 , -0.438]
AbdelMigid et al. (2017)	[0.116 , -0.263]	[0.054 , -0.394]	[0.031 , -0.434]

6.9.2 Wavemaker

A numerical wave tank with a wave generator is simulated with the presently developed BEM and CFD codes. BEM simulations with both flap-type and piston-type wave generators are presented. Only a flap-type wave generator is simulated with the CFD. The BEM simulations are carried out by varying the panel size

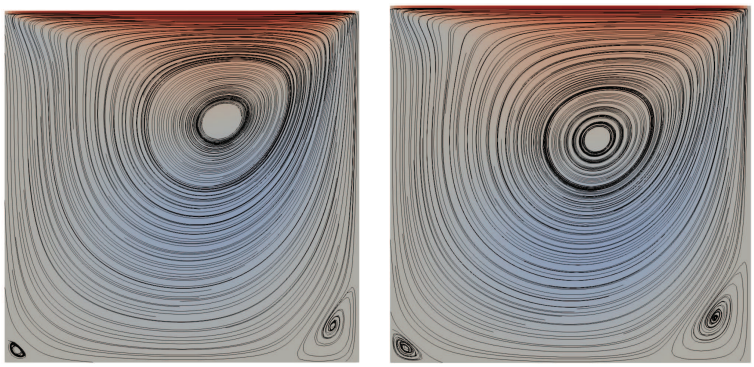

(a) $\mathrm{Re} = 100$.

(b) $\mathrm{Re} = 400$.

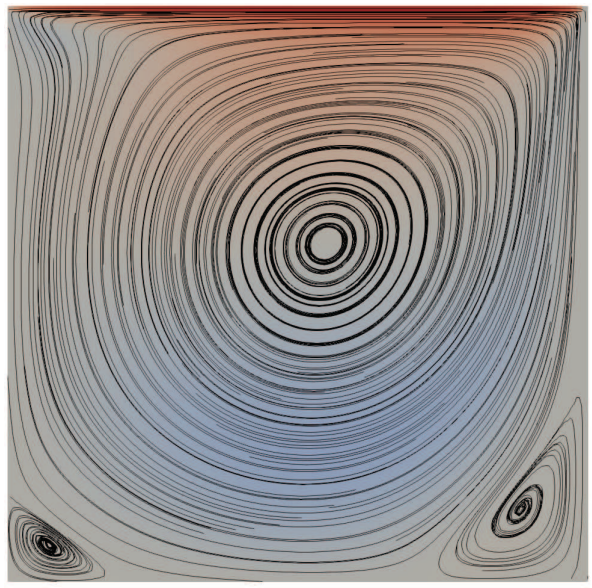

(c) $\mathrm{Re} = 1000$.

Figure 6.14: Cavity flow results from the present CFD code with 10,000 cells. The horizontal velocity at the top lid is $U = 1$ m/s. Stream lines are presented for three different Reynolds numbers. The colors indicate horizontal velocity from -1 m/s (blue) to 1 m/s (red).

on the free-surface as $\Delta x_f = \lambda/N_{per,BEM}$, where $N_{per,BEM}$ is varied between 5 and 80. The CFD simulations are carried by varying the cell sizes as $\Delta x = \Delta z = \lambda/N_{per,CFD}$, where $N_{per,CFD}$ is varied between 4 and 30. No stretching is applied. A numerical beach at the opposite end of the wavemaker is applied. Numerical simulations with a wave probe located at the middle of the NWT are presented. The time step size in the simulations is $\Delta t = T/100$, where T is the wave period. The water depth is 1.0 m (i.e. same as in the model tests in the wave flume). The CFD simulations are carried out with wave steepness H/λ = 1/100, where H and λ are the wave height and wavelength, respectively.

The BEM simulations are compared with (3.8) in Figure 6.15(a). The BEM results are in good agreement with theory for $N_{per,BEM} > 40$, with differences less than 1 % compared with theory. The CFD simulations with a flap-type wavemaker are compared with theory in Figure 6.15(b). Satisfactory agreement between theory and CFD is obtained with $N_{per,CFD} > 12$, where the differences compared with theory are, in general, less than 4.5 %.

In the BEM simulations presented in this thesis, the number of panels per wavelength is chosen as $N_{per,BEM} = 80$. The CFD simulations are carried out with $N_{per,CFD} = 15$ in forced motion simulations. In freely floating conditions with incident waves, $N_{per,CFD} = 20$ is used.

6.9.3 Free decay

Simulations with the BEM and CFD in heave decay are carried out to validate the codes in freely floating conditions. A rectangular section with $L/D = 4$, where L and D are the length and draft of the body, is simulated. Heave decay simulations are carried out with an initial displacement, η_{3i}, and zero initial velocity. The results are compared against digitized data from theoretical results as presented by Yeung (1982). A water depth of 1.0 m is used. The number of panels per wavelength in the BEM simulations is $N_{per,BEM} = 80$. In the CFD simulations, $N_{per,CFD} = 15$ is used far away from the body, and $\Delta x = \Delta z = 0.01$ m is used in the proximity of the body (40 cells along the length of the body). A stretching factor of $r = 1.07$ is applied. The wavelength is determined from the natural period in heave, which is $T_3 = 1.01$ s. The time step size in the BEM and CFD simulations is $\Delta t = T_3/120$.

Time-series of the heave motion of the rectangular section from the BEM and CFD simulations are compared against results as presented by Yeung (1982) in Figure 6.16. In general, good agreement between the BEM and CFD simulations is illustrated. However, some discrepancies between Yeung's theory and the present simulations are observed, especially around the first negative peak. Kristiansen

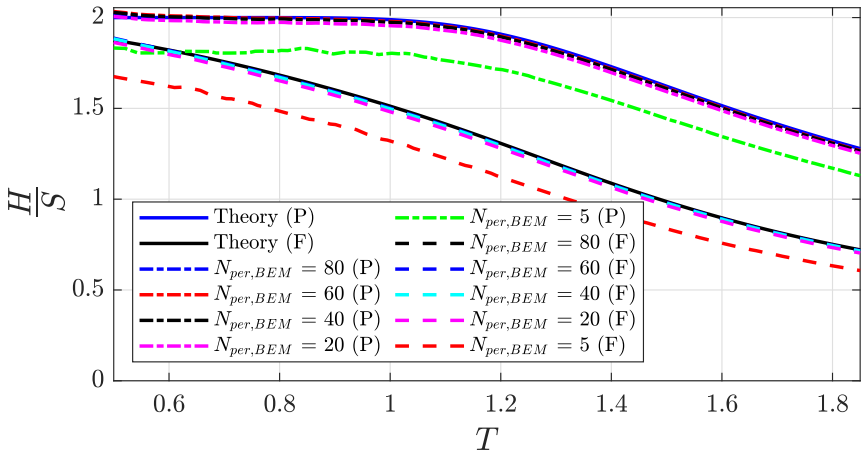

(a) BEM results compared against theory with flap-type (F) and piston-type (P) wave generators.

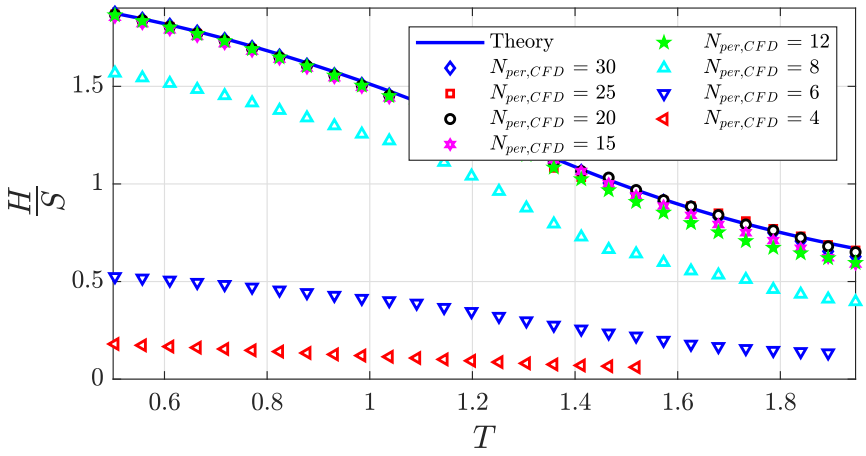

(b) CFD results compared against theory with flap-type wave generator.

Figure 6.15: BEM and CFD simulations in a NWT compared against theory as given in (3.8). Numerical results with a numerical wave probe located at the center of the NWT are presented.

(2009) reported similar results, where his linear and nonlinear BEM simulations slightly under-estimated the first two negative peaks. This is also observed with the present CFD code. However, with the present linear BEM, the second negative peak is in good agreement with theory. The second positive peak (at $t = 1.03$ s) is slightly over-predicted by BEM for unknown reasons. Refining the mesh size and the time step size did not yield any noteworthy improvements.

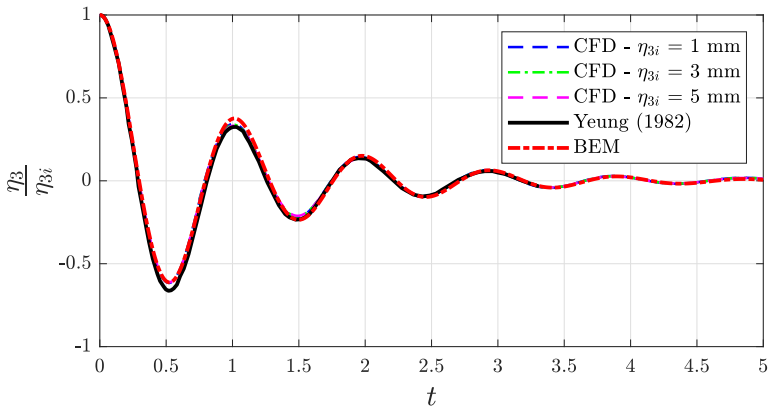

Figure 6.16: Free decay of a body with $L/D = 4$. The BEM and CFD simulations are compared against results as presented by Yeung (1982). CFD simulations with three different initial positions, η_{3i}, are presented.

Part III

Results, Discussions and Conclusions

Chapter 7

Forced heave of 2DMR and 3DQ

Model tests and numerical simulations in forced heave of models with varying moonpool shape and size are discussed in this chapter. The results are presented in terms of amplitude-dependent moonpool RAOs. The moonpool RAOs are defined as ζ_{mp}/η_{3a}, where both quantities are amplitudes of the first harmonic steady-state responses. Moonpool RAOs for the 2DMR configurations from the forced heave tests are presented along with numerical simulations using the presently implemented CFD and BEM (cf. §7.1).

Amplitude-dependent moonpool RAOs from the forced heave experiments and PVC3D simulations for the 3DQ configurations are presented in §7.2. For reference, PVC3D and WAMIT simulations in forced heave and forced surge with the models tested in the Ocean Basin are presented in §9.2.

7.1 Forced heave with 2DMR configurations

Findings in Molin (2017) were the inspiration for the forced heave experiments of two-dimensional moonpools with recess (2DMR) configurations. He observed a significant change in the piston mode shape, compared to the piston mode shape for clean moonpools (i.e. no recess), due to the presence of the recess. We investigate the piston mode and first sloshing mode response shapes experimentally, and observe results consistent with his theory. Further, dominant damping due to flow separation at the moonpool inlets is discussed, both at the piston and first sloshing modes. Nonlinear free-surface effects at the first sloshing modes are also discussed. The results presented in this section were published in Ravinthrakumar et al. (2019a).

7.1.1 Piston and first sloshing mode shapes and natural periods

We first discuss natural periods. The piston mode and first sloshing mode periods as predicted by BEM, the present Domain Decomposition (DD) method (cf. §2.1.2) and from the model tests are presented in Table 7.1. The natural periods denoted BEM are determined by identifying the peaks in the moonpool RAOs. Similarly, the peaks in the experimental moonpool RAOs are presented for two forced heave amplitudes. Good agreement between the natural periods as predicted with the present DD method, BEM and experiments is illustrated. The piston mode period increases with increasing recess length, which is consistent with theory presented by Molin (2017), with 1.18 s for Case 1, where the recess floor covers 25 % of the moonpool inlet, to 1.35 s for Case 3, where the recess floor covers 50 % of the inlet (for a clean moonpool the piston mode period is 1.08 s). We recall that the present DD method is based on similar theory as by Molin (2017), where the difference is that his work was for deep water, whereas ours is for finite water depth with a flat sea floor. The piston mode period increases somewhat with increasing forced heave amplitudes. In §2.1.1, we discussed that the term denoted ① in (2.2) could be interpreted as a virtual added mass term. The fact that the piston mode period increases with increasing forced heave amplitudes is explained by that flow separation affects the virtual added mass, causing amplitude-dependent added mass, in addition to amplitude-dependent damping. The first sloshing mode periods from the experiments differ somewhat from those predicted by the present DD method and BEM, due to Duffing-type moonpool responses, as discussed further in §7.1.3.

Table 7.1: Natural periods as predicted by the present BEM simulations and DD method (truncated after 25 terms). Experimental results (Exp.) are also presented for two forced heave amplitudes.

Mode	DD	BEM	Exp. η_{3a} = 1 mm	Exp. η_{3a} = 5 mm
Case 1				
Piston mode	1.17 s	1.18 s	1.18 s	1.20 s
First sloshing mode	0.53 s	0.53 s	0.53 s	0.55 s
Case 2				
Piston mode	1.25 s	1.25 s	1.26 s	1.27 s
First sloshing mode	0.54 s	0.53 s	0.53 s	0.56 s
Case 3				
Piston mode	1.33 s	1.35 s	1.35 s	1.37 s
First sloshing mode	0.56 s	0.55 s	0.55 s	0.57 s

The piston and first sloshing mode shapes as predicted by the present DD method are presented in Figure 7.1 along with the experimental response shapes for Cases 1-3. Cases 1-3 involve configurations with varying recess floor lengths, cf. Table 4.1. The experimental response shapes are in agreement with the present DD method. The small discrepancies between the experimental response shapes and theoretical mode shapes are believed to be within the experimental uncertainty, which are slightly more pronounced for the first sloshing mode response shapes than for the piston mode response shapes.

Both the present DD method and the model tests suggest that the largest piston mode responses occur at the recess wall end, while the largest sloshing mode responses at the opposite wall end. Therefore, the piston mode responses measured with WP8, and sloshing mode responses measured with WP1, are presented herein (cf. Figure 4.13).

The piston mode shapes for clean moonpools are near-uniform. The piston mode shapes for moonpools with recess are non-uniform, and this is most pronounced for moonpools with large recess lengths; for Case 3, where the recess floor covers as much as half of the moonpool inlet, the response at the low-amplitude side is about 0.7 of that at the opposite side. The differences in the first sloshing mode shapes for the presently investigated configurations - compared to those for clean moonpools - are less prominent than for the piston mode shapes.

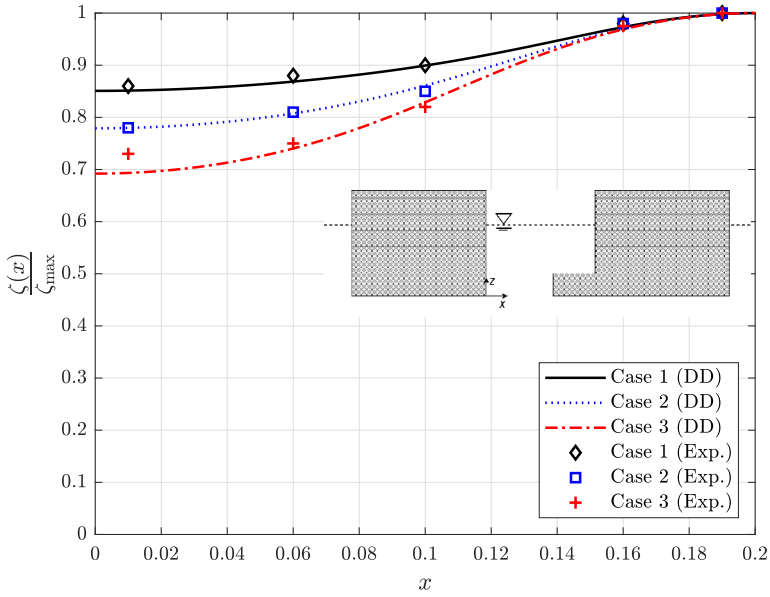

(a) Piston mode

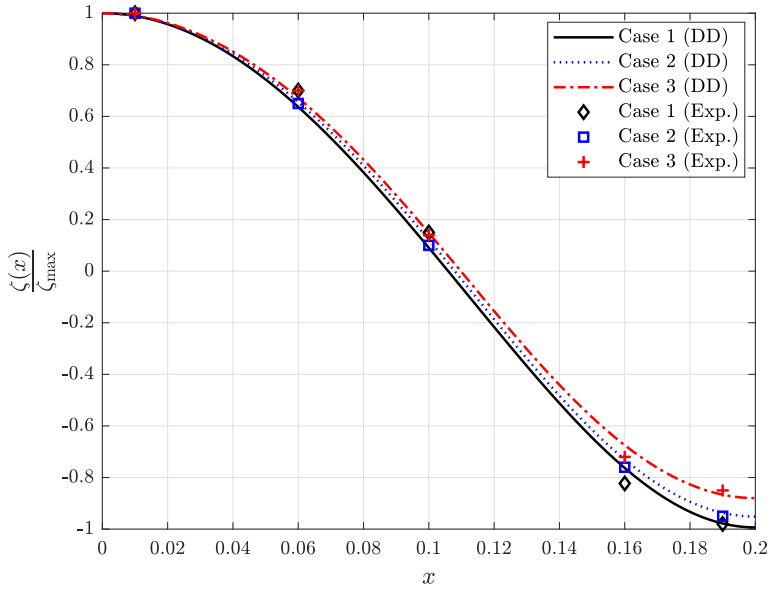

(b) First sloshing mode

Figure 7.1: Mode shapes as predicted by the present Domain Decomposition (DD) method and from the experiments. Experimental response shapes with forced heave amplitude $\eta_{3a} = 1$ mm. The experimental response shapes are the first harmonic response amplitudes made non-dimensional with respect to the largest first harmonic response amplitude in the moonpool, $\zeta_{\max}$.

7.1.2 Piston mode RAOs

The main source of damping at the piston mode period for moonpools with recess is investigated in the following. Amplitude-dependent piston mode RAOs for Cases 1-3 are presented in Figure 7.2. Experimental results are presented along with BEM, VBEM and present CFD simulations. We recall that VBEM is our 2D BEM with a physically-based damping term in the dynamic free-surface condition. BEM clearly over-predicts the responses at resonance, since damping due to flow separation is not accounted for. The amplitude-dependent experimental RAOs indicate, however, that damping due to flow separation matters and accounts for in the order of half the total damping in the proximity of the piston mode. Wave radiation damping caused by the piston mode response accounts for the other "half". This is as observed for clean moonpools (see e.g. Kristiansen and Faltinsen (2012)). Snapshots of flow fields from the CFD simulations are presented in Figure 7.3, where flow separation at the sharp corners is illustrated for Case 1. The snapshots show clear flow separation at both the moonpool entrance and the top corner of the recess floor.

In general, CFD and experiments compare well in the proximity of the piston mode. The VBEM is, perhaps surprisingly, successful in representing the damping for Case 1. This is interesting from an engineering point of view, since it serves as the first physically-based damping model for moonpool piston mode resonance. For Case 2, the results are also quite good, whereas for Case 3, where the recess floor covers half the moonpool inlet, the VBEM yields conservative results. This is mainly attributed to the fact that the presently adopted VBEM method is based on theory presented by Faltinsen and Timokha (2015) for clean moonpools. The pressure drop coefficient, K, does not account for the details in the moonpool, for instance local flow separation caused by the recess floor, cf. Figure 7.3, where clear flow separation occurs at the recess floor top corner, in addition to the two moonpool inlet corners. It is, however, interesting to note that the method serves as a fair engineering tool to obtain first estimates of the moonpool responses, at least for small recess floor sizes.

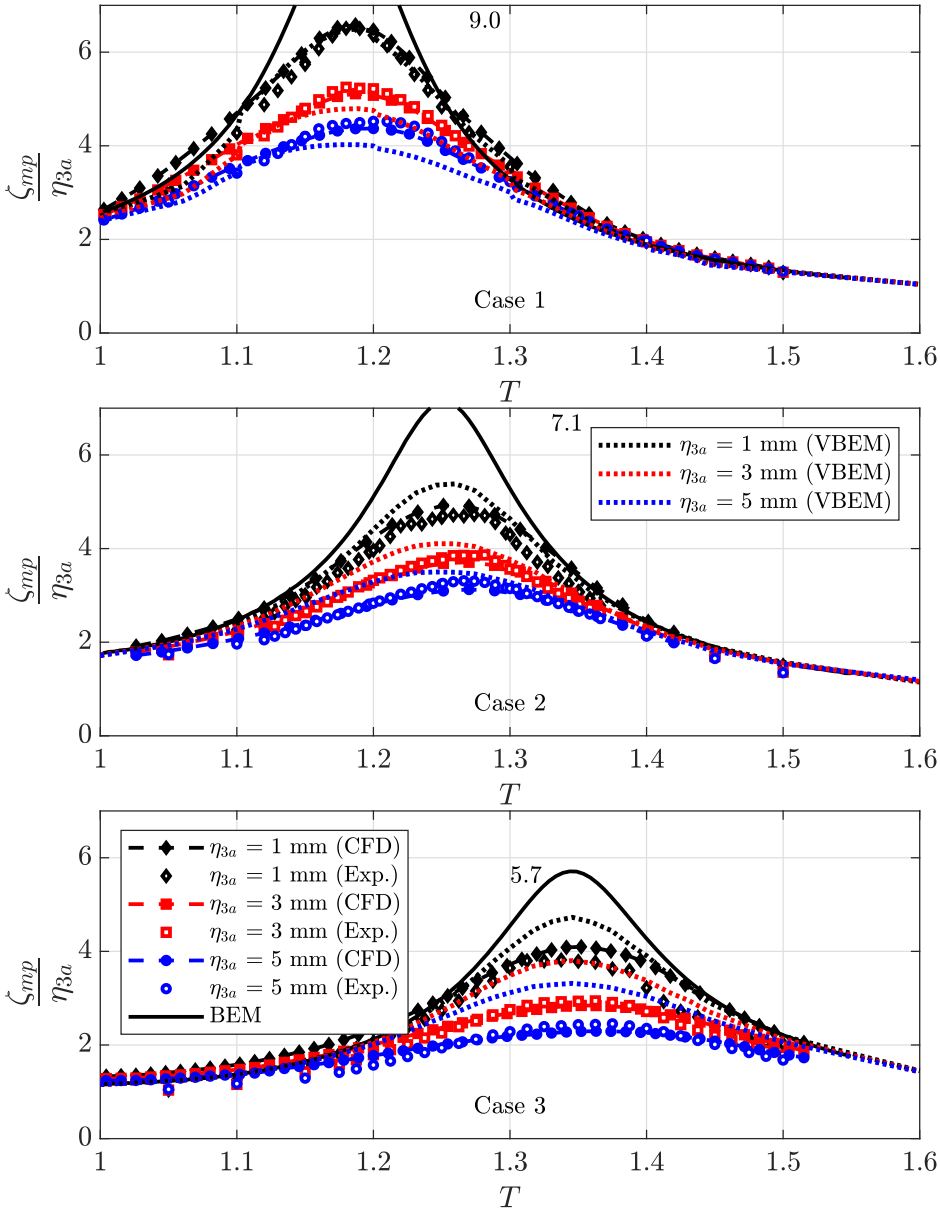

Figure 7.2: Numerical and experimental piston mode RAOs (WP8). The first harmonic moonpool response amplitude, ζ_{mp}, made non-dimensional with respect to the first harmonic forced heave amplitude, η_{3a}. The results are presented in an Earth-fixed coordinate system. The numbers indicate the piston mode response at resonance as predicted with BEM.

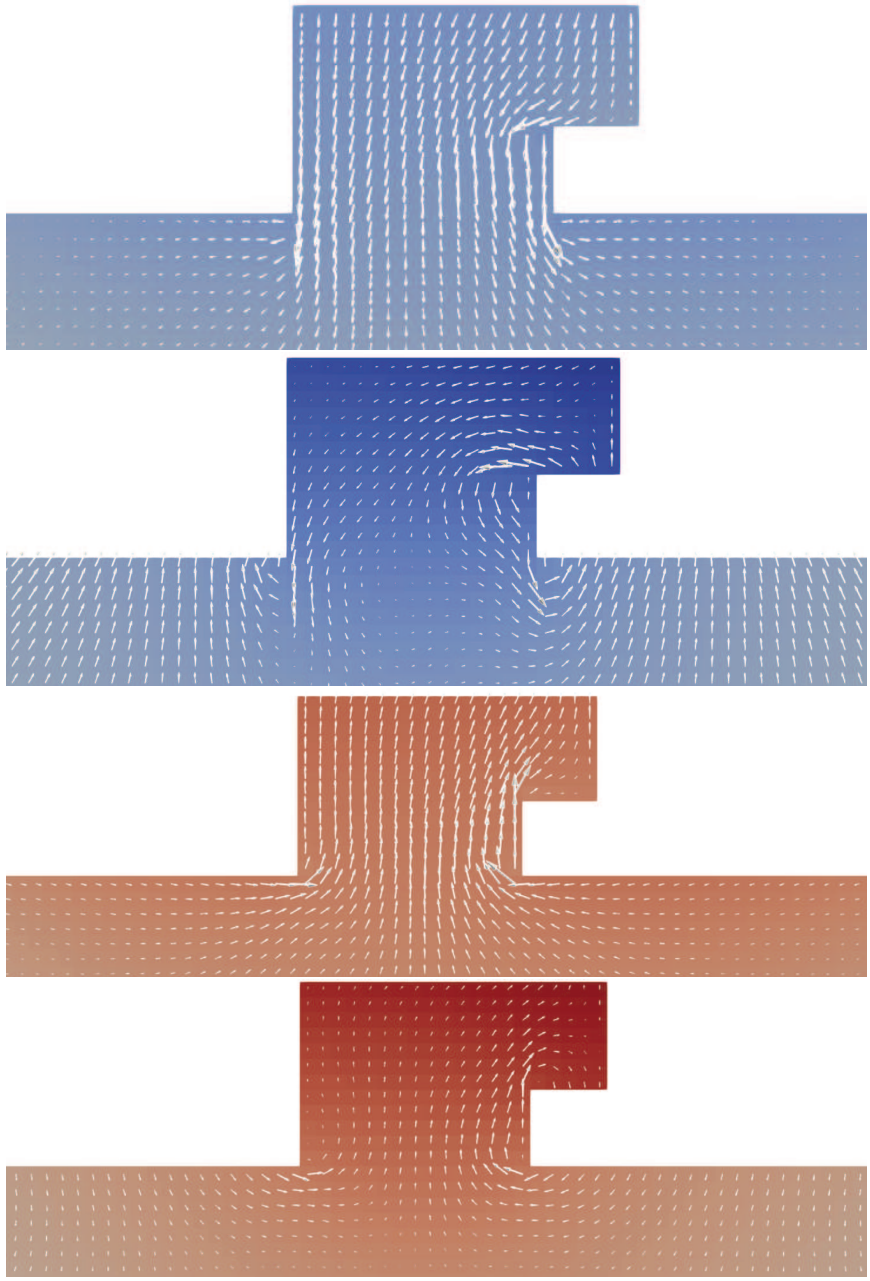

Figure 7.3: Selected snapshots of flow fields from CFD simulations at the piston mode for Case 1 at four time instants, approximately $T/4$ apart. The colors indicate the dynamic pressure, ranging from blue (minimum pressure) to red (maximum pressure). The white arrows are the flow velocity vectors.

7.1.3 First sloshing mode RAOs

The main source of damping in the vicinity of the first sloshing mode for Cases 1-3 is studied in terms of model tests and numerical simulations both in forced heave and forced surge (no experiments were performed in forced surge). We discuss the dominant damping due to flow separation at the moonpool inlets, in particular flow separation at the recess floor top corner. The amplitude-dependent first sloshing mode RAOs from experiments, CFD and BEM in forced heave for Cases 1-3 are presented in Figure 7.4. BEM clearly over-predicts the responses, more so than for the piston mode. This indicates that the wave radiation damping is small. This is due to that the flow through the moonpool inlet is small compared to the flow through the moonpool inlet at the piston mode. This implies that the communication with the outer domain is small. The amplitude-dependence in the moonpool RAOs suggests that damping due to flow separation is dominant.

Numerical simulations for Case 3 in forced surge with CFD and BEM are performed to discuss the importance of damping due to flow separation in the proximity of the first sloshing mode. The moonpool responses in forced surge, defined as $\eta_1 = \eta_{1a}\sin(\omega t)$, are compared with simulations for a closed sloshing tank with similar recess dimensions in Figure 7.5. By this, we investigate the importance of flow separation at the recess floor top corner. There is a slight difference in the first sloshing mode periods for the moonpool and closed tank cases. The resonant responses at the first sloshing mode, however, are fairly similar. This suggests that damping due to flow separation at the top corner of the recess floor is dominant, and that damping due to flow separation at the moonpool entrance is of secondary importance with respect to the first sloshing mode responses for the 2DMR configurations.

One of the main objectives of the forced 2DMR studies was to identify the importance of the viscous damping in the proximity of the first sloshing mode. Although damping due to flow separation explains large parts of the differences between BEM and model test results (cf. Appendix C.1.3), the experimental moonpool RAOs presented in Figure 7.4 illustrate clear Duffing-type behavior due to nonlinear free-surface effects. We say that the moonpool RAOs resemble the responses of a Duffing oscillator based on the resemblance between the present experimental moonpool RAOs in the vicinity of the first sloshing mode, and the sloshing RAOs presented by Firoozkoohi (2013). This is observed for Cases 1-3, where the experimental moonpool RAOs follow a soft Duffing oscillator-like behavior at the first sloshing mode. Selected snapshots of the flow field from the CFD simulations at the first sloshing mode are presented in Figure 7.6.

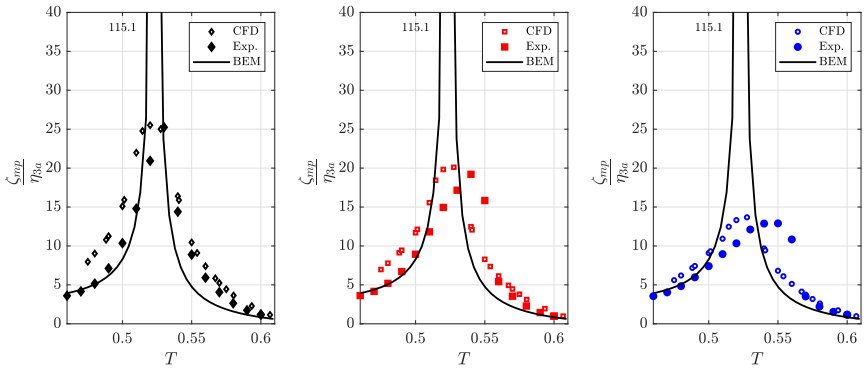

(a) Case 1 - $\eta_{3a} = 1$ mm. **(b)** Case 1 - $\eta_{3a} = 3$ mm. **(c)** Case 1 - $\eta_{3a} = 5$ mm.

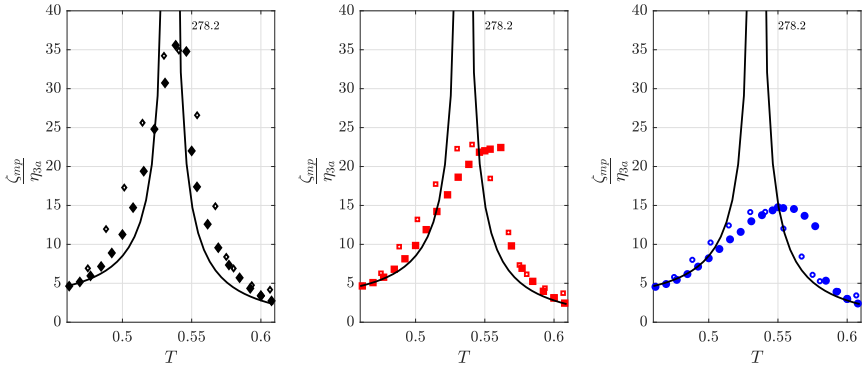

(d) Case 2 - $\eta_{3a} = 1$ mm. **(e)** Case 2 - $\eta_{3a} = 3$ mm. **(f)** Case 2 - $\eta_{3a} = 5$ mm.

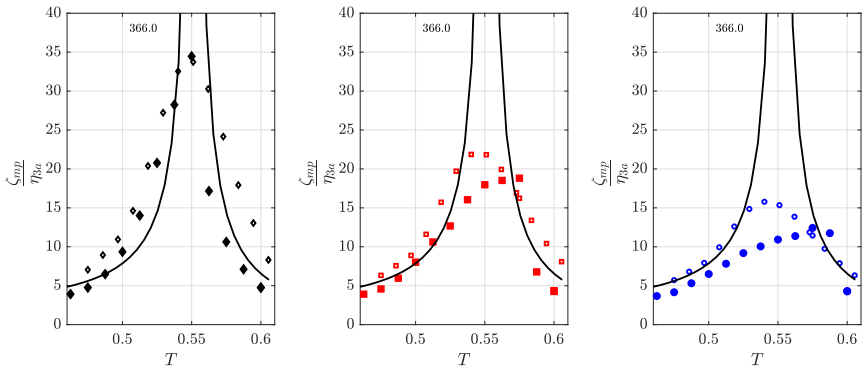

(g) Case 3 - $\eta_{3a} = 1$ mm. **(h)** Case 3 - $\eta_{3a} = 3$ mm. **(i)** Case 3 - $\eta_{3a} = 5$ mm.

Figure 7.4: Experimental and numerical first sloshing mode RAOs (WP1). The first harmonic moonpool response amplitudes are made non-dimensional with respect to the first harmonic forced heave amplitude. The results are presented in an Earth-fixed coordinate system. The numbers indicate the first sloshing mode responses as predicted with BEM.

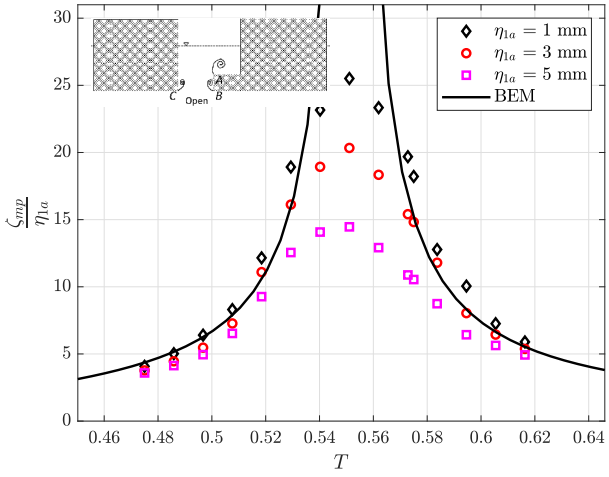

(a) Open moonpool entrance

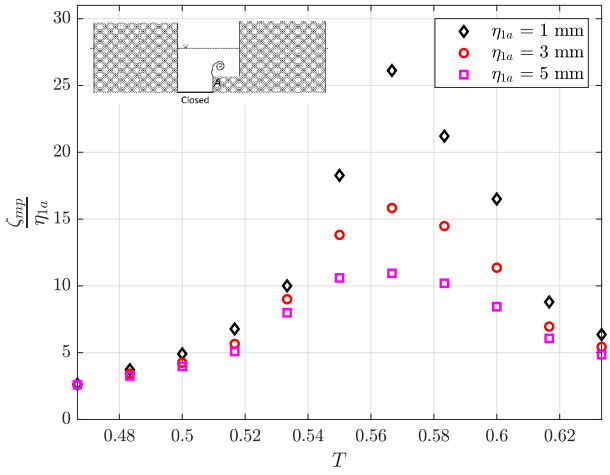

(b) Closed moonpool entrance

Figure 7.5: Amplitude-dependent first sloshing mode RAOs as predicted by the present CFD for Case 3 with forced surge motions (WP1), with open and closed moonpool entrance. Viscous damping due to flow separation at the sharp corner at point A is dominant at the first sloshing mode. Flow separation at points B and C are of secondary importance due to small water flux through the moonpool entrance.

The CFD and experimental moonpool RAOs indicate that the nonlinear effects increase with increasing recess length. For Cases 1 and 2, the maximum responses in the experimental RAOs are in fair agreement with the maximum responses predicted by CFD for all η_{3a}. For Case 3, the nonlinear effects are more significant, with a discrepancy at resonance between the experiments and CFD of about 20

%, where CFD over-predicts. The moonpool RAOs predicted by CFD are somewhat broader than those from the model tests and BEM simulations. We are not confident on the reason for the differences. Possible candidates are the validity of the linearized body-boundary and linearized free-surface conditions. The flow is dominated by the water motions in this forced heave period range, hence justifying the use of linearized body-boundary conditions. However, the model tests show that linearized free-surface conditions are questionable in this forced heave period range, which could be a possible reason for the broader moonpool RAOs.

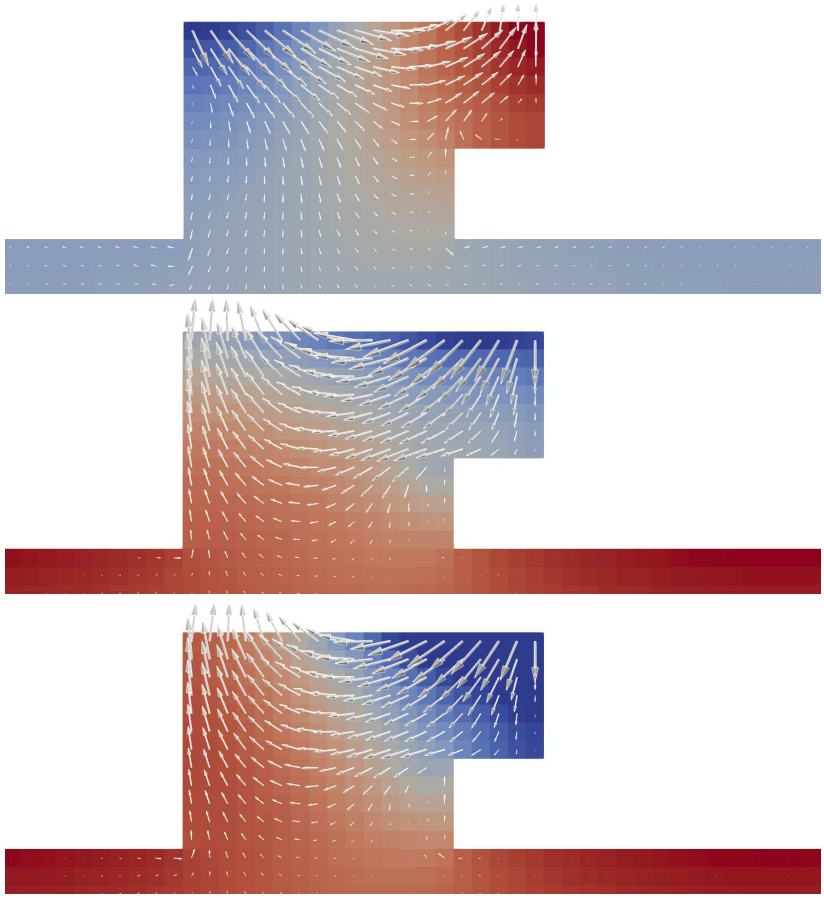

Figure 7.6: Selected snapshots of flow fields from CFD simulations at the first sloshing mode for Case 1. The first two snapshots are approximately $T/2$ apart. The last snapshot is approximately $T/40$ apart the second snapshot. The white arrows indicate the flow velocity vectors. The colors indicate the dynamic pressure, ranging from blue (minimum pressure) to red (maximum pressure).

For the present cases, h/L_m is 0.3, where h and L_m are the recess height and

moonpool length at the mean waterline. Faltinsen and Timokha (2009) showed that the RAOs change from hard to soft spring behavior at $h_{st}/L_{st} = 0.3368$ for closed sloshing tanks, where h_{st} and L_{st} are the water depth and length of a closed sloshing tank. We believe that similar changes from hard to soft spring behavior can occur for moonpools with recess, depending on the moonpool and recess dimensions, although any dedicated studies towards identifying this was not conducted. The Duffing-type behavior is not investigated any further by means of numerical simulations with nonlinear free-surface and nonlinear body-boundary conditions, although we acknowledge that nonlinear effects are important in the proximity of the first sloshing mode.

A model scale of 1:50 is imagined. This corresponds to a moonpool length of 10 m in full scale. The piston mode is then excited at $T = 9.5$ s, and the first sloshing mode at $T = 3.9$ s. This implies that the first sloshing mode is outside the wave period range where ocean waves in the North Sea contain significant wave energy. Hence, the first sloshing mode is perhaps not as relevant as the piston mode for ships operating in the North Sea. Guo et al. (2017) investigated the moonpool responses for moonpools with recess, where $H_r/D = 0.65$ and $L_r/L_m = 0.35$. For the present 2DMR cases, $H_r/D = 0.45$ and $L_r/L_m = 0.25, 0.375$ and 0.5 for Cases 1-3, respectively. Guo et al. (2017) observed significant amplification of the second harmonic moonpool responses at $T = 2T_1$, where T_1 is the first sloshing mode period, which suggests that secondary resonance was important for small recess heights, although this was not discussed therein. The H_r/D-ratio for the present cases is approximately 30 % smaller than for the moonpool investigated therein. Although the first sloshing mode for the present cases is outside the wave period range of interest, the amplification of higher modes in a relevant range of wave periods can be dominant, hence important to consider, depending on the moonpool and recess dimensions. The higher harmonic moonpool responses at twice the first sloshing mode period is negligible for the present cases, most likely due to that we have a smaller H_r/D-ratio as compared to that investigated by Guo et al. (2017). We discuss secondary resonance and amplification of higher modes in §9.8 for clean moonpools.

7.1.4 Phase angle of the moonpool response

We discuss the phase angles between the forced heave motion and the moonpool responses. For a simple mass-spring system, one expects that the phase angle between the excitation and the response is 90 degrees out of phase at resonance. The moonpool responses for moonpools with recess are more complex. For the present 2DMR cases, the phase angle at the piston mode is different from 90 degrees. The experiments and CFD at the lowest forced heave amplitude are in good agreement with BEM in the vicinity of the piston mode. At the first sloshing mode,

where Duffing-type moonpool responses were observed, the trends are less clear.

The phase angles between the moonpool responses and the forced heave motion, ϵ_{mp}, are presented in Figure 7.7 for Cases 1-3. The phase angles of the moonpool responses at WP1 relative to the forced heave motion are presented. At the first sloshing mode, the moonpool response is approximately 90 degrees out of phase with the forced heave motion. For periods lower than the first sloshing mode period, the forced heave motion and moonpool response are 180 degrees out of phase.

For clean moonpools, the phase angle between the heave and moonpool responses is typically close to 90 degrees at resonance at the piston mode, as discussed by e.g. Kristiansen (2009) and Fredriksen (2015). For moonpools with recess, however, we observe that the phase angle is not necessarily 90 degrees, and the phase angle at the piston mode depends on the recess length. This effect is further exemplified in Figure 7.8, where the phase angle between the heave and moonpool responses at WP1 are presented for different L_r/L_m-ratios are presented, with $L_m = 0.2$ m. Note that the piston mode period increases with increasing recess lengths, as discussed in §7.1.1. The BEM simulations with $L_r/L_m = 0$ are consistent with results presented by Kristiansen (2009) for clean moonpools. Hence, it is clear that the presence of the recess affects the phase angle between the heave and moonpool responses at the piston mode.

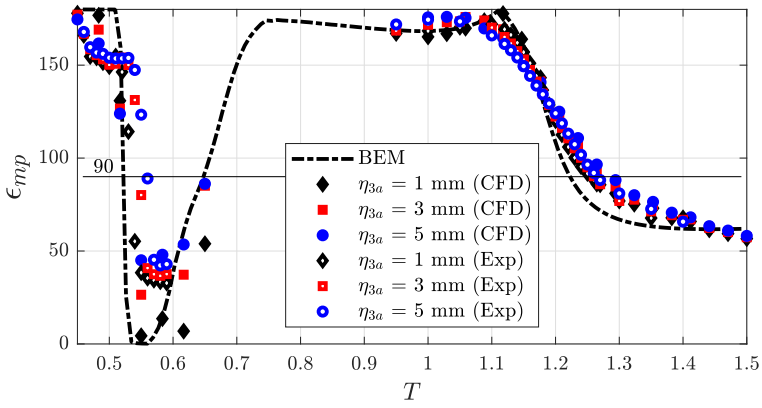

(a) Case 1. $T_0 = 1.18$ s, $T_1 = 0.53$ s.

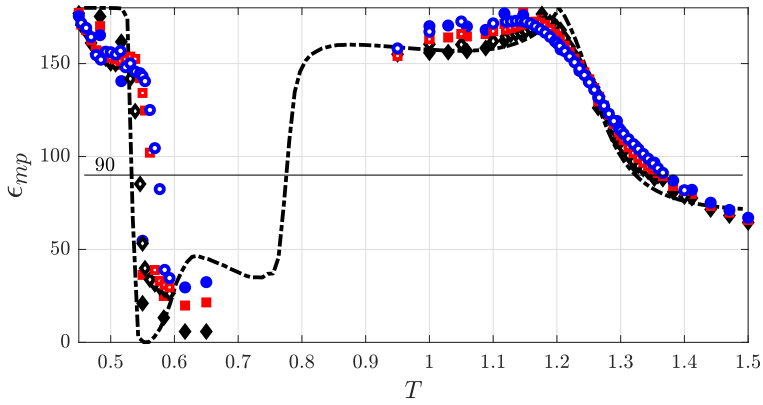

(b) Case 2. $T_0 = 1.25$ s, $T_1 = 0.53$ s.

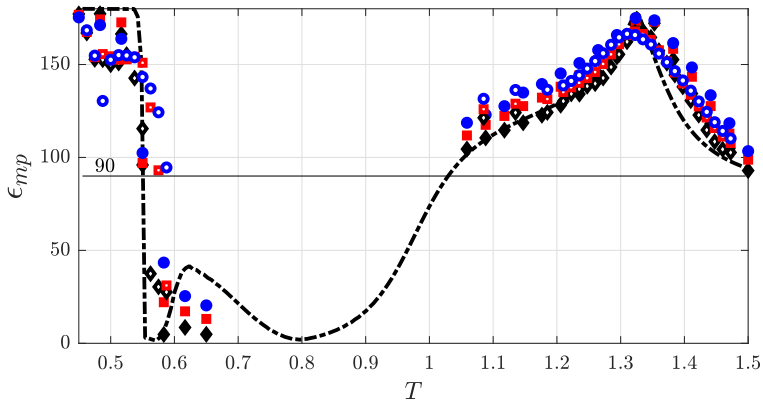

(c) Case 3. $T_0 = 1.35$ s, $T_1 = 0.55$ s.

Figure 7.7: Phase angles, ϵ_{mp}, between forced heave motion and moonpool response from the experiments and as determined with the present BEM and CFD codes at WP1. Phases with three different forced heave amplitude are presented for Cases 1-3 (cf. Table 4.1).

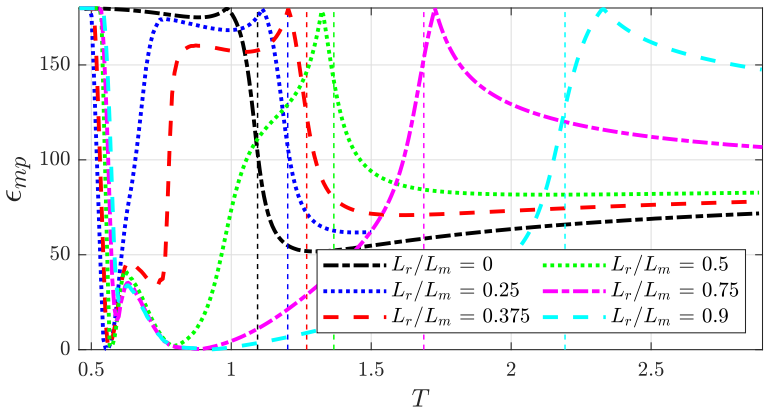

Figure 7.8: Phases between forced heave motion and moonpool response from BEM simulations for different L_r/L_m-ratios by varying L_r, where L_r and L_m are the length of the recess and length of moonpool at the mean waterline, respectively. L_m, L and D are the same as in Table 4.1. The dashed vertical lines indicate the piston mode periods.

7.2 Forced heave with 3DQ configurations

In order to study 3D effects, we present model test results and PVC3D simulations for what we denote quasi 3D geometries, referred to as 3DQ. These are Cases 4-6 in Table 4.1. The 2D model is modified by adding two rectangular boxes such that the setting becomes three-dimensional in a "two-dimensional" wave flume. There is no recess in any of the present 3DQ cases. The difference between Cases 4-6 is the moonpool size, with $V_{MP}/V_S = 0.022, 0.045$ and 0.094, respectively .

Cases 4-6 are similar to the set-up by Kristiansen et al. (2013), where $V_{MP}/V_S = 0.065$ in their study. They obtained a moonpool RAO of 18 at the piston mode period with $\eta_{3a} = 2.5$ mm, while they obtained 10 with the (equivalent) 2D configuration in Kristiansen and Faltinsen (2008). There is more horizontal area on the bottom of the model relative to the horizontal cross-sectional area of the moonpool for the 3DQ configurations (i.e. the V_{MP}/V_S-ratio is smaller), relative to a similar 2D configuration, which is the cause of the high moonpool responses. On the other hand, the flow separation can take place along four edges relative to the two for a 2D configuration, potentially increasing the damping. This is demonstrated by that Kristiansen and Faltinsen (2008) obtained moonpool RAO of approximately 13 at the piston mode period with their linear potential flow solver in a two-dimensional setting, whereas Kristiansen et al. (2013) obtained approximately 70 with their potential flow solver for their 3DQ configuration, which is significant compared to a moonpool RAO of 18 at the piston mode period with $\eta_{3a} = 2.5$ mm.

Amplitude-dependent moonpool RAOs from the forced heave experiments and PVC3D simulations for Cases 4-6 are presented in Figure 7.9. The agreement between PVC3D and the experiments is good. Snapshots of flow fields from the PVC3D simulations in regular forced heave motion are provided in Figures 7.10 and 7.11, where the snapshots show that flow separation at the moonpool entrance is important. There are clear concentrations of vorticity at the moonpool inlets.

The piston mode periods as predicted using theory presented by Molin (2001) are 0.89 s, 0.93 s and 0.99 s for Cases 4-6, respectively. This agrees well with our results, despite the fact that the method by Molin (2001) is valid for a infinitely large barge with a moonpool, while the present 3DQ configuration is equivalent to a barge with length $L = 0.8$ m and infinite beam, with infinitely many moonpools. Note that the agreement is best for the smallest forcing amplitude, $\eta_{3a} = 1$ mm, whereas the peaks in the moonpool RAOs are slightly shifted for higher forcing amplitudes, consistent with previous discussions on the effect of flow separation on the virtual added mass term.

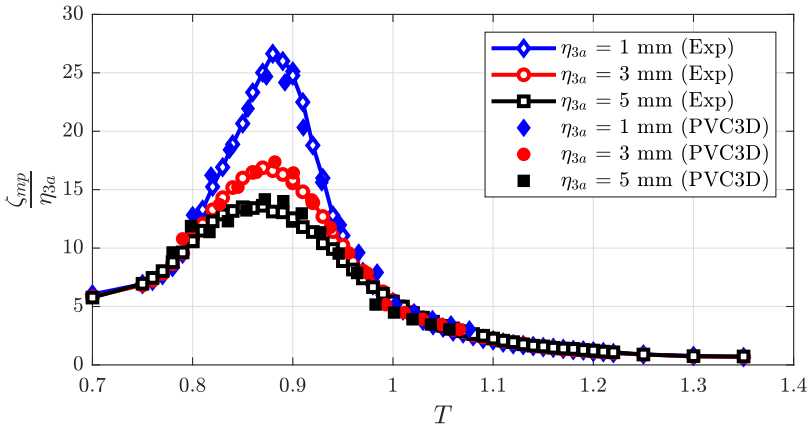

(a) Case 4

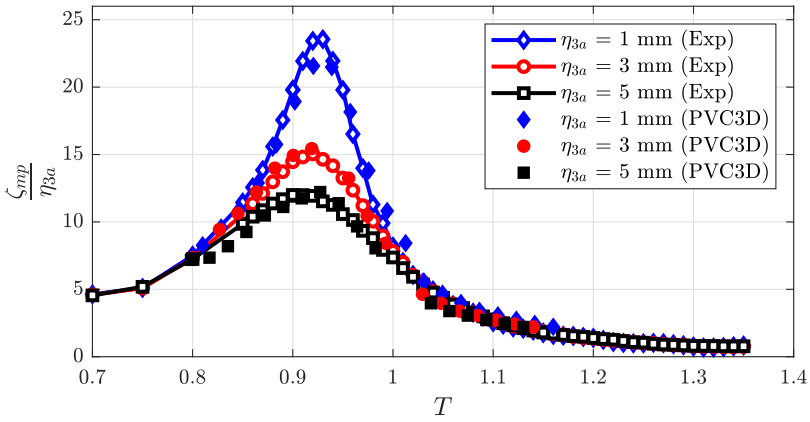

(b) Case 5

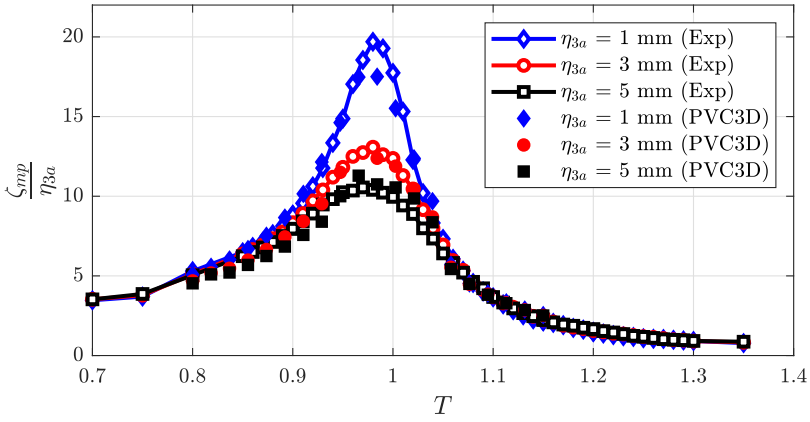

(c) Case 6

Figure 7.9: Piston mode RAOs from the experiments and PVC3D for the quasi three-dimensional (3DQ) configurations. The moonpool responses at WP1 in a body-fixed coordinate system are presented (cf. Figure 4.14).

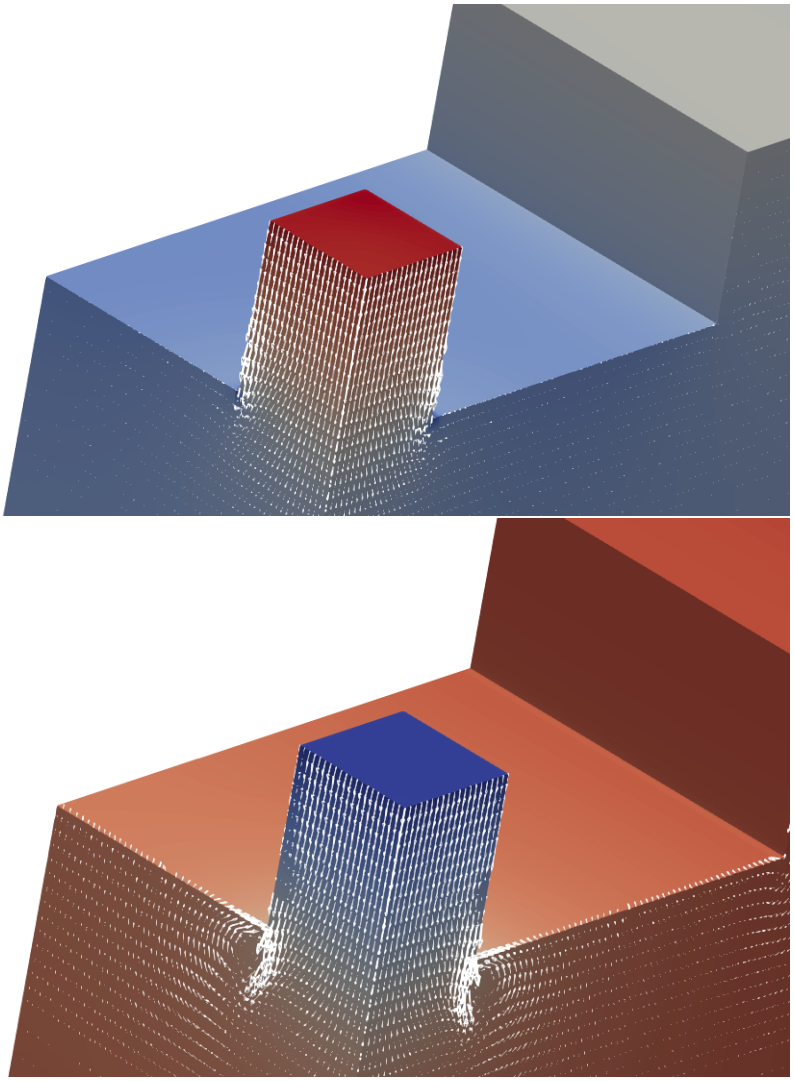

Figure 7.10: Snapshots of flow fields from PVC3D simulations with regular forced heave motion for Case 6. Only one quarter of the physical domain is modelled in the PVC3D simulations. The arrows indicate the velocity field at the xz- and yz- symmetry planes at $y = 0$ and $x = 0$, respectively. The colors indicate the dynamic pressure field, ranging from blue (minimum pressure) to red (maximum pressure). The snapshots are approximately $T/4$ apart, where T is the forced heave period.

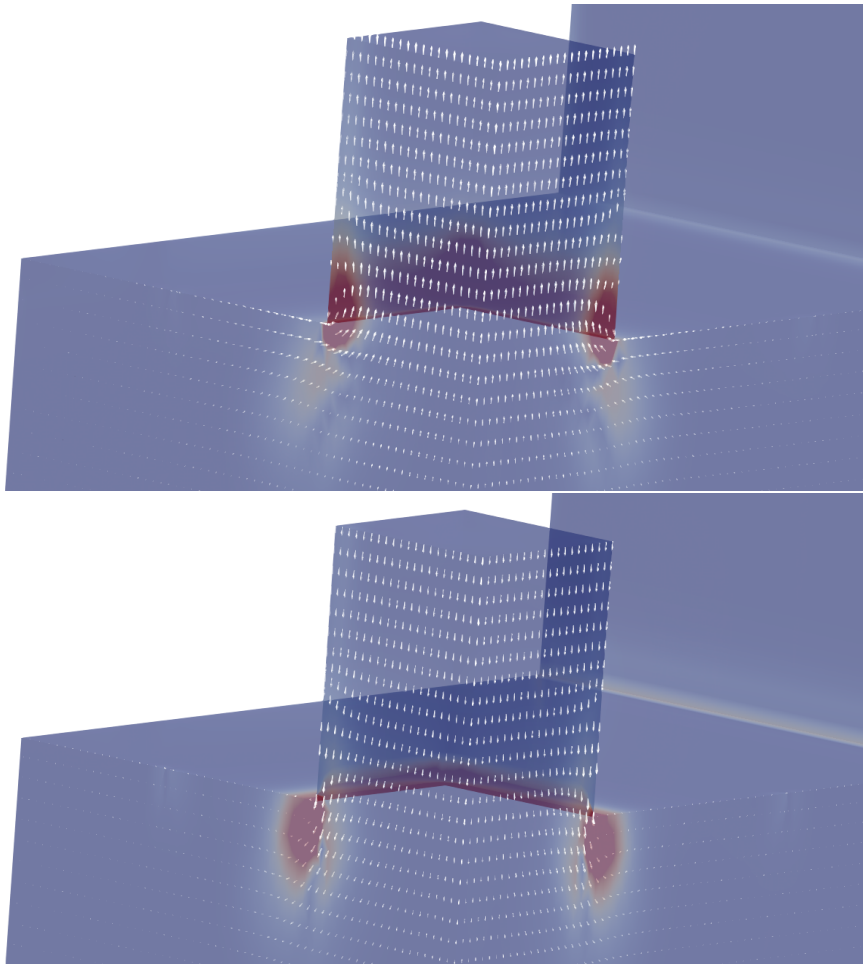

Figure 7.11: Same as Figure 7.10, but the colors indicate the vorticity, ranging from blue (zero vorticity) to red (maximum vorticity).

Experiments in forced irregular heave motion were conducted in an attempt to obtain moonpool RAOs faster than by performing experiments in regular forced heave motion. The irregular forced heave tests for a given η_{3S} took 15 minutes, where η_{3S} is the average of the 1/3 largest peaks of the forced irregular heave motion (inspired by significant wave height in a sea state). By contrast, the time to obtain the moonpool RAOs from the regular forced heave tests took approximately 240 minutes for one forced heave amplitude. Pink noise spectra are used to define the irregular forced heave motions, as discussed in §4.1.2. Selected time-series from the model tests and PVC3D simulations are presented in Figures 7.12 and 7.13. Note that two different realizations are used for the irregular forced

heave motions in the model tests and PVC3D simulations. The time-series clearly illustrate the significant amplification due to resonance in forced heave conditions.

The moonpool RAOs for Cases 4 and 6, presented in Figure 7.14, illustrate that the moonpool RAOs from the irregular wave tests are considerably larger than in regular forced heave conditions. For instance, for Case 4 with $\eta_{3a} = 1$ mm, the piston mode response from the regular forced heave tests is approximately 28 at resonance, while the piston mode response from the irregular forced heave tests with $\eta_{3S} = 1$ mm is approximately 48. The model tests and the PVC3D simulations are consistent; in irregular forced heave, the moonpool RAOs are considerably larger than in regular forced heave conditions.

We believe the differences in the moonpool RAOs between the regular and irregular forced heave tests are attributed to the fact that we define pink noise spectra as $S_{\eta_3}(\omega) = c_c$, where the c_c is a constant tuned such that specified values η_{3S} are obtained. In hindsight, we realize that the forced heave spectra should be defined as for the irregular waves (PNWW) used in the Ocean Basin (cf. §5.5), that is; the magnitude of the spectrum, $S_{\eta_3}(\omega)$, for a given forced heave amplitude, η_{3a}, and forced heave circular frequency, ω, should be determined based on the spectrum value of a regular forced heave time-series, i.e. $\eta_3 = \eta_{3a}\sin(\omega t)$. This is not what has been done when we use significant heave as measure. The results presented in Chapter 9 show that the PNWW approach yields consistent results between the regular and irregular wave tests.

The reason to why the present model tests with the pink noise spectra fail to match with the regular forced heave tests is because the c_c becomes smaller the broader the pink noise spectrum becomes, since we scaled the c_c such that a specified value of η_{3S} was obtained. To illustrate this, we imagine that a very narrow pink noise spectrum band around the piston mode period is applied instead. In this scenario, the forced irregular motion would be fairly similar to a regular forced heave motion at the piston mode period, and yield similar moonpool RAOs for $\eta_{3a} = \eta_{3S}$. The similarity would be a consequence of that the c_c is tuned to match pre-defined values of η_{3S}. By broadening the forced heave period range for the pink noise spectrum, the constant c_c decreases, and hence, the relative damping due to flow separation at the piston mode becomes smaller in the irregular forced heave tests. The reason why the c_c becomes smaller by widening the pink noise spectrum can be explained by using that; $\eta_{3S} = 4\sqrt{m_0}$, where $m_0 = \int_0^\infty S_{\eta_3}(\omega)d\omega$ is the zeroth spectral moment (Faltinsen 1993). Since the presently used pink noise spectrum is fairly rectangular, we can use that $m_0 = c_c \cdot T_{range}$, where T_{range} is the band width of the pink noise spectrum. Since we have specified η_{3S}, and thereby also m_0, making the spectrum wider yields smaller c_c, and hence, less spectral energy

in the vicinity of the piston mode period. In order to obtain comparable moonpool RAOs with both the regular and irregular forced heave tests, c_c must be chosen such that the energy is similar to that for the regular forced heave test for a given forced heave period, and not tuned to match a pre-defined η_{3S} (as done in the present study).

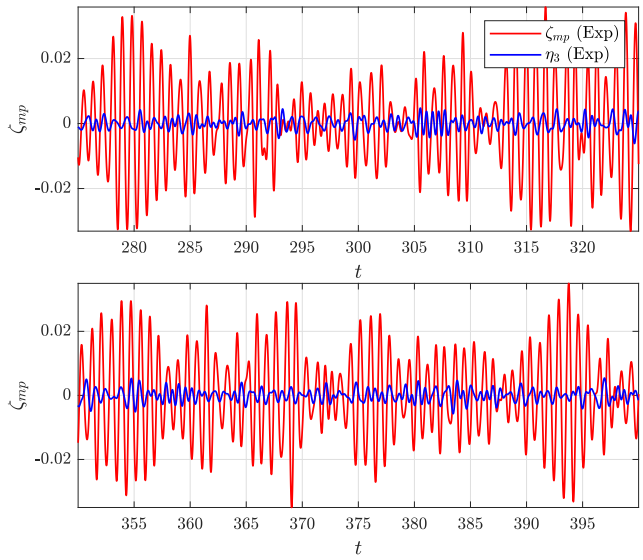

Figure 7.12: Time-series of the moonpool response and forced irregular heave motion with $\eta_{3S} = 3$ mm from the model tests for Case 4. The moonpool responses from model tests are presented in a body-fixed coordinate system.

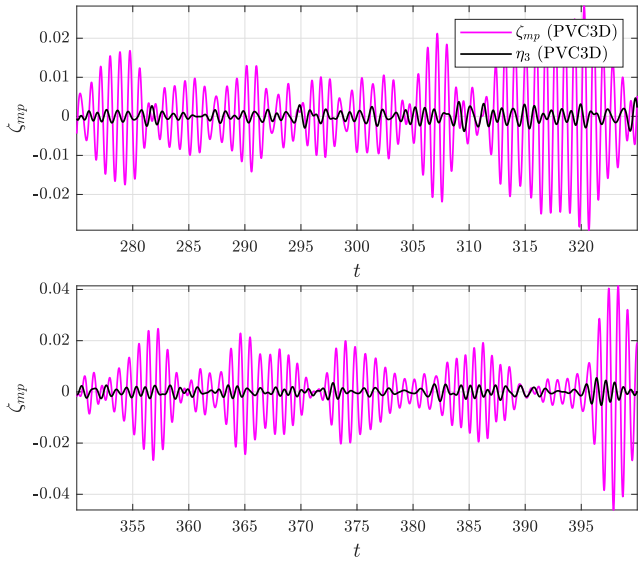

Figure 7.13: Time-series of the moonpool response and forced irregular heave motion with $\eta_{3S} = 3$ mm from the PVC3D simulations for Case 4. The moonpool responses from PVC3D simulations are presented in a body-fixed coordinate system.

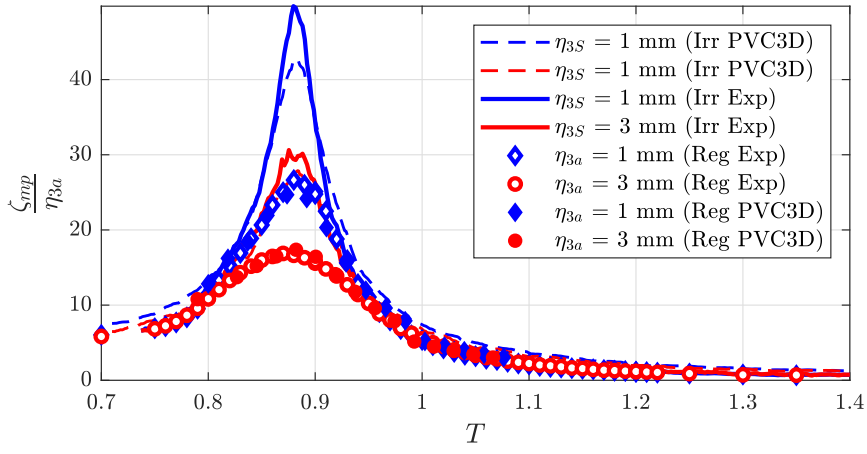

(a) Case 4

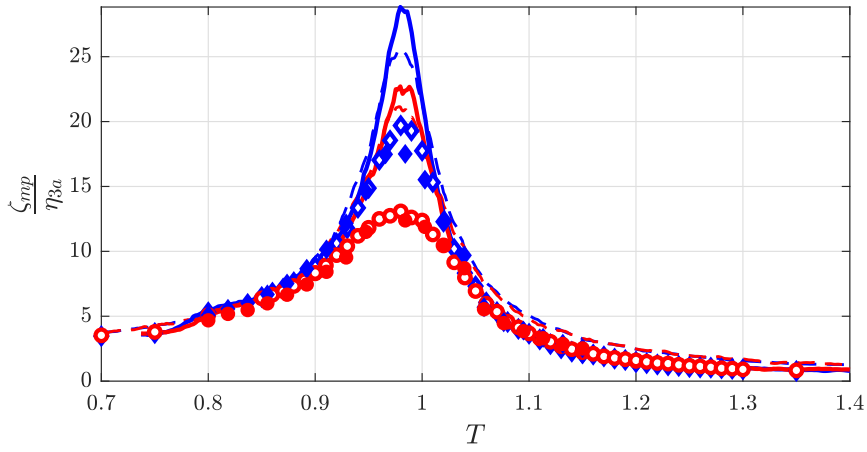

(b) Case 6

Figure 7.14: The moonpool responses from forced regular (Reg) and irregular (Irr) forced heave motions at WP1 in a body-fixed coordinate system are presented (cf. Figure 4.14) for Cases 4 and 6. Two forced heave amplitudes are presented, although five were tested, for the sake of clarity.

Chapter 8

Freely floating models in the wave flume

Results from the freely floating model tests for the 2DMR and 3DQ configurations are presented in terms of amplitude-dependent moonpool, heave and pitch RAOs. This means that we are studying 2D model with recess and quasi 3D models without recess, as listed in Table 4.2. However, the effect of the recess is considered secondary in the present investigation, where the purpose is to investigate the importance of the moonpool volume to ship volume ratio, V_{MP}/V_S, in the hydrodynamic interaction between the ship and moonpool responses. Note that we use the term hydrodynamic interaction to discuss the hydrodynamic effects caused by the presence of the moonpool, and is, strictly speaking, not the same as that for the hydrodynamic interaction between multiple bodies (cf. discussion in §2.2). The model tests in the wave flume were conducted as preliminary studies to the ones carried out in the Ocean Basin (cf. Chapter 9). Numerical and experimental results are presented. Additionally, we present results from 2D BEM simulations for a model without a moonpool, i.e. a rectangular body with $L = 0.8$ m and $D = 0.11$ m. Results with three different wave steepnesses, H/λ, are presented for a range of wave periods, T. The moonpool RAOs are presented in a body-fixed coordinate system.

8.1 Heave, pitch and moonpool responses

One important difference in freely floating conditions is the difference in the piston mode periods relative to those predicted in forced heave. The difference is dependent on the V_{MP}/V_S-ratio, which is 0.022, 0.045, 0.094 and 0.203 for Cases 4-6 and Case 2, respectively. The piston mode periods in freely floating conditions,

as predicted from the peaks in the moonpool RAOs from the model tests, are 0.88 s, 0.90 s, 0.93 s and 1.14 s for Cases 4-6 and Case 2, respectively. This corresponds to differences of 1.1 %, 3.2 %, 6.1 % and 8.8 % relative to the piston mode periods as determined by solving the eigenvalue problem, i.e. by disregarding the coupling between ship and moonpool responses (cf. results in Chapter 7). The model tests suggest that the hydrodynamic interaction between moonpool and ship responses are negligible for Cases 4 and 5, which have the smallest moonpools. For Cases 2 and 6, the hydrodynamic interaction is non-negligible. Hence, the hydrodynamic interaction between ship and moonpool responses is dependent on the V_{MP}/V_S-ratio. Another, perhaps more significant difference, is that the moonpool responses are notably smaller in freely floating conditions than in forced heave.

The moonpool responses for the two-dimensional configuration (Case 2), presented in Figure 8.1, illustrate that damping due to flow separation at the moonpool entrance is dominant in the proximity of the piston mode in freely floating conditions, as documented for forced heave in Chapter 7. BEM clearly over-predicts the moonpool responses, as expected. The moonpool RAOs from the CFD simulations are in fair agreement with the experiments. The experimental moonpool RAOs for Cases 4-6 also illustrate dominant viscous damping, as illustrated in Figure 8.2.

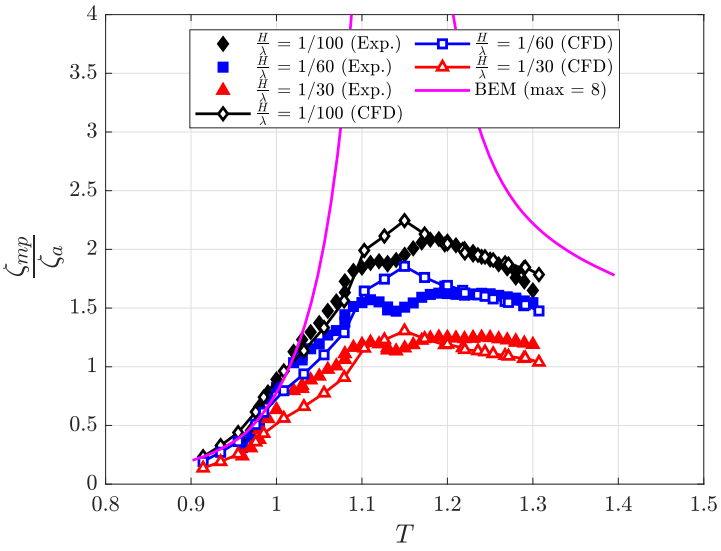

Figure 8.1: Amplitude-dependent moonpool RAOs for Case 2. Moonpool responses measured in a body-fixed coordinate system at WP10 are presented (cf. Figures 4.16). ζ_a is the incident wave amplitude.

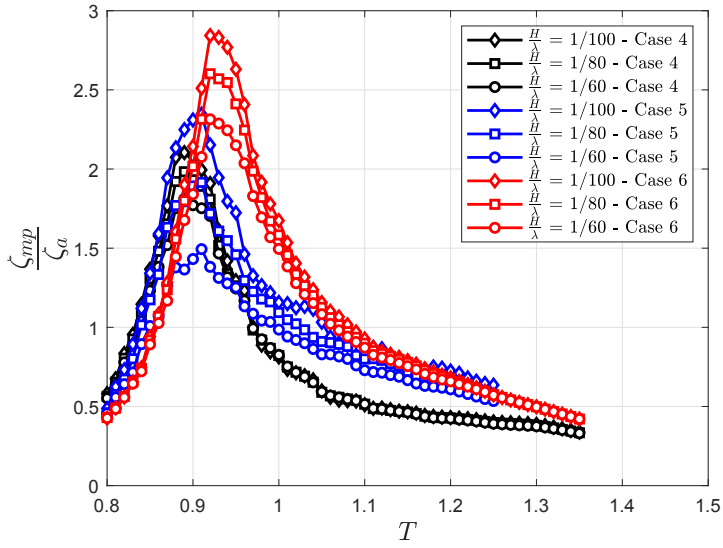

Figure 8.2: Experimental amplitude-dependent moonpool RAOs for Cases 4-6. Moonpool responses measured in a body-fixed coordinate system at WP1 are presented (cf. Figures 4.14).

The degree of hydrodynamic interaction between heave and moonpool responses is illustrated in Figure 8.3. The coupling between the heave and moonpool responses is significant for Case 2, which is the 2D case with $V_{MP}/V_S = 0.203$, since a local peak is observed in the proximity of the piston mode period in the heave RAOs. For a similar vessel without moonpool, there is only one peak in the heave RAO (at heave resonance). The heave RAOs suggest that the moonpool responses influence the heave motions (and vice versa). Although we do not have model tests or CFD for body without moonpool, the potential flow simulations by BEM clearly indicate strong hydrodynamic interactions. As illustrated in Figure 8.4, there is clear evidence hydrodynamic interaction also for Case 6, although the hydrodynamic interaction is not as prominent as for Case 2. This is due to that the V_{MP}/V_S-ratio is 0.094 for Case 6, which is approximately half that of Case 2. For Cases 4 and 5, with V_{MP}/V_S-ratios of 0.022 and 0.045, there is no clear evidence of the hydrodynamic coupling between ship and moonpool responses. This implies that, in practice, the ship responses for vessels with small moonpools can be determined to a reasonable degree of accuracy by disregarding the presence of the moonpool. This is also discussed in §9.3 for the MP1 model tested in the Ocean Basin, where we compare the responses from the experiments against WAMIT simulations for models with and without moonpool.

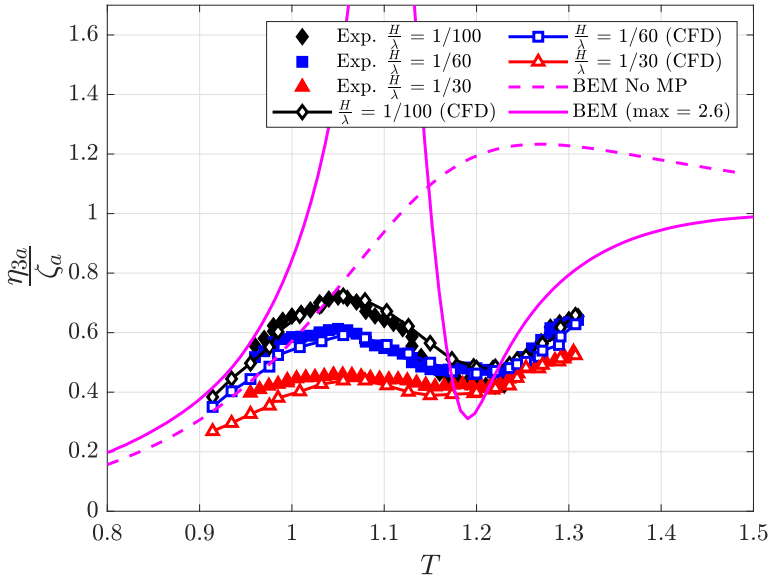

Figure 8.3: Amplitude-dependent heave RAOs for Case 2. η_{3a} and ζ_a are the heave response amplitude and incident wave amplitude, respectively.

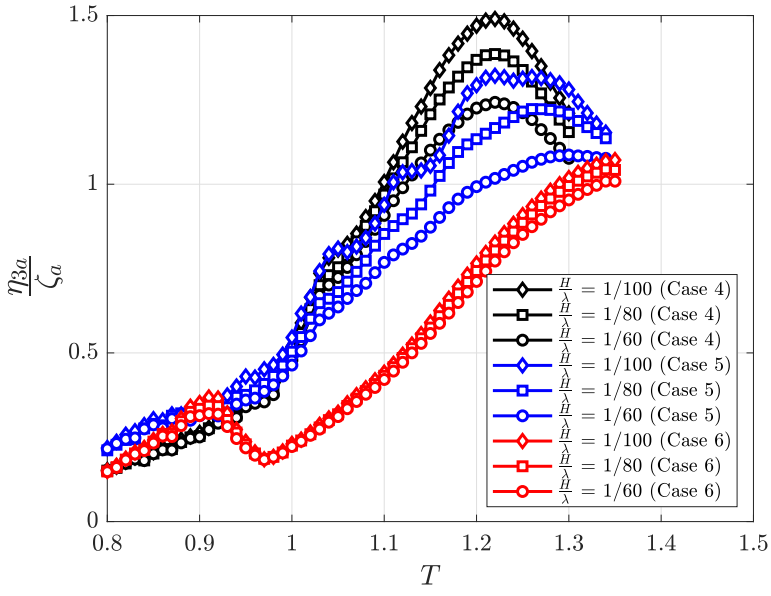

Figure 8.4: Same as Figure 8.3, but for Cases 4-6.

Pitch RAOs are presented in Figure 8.5. The pitch RAOs for Cases 4-6 show no

evidence of hydrodynamic interaction between the moonpool and pitch responses, as expected, since the models have no recess, and the model is fore-aft symmetric. Some ships have the moonpool center located away from the center of the vessel. In such cases, it is expected that the hydrodynamic interaction between pitch and moonpool responses is of importance. This is discussed in Chapter 9. For Case 2, the experimental pitch RAOs indicate that the hydrodynamic interaction between the pitch and moonpool responses is present, but small. The BEM simulations suggest that the hydrodynamic interaction is more significant.

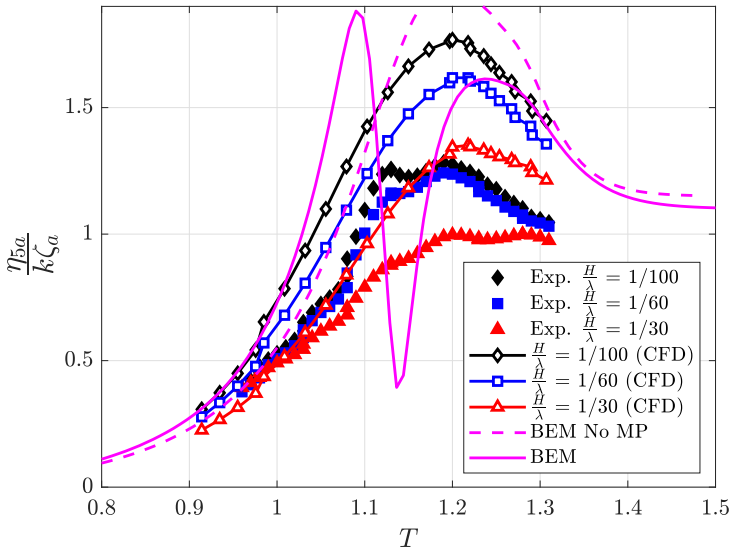

(a) Pitch RAOs for Case 2.

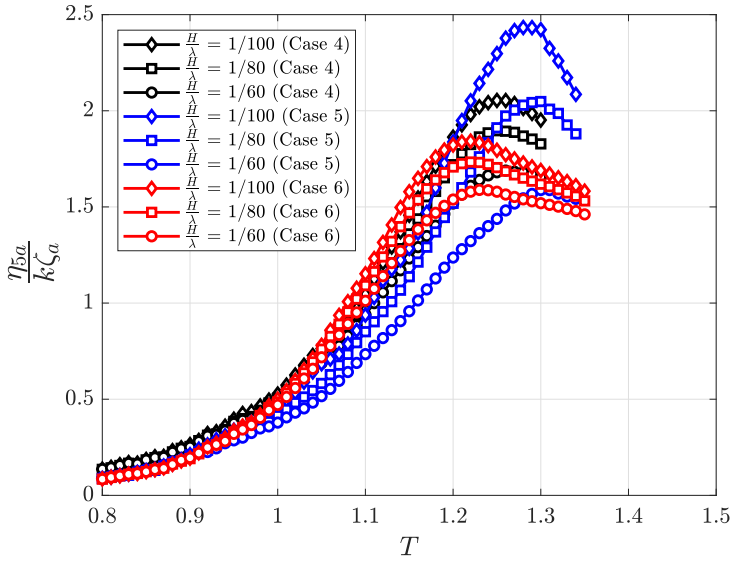

(b) Pitch RAOs for Cases 4-6.

Figure 8.5: Amplitude-dependent pitch RAOs. η_{5a}, ζ_a and k are the pitch response amplitude, incident wave amplitude and wave number, respectively.

The CFD and BEM simulations over-predict the pitch responses. Damping due to flow separation at the sharp corners at the ends of the model is important for the pitch responses at pitch resonance. This effect is not captured by BEM. The damping in pitch in the CFD simulations is smaller than in the model tests. We believe that this is due to that linearized body-boundary conditions are applied. Fredriksen et al. (2015) investigated roll motion of a 2D rectangular barge, similar to ours, and showed that linearized body-boundary conditions do not permit full development of the vortical structures at the lateral corners (bilges) of the body, causing under-estimation of damping, which in turn leads to that the pitch responses are over-predicted.

The experimental moonpool and heave RAOs for Case 5 are not as "neat" as for the other cases. We believe this is due to wave reflection from the parabolic beach at the opposite end of the wavemaker, although the experiments were conducted carefully to avoid errors due to re-reflection. This is especially clear in the wave period range $1.0 \text{ s} < T < 1.3 \text{ s}$ with wave steepness $H/\lambda = 1/100$. The re-reflection from the parabolic beach clearly affects the moonpool and heave responses for Case 5.

The heave, pitch and moonpool RAOs clearly suggest that the V_{MP}/V_S-ratio is a dominant parameter in the hydrodynamic interaction between ship and moon-

pool responses, in particular between heave and moonpool responses. BEM considerably over-predicts the hydrodynamic interaction between ship and moonpool responses, due to that the wave radiation damping is small. The hydrodynamic interaction is reduced due to flow separation causing important damping. However, even with dominant damping due to flow separation at the moonpool inlet, the experiments and CFD suggest that the hydrodynamic interaction between ship and moonpool responses is important to consider for Cases 2 and 6, meaning that moonpool sizes with 10-20 % or more of the displaced volume calls for the necessity of a combined motion analysis. In Chapter 9, we investigate the hydrodynamic interaction between the moonpool and ship responses further, including the piston and sloshing mode responses, for a freely floating body in a fully three-dimensional setting.

8.2 Modified VBEM

In this section, we investigate whether damping due to flow separation at the moonpool entrance can be modelled empirically in freely floating conditions with what we denote as Viscous BEM (VBEM). Two versions of VBEM are presented, referred to as VBEM1 and VBEM2. In the former version, empirical damping is only included in the dynamic free-surface condition, as in forced heave (cf. §7.1.2). In the latter version, empirical damping is included in the dynamic free-surface condition and the equation of motion in heave.

Simulations with VBEM1, presented in Figure 8.6, are conducted in an attempt to empirically account for damping due to flow separation at the moonpool entrance in freely floating conditions. The moonpool RAOs from the experiments and CFD suggest that VBEM1 over-predicts the moonpool responses to a greater extent than in forced heave (cf. §7.1.2). The heave responses are also considerably over-predicted by VBEM in the proximity of the piston mode. Furthermore, the near-cancellation effect due to the hydrodynamic interaction between heave and moonpool responses at $T = 1.2$ s, is wrongly captured by VBEM1, where the heave responses increase with increasing wave steepness.

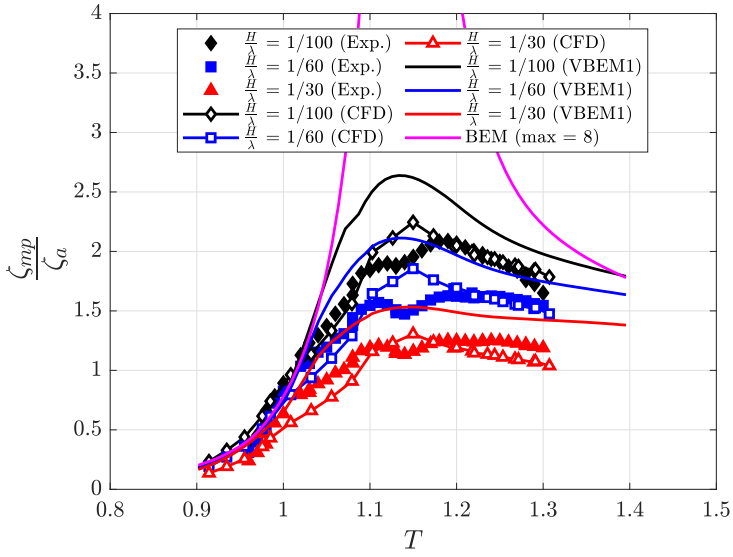

(a) Moonpool RAOs

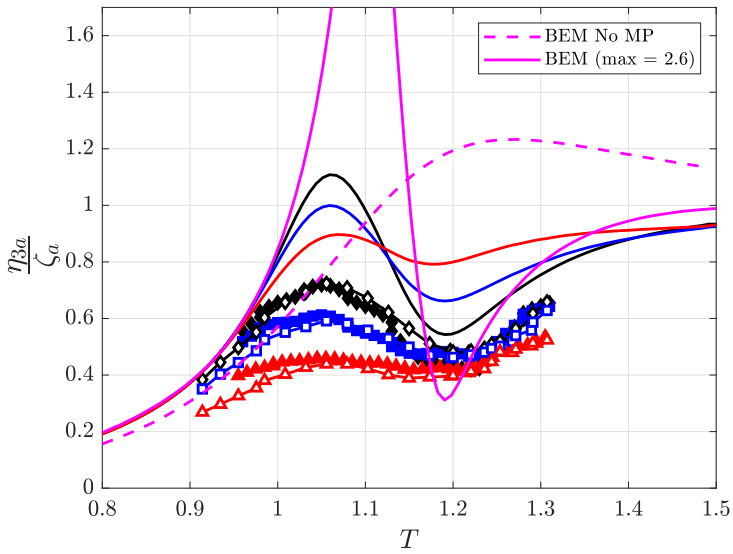

(b) Heave RAOs

Figure 8.6: Heave and moonpool RAOs for Case 2. No empirical damping is applied to the heave motion (VBEM1).

VBEM1 over-estimates the moonpool and heave responses at the piston mode. A main candidate is that the drop in pressure due to flow separation at the moonpool entrance is not explicitly incorporated in the heave motion. We account for this

by modifying the equation of motion in heave, such that the drop in pressure due to flow separation is incorporated in the heave equation of motion. Details of the modified VBEM, referred to as VBEM2, are provided in Appendix B.1.

The moonpool and heave responses with the VBEM2 are presented in Figure 8.7. The VBEM2 improves the results considerably. Without accounting for the drop in pressure in the equation of motion in heave, the near-cancellation at $T = 1.2$ s in Figure 8.6(b) was inaccurate. The heave RAOs with VBEM2 illustrate that the near-cancellation at $T = 1.2$ s is improved considerably, in addition to the heave responses at the piston mode.

The moonpool RAOs are slightly under-estimated with VBEM2, while they were considerably over-estimated without the modification. With the modification, however, the agreement with the model tests and CFD is improved and quite acceptable. An alternative to obtain better agreement for both the heave and moonpool responses could be to use two different pressure drop coefficients for the heave and moonpool responses. This is not done in the present work, since it implies that the coefficients need to be tuned to fit model tests. Our aim in the present work is to develop a method that did not require such tuning of the pressure drop coefficient, but rather implement the method as presented by Faltinsen and Timokha (2015), and incorporate their method in freely floating conditions. The simulations with modified VBEM suggest that the method can be used to obtain first estimates of the ship and moonpool responses, although a Navier–Stokes solver or model tests are required for more accurate estimates.

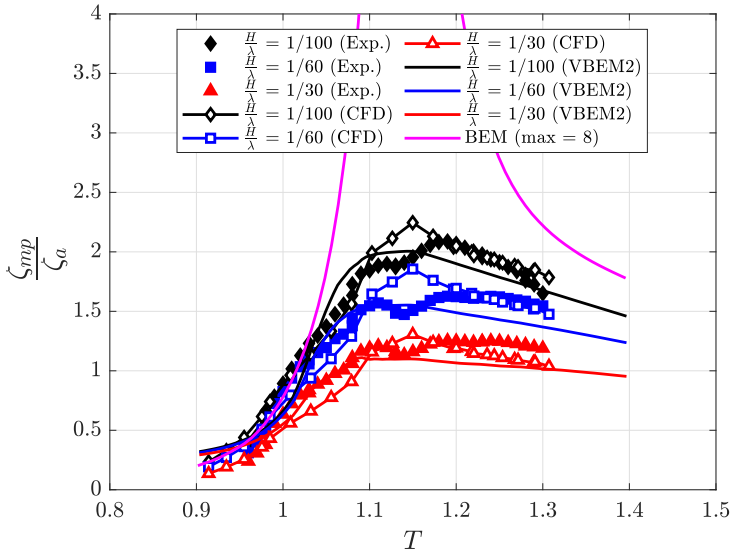

(a) Moonpool RAOs

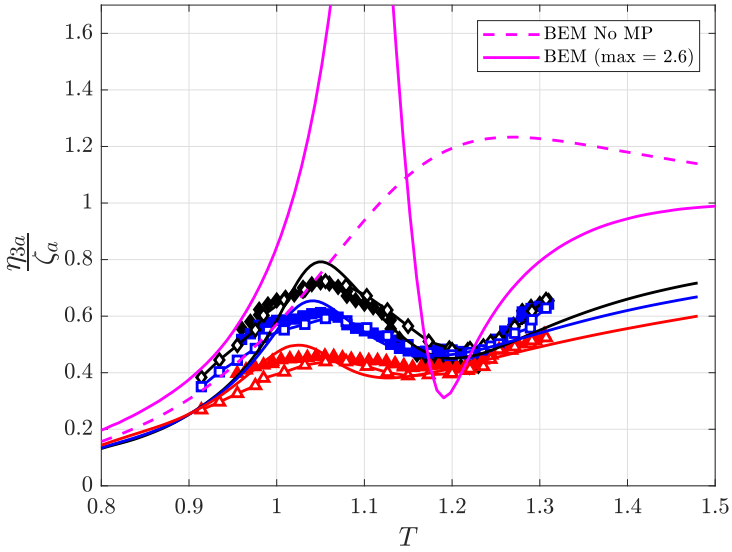

(b) Heave RAOs

Figure 8.7: Heave and moonpool RAOs for Case 2. Empirical damping is applied to the heave motion (VBEM2).

Chapter 9

MP1, MP2 and MP3 in forced motion and freely floating in waves

The importance of the V_{MP}/V_S-ratio on the hydrodynamic interaction effect between ship and moonpool responses is discussed further in the following in a pure three-dimensional setting with a realistic moonpool vessel shape. Experimental and numerical results in freely floating conditions are presented. First, we present numerical PVC3D and WAMIT simulations in forced motion for MP1, MP2 and MP3 in §9.2. In the remaining part of the chapter, results from the model tests in the Ocean Basin are presented in terms of amplitude-dependent RAOs, time-series, snapshots from video recordings and moonpool response shapes. The moonpool RAOs for freely floating are presented in a body-fixed coordinate system in head and beam seas. The heave RAOs are presented in head and beam seas. The surge and pitch RAOs are presented in head seas, while the sway RAOs are presented in beam seas. The roll RAOs in beam sea are presented in §9.6. The results for MP1, MP2 and MP3 are presented separately. MP1 has the smallest moonpool with $V_{MP}/V_S = 0.015$, cf. Table 5.1, which is most relevant for conventional moonpool vessels. MP2 has a moonpool that is four times larger than MP1, with $V_{MP}/V_S = 0.064$. MP3 has the largest moonpool with $V_{MP}/V_S = 0.427$. The results presented in the following were published in Ravinthrakumar et al. (2020a), where video recordings of the moonpool responses are presented as supplementary material.

9.1 Natural periods for MP1, MP2 and MP3

It is well-established that the natural periods of a freely floating and fixed moonpool vessel differ (especially the piston mode period). The reason may be explained by the fact that there is a hydrodynamic interaction between the vessel and moonpool responses, although hydrodynamic interaction is a term associated with the interaction between multiple bodies in water, whilst for a ship with moonpool, there is only one body (cf. discussions in §2.2).

The piston and sloshing mode periods as predicted by WAMIT in forced motions and freely floating conditions are presented in Table 9.1. In freely floating conditions, the piston mode periods are 0.9 %, 3.4 % and 10.3 % lower than in forced heave for MP1, MP2 and MP3, respectively. This is a consequence of that the hydrodynamic interaction between ship and moonpool responses is more pronounced with increasing V_{MP}/V_S-ratios and is consistent with the results presented in Chapter 8.

To elaborate on the changed piston mode period, we perform a simplified analysis of a coupled two degree of freedom system. The resulting coupled piston mode periods, T_0, are presented in Figure 9.1. The coupled piston mode periods are determined using the coupled two DOF system presented in §2.2, and solving (2.12). The heave added mass coefficient, A_{33}, is determined using WAMIT. The added mass term in the single mode approximation by Molin (2001) (cf. discussion in §2.1.1) is used to determine the piston mode added mass coefficient, A_{77}. Note that A_{77} is the added mass coefficient of a rigid body with dimensions $L_m \times B_m \times D$, which equivalent to the frozen approximation by Molin (2001) as discussed in §2.1.1. The coupled added mass coefficient, $A_{37} = A_{73}$, is unknown, hence we present T_0 as a function of A_{37} using a reasonable estimate range of the coupled added mass coefficient. The simplified analysis presented in Figure 9.1 illustrates that A_{37} increases with increasing V_{MP}/V_S-ratio. For instance, the simplified analysis suggests that A_{37} should be of same order of magnitude as A_{33} for MP3, while A_{37} is 1.75 % of A_{33} for MP1, which suggests that the heave responses are considerably affected by the moonpool responses for large V_{MP}/V_S-ratios. For small V_{MP}/V_S-ratios, the hydrodynamic interaction between heave and moonpool responses is less important.

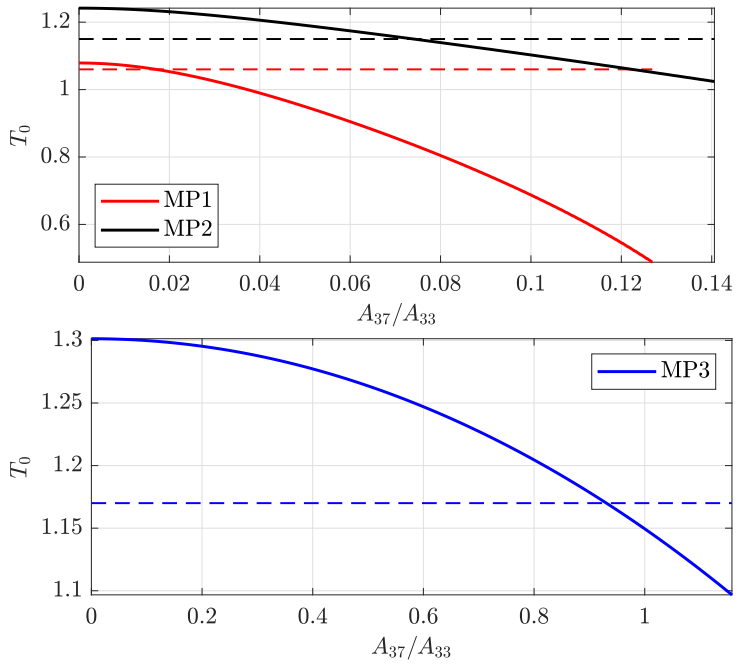

Figure 9.1: Coupled piston mode periods, T_0, determined using (2.12). Coupled piston mode period as determined by WAMIT are indicated by dashed lines. The intersection between the two lines gives an indication of the magnitude of the unknown coupled added mass coefficient, A_{37}.

Table 9.1: Natural periods as predicted by WAMIT in forced motion and freely floating conditions. Natural periods for $T < 0.55$ s are not calculated with WAMIT, since a finer mesh than the presently adopted mesh is needed to obtain converged results in this period range. $T < 0.55$ s is outside the relevant wave period range. Thus, for $T < 0.55$ s, natural periods as determined using theory by Molin (2001) are presented. Natural periods that are not important with respect to the results presented in this thesis are presented in grey text color. * implies that the natural periods in forced motion are practically the same as in the freely floating conditions.

Condition (mode)	MP1	MP2	MP3	Mode no.
Forced motion (Piston mode)	1.07 s	1.19 s	1.30 s	0
Freely floating (Piston mode)	1.06 s	1.15 s	1.17 s	0
Forced motion (First longitudinal sloshing mode)	0.51 s	0.71 s	1.19 s	1
Freely floating (First longitudinal sloshing mode)	-	0.71 s	1.19 s	1
Forced motion (First transverse sloshing mode)	0.51 s	0.71 s	0.71 s	1
Freely floating (First transverse sloshing mode)	-	0.71 s	0.71 s	1
Forced motion (Second longitudinal sloshing mode)	0.36 s	0.51 s	1.03 s	2
Freely floating (Second longitudinal sloshing mode)	-	-	1.04 s	2
Forced motion (Third longitudinal sloshing mode)	0.29 s	0.41 s	0.89 s	3
Freely floating (Third longitudinal sloshing mode)	-	-	0.89 s	3
Forced motion (Fourth longitudinal sloshing mode)	0.25 s	0.36 s	0.79 s*	4
Forced motion (Fifth longitudinal sloshing mode)	0.22 s	0.32 s	0.71 s*	5
Forced motion (Sixth longitudinal sloshing mode)	0.21 s	0.29 s	0.66 s*	6
Forced motion (Seventh longitudinal sloshing mode)	0.19 s	0.27 s	0.60 s*	7

9.2 Forced motions with MP1, MP2 and MP3 - Numerical

Forced motion simulations of the models tested in the Ocean Basin, that is, MP1, MP2 and MP3 are discussed. Experiments in forced heave were not performed. Results from forced heave simulations with WAMIT and PVC3D are presented in Figure 9.2 in terms of amplitude-dependent RAOs for MP1-3. The moonpool RAOs are presented in an Earth-fixed coordinate system. The aim of the numerical simulations is to illustrate the main sources of damping in the proximity of the resonant moonpool responses, especially in the vicinity of the sloshing modes. The natural periods as determined with WAMIT are summarized in Table 9.1. The natural periods from the PVC3D simulations are in good agreement with the WAMIT simulations, although there is a small difference in the piston mode period for MP1; WAMIT predicts that the piston mode period is $T = 1.07$ s, while PVC3D gives $T = 1.08$ s. The main candidates for the difference in the piston mode periods are; amplitude-dependent added mass and damping due to flow separation (as discussed in §7.1.2), which is not captured by linear potential flow theory. Another possible candidate is numerical dispersion error. Although numerical dispersion error has not been studied in detail in the present work, it is believed to be small.

Clear amplitude-dependence in the moonpool RAOs is illustrated in Figure 9.2. For MP1 and MP2, the amplitude-dependence in the proximity of the piston modes at $T = 1.07$ s and $T = 1.19$ s, respectively, illustrates that damping due to flow separation is dominant, consistent with the discussions for the 3DQ configuration in §7.2. WAMIT over-predicts the moonpool responses considerably, since the wave radiation damping is small (especially for MP1). The moonpool responses predicted by PVC3D are significantly smaller, although they are very much larger than the forced heave amplitude. We emphasize that such high moonpool RAO values do not occur in freely floating conditions, as will be shown later for MP1-3, and discussed earlier for the 3DQ cases.

The PVC3D simulations in the proximity of the piston mode at $T = 1.30$ s for MP3 illustrate moderate amplitude-dependence of the piston mode responses. This suggests that the wave radiation damping of the piston mode response is dominant, and that the damping due to flow separation at the sharp edges at the moonpool entrance is less important than for MP1 and MP2. Since the moonpool size is significant compared to the ship dimensions, it is reasonable that wave radiation damping is clearly important.

The amplitude-dependence in the proximity of the second longitudinal sloshing mode at $T = 1.03$ s for MP3 suggest that damping due to flow separation is dominant also for the sloshing response. For instance, the value of the moonpool RAO

at the second longitudinal sloshing mode as predicted with WAMIT is approximately 15, which is almost five times larger than the responses as predicted with PVC3D with $\eta_{3a} = 3$ mm. Similarly, dominant damping due to flow separation is illustrated in the proximity of the fourth longitudinal sloshing mode at $T = 0.79$ s. The fact that flow separation of the sloshing motion in a moonpool is dominant for damping has not been discussed in earlier literature, but is reasonable considering the relatively large water motions at the moonpool inlet also at sloshing. At the second longitudinal sloshing mode for MP3, the water motions at the moonpool inlets are approximately 50 % of that at the free-surface in the moonpool, as illustrated Figure 9.3.

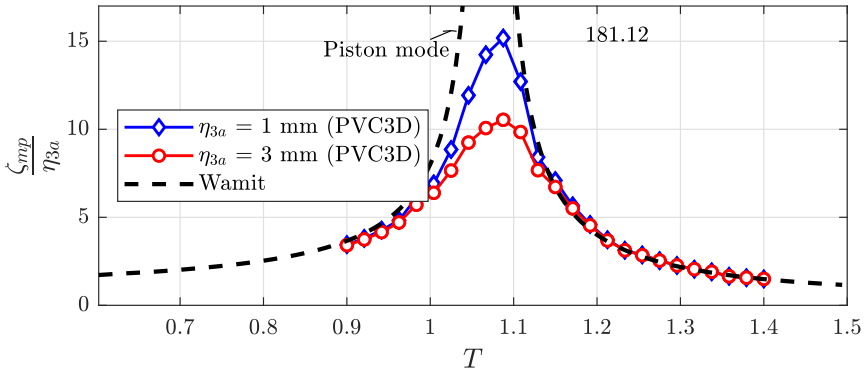

(a) MP1

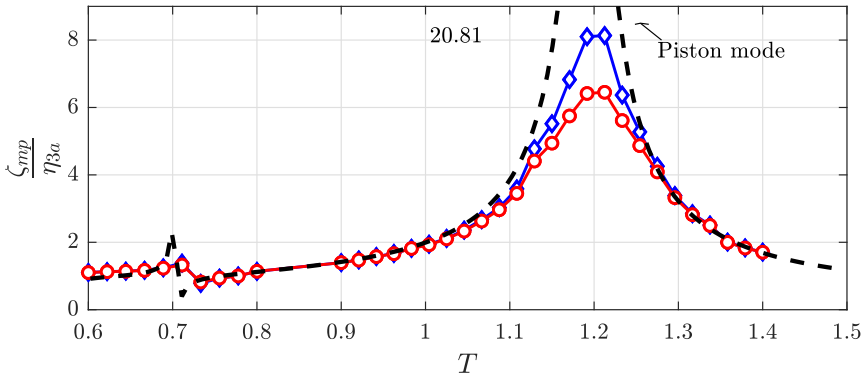

(b) MP2

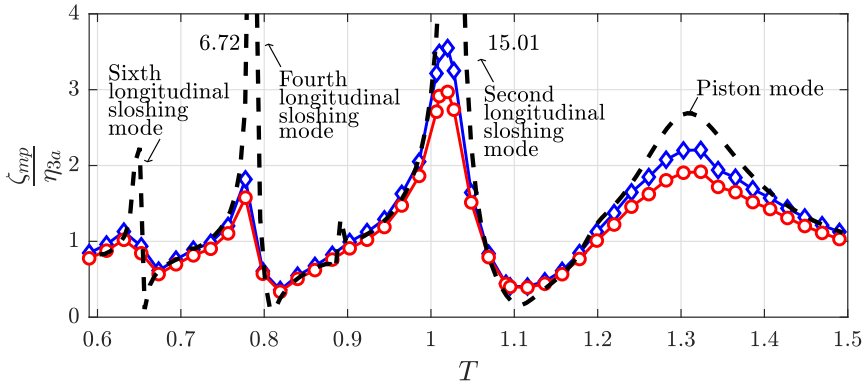

(c) MP3

Figure 9.2: Amplitude-dependent moonpool RAOs at WP1 (cf. Figure 5.3) from WAMIT and PVC3D simulations in forced heave. The RAOs are presented in an Earth-fixed coordinate system. The numbers indicate the peaks from the WAMIT simulations.

We investigate the moonpool responses in forced surge numerically, such that the damping at the odd sloshing modes are also addressed. Moonpool RAOs from forced surge simulations for MP2 in the vicinity of the first longitudinal sloshing mode period are presented in Figure 9.4(a). WAMIT over-predicts the moonpool responses significantly in the proximity of the first longitudinal sloshing mode at $T = 0.71$ s, and the simulations with PVC3D demonstrate that damping due to flow separation is dominant, also in the vicinity of the first longitudinal sloshing mode. We can say so because the main difference between the WAMIT and PVC3D simulations is that the Navier–Stokes equations are solved in the latter. The boundary conditions in both WAMIT and PVC3D are linearized. For MP2, the beam-to-draft-ratio (B_m/D) is $B_m/D = 2$, and the wavelength of the standing wave at the first sloshing mode is $\lambda \approx 2B_m = 0.8$ m. According to linear theory, assuming infinite water depth, the fluid velocity at the moonpool entrance is $\exp(-kD) \approx 0.2$ of that at the free-surface in the moonpool, consistent with that presented in Figure 9.5(a) from the present WAMIT simulations. With $\eta_{3a} = 1$ mm, the first longitudinal sloshing mode RAO from the PVC3D simulations at the free-surface in the moonpool is approximately 15 at the first longitudinal sloshing mode, which implies that the water motions at the moonpool entrance is approximately 3 times the forced surge motion at the moonpool entrance. Hence, one can argue that the relative flow at the moonpool entrance is dominated by the water motions.

Moonpool RAOs from forced surge simulations for MP3 are presented in Figure 9.4(b). Four sloshing modes are excited in the simulated forced surge period

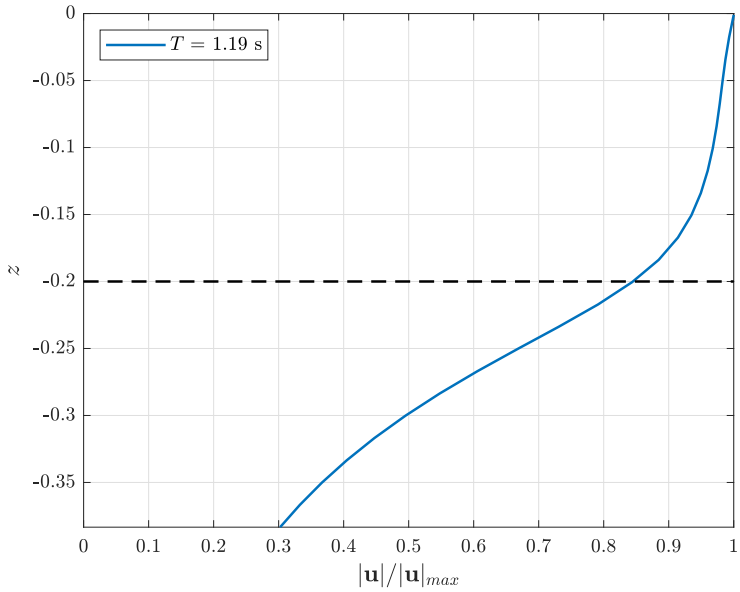

(a) MP2 ($x = 0.7$ m and $y = 0$ m).

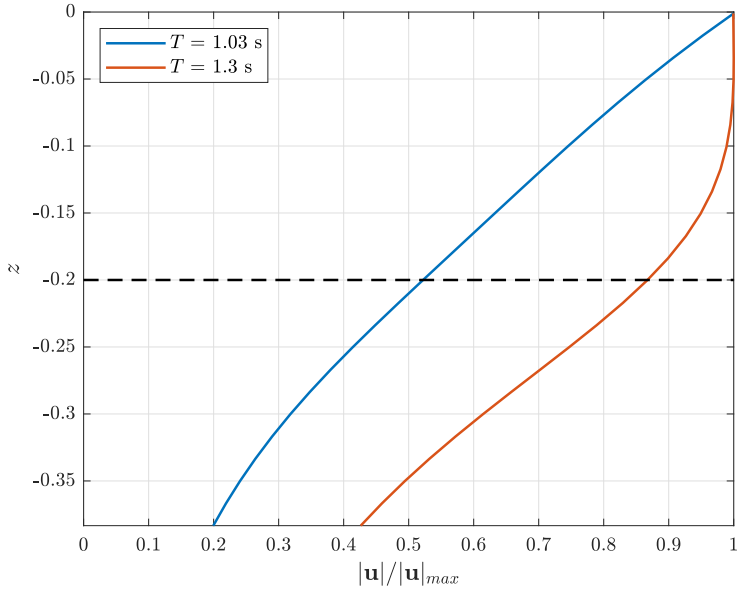

(b) MP3 ($x = 0.8$ m and $y = 0$ m).

Figure 9.3: Magnitude of fluid velocity, $|\boldsymbol{u}|$, from forced heave simulations with WAMIT. The dashed line indicates the location of the moonpool entrance. $T = 1.19$ s is the piston mode for MP2. $T = 1.03$ s and $T = 1.30$ s are the second longitudinal sloshing and piston modes, respectively, for MP3.

range. Again, the amplitude-dependence in the proximity of the first longitudinal sloshing modes at $T = 1.03$ s for MP3 suggest that damping due to flow separation is dominant. Similarly, dominant damping due to flow separation is illustrated in the proximity of the third and fifth longitudinal sloshing modes at $T = 0.89$ s and $T = 0.71$ s, where the moonpool RAOs are larger than at the first longitudinal sloshing mode. Selected snapshots of flow fields from the present PVC3D simulations are presented in Appendix B.4 and Appendix B.5. Note in particular the vortices at the moonpool inlet. From these, and in combination with the moonpool RAOs, we infer that flow separation at the moonpool entrance provide dominant damping of the moonpool responses at resonance.

At the higher sloshing modes for MP3 (for instance the sixth and seventh longitudinal sloshing modes), the water flow is not dominant relative to the body motions at the moonpool entrance. Hence, the validity of the PVC3D simulations - which applies linearized body-boundary conditions - is questionable. In order to obtain more accurate estimates of the moonpool responses for the higher sloshing modes, where the fluid motion decays quickly, nonlinear body-boundary conditions are needed. The purpose of the present PVC3D simulations is, however, to underline the importance of damping due to flow separation even for higher sloshing modes. The damping due to flow separation is proportional to the relative velocity squared. Although the fluid motion at the moonpool entrance at the higher sloshing modes is small/moderate due to the rapid decay vertically through the moonpool, the forcing frequency, ω, increases. Note that the flow velocity at the moonpool entrance, here denoted $u_{mp,e}$, is $u_{mp,e} = \omega p_{mp,e}$, where $p_{mp,e}$ is the fluid motion at the moonpool entrance. Since the damping due to flow separation is proportional to the relative velocity squared at the moonpool entrance, the fact that ω increases for higher sloshing modes plays an important role, although the fluid motion at the moonpool entrance is moderate (or even small).

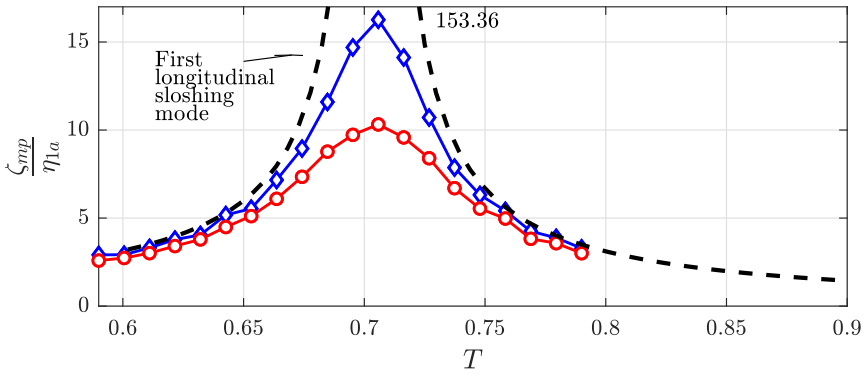

(a) MP2

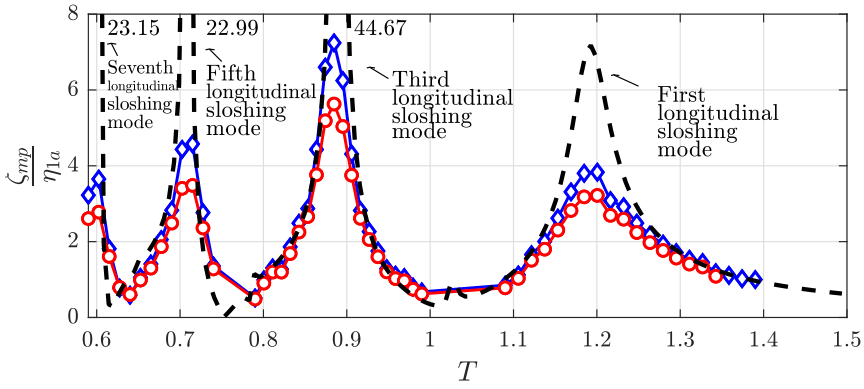

(b) MP3

Figure 9.4: Same as Figure 9.2, but simulations in forced surge. The numbers indicate the peaks from the WAMIT simulations.

The phase angles between the forced heave motion and the moonpool responses at WP1 for MP1-3 from WAMIT and PVC3D simulations are presented in Figure 9.6. At the piston mode period, the moonpool responses are approximately 90 degrees out of phase with the forced heave motion, consistent with the discussion in §7.1.4 for clean moonpools. The abrupt change in the phase angle at resonance as predicted by WAMIT is somewhat relaxed by PVC3D. This was also illustrated for the forced heave experiments with the 2DMR cases. This is due to that the damping is considerably smaller with the potential flow solvers. The rapid change in the phase angles, for instance close to the second longitudinal sloshing mode for MP3, is important with respect to the relative moonpool responses in this period range.

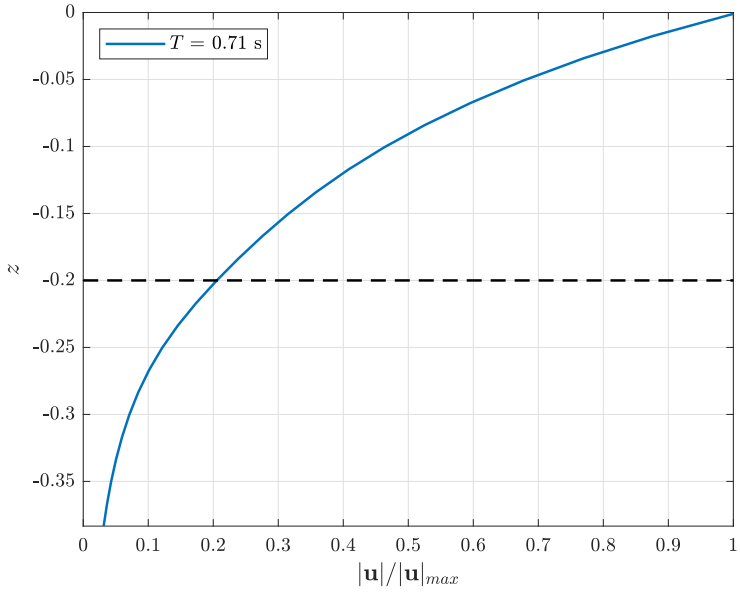

(a) MP2 ($x = 0.7$ m and $y = 0$ m).

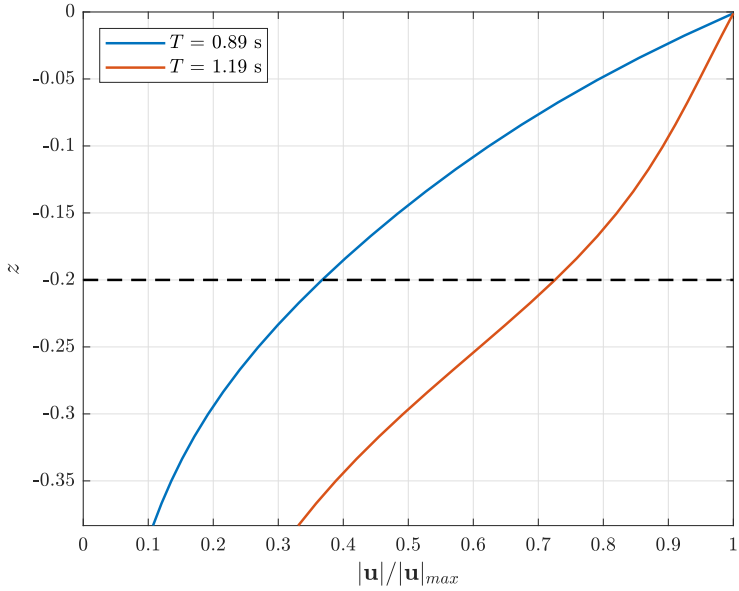

(b) MP3 ($x = 0.8$ m and $y = 0$ m).

Figure 9.5: Same as Figure 9.3, but from forced surge simulations with WAMIT. $T = 0.71$ s is the first longitudinal sloshing mode for MP2. $T = 0.89$ s and $T = 1.19$ s are the third longitudinal sloshing and first longitudinal sloshing modes, respectively, for MP3.

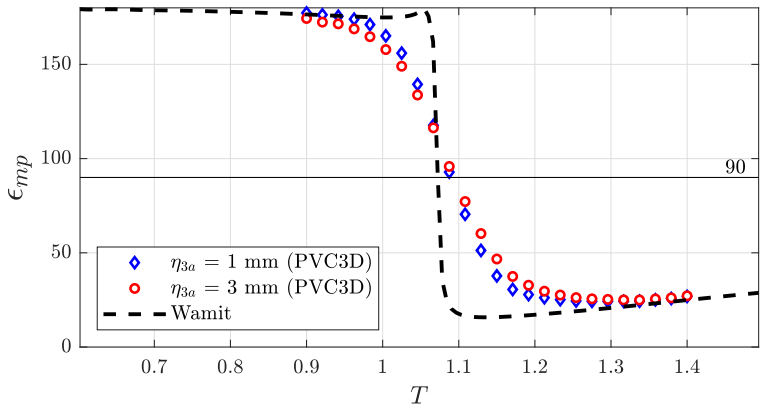
150
100
50
0
90
ϵ_{mp}
0.7
0.8
0.9
1
1.1
1.2
1.3
1.4
T
η_{3a} = 1 mm (PVC3D)
η_{3a} = 3 mm (PVC3D)
Wamit

(a) MP1

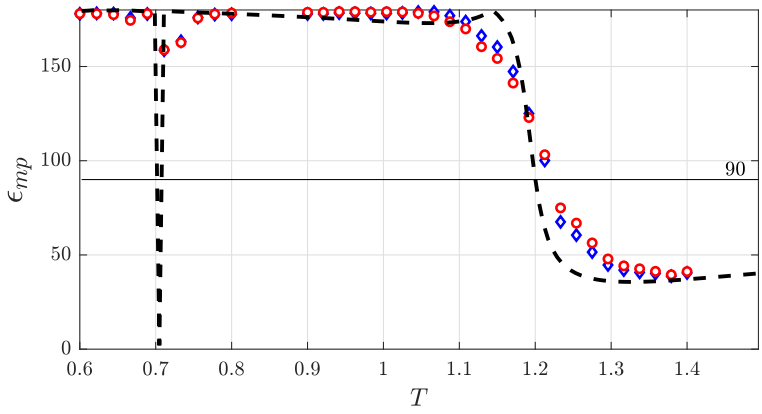
150
100
50
0
90
ϵ_{mp}
0.6
0.7
0.8
0.9
1
1.1
1.2
1.3
1.4
T

(b) MP2

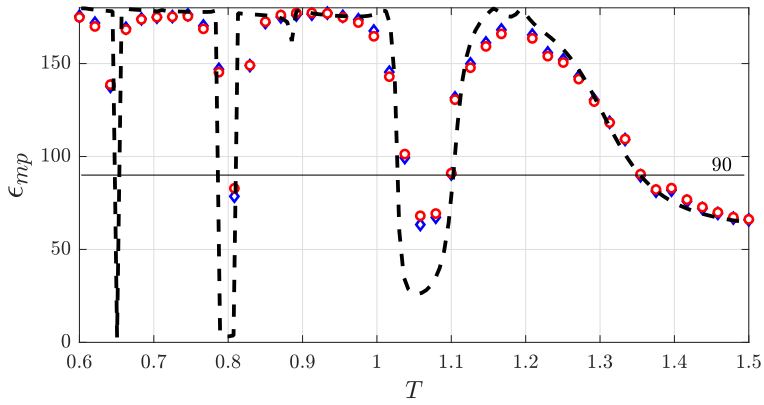

(c) MP3

Figure 9.6: Phase angles between the forced heave motion and moonpool responses (at WP1) measured in an Earth-fixed coordinate system from PVC3D and WAMIT simulations for the models tested in the Ocean Basin in forced heave.

9.3 Responses for MP1

We now turn the attention to the moonpool and ship responses for MP1 in freely floating conditions. Selected time-series of the incident irregular waves, heave response and moonpool responses are presented in Figure 9.7. The moonpool response is in the same order as, or slightly smaller than, the incident wave and heave motion, in contrast to the large moonpool responses in forced heave exemplified in Figures 7.12 and 7.13. The fact that the moonpool responses appear lower than the incident wave may seem inconsistent with the moonpool RAOs presented in Figure 9.8. The explanation to this seemingly inconsistency lies, however, in the fact that the moonpool response is more or less bounded in a rather narrow wave period band. There, the magnification (RAO) is 2-3.5, whereas for most of the wave period range, the moonpool RAO is less than unity. The moonpool responses are clearly over-predicted by WAMIT, as expected, since damping due to flow separation is important. This is indicated by the clear amplitude-dependence in the moonpool RAOs at the piston mode, and further supported by the forced heave simulations presented in §9.2. At the piston mode period, the experimental moonpool RAOs are approximately 2-3.5, which is a considerable magnification in practice.

Snapshots from video recordings of the piston mode responses in head sea are presented in Figure 9.9. The piston mode response shape for MP1 is near-uniform, which is consistent with the theory presented by Molin (2001). The piston mode period, as discussed earlier, is almost not affected by the coupling between the moonpool and ship responses, as we see for larger moonpools. In contrast to that observed for MP2 and MP3, no nonlinear moonpool responses are observed for MP1. Hence, the regular and irregular (PNWW) wave tests with $H/\lambda = 1/60$ yield consistent results. For instance, at the piston mode period, the value of the moonpool RAOs from the regular and irregular wave tests are both approximately 2.5-2.6. This applies to both head and beam sea. In fact, the moonpool responses are very similar in head and beam sea for MP1. This is not obvious, since the vessel motions differ quite much in the two wave headings.

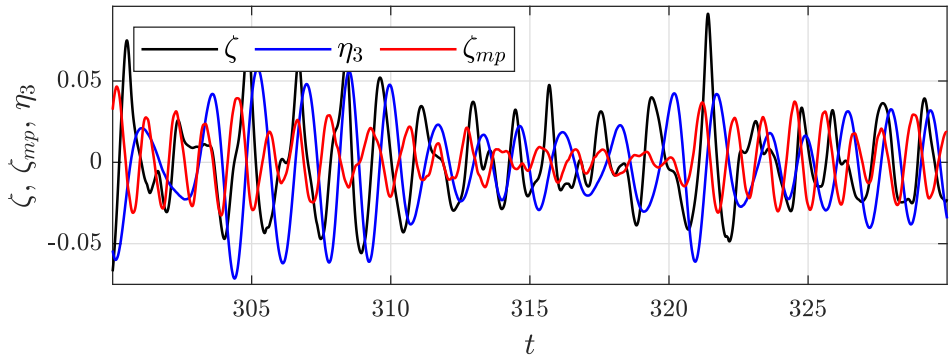

Figure 9.7: Selected time-series from irregular wave tests with PNWW spectrum. Time-series of incident wave (ζ), heave response (η_3) and moonpool response (ζ_{mp} at WP1) for MP1 in beam sea with $H/\lambda = 1/60$.

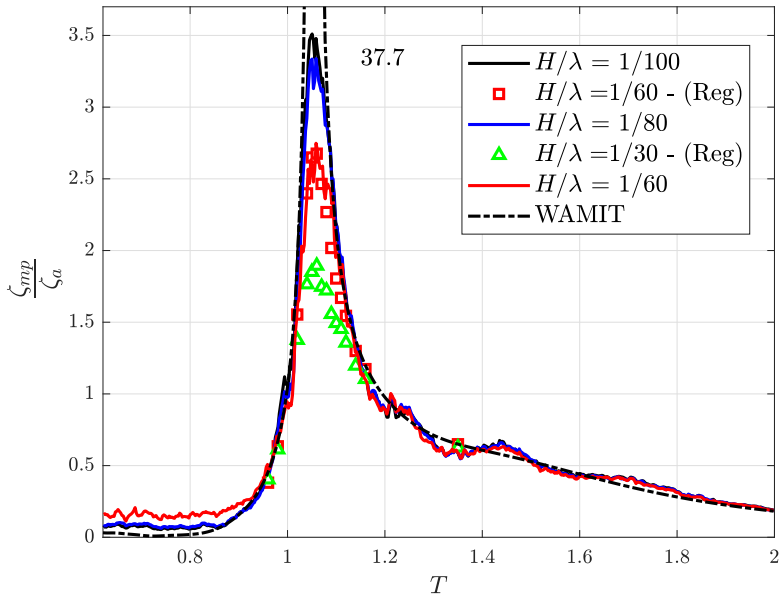

(a) Head sea (MP1)

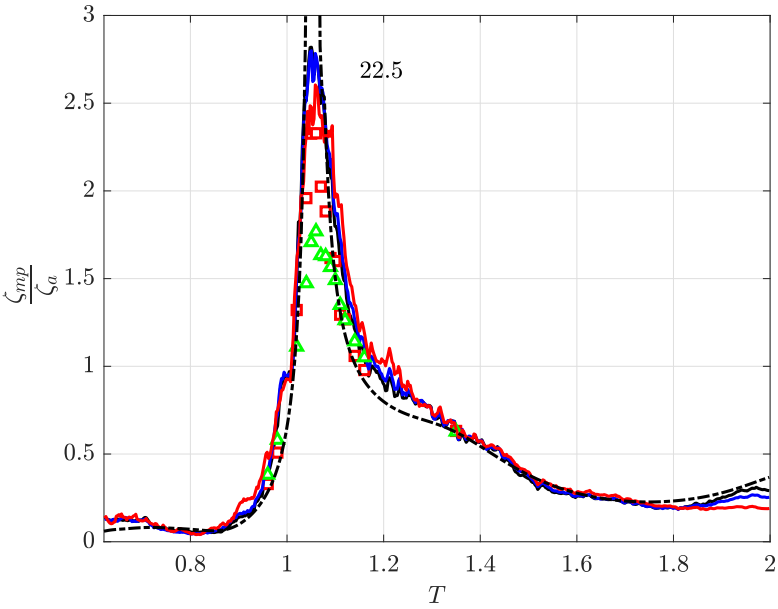

(b) Beam sea (MP1)

Figure 9.8: Amplitude-dependent moonpool responses in head and beam sea for MP1 (V_{MP}/V_S = 0.015). Moonpool responses are presented at the location of WP1 in a body-fixed coordinate system. The numbers indicate the piston mode responses as predicted by WAMIT.

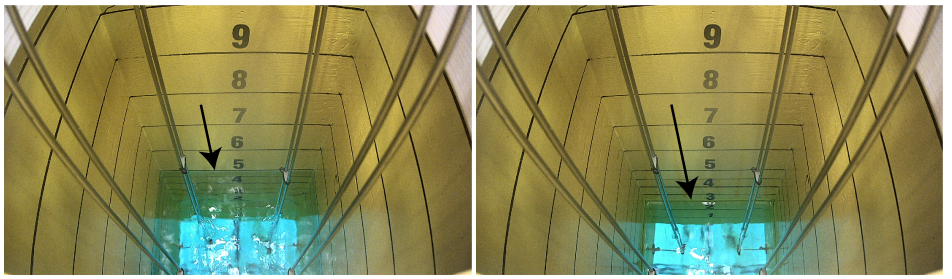

Figure 9.9: Two snapshots from video recordings of the piston mode response for MP1 in head sea in regular waves with $T = 1.06$ s. The arrows in the snapshots point to the free-surface in the moonpool. The time instants are approximately $T/2$ apart, where T is the wave period. $H/\lambda = 1/60$.

The heave RAOs, presented in Figure 9.10, are in general in reasonable agreement with the WAMIT simulations, except at the piston mode period, where WAMIT over-predicts the heave response significantly in a narrow wave period range due to that the moonpool response is over-predicted. The experiments show that the hy-

drodynamic interaction between moonpool and heave responses is small by comparing with WAMIT simulations for MP0, except in a narrow wave period range at the piston mode period, where there is a small peak in the heave RAOs.

In head sea, for $T > 1.2$ s, we observe systematic differences between the WAMIT simulations and the irregular wave tests. The irregular wave tests in beam sea show similar trends, although it is somewhat less pronounced than in head sea. In this wave period range, we expect that the model tests and WAMIT yield basically the same results. The differences between WAMIT and irregular waves for $T > 1.2$ s are attributed to re-reflection from the side walls of the basin. Time-series of the heave response at $T = 1.2$ s from the regular wave tests with $H/\lambda = 1/60$ for MP2 is presented in Figure 9.11(a). The time-series suggests that re-reflection from the side wall affects the heave responses considerably. The re-reflection appears to be consistent with that predicted by linear wave theory, i.e. modulations in the heave amplitude starts approximately at $t > t_r + 2L_s/c_g$, indicated by dashed vertical lines, where L_s is the distance from the model to the side wall. c_g is the group velocity as predicted by linear wave theory. t_r is the time instant when the steady-state incident waves have reached the model. Similar trends are observed for the pitch responses, although not as pronounced as for heave. Wave re-reflection also affects the heave and pitch RAOs for MP2 and MP3, cf. results in §9.4 and §9.5. Fortunately, this is outside the most interesting wave period range; the moonpool resonances all occur for $T < 1.2$ s.

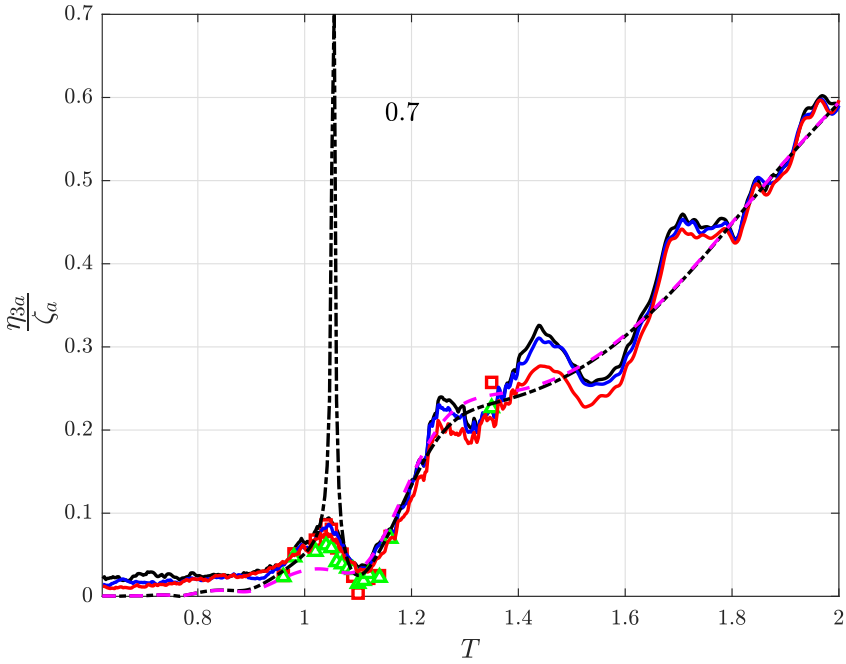

(a) Head sea (MP1)

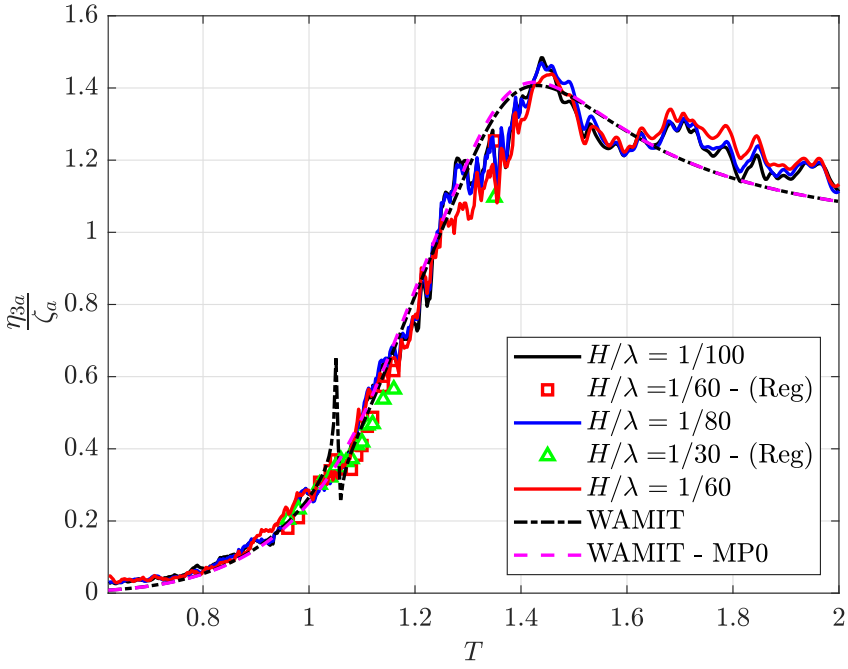

(b) Beam sea (MP1)

Figure 9.10: Amplitude-dependent heave RAOs in head and beam sea for MP1 (V_{MP}/V_S = 0.015). Results for MP0 (ship without moonpool) are presented as pink dashed lines.

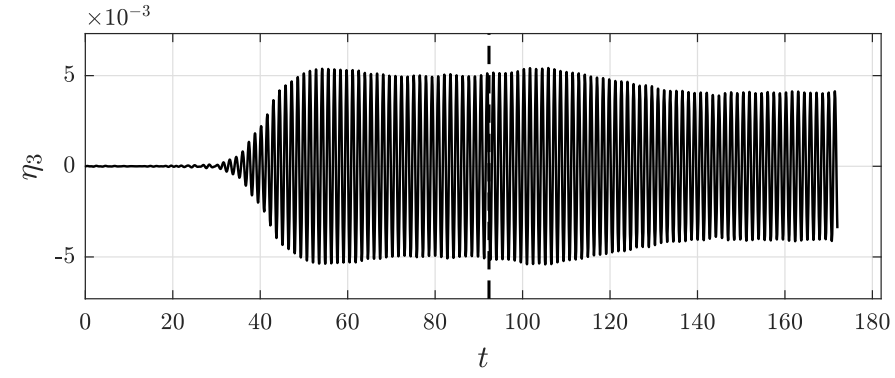

(a) Heave response

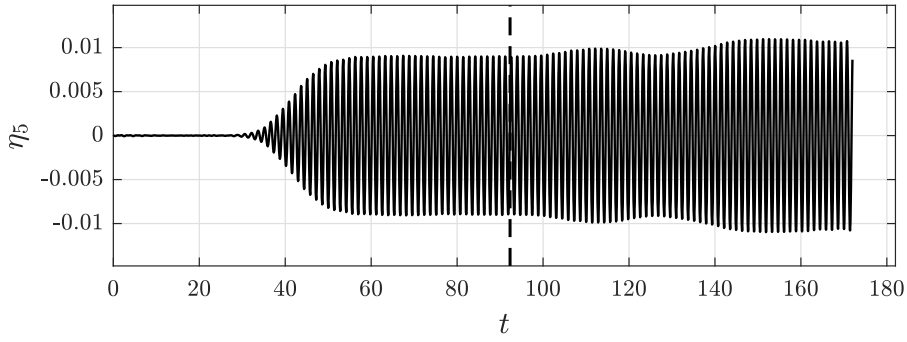

(b) Pitch response

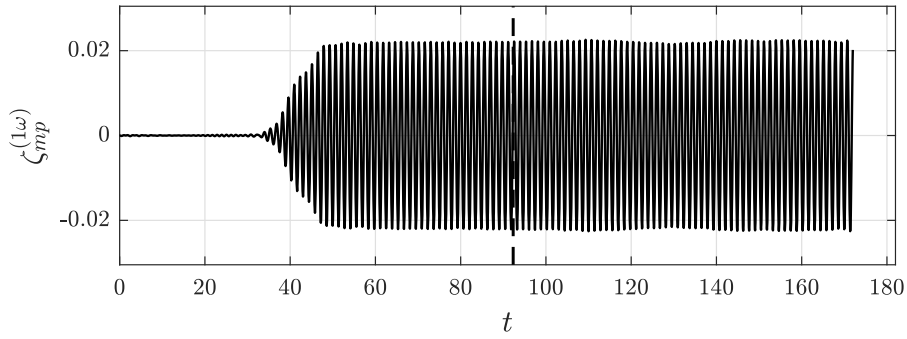

(c) Moonpool response at WP1

Figure 9.11: Time-series of responses for MP2 with $T = 1.4$ s in regular waves. $H/\lambda = 1/60$. The dashed lines indicate the time at which re-reflection from the side-wall of the basin is expected, as predicted by linear wave theory.

The experimental pitch RAOs in Figure 9.12 are in general in fair agreement with the WAMIT simulations, although WAMIT over-predicts the pitch responses in a narrow wave period range in the proximity of the piston mode. The model tests

indicate that the hydrodynamic interaction between the moonpool and pitch responses are negligible for all practical purposes. This demonstrates that the ship motions can be determined without accounting for the presence of the moonpool for MP1. As discussed earlier, the pitch RAOs from the irregular wave tests are affected by wave reflection from the side wall for $T > 1.2$ s.

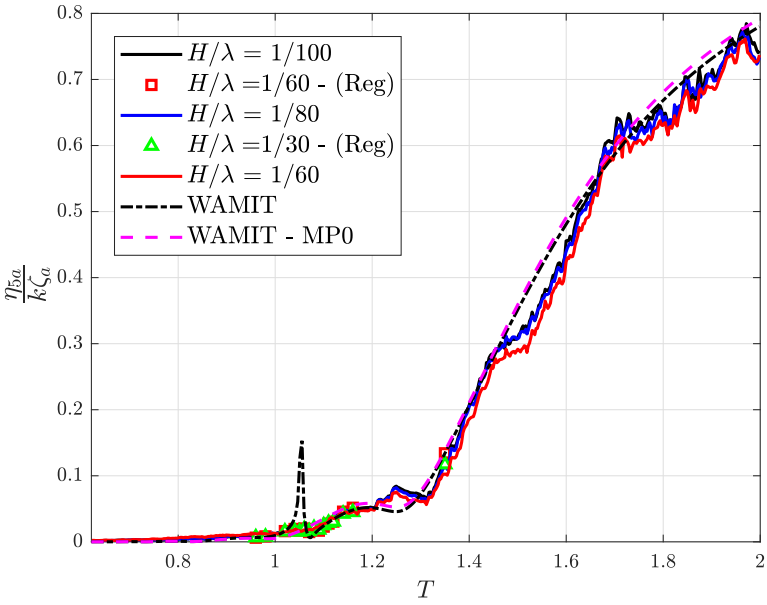

Figure 9.12: Amplitude-dependent pitch responses in head sea for MP1 (V_{MP}/V_S = 0.015). Results for MP0 (ship without moonpool) are presented as pink dashed lines.

The irregular wave tests with the Pink Noise for Water Waves (PNWW) spectrum and regular wave tests with wave steepness $H/\lambda = 1/60$ illustrate consistent results. This applies for both the moonpool and vessel responses. The PNWW spectrum was presented in §5.5. We believe this is opens for efficient model testing, although care must be taken when nonlinear free-surface effects are dominant.

9.4 Responses for MP2

A main difference for MP2 relative to MP1 is the V_{MP}/V_S-ratio. The V_{MP}/V_S-ratio for MP2 is approximately four times that for MP1. The heave and pitch (in particular heave) responses are clearly affected by the moonpool responses, in contrast to that for MP1. Another consequence is that sloshing is excited in a relevant wave period range, where also swirling is observed.

Selected time-series of the incident irregular waves, heave responses and moonpool responses for MP2 in beam sea are presented in Figure 9.13. The moonpool responses appear to be on the same order as the incident wave, i.e. larger than for MP1. This is explained by that the experimental RAOs are in fact higher for MP2 than for MP1 (see Figure 9.14). Amplitude-dependent moonpool RAOs in head and beam sea conditions are presented in Figure 9.14. The WAMIT simulations clearly suggest that wave radiation damping is small in the vicinity of the first longitudinal and first transverse sloshing modes, both excited at $T = 0.71$ s. Even smaller than at the piston mode. This is as expected, since the water motions through the moonpool to the outer domain is smaller at the first longitudinal and transverse sloshing modes, than at the piston mode. Our experimental results are consistent with the forced surge simulations for MP2 in §9.2, where the PVC3D simulations demonstrated that damping due to flow separation was dominant at the first longitudinal sloshing mode, and WAMIT greatly over-predicted the first longitudinal sloshing mode responses.

At the piston mode, the responses are clearly amplitude-dependent. This illustrates that damping due to flow separation is dominant at the piston mode also for MP2 in freely floating conditions. The model test results show amplitude-dependence in the proximity of the first longitudinal and first transverse sloshing modes. The moonpool RAOs from the irregular wave tests in the vicinity of the first sloshing modes, in contrast to that observed at the piston mode, *increase* with increasing wave steepness. The PVC3D forced motion simulations presented in §9.2 illustrated that damping due to flow separation was dominant at the first longitudinal sloshing mode for MP2. Hence, from these simulations, one would expect that the moonpool RAOs decrease with increasing wave steepness, as for the previously discussed cases. The present model tests, however, shows that nonlinear free-surface effects are important, in addition to the dominant damping due to the flow separation at the moonpool entrance. In head sea, the first harmonic moonpool response at the first longitudinal sloshing mode in regular waves is considerably smaller than the moonpool RAOs from the irregular wave tests using the PNWW spectra. This is due to that the second harmonic moonpool responses at the basic wave period $T = 1.42$ s, which is twice the first longitudinal sloshing mode period

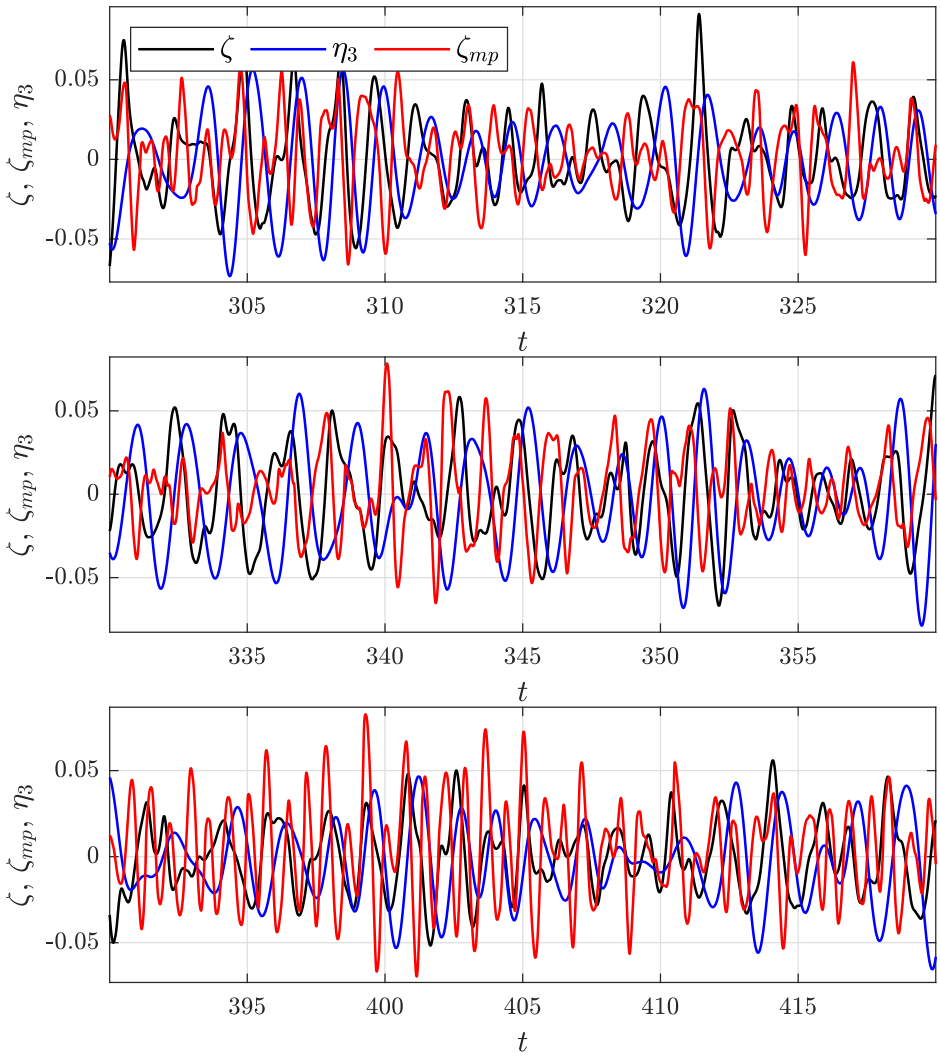

Figure 9.13: Selected time-series from irregular wave tests with PNWW spectrum. Time-series of incident wave (ζ), heave response (η_3) and moonpool response (ζ_{mp} at WP1) for MP2 in beam sea with $H/\lambda = 1/60$. Both the piston and first sloshing modes are excited.

$T = 0.71$ s, is considerably larger than the first harmonic moonpool responses in regular waves with $T = 0.71$ s. We investigate this in some detail in §9.8, where we discuss secondary resonance.

In beam sea, the moonpool responses at the first transverse sloshing mode, both in regular and irregular seas, are significant. We observed that swirling occurred in regular waves at $T = 0.71$ s in beam sea (swirling was not excited in head sea). This is illustrated by four video snapshots in Figure 9.15. We used video recordings and the phases between the measurements with WP1, WP2, WP5 and WP6 inside the moonpool to confirm that swirling occurred. See the time-series of the moonpool responses in the four corners of the moonpool in Figure 9.16. The time-series clearly show evidence of swirling, since the different wave probes measurements are $T/4$ apart and with basically equal amplitude. Swirling is a nonlinear effect, and is a combination of two antisymmetric standing waves (Faltinsen and Timokha 2009, p. 4 and 135), which results in a progressive wave in the angular direction. The direction of the angular water motion depends on the transient conditions in the moonpool. We performed eight repetition tests at the first transverse sloshing mode in beam sea. Swirling occurred in the counter-clockwise direction (seen from the ship deck) in each test. This means that the model tests were repeatable, as discussed in §5.7.4. A main candidate for that swirling occurs in the same direction each time could be that the vessel is not fore-aft symmetric. Another candidate is that it is impossible, in practice, to achieve exactly 90 degrees heading angle in the model tests. Hence, the fact that the model is offset slightly from the desired heading angle could be a possible reason for the fact that swirling occurred in the same direction each time.

Swirling in closed sloshing tanks might induce significant loads in the longitudinal and transverse direction, which could be of concern with respect to the support structure. Swirling in moonpools induces loads on the vessel both in the x- and y-directions, in contrast to a single standing wave, which only induces a force in the direction of the standing wave. The problem swirling in moonpools presents is twofold; firstly, it can affect the operability of the moonpool, and secondly, it may influence the ship motions. The present experimental results indicate that the influence of the swirling motion is small on the surge and sway motions, as illustrated in Figure 9.17 at $T = 0.71$ s. Although the swirling-induced surge motion in regular waves with wave steepness $H/\lambda = 1/60$ is five times larger than the surge motion predicted by WAMIT, the surge responses are relatively small. The swirling-induced sway motion in regular waves is also quite small in the present test conditions, although in more extreme wave conditions, the swirling-induced surge and sway motions may matter, even for this relatively small moonpool. Moreover, the swirling motion might induce large loads on an object in the moonpool, and

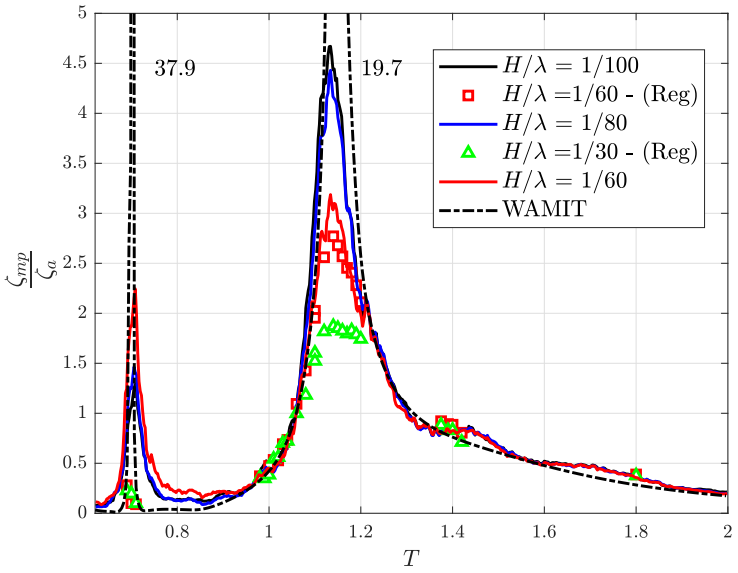

(a) Head sea (MP2)

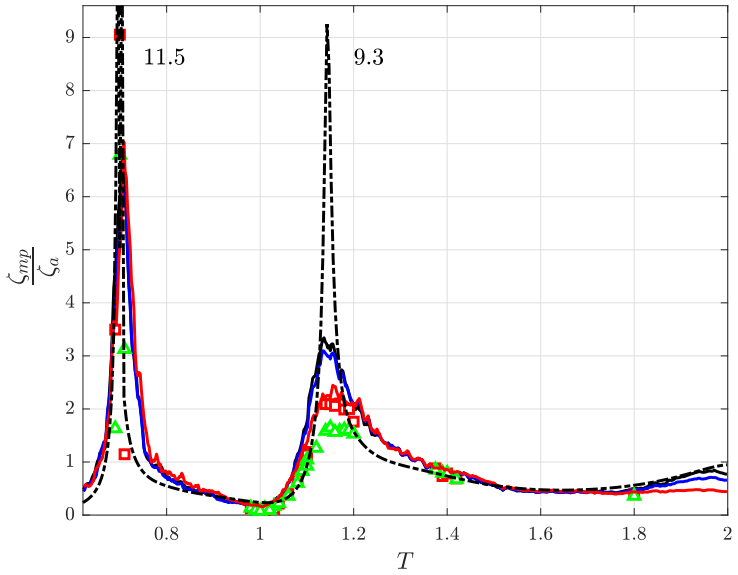

(b) Beam sea (MP2)

Figure 9.14: Amplitude-dependent moonpool RAOs in head and beam sea for MP2 (V_{MP}/V_S = 0.064). Moonpool responses are presented at the location of WP1 in a body-fixed coordinate system. The numbers indicate the peak values from the WAMIT simulations.

therefore important with respect to the operability of the moonpool.

In the vicinity of the piston mode, the surge responses in beam sea are overestimated by WAMIT, as illustrated in Figure 9.17(a). The sway responses in beam sea indicate relatively large differences between the model tests and WAMIT for $T \gtrapprox 1.2$ s (cf. Figure 9.17(b)). This is due to that the sway motion is coupled with the roll motion. WAMIT does not correctly predict the roll responses in this wave period range. We discuss roll briefly in §9.6.

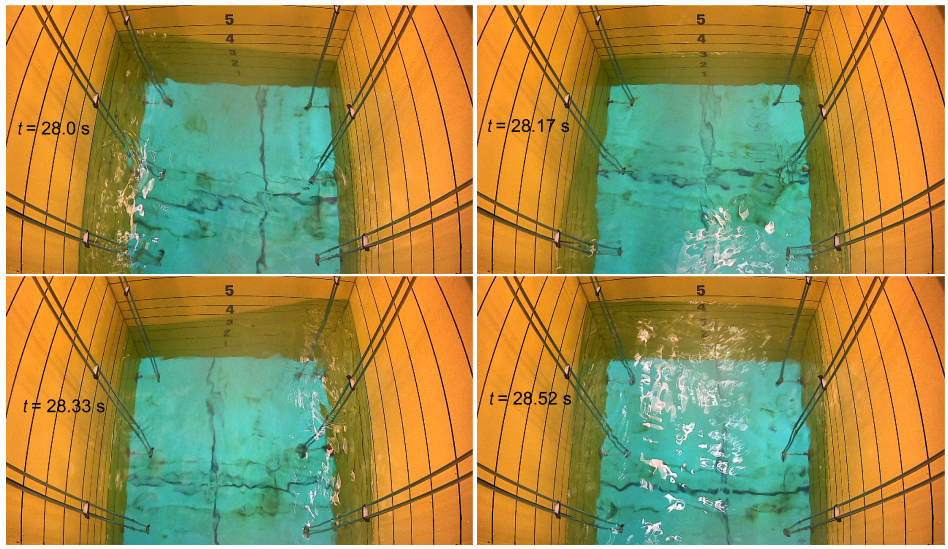

Figure 9.15: Four snapshots with $\Delta t = T/4$ from video recordings of the moonpool response for MP2 in beam sea, where swirling occurred at $T = 0.71$ s in regular waves. $H/\lambda = 1/60$. Here, $t = 0$ s is when the incident waves have reached the model. Swirling occurs in the counterclockwise direction.

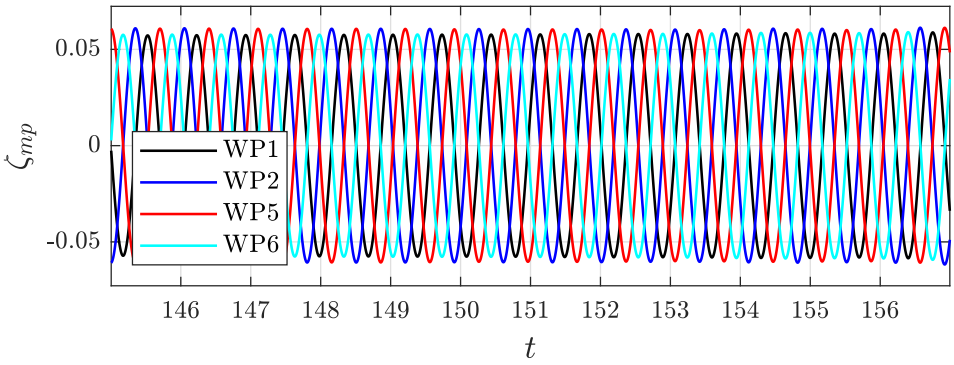

Figure 9.16: First harmonic steady-state moonpool responses as measured by wave probes close to the corners of the moonpool for MP2 in beam sea at $T = 0.71$ s (cf. Figure 5.3). Zoomed in to illustrate the phase difference between the measurements, indicating that swirling occurred. $H/\lambda = 1/60$.

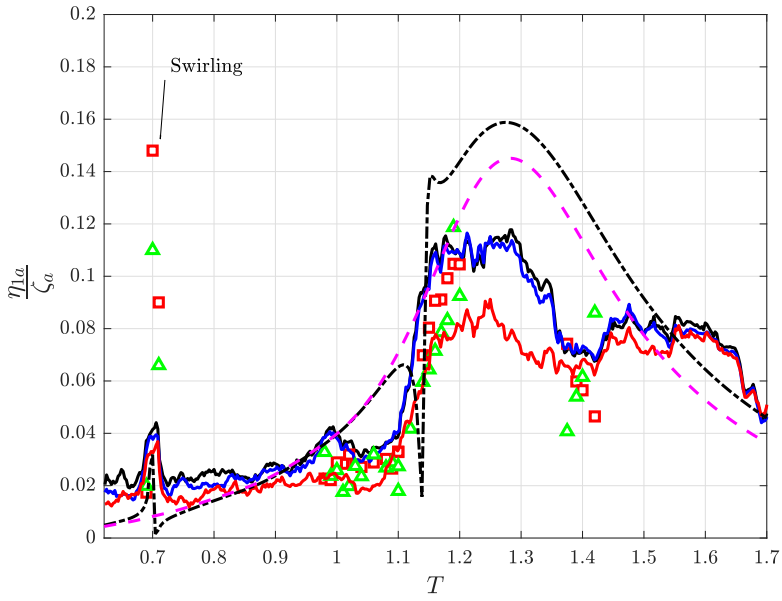

(a) Surge response

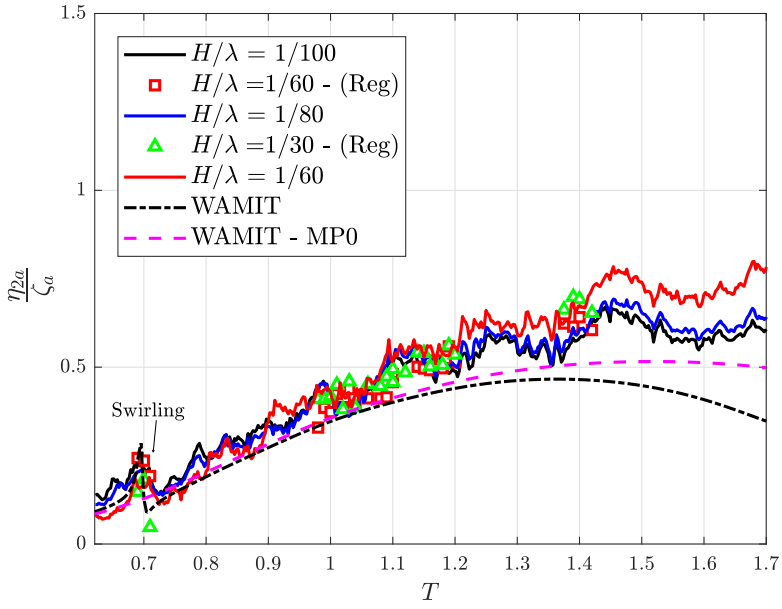

(b) Sway response

Figure 9.17: Surge and sway RAOs in beam sea for MP2 (V_{MP}/V_S = 0.064). Results for MP0 (ship without moonpool) are presented as pink dashed lines. Although the swirling motion is significant, the swirling-induced surge and sway motions are small.

The coupling between vessel in all six degrees of freedom and moonpool responses for MP1 were negligible. The heave RAOs for MP2, presented in Figure 9.18, indicate that the hydrodynamic interaction between the heave and moonpool responses are significant. MP2 has four times larger moonpool volume than MP1. In the proximity of the piston mode in head sea, the experimental heave RAOs are one order of magnitude larger than for MP0. In reality, ships operate in freely floating conditions. The model tests for MP2 clearly suggest that the hydrodynamic interaction between ship and moonpool responses are important to consider with respect to the operability of the vessel, in addition to the operability of the moonpool. Thus, the ship motions cannot be predicted by neglecting the presence of the moonpool, as argued for MP1 in §9.3. Furthermore, linear potential flow theory is not sufficient, both due to dominant damping due to flow separation and nonlinear free-surface effects, such as swirling. Damping lid methods are often used in practice. However, their use is questionable. This leaves us with model tests and PVC3D-type simulations, unless even more rational physically based methods are developed, as for instance the VBEM. At present time, for practical purpose with respect to CPU time, hybrid Navier–Stokes solvers, such as that PVC3D is based

on, is needed. As far as VBEM is concerned, the present 2D study is promising, but more work is needed to generalize to three-dimensional problems.

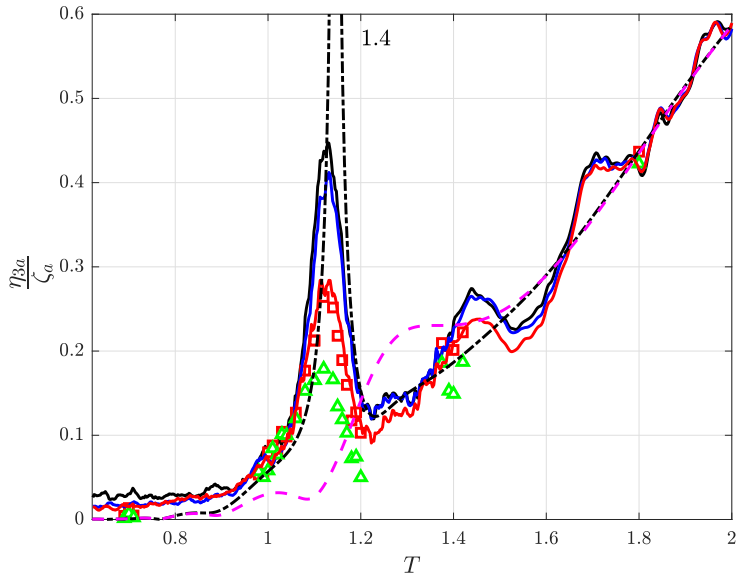

(a) Head sea (MP2)

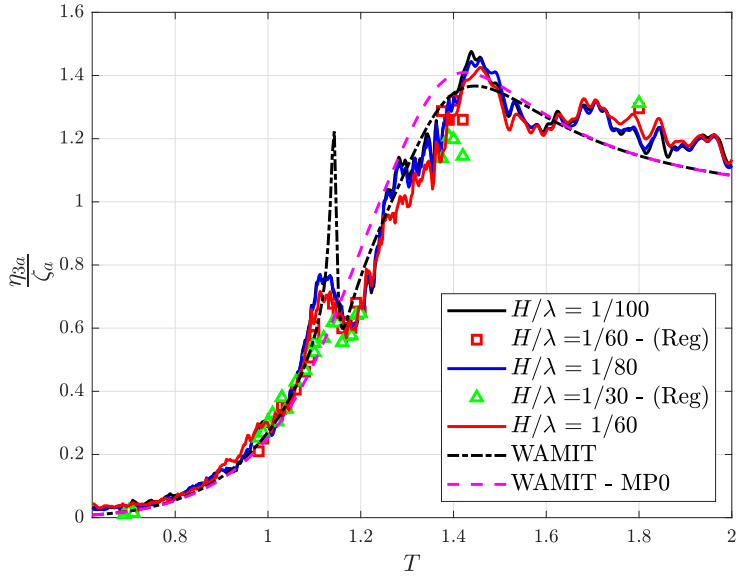

(b) Beam sea (MP2)

Figure 9.18: Amplitude-dependent heave RAOs in head and beam sea for MP2 (V_{MP}/V_S = 0.064). Results for MP0 (ship without moonpool) are presented as pink dashed lines.

The pitch and moonpool responses are coupled since the moonpool center is located $0.2L$ away from the center of the ship. A non-negligible, but narrow, resonance peak is observed in the pitch RAOs, cf. Figure 9.19, although the experimental peaks are not as pronounced as suggested by WAMIT. The coupling between pitch and the moonpool response in head sea is smaller than in heave. In beam sea, the pitch responses are small, despite the fact that the ship is not fore-aft symmetric. Therefore, the pitch responses in beam sea are not presented.

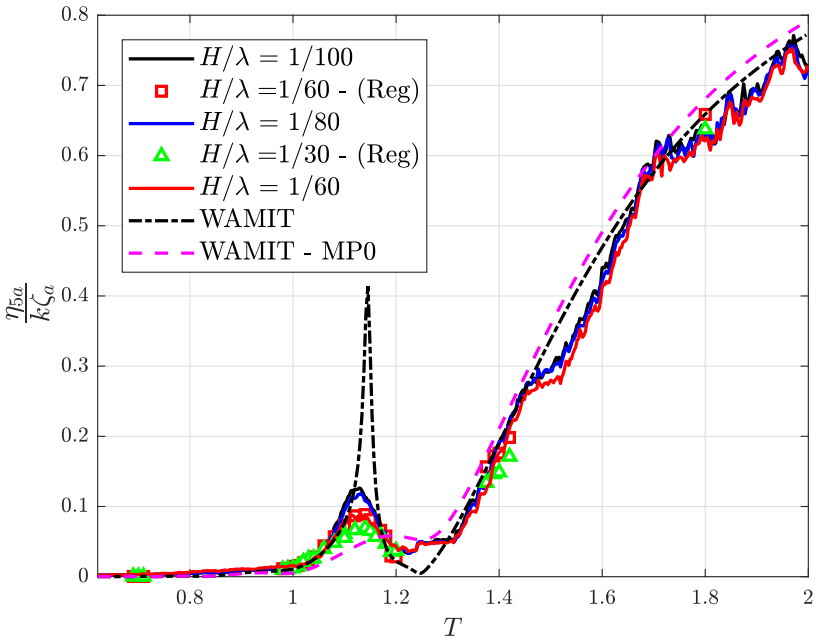

Figure 9.19: Pitch RAOs in head sea for MP2 (V_{MP}/V_S = 0.064). Results for MP0 (ship without moonpool) are presented as pink dashed lines.

In summary, the irregular (PNWW) and regular wave tests with wave steepness $H/\lambda = 1/60$ illustrate consistent results, both for the ship and moonpool responses. In the proximity of the first longitudinal and first transverse sloshing modes, however, the irregular wave tests are inconsistent with the regular wave tests, due to secondary resonance.

9.5 Responses for MP3

MP3 has a significantly larger moonpool than MP1 and MP2, with $V_{MP}/V_S = 0.427$. In the tested range of wave periods, several sloshing modes are excited, in addition to the piston mode. The resonant moonpool responses affect the ship motions, and vice versa, to a greater extent than for MP1 and MP2. The interaction is considerable even for some of the sloshing modes. This is discussed in the following. Selected time-series of the incident irregular waves, heave responses and moonpool responses for MP3 in head sea are presented in Figure 9.20. The magnitude of the moonpool response is similar to that of the two smaller moonpool vessels, but with a considerably broader wave period content.

An interesting observation for this configuration is that the piston and first longitudinal sloshing modes are difficult to separate in freely floating conditions. The piston mode period is shifted significantly (from 1.30 s to 1.17 s) due to the hydrodynamic coupling between the moonpool and vessel responses, as discussed in §9.1. Amplitude-dependent moonpool RAOs for MP3 in head and beam seas are presented in Figure 9.21. The two highest natural periods are so close that the two peaks in the moonpool RAOs are not separated (see ⓔ in Figure 9.21(a)). Therefore, it is difficult to distinguish which mode contributes to the different hydrodynamic effects in the proximity of the piston and first longitudinal sloshing modes in head sea. In the proximity of the piston and first sloshing modes, the moonpool responses are clearly over-predicted by WAMIT. The model tests indicate that damping due to flow separation provides major contribution to damping for these modes, although wave radiation damping is not negligible.

The moonpool responses at the second longitudinal sloshing mode are presented at ⓓ in Figure 9.21(a) in head sea and ⓒ in Figure 9.21(b) in beam sea. The results indicate that wave radiation damping is small, and that damping due to flow separation at the moonpool entrance is dominant. For traditional moonpools, the water motions at the moonpool entrance at the sloshing modes are considerably smaller than the free-surface motions in the moonpool. For instance, for MP2, the water motions at the moonpool entrance is approximately 20 % of the free-surface motions at the first sloshing mode, as illustrated in Figure 9.22. For MP3, the water motion at the moonpool entrance, is in the same order of magnitude as the free-surface motions in the moonpool. This is due to that the ratio between the moonpool length and ship draft, L_m/D, is large for MP3, which implies that the water motions at the sloshing modes decays more slowly with depth than for traditional moonpools.

At the third longitudinal sloshing mode in head sea (see ⓒ in Figure 9.21(a)), the moonpool RAOs illustrate clear evidence of dominant nonlinear free-surface ef-

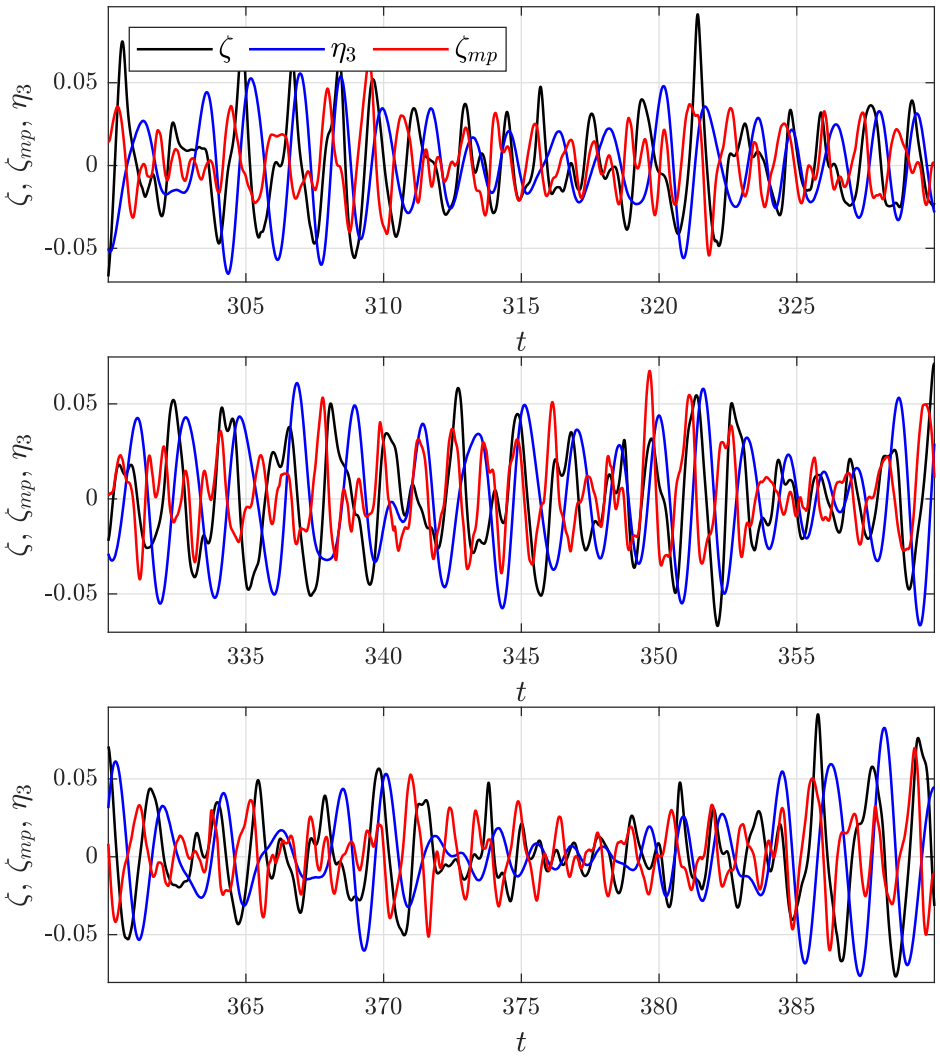

Figure 9.20: Selected time-series from irregular wave tests with PNWW spectrum. Time-series of incident wave (ζ), heave response (η_3) and moonpool response (ζ_{mp} at WP1) for MP3 in head sea with $H/\lambda = 1/60$.

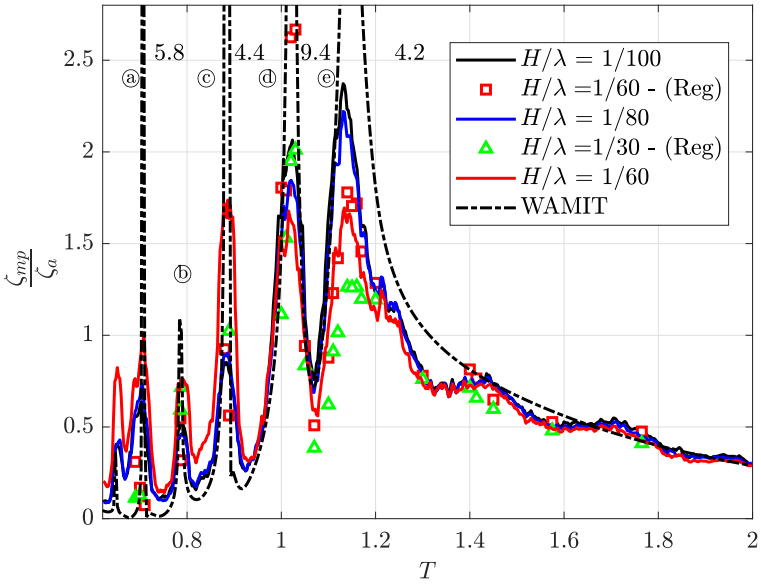

(a) Moonpool response - Head sea (MP3). ⓐ: Fifth longitudinal sloshing mode. ⓑ: Fourth longitudinal sloshing mode. ⓒ: Third longitudinal sloshing mode. ⓓ: Second longitudinal sloshing mode. ⓔ: First longitudinal sloshing and piston modes.

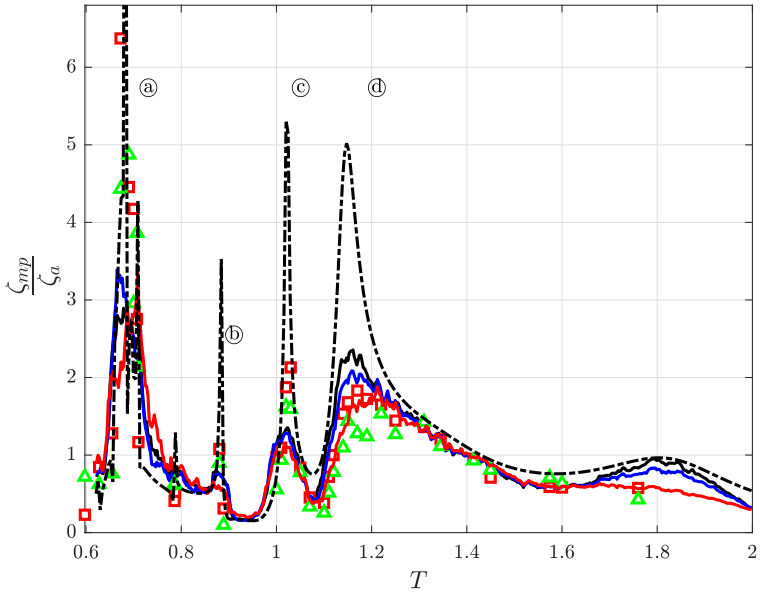

(b) Moonpool response - Beam sea (MP3). ⓐ: Sixth longitudinal sloshing and first transverse sloshing modes. ⓑ: Third longitudinal sloshing mode. ⓒ: Second longitudinal sloshing mode. ⓓ: Piston mode.

Figure 9.21: Moonpool responses in head and beam sea for MP3 (V_{MP}/V_S = 0.427). Moonpool responses are presented at the location of WP1 in a body-fixed coordinate system. The numbers indicate the peak values from the WAMIT simulations.

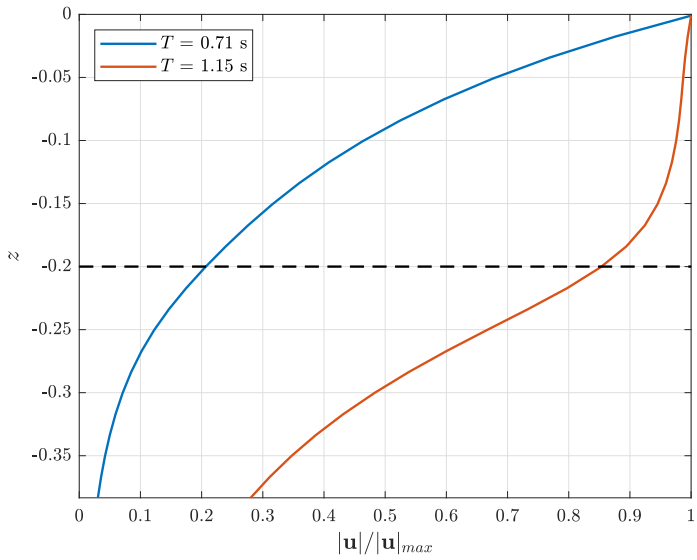

(a) MP2 ($x = 0.7$ m and $y = 0$ m).

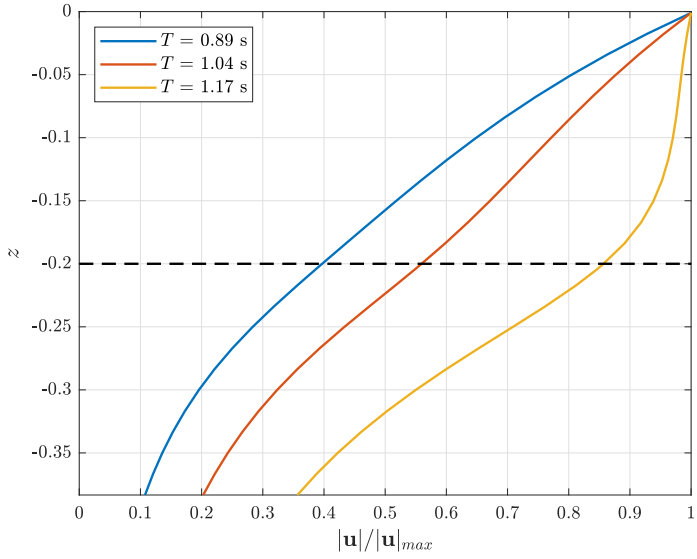

(b) MP3 ($x = 0.8$ m and $y = 0$ m).

Figure 9.22: Magnitude of fluid velocity, $|\boldsymbol{u}|$, from WAMIT simulations in head sea. The dashed line indicates the location of the moonpool entrance. $T = 0.71$ s and $T = 1.15$ s are the first longitudinal sloshing and piston modes, respectively, for MP2. $T = 0.89$ s, $T = 1.04$ s and $T = 1.17$ s are the third longitudinal sloshing, second longitudinal sloshing and piston + first longitudinal sloshing modes, respectively, for MP3.

fects, due to secondary resonance. The consequence of the secondary resonance is that the resonant moonpool responses increases nonlinearly with increasing wave steepness. This is particularly evident for the irregular wave tests with wave steepness 1/60 at the third longitudinal sloshing mode (ⓒ), where the moonpool RAOs are as large as at the second longitudinal sloshing mode (ⓓ), and the piston and first longitudinal sloshing modes (ⓔ). This is similar as that discussed for MP2 at the first longitudinal sloshing mode (cf. §9.4). The forced heave simulations, presented in §9.2, showed that damping due to flow separation was important at the third longitudinal sloshing mode. The model tests in freely floating conditions illustrate that the nonlinear free-surface effects are also important, in addition to the flow separation damping. The two aforementioned effects counter-act each other; the moonpool RAOs decrease with increasing wave steepness due to the viscous damping, while the nonlinear free-surface effects contribute to that the moonpool RAOs increase with increasing wave steepness.

The first transverse sloshing mode is excited at $T = 0.71$ s in beam sea, as illustrated in Figure 9.21(b). The moonpool response at $T = 0.71$ s is significant, where the moonpool response is approximately four times the incident wave amplitude for the lowest wave steepness in regular waves. At $T = 0.66$ s, the sixth longitudinal sloshing mode is excited, where the sixth longitudinal sloshing mode response in regular waves are 5-6 times larger than the incident wave amplitude. Hence, there are two closely spaced peaks at ⓐ in Figure 9.21(b). In irregular waves, the moonpool responses are somewhat smaller than in the regular waves at both $T = 0.66$ s and $T = 0.71$ s. This is due to secondary resonance, which is discussed in somewhat more detail in §9.8, where we see that secondary resonance can yield lower moonpool RAOs in irregular waves too, in contrast to that observed until now.

The moonpool responses at the piston and first longitudinal sloshing modes clearly affect the heave responses, and vice versa. This is illustrated in Figure 9.23. For instance, in head sea, the heave RAO with wave steepness $H/\lambda = 1/60$ is approximately three times larger than for a similar vessel without moonpool in the vicinity of the piston and first longitudinal sloshing modes. Similarly, at the second longitudinal sloshing mode ($T = 1.04$ s), the heave RAOs with wave steepness $H/\lambda = 1/60$ is approximately ten times larger than for a similar vessel without moonpool. The heave RAOs also illustrate clear near-cancellation effects due to the hydrodynamic coupling between heave and moonpool responses at $T = 1.1$ s. Thus, the model tests for MP3 suggest that it is important to consider the hydrodynamic interaction between ship and moonpool responses with respect to the operability of the vessel. As discussed earlier, linear potential flow theory is not sufficient to estimate the responses, and other methods (model tests or PVC3D-

type simulations) are needed. It is less obvious how to develop physical-based empirical methods, such as VBEM, for MP3-sized moonpools. For instance, the piston mode response shape for MP3 is not uniform (cf. discussion in §9.7), which makes it difficult to develop physical-based methods, as done by Faltinsen and Timokha (2015) for small moonpools, where the piston mode response shape is near-uniform. The fact that the motion RAOs are rapidly varying means that the operability of the vessel is sensitive to the frequency content in the wave spectrum.

The previous discussions have illustrated that larger moonpools involve stronger hydrodynamic coupling between the ship and moonpool responses. Larger V_{MP}/V_S-ratio implies that the ship responses are affected by the moonpool responses to a greater extent, and vice versa. In order to show this directly, we compare heave RAOs in head and beam sea of the four vessels (MP0-3). The coupling between moonpool and ship responses for MP3 is significantly more pronounced compared to that for MP1 and MP2. This is illustrated in Figure 9.24, where we compare the heave RAOs of the four different vessels. In general, the heave responses for MP1-3 are larger than for MP0, especially in a relevant wave period range. For instance, $T = 1.0$ s in model scale corresponds to $T = 5.9$ s in full scale (a model scale of 1:34.5 is imagined), which is in a wave period range where ocean waves in the North Sea contain significant wave energy. In addition to the piston mode, increased number of sloshing modes are excited in a relevant wave period range for increasing moonpool sizes. See Appendix C.4 for more comparisons of the responses for MP1, MP2 and MP3.

There is, in general, rather minor effect of the moonpool on the pitch motions, despite the fact that the longitudinal sloshing modes potentially can cause significant moments due to sloshing-induced pressures at the fore and aft of the vessel. The only notable hydrodynamic interaction effect is in the proximity of the piston and first sloshing modes, where there is a clear pitch resonance peak, as illustrated at $T = 1.15$ s in Figure 9.25. The pitch RAOs are approximately five times larger than for MP0 at the piston and first longitudinal sloshing modes. Due to that the piston and first sloshing modes almost coincide, we cannot distinguish whether the coupling between pitch and moonpool responses is due to the piston or first longitudinal sloshing mode. One can argue that since the moonpool center is close to the ship's center, the piston mode should not affect the pitch responses greatly, as discussed in §8.1. However, this is only true if the piston mode shape is near-uniform. The piston mode shape, as discussed in §9.7, is non-uniform for MP3 (cf. Figure 9.27). Thus, both the piston and first longitudinal sloshing modes contribute to the hydrodynamic interaction between moonpool and pitch responses for MP3.

For MP1 and MP2, the surge and sway motions were, in practice, unaffected by the

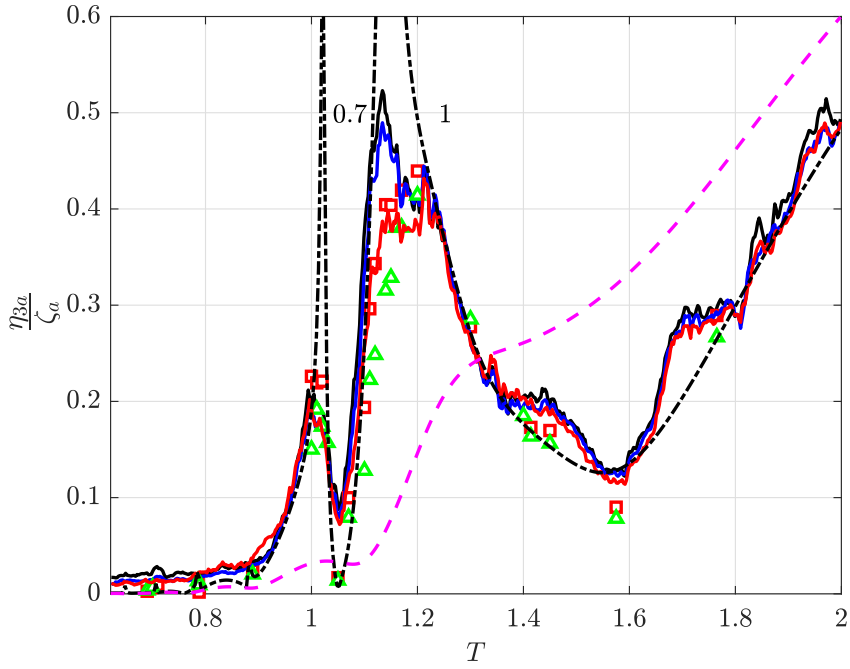

(a) Head sea (MP3)

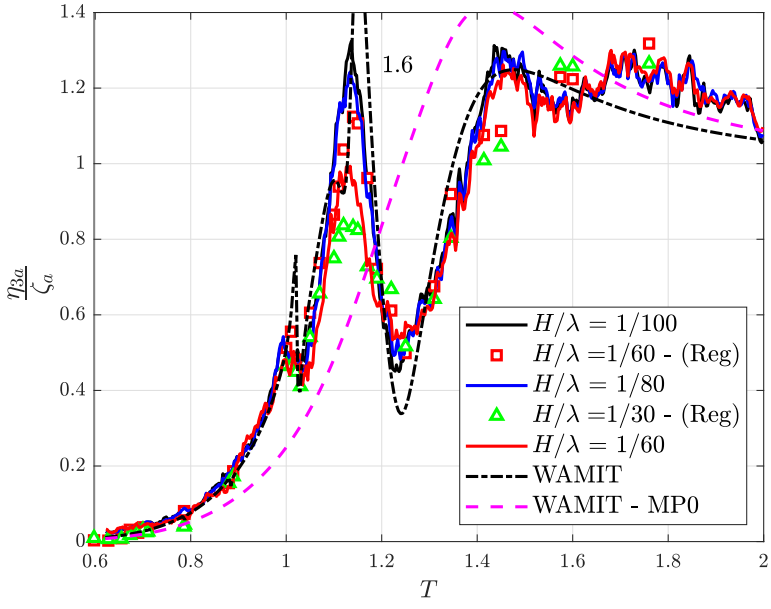

(b) Beam sea (MP3)

Figure 9.23: Heave responses in head and beam sea for MP3 (V_{MP}/V_S = 0.427). The numbers indicate the peak values from the WAMIT simulations. Results for MP0 (ship without moonpool) are presented as pink dashed lines.

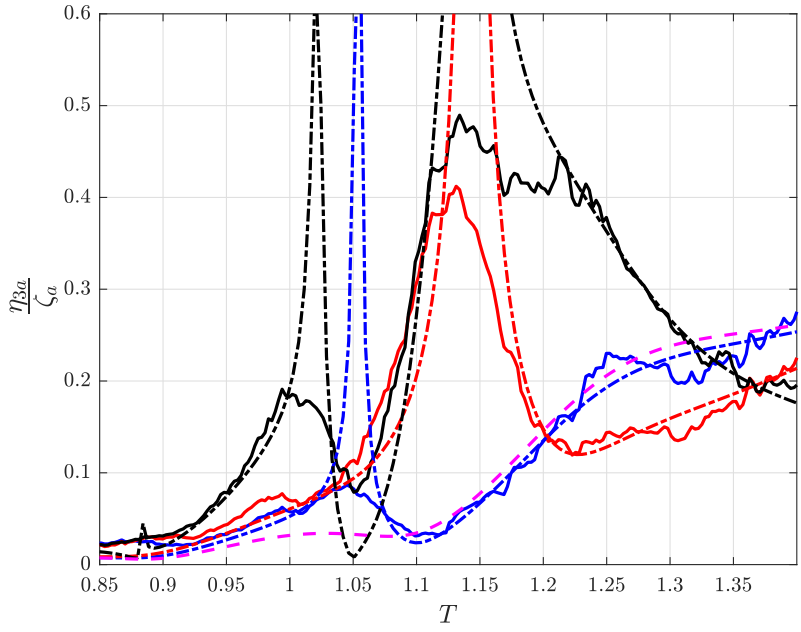

(a) Head sea.

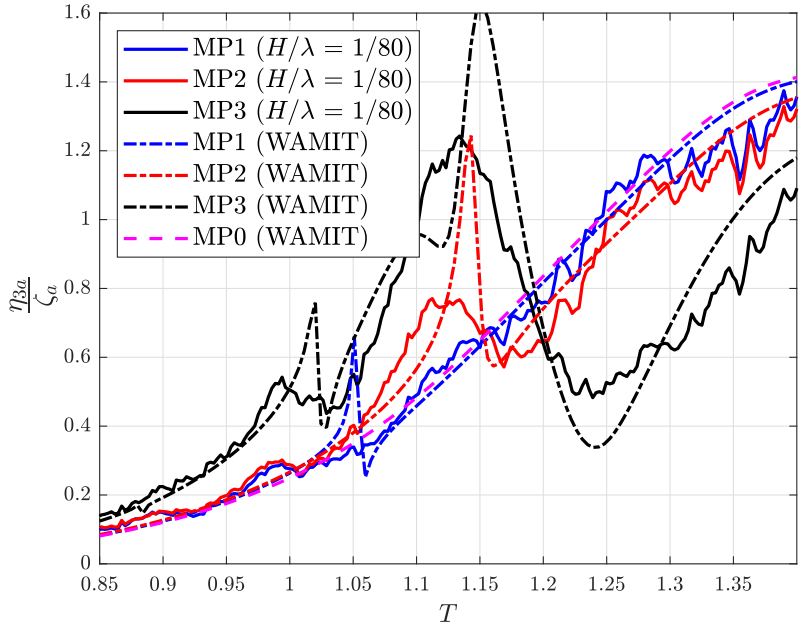

(b) Beam sea.

Figure 9.24: Heave RAOs from the irregular wave tests with $H/\lambda = 1/80$ in head and beam sea for MP1 (V_{MP}/V_S = 0.015), MP2 (V_{MP}/V_S = 0.064) and MP3 (V_{MP}/V_S = 0.427). WAMIT results are presented as dashed lines. The coupling between the heave and moonpool responses is clear for MP2 and MP3, while it is negligible for MP1.

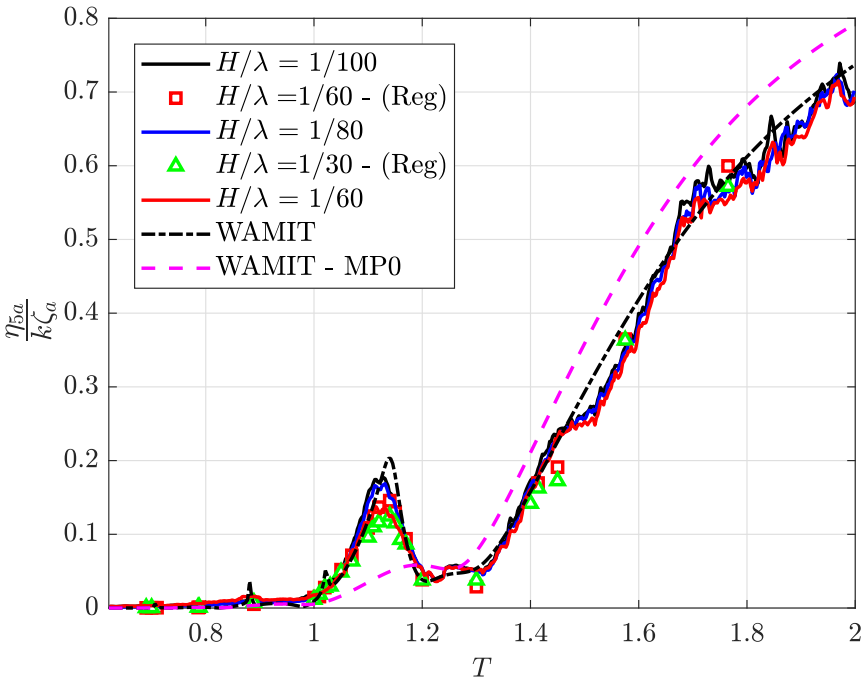

Figure 9.25: Pitch RAOs in head and beam sea for MP3 (V_{MP}/V_S = 0.427). Results for MP0 (ship without moonpool) are presented as pink dashed lines.

moonpool responses. For MP3, the surge and sway motions are strongly coupled with the moonpool responses. This is illustrated in Figure 9.26. In the vicinity of the piston and first sloshing modes, the surge RAOs from the model tests with $H/\lambda = 1/60$ are approximately six times larger than for a similar vessel without moonpool. The sway RAOs at the first transverse sloshing mode in beam sea is approximately five times larger than for MP0 in a narrow wave period range. This is, as mentioned earlier, important to consider with respect to the operability of the vessel. In the wave period range $1.2 \text{ s} < T < 1.6$ s, WAMIT under-estimates the sway responses in beam sea due to roll. We therefore briefly investigate roll in the following section.

Assuming that such a large moonpool is built in reality, it could be imagined it would be with a purpose of lowering relatively large marine structures into the sea through the moonpool. In addition to the significant vertical loads that the object will be exposed to, large horizontal loads on the structure due to sloshing motion in the moonpool must also be considered. For instance, in a scenario where the first sloshing mode is excited, the largest vertical water motion and acceleration of the moonpool will be close to the moonpool ends, while the largest horizontal motion and acceleration will be close to the center of the moonpool. This means that the large moonpool motion can induce large vertical and/or horizontal loads on the structure depending on where the structure is lowered through. For small-volume bodies the loads may to a first approximation be estimated by the Morison model with the (undisturbed) coupled moonpool response as ambient flow. For larger objects, the hydrodynamic interaction with the vessel (and moonpool) must be considered, possibly with both effects due to flow separation and on the resonance periods of the coupled moonpool and vessel responses. Kristiansen et al. (2015) investigated a box-shaped cylinder in the moonpool in forced heave with PVC3D. Their PVC3D simulations showed good agreement with the model tests, which suggests that PVC3D could be used to investigate the loads on an object in the moonpool if one is able to successfully implement a freely floating body in incident waves in PVC3D.

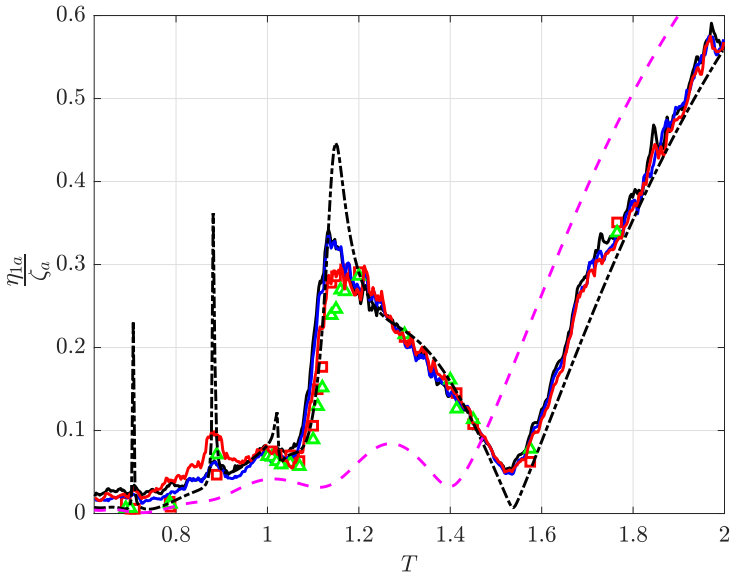

(a) Surge response - Head sea

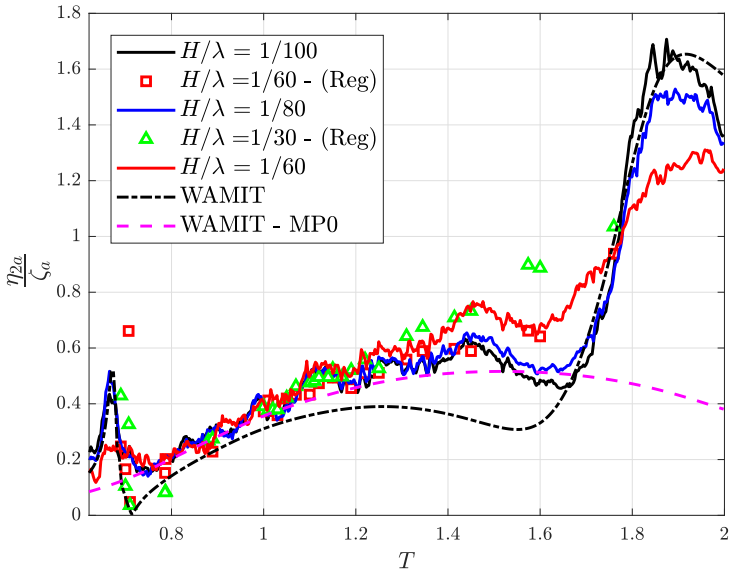

(b) Sway response - Beam sea

Figure 9.26: Surge and sway RAOs in head and beam sea for MP3 (V_{MP}/V_S = 0.427). Results for MP0 (ship without moonpool) are presented as pink dashed lines.

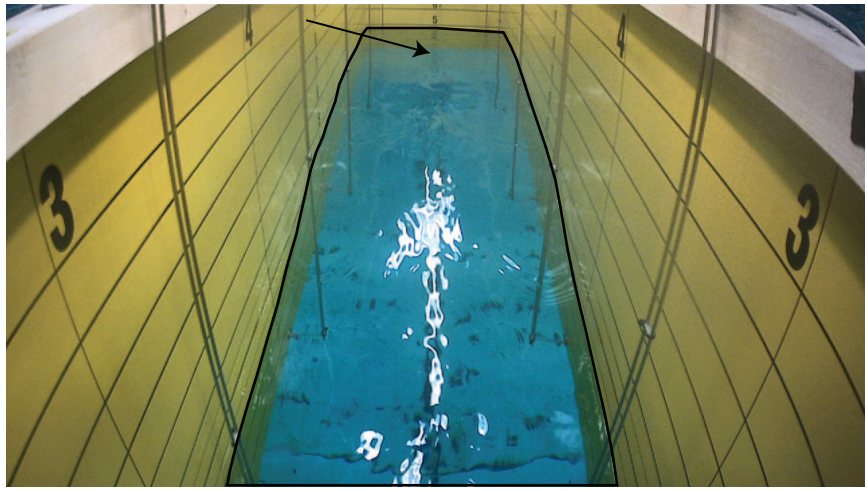

Figure 9.27: Snapshot from video recordings of the piston (and first longitudinal sloshing) mode response for MP3 in head sea in regular waves at $T = 1.15$ s. $H/\lambda = 1/60$. The arrow points at the maximum moonpool response.

9.6 Roll responses for MP1, MP2 and MP3

We discuss the roll responses for MP1, MP2 and MP3 in beam sea in the following. Amplitude-dependent roll RAOs for MP1, MP2 and MP3 are presented in Figure 9.28. The results for a similar vessel without moonpool, MP0, are also presented. The damping coefficient in (6.13) is tuned such that the peak from the roll RAOs from WAMIT are in fair agreement with the peak in the experiments with wave steepness $H/\lambda = 1/100$ for MP3. By tuned, we mean that a damping coefficient approximately 10 % lower than predicted by Ikeda et al. (1993) is used in the present simulations, since the present ship models are somewhat unconventional. Note that roll resonance period range is not tested in the model tests for MP1 and MP2. Although the peaks in the roll RAOs for MP3 are in fair agreement, the shape of the RAOs are different, especially in the proximity of roll resonance. We do not fully understand the reason for this discrepancy. The fact that the roll responses are over-predicted by WAMIT outside roll resonance results in that the sway responses are incorrectly predicted, as illustrated in Figures 9.17(b) and 9.26(b). The roll resonance period for MP1-3 vary due to that the hydrostatic restoring and added mass coefficients, in addition to the moment of inertia in roll, vary for the three configurations. The fact that the roll resonance period decreases with increasing moonpool size suggests that the inertia terms decrease more than the hydrostatic restoring coefficient with increasing moonpool sizes.

The roll RAOs suggest that there is negligible coupling between the moonpool and roll responses, as expected when transverse sloshing does not occur, since the models are bilaterally symmetric. Although the first transverse sloshing mode for MP2 and MP3 is excited in beam sea, cf. §9.4 and §9.5, the roll responses are almost unaffected also by the transverse sloshing mode responses.

Large roll responses may limit marine operations with cranes, since large roll responses may yield large loads on the crane hook. Moreover, large roll motions may cause discomfort for the on board personnel. In general, ships typically operate with a heading angle of approximately 15 degrees angle relative to the incident waves. By that, one avoids large roll motions, and achieves a partially sheltered region downstream of the vessel, where incident waves with wave periods lower than about 5 s, in full scale, are diffracted (Peter Sandvik, personal conversations). Many resonant moonpool modes are excited for MP3 in a relevant wave period range, in particular in head sea. We believe that the vessel and moonpool responses will be fairly similar in head sea and 15 degree heading angles. Given that the purpose of the operation is to lower an object through the moonpool, one could investigate whether operating in beam sea could be a better option than in head sea (or 15 degrees heading) for MP3.

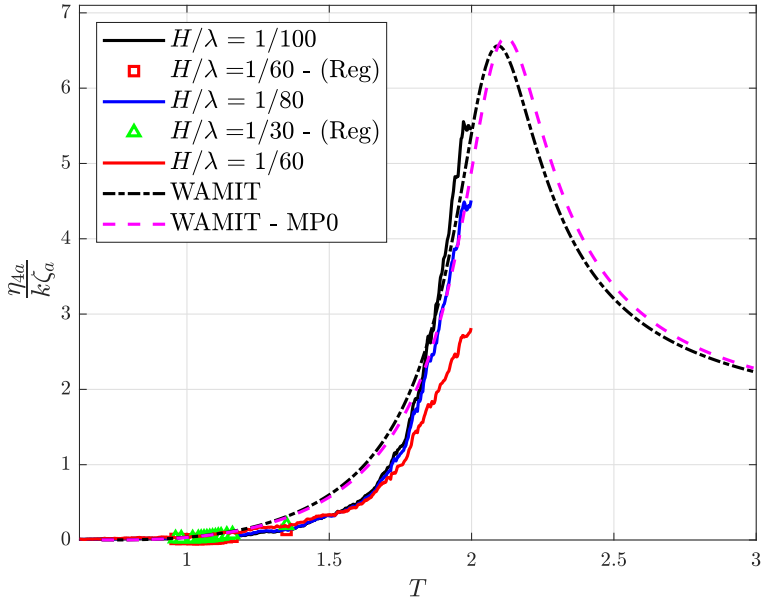
$H/\lambda = 1/100$
H/λ =1/60 - (Reg)
$H/\lambda = 1/80$
H/λ =1/30 - (Reg)
$H/\lambda = 1/60$
WAMIT
WAMIT - MP0
$\frac{\eta_{4a}}{k\zeta_a}$
T

(a) MP1

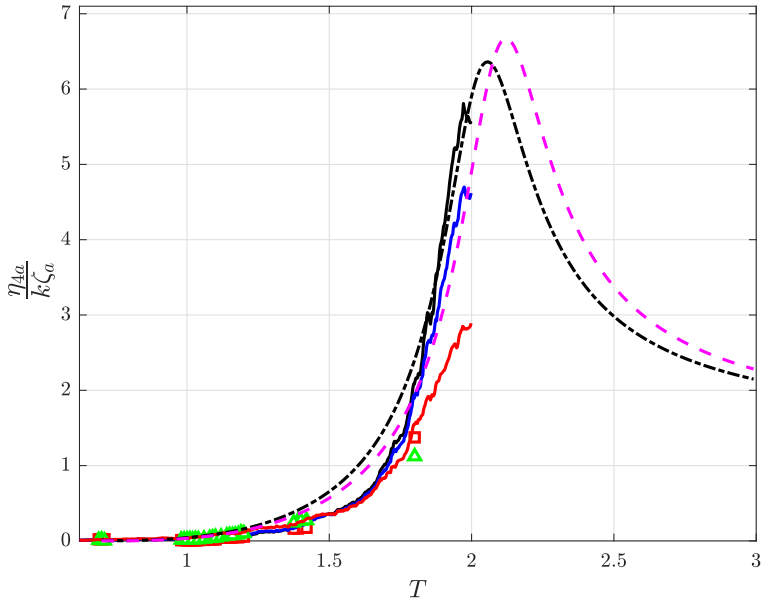
$\frac{\eta_{4a}}{k\zeta_a}$
T

(b) MP2

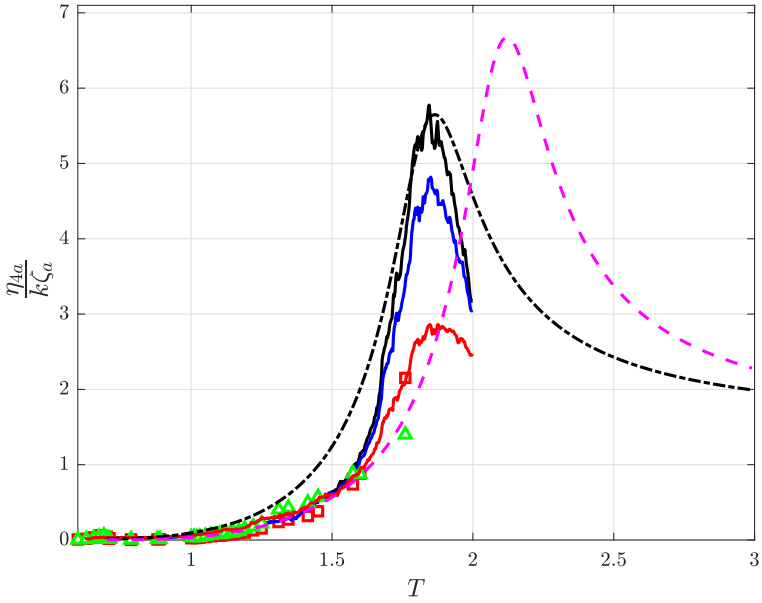

(c) MP3

Figure 9.28: Amplitude-dependent roll RAOs from the model tests in the Ocean Basin and WAMIT simulations in beam sea.

9.7 Piston mode response shapes

The piston mode response shapes for MP1, MP2 and MP3 are discussed in the following. We distinguish between the terms *mode shapes* and mode *response shapes*. When discussing mode shapes, the term is associated with those found by solving the spectral problem, such as by Molin (2001). The natural modes and corresponding mode shapes are then independent of the excitation. The mode response shape, on the other hand, is a snapshot of the mode response at a given time instant. We discuss the piston mode response shapes in the radiation and diffraction problems. This is done since it is of relevance with respect to ship motions and loads on a structure being lowered through the moonpool, as well as with respect to future development of rational methods such as the present VBEM. We present the first harmonic steady-state moonpool response shapes at a time instant where the maximum moonpool response occurs, both from WAMIT simulations and model tests. The first harmonic steady-state maximum moonpool response at a point in the moonpool oscillates as $\zeta_m = \zeta_{mp,\max}\sin(\omega t + \epsilon_m)$, where $\zeta_{mp,\max}$ and ϵ_m are the first harmonic maximum piston mode response amplitude and phase angle of the response relative to the incident wave, respectively. For instance in forced heave, the maximum piston mode responses occur at the center of the moonpool. We present the piston mode response shapes at $t = (\pi/2 - \epsilon_m)/\omega$. WAMIT simulations with a fixed body in incident waves, in forced heave and in freely floating conditions are carried out with the purpose of discussing the difference in the piston mode response shapes in the different circumstances.

Figure 9.29 presents the piston mode response shapes in forced heave and fixed ship in incident head sea wave conditions as predicted by WAMIT. The difference in the piston mode response shape in fixed and forced heave conditions is negligible for MP1 and MP2. However, a significant difference is observed in the piston mode response shape for MP3. In fixed conditions, the piston mode response shape is significantly different relative to the response shape in forced heave due to the variation in the wave excitation over the moonpool length due to the incident wave. This effect is negligible for MP1 and MP2, since the moonpool length, L_m, is small compared to the wavelength of the incident wave, λ. The L_m/λ-ratio at the piston mode is approximately unity for MP3 ($L_m/\lambda = 0.97$), which implies that the piston mode response shape is affected by the non-uniform excitation along the moonpool entrance. As a consequence, the piston mode response shape resembles a wave.

Figure 9.30 presents the piston mode response shapes in freely floating conditions as predicted by WAMIT and obtained in the experiments. The piston mode response shapes for MP1 and MP2 are nearly uniform, as in forced heave and fixed

conditions. However, for MP3, the piston mode response shape is considerably different in freely floating conditions in head sea waves relative to that in forced heave in calm water, as suggested by both the experiments and the numerical simulations (cf. Figure 9.31). It also slightly differs from that for a fixed vessel in waves. Traditionally, we use the term piston mode to refer to the zeroth mode in a moonpool. The term indicates that the moonpool oscillates nearly uniformly in the vertical direction, and that the water motions in the horizontal plane are small. The present results demonstrate that this is a good approximation for traditional moonpools, but is not so for a ship with a large moonpool in freely floating conditions with incident head sea waves.

The fact that the piston mode response shape is non-uniform has implications; the piston mode affects the ship motions, in particular the surge response, in addition to the heave response, as discussed in §9.5. The non-uniform piston mode response shape also affects the loads on the object lowered through the moonpool. For traditional moonpool, one is primarily concerned about the vertical loads induced by the piston mode responses. For large moonpools, the horizontal fluid motion must also be considered for ships with large moonpools operating in waves.

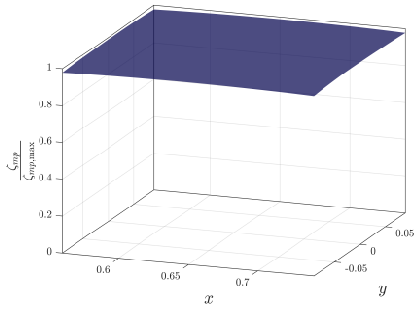

(a) MP1 - T = 1.07 s (forced heave)

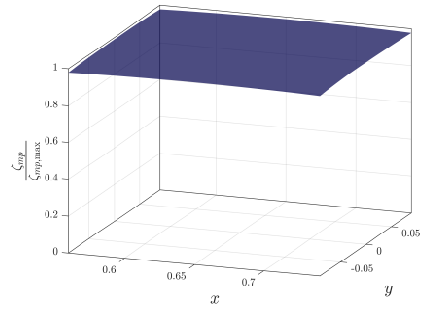

(b) MP1 - T = 1.07 s (fixed)

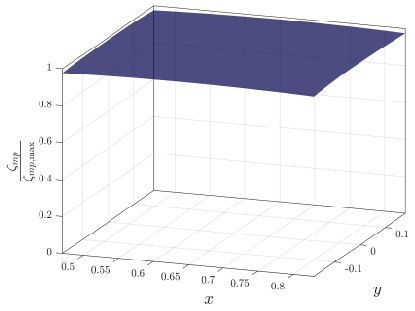

(c) MP2 - T = 1.19 s (forced heave)

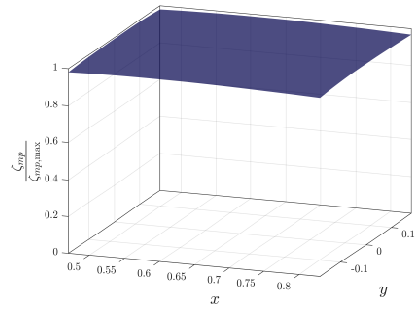

(d) MP2 - T = 1.19 s (fixed)

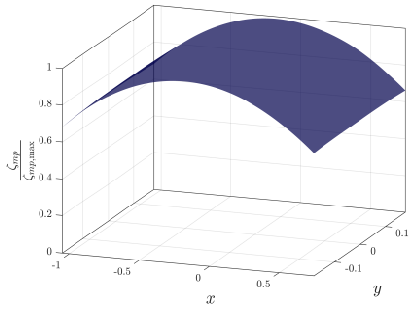

(e) MP3 - T = 1.30 s (forced heave)

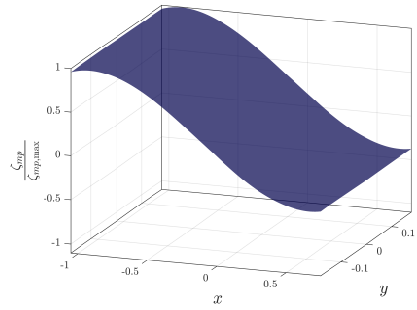

(f) MP3 - T = 1.30 s (fixed)

Figure 9.29: Piston mode response shapes as predicted by WAMIT in forced heave conditions and fixed ship with incident head sea waves, where the response shapes are established using 1000 evenly distributed points on the moonpool free-surface. The response shapes are made non-dimensional with respect to the maximum response in the moonpool, $\zeta_{mp,\max}$.

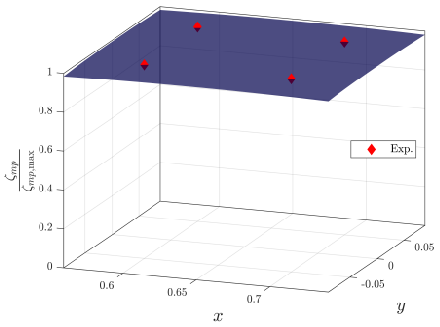

(a) MP1 head sea - $T = 1.06$ s

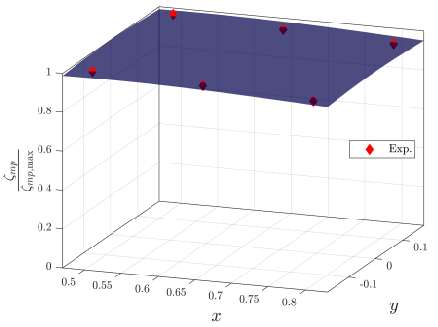

(b) MP2 head sea - $T = 1.15$ s

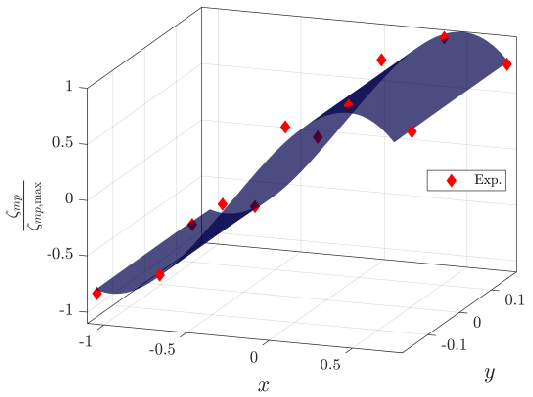

(c) MP3 head sea - $T = 1.17$ s

Figure 9.30: Piston mode response shapes in freely floating conditions from WAMIT and experiments (Exp.). The response shapes from WAMIT are established using 1000 evenly distributed points on the moonpool free-surface. The response shapes are made non-dimensional with respect to the maximum response in the moonpool, $\zeta_{mp,\max}$, in freely floating conditions. The experimental response shapes are from the regular wave tests with H/λ = 1/30, where we present the first harmonic response amplitudes.

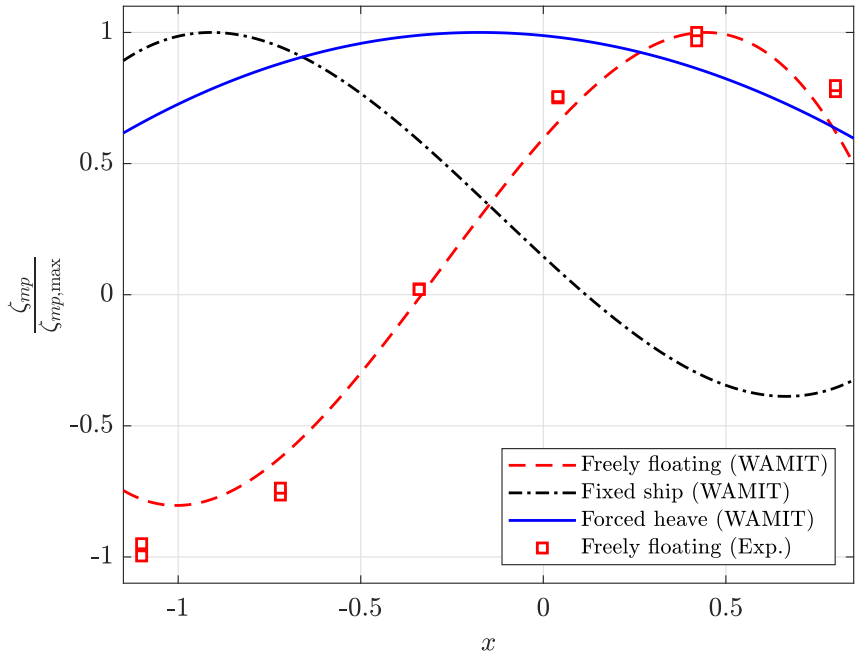

Figure 9.31: Piston mode response shapes as predicted by WAMIT in forced heave, fixed ship in incident waves and freely floating conditions. The response shapes are for MP3 in head seas at $y = 0$ m, where the response shapes from WAMIT are established using 1000 evenly distributed points on the moonpool free-surface. The experimental response shapes are from the regular wave tests with H/λ = 1/30, where we present the first harmonic response amplitudes. The response shapes are made non-dimensional with respect to the maximum response in the moonpool, $\zeta_{\max}$. Experimental and numerical results in freely floating conditions at $T = 1.17$ s are presented. In fixed ship and forced heave, the wave and forced heave periods are both $T = 1.30$ s.

9.8 Higher harmonic moonpool responses

We pointed out nonlinearities in the moonpool RAOs from the irregular wave tests for MP2 and MP3 in certain wave period ranges in §9.4 and §9.5, where the moonpool RAOs increase with increasing wave steepness. This is due to that higher modes are excited nonlinearly. The time-series of the moonpool responses in selected regular wave tests, presented in Figure 9.32, illustrate that higher harmonic responses may become significant. A 2ω component is gradually increasing in amplitude after an initial growth of the basic frequency ω. The activation of a higher mode is called secondary resonance (Faltinsen and Timokha 2009, p. 128), and is a nonlinear effect where the primary mode excites a higher mode. This means that energy is transferred from the primary mode of oscillation, to the higher modes.

To discuss this, we present the second and third harmonic moonpool RAOs. The nth harmonic moonpool response is made non-dimensional with respect to $k^{n-1}\zeta_a^n$. We do so since we observe that the second harmonic moonpool responses are, in general, of $\mathcal{O}((k\zeta_a)^2)$. The third harmonic moonpool responses are larger than $\mathcal{O}((k\zeta_a)^3)$, but they contribute, in general, significantly less to the total moonpool response. The higher harmonic vessel responses are negligible for all practical purposes, and are not presented herein. Selected time-series of the first and second harmonic moonpool responses are presented in Appendix C.3.2, where we see that the second harmonic moonpool responses are significant, similar to that presented in Figure 9.32.

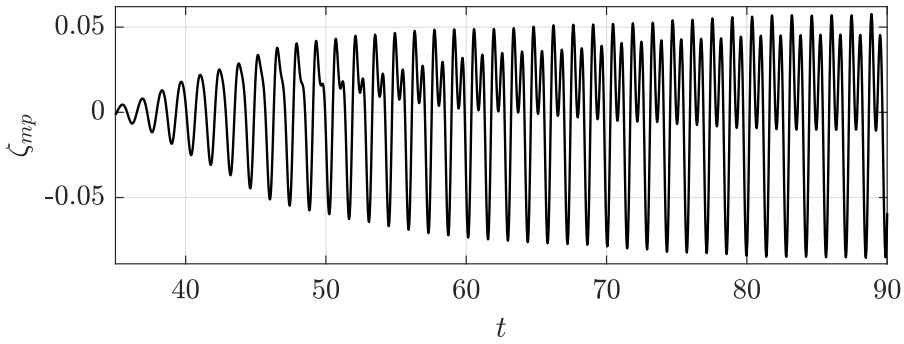

(a) MP2 - $T = 1.42$ s and $H/\lambda = 1/30$.

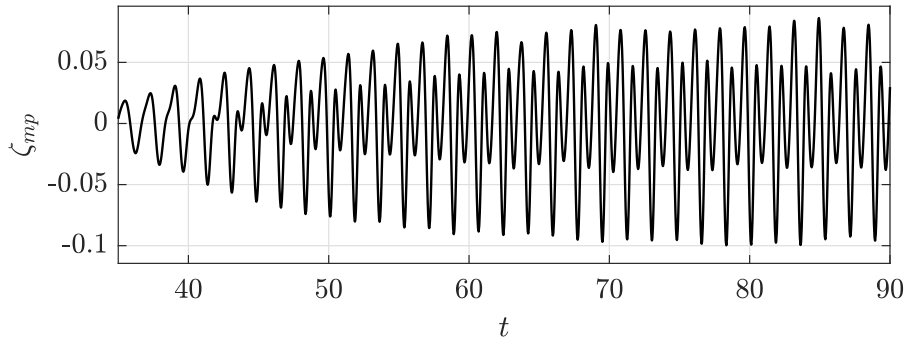

(b) MP3 - $T = 1.78$ s and $H/\lambda = 1/30$.

Figure 9.32: Selected time-series of the moonpool response measured at WP1 from the regular wave tests in head sea. The measurements suggest that higher harmonic (mostly 2ω) moonpool responses are significant.

The first harmonic moonpool responses at the first longitudinal sloshing mode in head sea for MP2 were moderate (cf. $T = 0.71$ s Figure 9.14(a)). By contrast, the RAOs from the irregular wave tests were significant. Second harmonic moonpool RAOs for MP2 in head sea are presented in Figure 9.33, where the linear RAOs obtained from the irregular wave tests presented earlier suggest that the first longitudinal sloshing mode is excited in waves with wave period $T = 1.42$ s due to secondary resonance. This is illustrated in Figure 9.34, where we present snapshots from video recordings from the model tests in regular waves with $T = 1.42$ s. The second harmonic moonpool responses at $T = 1.42$ s are significant, as illustrated at ⓑ in Figure 9.33. This explains the nonlinear behavior of the RAOs in the irregular wave tests in Figure 9.14(a). Energy is transferred from the primary mode to higher modes due to secondary resonance, such that the RAOs increase with increasing wave steepness.

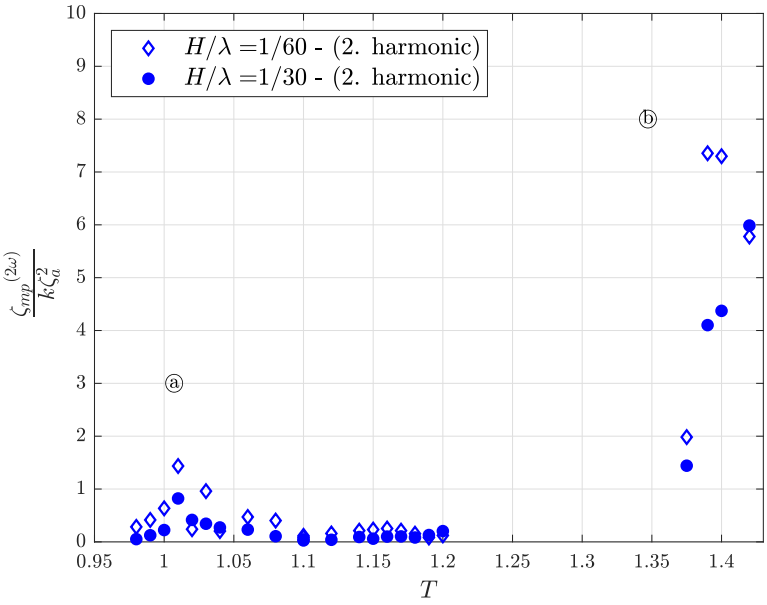

Figure 9.33: Second harmonic moonpool responses at WP1 for MP2 in head sea regular waves. ⓐ: Second longitudinal sloshing mode. ⓑ: First longitudinal sloshing mode (three different wave periods are tested).

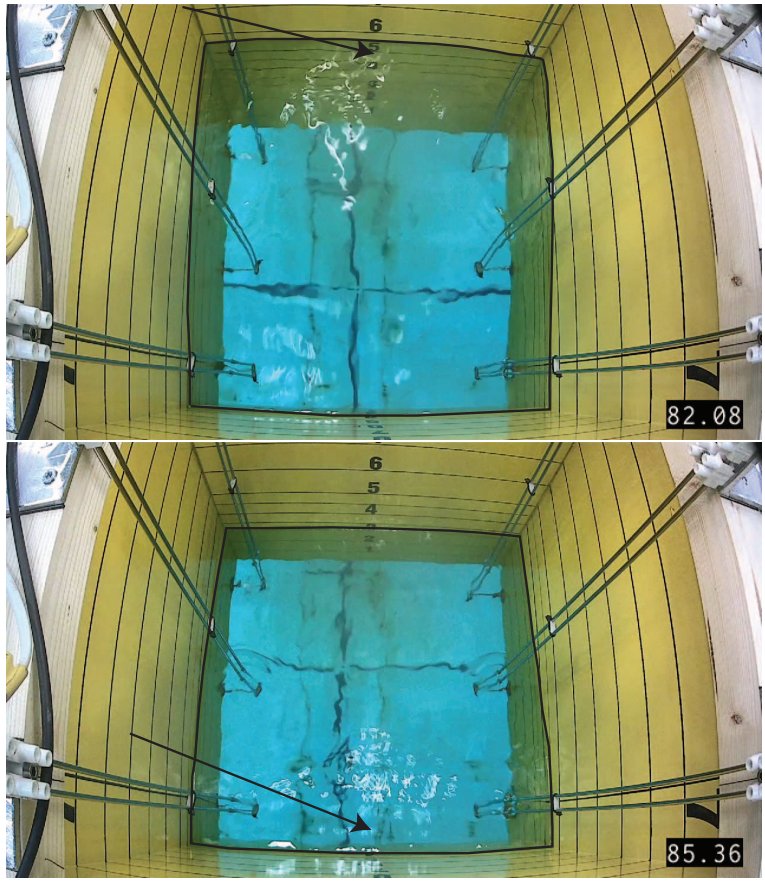

Figure 9.34: Two snapshots from video recordings of the moonpool response for MP2 in head sea in regular waves at $T = 1.4$ s. Dominant excitation of the first longitudinal sloshing mode is observed due to energy transfer from the primary mode to higher modes, in particular the second harmonic. $H/\lambda = 1/60$. The arrow points to the maximum moonpool response.

The second harmonic moonpool RAOs for MP3 in head sea are presented in Figure 9.35(a). The second harmonic moonpool RAOs suggest that higher modes are excited due to secondary resonance, similarly as for MP2. For instance, the second longitudinal sloshing mode is excited at ⓔ ($T = 2.05$ s) due to secondary resonance, which is approximately twice the second longitudinal sloshing mode period ($T = 1.04$ s).

The third longitudinal sloshing mode period is $T = 0.89$ s. At the basic wave period $T = 1.78$ s, the third longitudinal sloshing mode responses due to secondary resonance are significant, as illustrated at ⓓ in Figure 9.35(a). Snapshots

from video recordings, illustrating higher modes at $T = 1.78$ s, are presented in Figure 9.36.

The second harmonic moonpool RAOs for MP3 in beam sea are presented in Figure 9.35(b), where the sixth longitudinal sloshing mode (ⓑ), first transverse sloshing mode (ⓒ) and second longitudinal sloshing mode (ⓓ) are activated due to secondary resonance. As in head sea, the activation of higher modes is significant in beam sea for MP3. For instance, at ⓑ in Figure 9.35(b), the excitation of the sixth longitudinal sloshing mode ($T = 0.66$ s) is significant at the basic wave period $T = 1.34$ s. The first harmonic sixth longitudinal sloshing mode responses at wave period $T = 0.66$ s in regular waves, as presented at ⓐ in Figure 9.21(b), were also significant. The moonpool RAOs from the irregular wave tests at $T = 0.66$ s, however, were 50 % lower than the first harmonic responses. Until now, we have discussed that the activation of higher modes yield larger moonpool RAOs in irregular waves. In beam sea, at this particular wave period (i.e. $T = 0.66$ s), we see that secondary resonance yields smaller moonpool RAOs from the irregular wave tests at $T = 0.66$ s. To explain this, we imagine the following; the first harmonic sixth longitudinal sloshing mode in regular waves with basic wave period $T_1 = 0.66$ s oscillates as $\zeta_{mp}^{(1)} = A_1 \sin(\omega t)$, where A_1 is the amplitude of the first harmonic moonpool response. Now, imagine that the second harmonic response at the basic wave period $T_2 = 2T_1$ oscillates as $\zeta_{mp}^{(2)} = A_2 \sin(\omega t + \epsilon)$, where A_2 is the second harmonic moonpool response amplitude, and ϵ is the phase angle of $\zeta_{mp}^{(2)}$ relative $\zeta_{mp}^{(1)}$. In irregular waves, we have a combination of the two responses, i.e. $\zeta_{mp} = \zeta_{mp}^{(1)} + \zeta_{mp}^{(2)}$. Depending on the phase angle, ϵ, the activation of the higher modes may yield an increase or decrease of the moonpool responses. For MP3 in beam sea, both the first harmonic moonpool responses at wave period $T = 0.66$ s, and the second harmonic moonpool responses at wave period $T = 1.34$ s, were significant. Hence, the total response, ζ_{mp}, was smaller in irregular waves, due to a "favourable" phase angle, ϵ. For MP2 and MP3 in head sea, this was, in general, not the case. For instance, for MP2 in head sea, the first harmonic moonpool response at wave period $T = 0.71$ s were small, as discussed earlier. The second harmonic moonpool responses at wave period $T = 1.42$ s were, however, significant. Hence, the moonpool responses in irregular waves for MP2 at $T = 0.71$ s were dominated by the energy transferred from $T = 1.42$ s, and the moonpool RAOs from the irregular wave tests increase with increasing wave steepness.

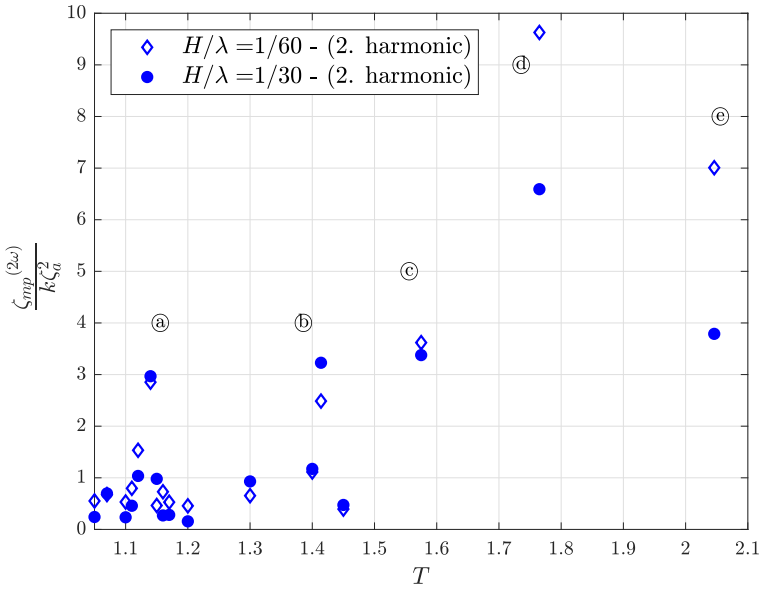

(a) Head sea. ⓐ: Seventh longitudinal sloshing mode. ⓑ: Fifth longitudinal sloshing mode. ⓒ: Fourth longitudinal sloshing mode. ⓓ: Third longitudinal sloshing mode. ⓔ: Second longitudinal sloshing mode.

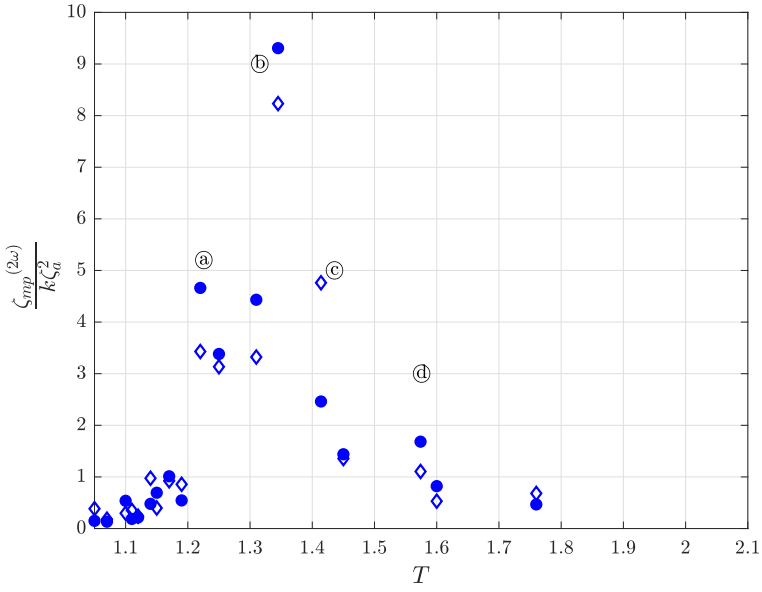

(b) Beam sea. ⓐ: Second transverse sloshing mode. ⓑ: Sixth longitudinal sloshing mode. ⓒ: First transverse sloshing mode. ⓓ: Second longitudinal sloshing mode.

Figure 9.35: Same as Figure 9.33, but for MP3.

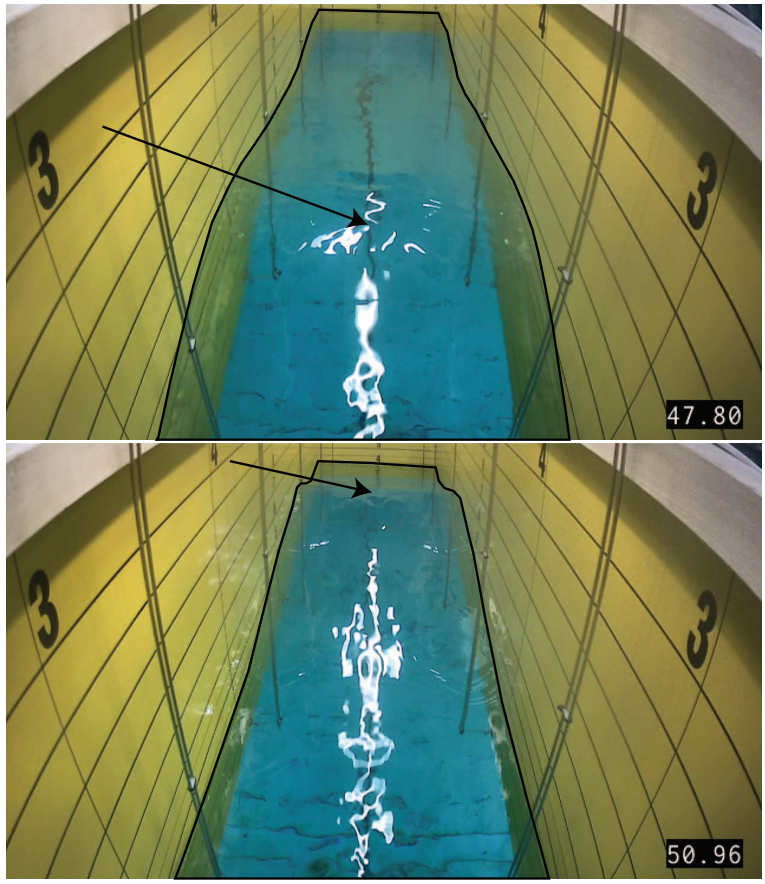

Figure 9.36: Two snapshots from video recordings of the moonpool response for MP3 in head sea in regular waves at $T = 1.78$ s. Dominant excitation of the third longitudinal sloshing mode is observed. The arrow points to the maximum moonpool response.

The third harmonic moonpool RAOs for MP3 in head sea are presented in Figure 9.37. Non-negligible third harmonic moonpool responses are observed at ⓐ and ⓑ, where the seventh and fifth longitudinal sloshing modes, respectively, are activated due to secondary resonance. For MP2, the third harmonic moonpool responses are small in the tested range of wave periods.

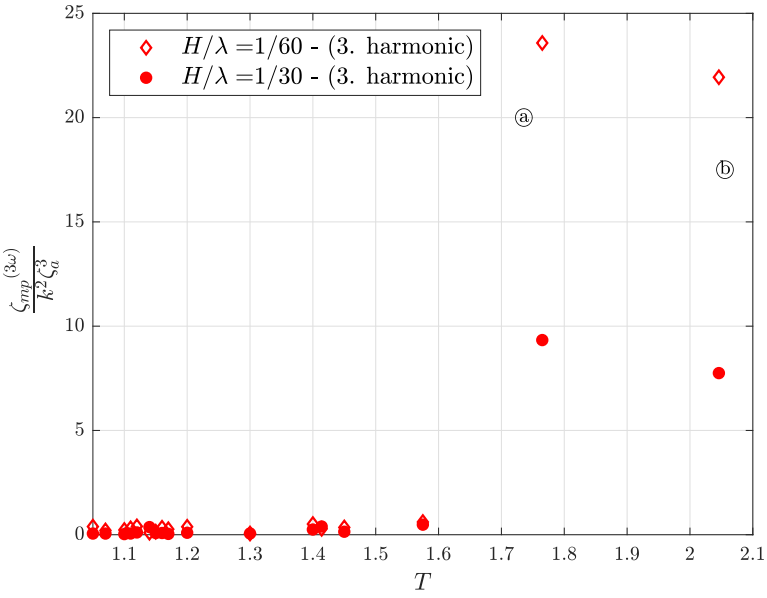

Figure 9.37: Third harmonic moonpool responses at WP1 for MP3 in head sea regular waves. ⓐ: Seventh longitudinal sloshing mode. ⓑ: Fifth longitudinal sloshing mode.

The higher harmonic moonpool RAOs suggest that damping due to flow separation is a main candidate to the amplitude-dependence, also for the higher harmonic responses. For instance, at ⓐ and ⓑ in Figure 9.37 there are clear amplitude-dependent third harmonic moonpool responses, where the third harmonic moonpool RAOs with wave steepness $H/\lambda = 1/30$ are approximately 65% - 70% lower than with wave steepness $H/\lambda = 1/60$. Similarly, the second harmonic moonpool responses at ⓓ and ⓔ in Figure 9.35(a) suggest that damping due to flow separation is dominant due to the amplitude-dependent second harmonic moonpool responses. This is also consistent with the PVC3D simulations presented in §9.2, where we discussed that damping due to flow separation is dominant for the sloshing modes for MP3 at least up to the sixth longitudinal sloshing mode. Similarly, the amplitude-dependence at ⓑ in Figure 9.33 indicates dominant damping due to flow separation at the second harmonic moonpool responses for MP2. This is also consistent with the PVC3D simulations in forced surge for MP2, cf. §9.2, where WAMIT clearly over-predicted the moonpool responses, and PVC3D simulations suggested that damping due to flow separation was important. Thus, a nonlinear potential flow solver is likely to over-estimate the higher harmonic moonpool responses considerably, and the flow separation at the moonpool entrance must be accounted for, for instance by a Navier–Stokes solver with nonlinear free-surface conditions to predict the moonpool responses accurately in this wave period range.

Ships operate in irregular waves in reality. The present irregular wave tests suggest that it is important to consider secondary resonance for MP2 and MP3. We observe that secondary resonance is increasingly important with increasing moonpool sizes. The present model tests are carried out in a wave period range that is relevant for a ship operating in the North Sea. A model scale of 1:34.5 is imagined (cf. Table 5.1). The first harmonic moonpool response for MP2 at $T = 0.71$ s from the regular wave tests in head sea is moderate, as mentioned earlier. This corresponds to a wave period of $T \approx 4$ s in full scale. In a realistic sea environment in the North Sea, the wave spectra will not contain significant energy in this wave period range. The second harmonic moonpool responses at twice the wave period, which corresponds to $T \approx 8$ s, the sea environment will contain significant wave energy in typical operational conditions. The moonpool responses due to secondary resonance are considerable in this wave period range. Therefore, secondary resonance is important to consider for MP2 and MP3. MP3 can be considered a large moonpool, and it is unknown to the author whether such a moonpool will be built in reality. However, we observe dominant second harmonic moonpool responses even for MP2. MP2 has moonpool dimensions 13.8 m $\times$ 13.8 m in full scale, which is relevant with respect to existing ships. Sun et al. (2010) and Sun et al. (2015) also observed excitation of higher modes in their set-up with two closely spaced barges, where they showed, by using first and second order potential flow theory, that energy is transferred from the primary mode to higher modes.

The present model tests were carried out with fairly linear waves (the maximum wave steepness was $H/\lambda = 1/30$). The incident waves become more nonlinear with increasing wave steepness. The possibility of exciting higher moonpool modes due to steep (nonlinear) waves is unknown, and a conclusion regarding nonlinear waves' influence on secondary resonance cannot be drawn based on the present findings. However, it is important to understand the main excitation mechanisms of the moonpool responses, which are; wave excitation, ship motions and the moonpool itself. The two former are widely discussed throught the thesis. The latter is when secondary resonance is excited, which is a consequence of that energy is transferred from the primary mode to higher modes. Since the wave velocity potential decays as $\exp(kz)$ vertically in infinite water depth, the velocity potential for the higher order components in nonlinear waves decay even faster (for instance, the second order component decays as $\exp(2kz)$). Hence, the wave excitation is not likely to induce significant higher harmonic moonpool responses even with nonlinear waves (note that these arguments are not based on any scientific findings, and that nonlinear waves might "trigger" secondary resonance). Assuming that the body motions are mainly linear, the body motions are also not very likely to excite any dominant higher harmonic moonpool responses. Based on this reasoning, it is believed that secondary resonance is the main and most import-

ant driver of the higher harmonic moonpool responses. This would be similar to that discussed for closed sloshing tanks by Faltinsen and Timokha (2009, p. 128), where the only excitation was pure (linear) sinusoidal surge motion, and results in amplification of higher modes due to secondary resonance.

9.9 Responses in irregular waves with the Pierson-Moskowitz spectra

We finally present and discuss model tests for MP3 in irregular waves with the Pierson-Moskowitz spectra. Earlier irregular wave tests with the PNWW spectra were discussed. The presently tested H_s and T_p values (cf. Table 5.5) are relevant in the North Sea, as shown by Faltinsen (1993, p. 30). In full scale, the spectra correspond to approximately $H_s = 2.4$ m, 3.5 m, 4.5 m, with corresponding T_p values of $T_p = 6.0$ s, 8.0 s and 10.0 s. The model tests with the PM spectra further support that nonlinear effects due to secondary resonance are indeed important to consider for ships with relatively large moonpools operating in irregular waves in freely floating conditions, similarly as for the more academic PNWW. The heave and pitch RAOs are presented in Figures 9.38(c)-9.38(e). The results are consistent with those from the irregular PNWW tests, as one may expect; in particular, dominant damping due to flow separation and secondary resonance are two main evident effects that cannot be neglected in a real stochastic sea.

Moonpool, heave and pitch RAOs with three different sea states using the Pierson Moskowitz spectra for MP3 are presented in Figure 9.38. The moonpool RAOs in head sea show the same trends as in Figure 9.21(a), where we presented the amplitude-dependent moonpool RAOs in head sea from the irregular wave tests using the PNWW spectra. At the piston and first sloshing modes, which almost coincide (cf. §9.5), the moonpool RAOs are somewhat smaller, since the PM spectra contain more energy in this wave period range than the PNWW spectra, and thus more (quadratic-type) damping.

The third and higher longitudinal sloshing modes responses in head sea are significant. The sloshing responses are most pronounced in the sea state with the most energy; $H_s = 0.13$ m and T_p = 1.7 s. If nonlinear effects were negligible, we expect that the sloshing mode RAOs with $T_p = 1.02$ s would yield similar moonpool RAOs as with $T_p = 1.7$ s, since the spectra contain almost the same amount of energy in the vicinity of the sloshing modes. However, due to secondary resonance, the moonpool RAOs in head seas at the third and higher longitudinal sloshing modes are larger with $T_p = 1.7$ s. Thus, as discussed in §9.8, the activation of higher modes due to secondary resonance must be considered for ships with large moonpools.

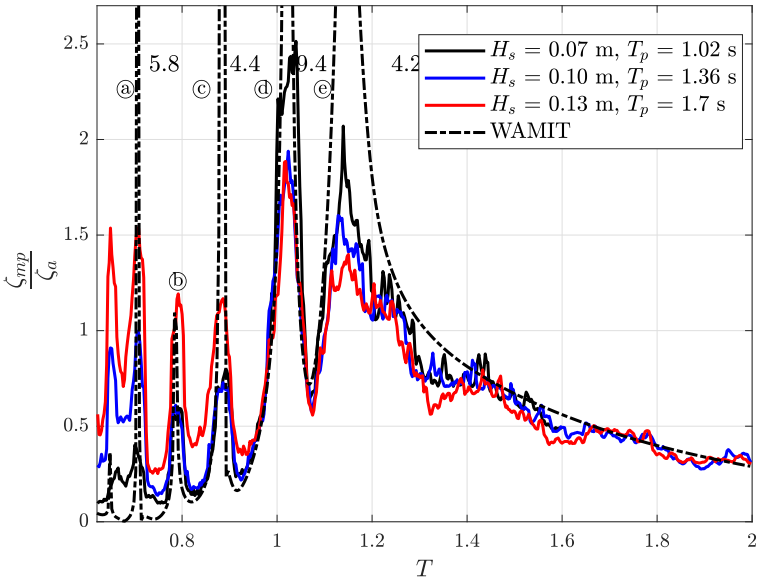

(a) Moonpool responses in head sea. ⓐ: Fifth longitudinal sloshing mode. ⓑ: Fourth longitudinal sloshing mode. ⓒ: Third longitudinal sloshing mode. ⓓ: Second longitudinal sloshing mode. ⓔ: First longitudinal sloshing and piston modes.

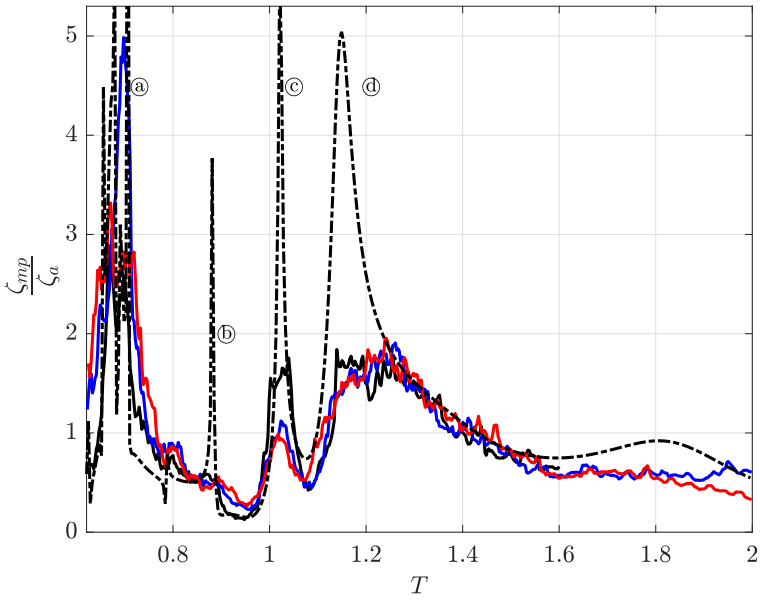

(b) Moonpool responses in beam sea. ⓐ: First transverse sloshing mode. ⓑ: Third longitudinal sloshing mode. ⓒ: Second longitudinal sloshing mode. ⓓ: Piston mode.

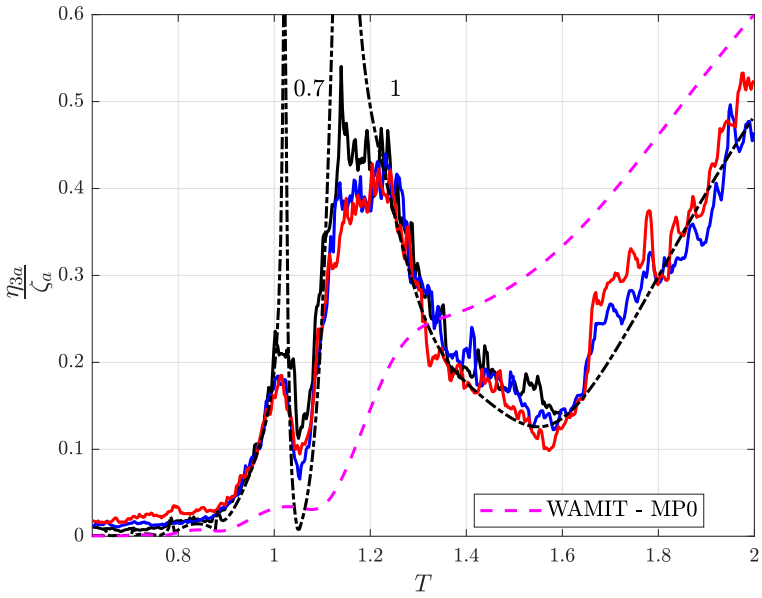

(c) Heave responses in head sea

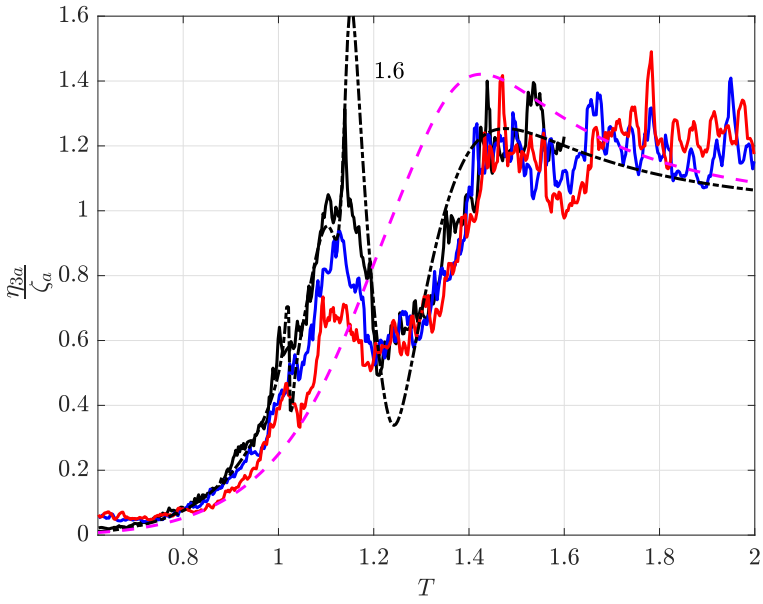

(d) Heave responses in beam sea

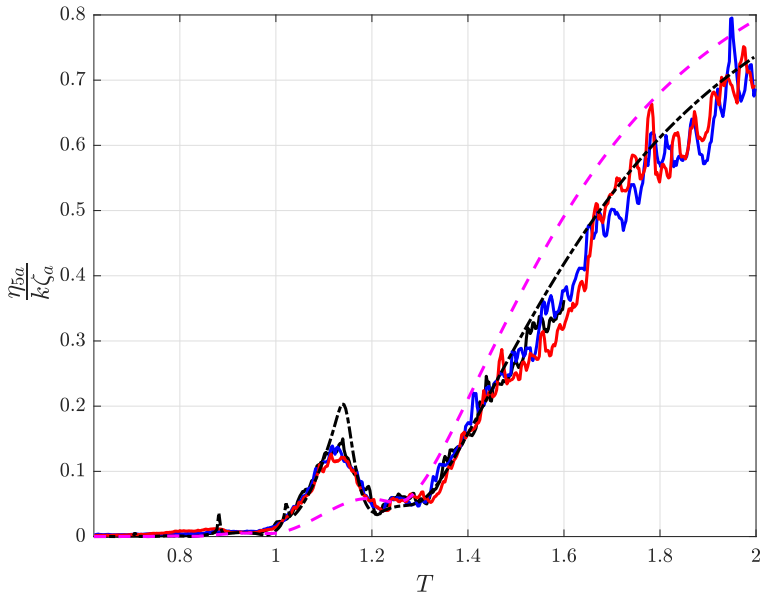

(e) Pitch responses in head sea

Figure 9.38: Moonpool, heave and pitch RAOs from the irregular wave tests with the PM spectra for MP3. Results for MP0 (ship without moonpool) are presented as pink dashed lines.

Chapter 10

Summary and further work

10.1 Summary of the present work

Four different rounds of model tests were carried out in the present work; first, forced heave experiments of a moonpool setup with recesses were conducted in a two-dimensional setting, referred to as 2DMR. Secondly, a 2DMR model was tested in freely floating conditions with incident regular waves. Thirdly, models with moonpools without recess were tested in a quasi three-dimensional setting, referred to as 3DQ, in both forced heave and in freely floating conditions with incident waves. All of the aforementioned model tests were carried out in a wave flume at NTNU. The investigations from these experimental studies, supported by numerical simulations, formed a basis for the final round of model tests; the model tests in the Ocean Basin at Sintef Ocean. The model tests in the Ocean Basin were carried out in a three-dimensional setting with a model that resembles a realistic ship with moonpool. Three different moonpool sizes were tested in order to investigate the importance of the V_{MP}/V_S-ratio, where V_{MP} and V_S are the moonpool and submerged ship volumes, respectively. The models tested in the Ocean Basin were referred to as MP1, MP2 and MP3, where V_{MP}/V_S = 0.015, 0.064 and 0.427, respectively. The model tests in the Ocean Basin were carried out with both regular and irregular waves, in both head and beam sea conditions, to investigate the mutual interaction between the moonpool and ship responses (referred to as hydrodynamic interaction in this thesis).

The model tests and numerical simulations with the 2DMR, 3DQ and MP1-3 models suggested that the V_{MP}/V_S-ratio is an important parameter with respect to the hydrodynamic interaction between ship and moonpool responses. The present model tests and numerical simulations indicated that for small V_{MP}/V_S-ratios, for

instance for MP1 ($V_{MP}/V_S = 0.015$), the hydrodynamic interaction between vessel and moonpool responses were negligible in practice. This implies that the ship motions for vessels with small moonpools can be estimated without accounting for the presence of the moonpool. For moderate and large V_{MP}/V_S-ratios, for instance for MP2 ($V_{MP}/V_S = 0.064$) and MP3 ($V_{MP}/V_S = 0.427$), the hydrodynamic interaction between ship and moonpool responses were significant. For MP2, the heave, pitch and moonpool responses were strongly coupled. For instance, the heave RAOs at the piston mode period were one order of magnitude larger than for a similar vessel without moonpool. For MP3, the hydrodynamic interaction between vessel and moonpool responses were even more pronounced than for MP2. In addition to heave and pitch, also surge and sway responses were affected by the resonant moonpool responses, and vice versa, due to the strong hydrodynamic interaction between ship and moonpool responses for MP3.

Both the vessel and moonpool RAOs were clearly amplitude-dependent. The main source of damping at the piston mode for clean moonpools is widely discussed in the literature. The main source of damping at the piston and first sloshing modes for moonpools with recess was investigated in forced heave of the 2DMR configurations. The main source of damping at the first sloshing mode was due to flow separation at the top corner of the recess floor. Similarly, dominant damping of the piston and sloshing modes due to flow separation at the moonpool entrance for MP1-3 was discussed with numerical simulations in forced heave and forced surge.

Several nonlinear free-surface effects were addressed in the present thesis work. For instance, for the 2DMR configurations, the moonpool RAOs at the first sloshing mode showed Duffing-type behavior. Although damping due to flow separation explained the majority of the differences between the BEM simulations and the model tests, the clear nonlinear effects suggested that nonlinear free-surface effects were important. The differences between the hybrid CFD simulations and the model tests were more pronounced for the case with the largest recess length, which indicated that the nonlinear free-surface effects become more pronounced with increasing recess lengths. Nonlinear free-surface effects were not captured by the present CFD simulations, since linearized free-surface conditions were applied.

Swirling was observed in the model tests in beam sea conditions for MP2. Although the model tests showed that the influence of swirling on the ship motions were small, swirling is important to consider with respect to the operability of the moonpool. The irregular wave tests showed that the moonpool RAOs increased with increasing wave steepness at certain resonant modes, due to secondary resonance. Significant excitation of higher modes was observed for both MP2 and

MP3. Secondary resonance occurred in a relevant wave period range for waves in the North Sea. Hence, secondary resonance is important to consider for moderate and large moonpool sizes. Dominant damping due to flow separation of the higher harmonic moonpool responses was illustrated, as for the first harmonic moonpool responses.

10.2 Recommendations for further work

Numerical simulations in freely floating conditions with nonlinear free-surface conditions are encouraged. The first and higher harmonic moonpool responses can then be compared against the present model tests in the Ocean Basin. With a potential flow solver, however, the damping due to flow separation will not be captured. Since there are important nonlinear free-surface effects occuring in the moderate and large moonpools, one should perform numerical simulations with a hybrid Navier–Stokes solver combined with nonlinear free-surface conditions. We propose two rational methods to numerically investigate both the effect of flow separation and nonlinear free-surface effects; (i) by combining a Navier–Stokes solver with nonlinear potential flow theory at the free-surface, or (ii) by combining a Navier–Stokes solver with a linear potential flow solver outside the moonpool (similar to the present CFD) and with VOF in the moonpool.

Model tests and numerical simulations where the location of the moonpool center is systematically changed is encouraged. One can then investigate whether there is an "optimal" location for the moonpool, where the hydrodynamic interaction between ship and moonpool responses is a driving guideline on what is optimal and not. Such a study has to model flow separation to get reliable conclusions, and in the case of moderate or large moonpool sizes, also nonlinear free-surface effects inside the moonpools.

In the present study, we investigated 2DMR configurations where weakly nonlinear moonpool responses were observed. In the future, moonpools with larger recess floor sizes should be investigated in detail, with focus on the strongly nonlinear free-surface flow. This could involve model tests, both in 2D and 3D, and numerical simulations with a Navier–Stokes solver combined with fully nonlinear free-surface conditions.

Bibliography

AB Aalbers. The water motions in a moonpool. *Ocean engineering*, 11(6):557–579, 1984.

Tamer A. AbdelMigid, Khalid M. Saqr, Mohamed A. Kotb, and Ahmed A. Aboelfarag. Revisiting the lid-driven cavity flow problem: Review and new steady state benchmarking results using gpu accelerated code. *Alexandria Engineering Journal*, 56(1):123 – 135, 2017.

Lorena A Barba and Gilbert F Forsyth. Cfd python: the 12 steps to navier-stokes equations. *Journal of Open Source Education*, 9:21, 2018.

Luca Bonfiglio and Stefano Brizzolara. Amplitude induced nonlinearity in piston mode resonant flow: A fully viscous numerical analysis. *Journal of Offshore Mechanics and Arctic Engineering*, 140(1), 2018.

Alexandre Joel Chorin. A numerical method for solving incompressible viscous flow problems. *Journal of Computational Physics*, 2(1):12 – 26, 1967.

K.H. Chua, R. Eatock Taylor, and Y.S. Choo. Hydrodynamic interaction of side-by-side floating bodies, part ii: Applications of modified linear potential flow and numerical analysis framework to fixed barges. *Ocean Engineering*, 164: 465 – 481, 2018.

Robert G Dean and Robert A Dalrymple. *Water wave mechanics for engineers and scientists*, volume 2. world scientific publishing Co Inc, 1991.

DNV. Dnv-rp-c205 environmental conditions and environmental loads. *Det Norske Veritas: Oslo, Norway*, 2010.

DNV. Dnv-rp-h103 modelling and analysis of marine operations. *Det Norske Veritas: Oslo, Norway*, 2011.

Douglas G. Dommermuth and Dick K. P. Yue. Numerical simulations of nonlinear axisymmetric flows with a free surface. *Journal of Fluid Mechanics*, 178:195–219, 1987. doi: 10.1017/S0022112087001186.

O. M. Faltinsen and A. N. Timokha. On damping of two-dimensional piston-mode sloshing in a rectangular moonpool under forced heave motions. *Journal of Fluid Mechanics*, 772:R1, 2015. doi: 10.1017/jfm.2015.234.

Odd M. Faltinsen, Olav F. Rognebakke, and Alexander N. Timokha. Two-dimensional resonant piston-like sloshing in a moonpool. *Journal of Fluid Mechanics*, 575:359–397, 2007. doi: 10.1017/S002211200600440.

Odd Magne Faltinsen. *Sea loads on ships and offshore structures*. Cambridge University Press, New York, 1993.

Odd Magnus Faltinsen and Alexander N Timokha. *Sloshing*. Cambridge University Press, 2009.

Joel H Ferziger and Milovan Perić. *Computational methods for fluid dynamics*, volume 3. Springer, 2002.

Reza Firoozkoohi. Experimental, numerical and analytical investigation of the effect of screens on sloshing. *PhD Thesis*, 2013.

Arnt G. Fredriksen. A numerical and experimental study of a two-dimensional body with moonpool in waves and current. *PhD Thesis*, 2015.

Arnt G Fredriksen, Trygve Kristiansen, and Odd M Faltinsen. Experimental and numerical investigation of wave resonance in moonpools at low forward speed. *Applied Ocean Research*, 47:28–46, 2014.

Arnt G Fredriksen, Trygve Kristiansen, and Odd M Faltinsen. Wave-induced response of a floating two-dimensional body with a moonpool. *Phil. Trans. R. Soc. A*, 373(2033):20140109, 2015.

U Ghia, K.N Ghia, and C.T Shin. High-re solutions for incompressible flow using the navier-stokes equations and a multigrid method. *Journal of Computational Physics*, 48(3):387 – 411, 1982.

Marilena Greco, G Colicchio, Claudio Lugni, and Odd Magnus Faltinsen. 3d domain decomposition for violent wave-ship interactions. *International Journal for Numerical Methods in Engineering*, 95(8):661–684, 2013.

Christopher J Greenshields. Openfoam user guide. *OpenFOAM Foundation Ltd, version*, 3(1):e2888, 2015.

Stéphan T Grilli. On the development and application of hybrid numerical models in nonlinear free surface hydrodynamics. In *Proc. 8th Int. Conf. on Hydrodynamics*, pages 21–50, 2008.

Xiaoxian Guo, Haining Lu, Jianmin Yang, and Tao Peng. Resonant water motions within a recessing type moonpool in a drilling vessel. *Ocean Engineering*, 129: 228–239, 2017.

Yoshiho Ikeda, Toshifumi Fujiwara, and Toru Katayama. Roll damping of a sharp-cornered barge and roll control by a new-type stabilizer. In *The Third International Offshore and Polar Engineering Conference*. International Society of Offshore and Polar Engineers, 1993.

Joseph Katz and Allen Plotkin. *Low-speed aerodynamics*, volume 13. Cambridge university press, 2001.

Erwin Kreyszig. *Advanced engineering mathematics, tenth edition*. John Wiley & Sons, 2011.

Trygve Kristiansen. Two-dimensional numerical and experimental studies of piston-mode resonance. *PhD Thesis*, 2009.

Trygve Kristiansen and Odd M Faltinsen. Application of a vortex tracking method to the piston-like behaviour in a semi-entrained vertical gap. *Applied Ocean Research*, 30(1):1–16, 2008.

Trygve Kristiansen and Odd M Faltinsen. Gap resonance analyzed by a new domain-decomposition method combining potential and viscous flow. *Applied Ocean Research*, 34:198–208, 2012.

Trygve Kristiansen, Thomas Sauder, and Reza Firoozkoohi. Validation of a hybrid code combining potential and viscous flow with application to 3d moonpool. In *ASME 2013 32nd International Conference on Ocean, Offshore and Arctic Engineering*, pages V009T12A029–V009T12A029. American Society of Mechanical Engineers, 2013.

Trygve Kristiansen, Babak Ommani, Kjetil Berget, and Rolf Baarholm. An experimental and numerical investigation of a box-shaped object in moonpool: A three-dimensional study. *International Conference on Offshore Mechanics and Arctic Engineering*, 1, 2015.

C Kuo. A controlled handling method for effective offshore support operations. In *Offshore Technology Conference*. Offshore Technology Conference, 1978.

CH Lee and JN Newman. Wamit user's manual, ver. 6.4, wamit. *Inc, MA, USA*, 2006.

Hamilton H Mabie and Fred W Ocvirk. *Mechanisms and dynamics of machinery*. John Wiley & Sons, 1957.

Ch Maisondieu and M Le Boulluec. Flow dynamics in a moon-pool experimental and numerical assessment. In *Proc. OMAE Conference, Rio de Janeiro, Brasil*, 2001.

P McIver. Complex resonances in the water-wave problem for a floating structure. *Journal of Fluid Mechanics*, 536:423–443, 2005.

Bernard Molin. On the piston and sloshing modes in moonpools. *Journal of Fluid Mechanics*, 430:27–50, 2001.

Bernard Molin. On natural modes in moonpools with recesses. *Applied Ocean Research*, 67:1 – 8, 2017.

Bernard Molin, X Zhang, H Huang, and F Remy. On natural modes in moonpools and gaps in finite depth. *Journal of Fluid Mechanics*, 840:530–554, 2018.

JN Newman. Progress in wave load computations on offshore structures. In *Proceedings of the 23rd International Conference Offshore Mechanics & Arctic Engineering, Vancouver, Canada, June*, pages 20–25, 2004.

Babak Ommani, Trygve Kristiansen, Kjetil Berget, Peter Sandvik, and Odd M Faltinsen. Investigation on moonpool blockage by box shaped object close to free surface. In *3rd International Conference on Violent Flows (VF-2016)*. Violent Flows (VF-2016), 2016.

Senthuran Ravinthrakumar, Trygve Kristiansen, Bernard Molin, and Babak Ommani. A two-dimensional numerical and experimental study of piston and sloshing resonance in moonpools with recess. *Journal of Fluid Mechanics*, 877:142–166, 2019a.

Senthuran Ravinthrakumar, Trygve Kristiansen, and Babak Ommani. On the Hydrodynamic Interaction Between Ship and Free-Surface Motions on Vessels With Moonpools. volume 7A: Ocean Engineering of *International Conference on Offshore Mechanics and Arctic Engineering*, 2019b.

Senthuran Ravinthrakumar, Trygve Kristiansen, Bernard Molin, and Babak Ommani. Coupled vessel and moonpool responses in regular and irregular waves. *Applied Ocean Research*, 96:102010, 2020a.

Senthuran Ravinthrakumar, Trygve Kristiansen, and Babak Ommani. A two-dimensional experimental and numerical study of moonpools with recess. *Journal of Offshore Mechanics and Arctic Engineering*, 142(1), 2020b.

H Schlichting. Boundary-layer theory. In *Boundary-layer theory*. McGraw-Hill, 1979.

Yan-Lin Shao and Odd M. Faltinsen. A harmonic polynomial cell (hpc) method for 3d laplace equation with application in marine hydrodynamics. *Journal of Computational Physics*, 274:312 – 332, 2014.

Hye-Jong Son, Soon-Ho Choi, Man-Hwan Kim, and Seung-Myun Hwangbo. Drag reduction of recess type moonpool under vessel's forward speed. In *ASME 2008 27th International Conference on Offshore Mechanics and Arctic Engineering*, pages 143–148. American Society of Mechanical Engineers, 2008.

S.H. Sphaier, F.G.S. Torres, I.Q. Masetti, A.P. Costa, and C. Levi. Monocolumn behavior in waves: Experimental analysis. *Ocean Engineering*, 34(11):1724 – 1733, 2007.

L. Sun, R. Eatock Taylor, and P.H. Taylor. First- and second-order analysis of resonant waves between adjacent barges. *Journal of Fluids and Structures*, 26 (6):954 – 978, 2010.

L. Sun, R. Eatock Taylor, and P.H. Taylor. Wave driven free surface motion in the gap between a tanker and an flng barge. *Applied Ocean Research*, 51:331 – 349, 2015.

MJ Tait, AA El Damatty, N Isyumov, and MR Siddique. Numerical flow models to simulate tuned liquid dampers (tld) with slat screens. *Journal of Fluids and Structures*, 20(8):1007–1023, 2005.

John Törnblom and Erik Hammargren. Effect of the moonpool on the total resistance of a drillship. *Master Thesis*, 2012.

Riaan van't Veer and Haye Jan Tholen. Added resistance of moonpools in calm water. In *ASME 2008 27th International Conference on Offshore Mechanics and Arctic Engineering*, pages 153–162. American Society of Mechanical Engineers, 2008.

C.Z. Wang and G.X. Wu. Analysis of second-order resonance in wave interactions with floating bodies through a finite-element method. *Ocean Engineering*, 35 (8):717 – 726, 2008.

C.Z. Wang, G.X. Wu, and B.C. Khoo. Fully nonlinear simulation of resonant motion of liquid confined between floating structures. *Computers & Fluids*, 44 (1):89 – 101, 2011.

Seung Ho Yang, Young Jun Yang, Sang Beom Lee, Jitae Do, and Sun Hong Kwon. Study on moonpool resonance effect on motion of modern compact drillship. *Journal of Ocean Engineering and Technology*, 27(3):53–60, 2013.

R. W. Yeung. The transient heaving motion of floating cylinders. *Journal of Engineering Mathematics*, 16(2):97–119, May 1982.

Xinshu Zhang, Haiyang Huang, and Xingyu Song. On natural frequencies and modal shapes in two-dimensional asymmetric and symmetric moonpools in finite water depth. *Applied Ocean Research*, 82:117–129, 2019.

Appendices

Appendix A

Ship model in Ocean Basin tests

A.1 Model in Ocean Basin tests

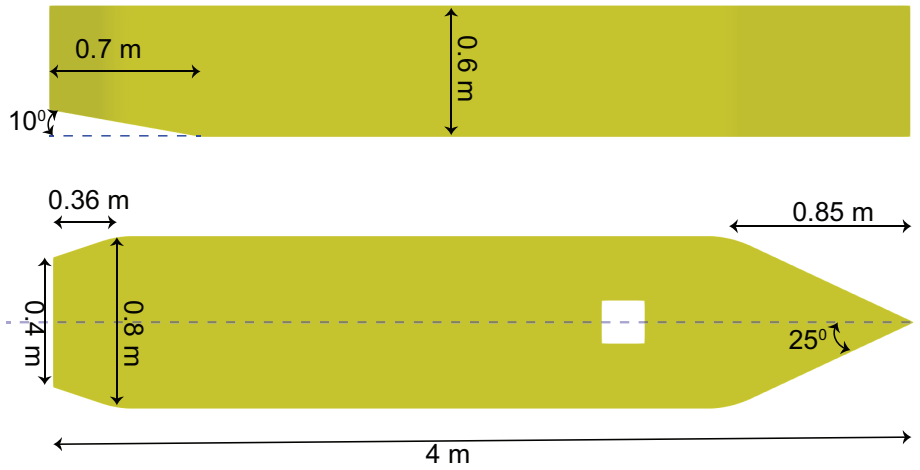

Figure A.1: Ship model tested in Ocean Basin, illustrating the shape of the hull.

A.2 Weights in the models

The weights used in the three models tested in the Ocean Basin (cf. Table 5.1) are indicated in Figure A.3. The mass of the weights for MP1 are indicated in Figure A.3(a). The same weights were used for MP2 and MP3, where the only difference is that some of the weights were moved slightly or removed completely.

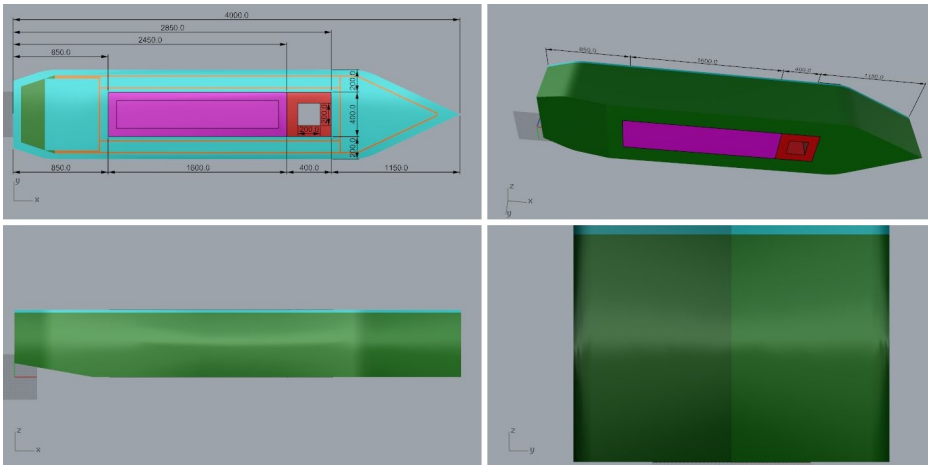

Figure A.2: Ship model tested in Ocean Basin, illustrating the boxes used to obtain different moonpool sizes. The measures are in mm.

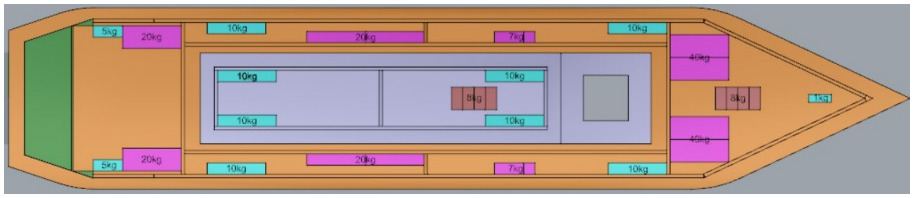

(a) Additional weights in MP1

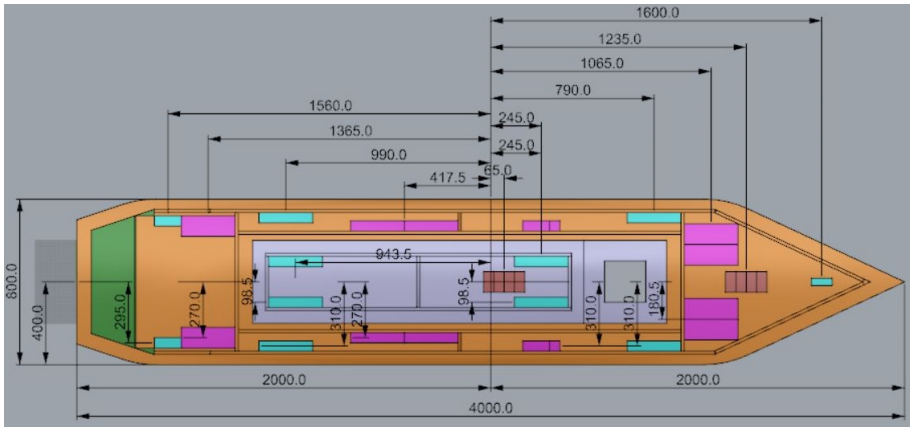

(b) MP1

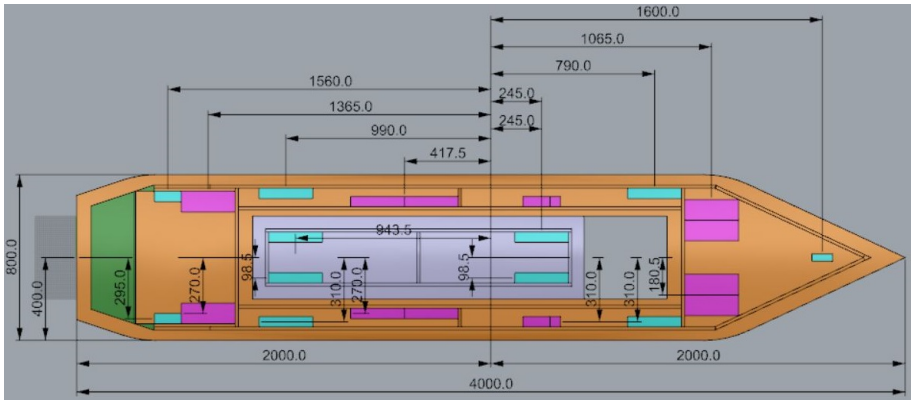

(c) MP2

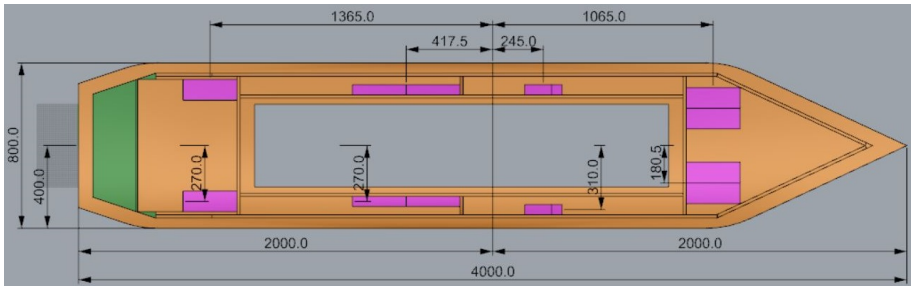

(d) MP3

Figure A.3: Weight distribution in the models. The measures are in mm and kg.

A.3 Free decay

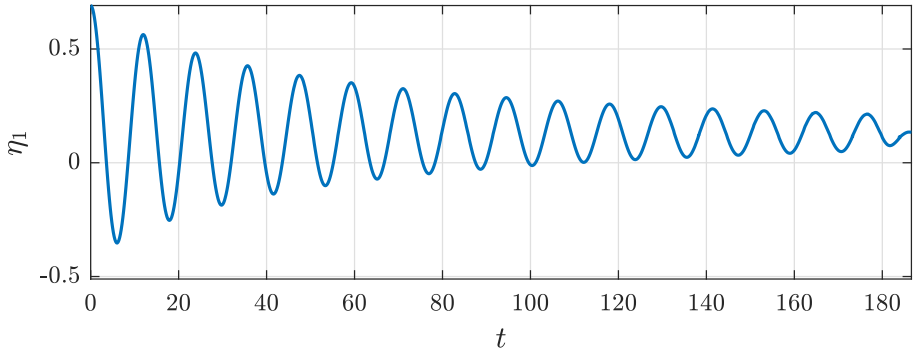

(a) Surge (MP1)

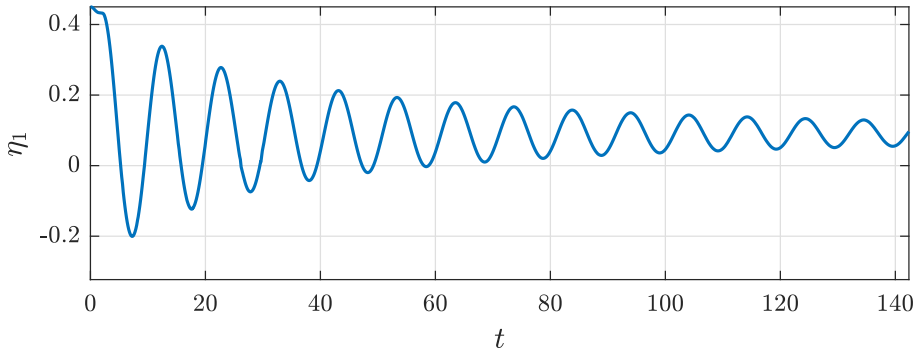

(b) Surge (MP3)

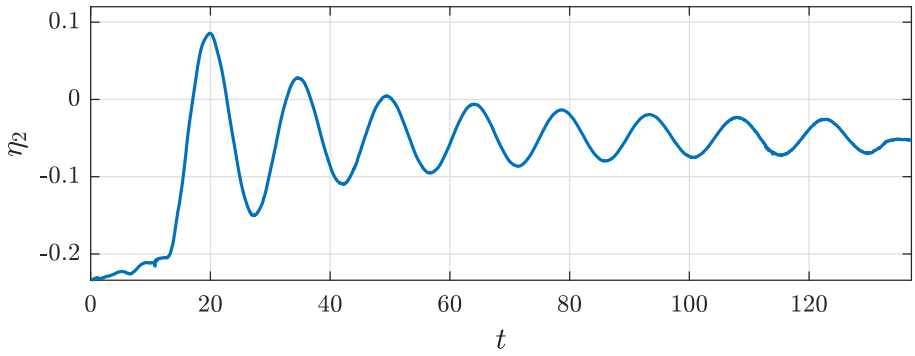

(c) Sway (MP1)

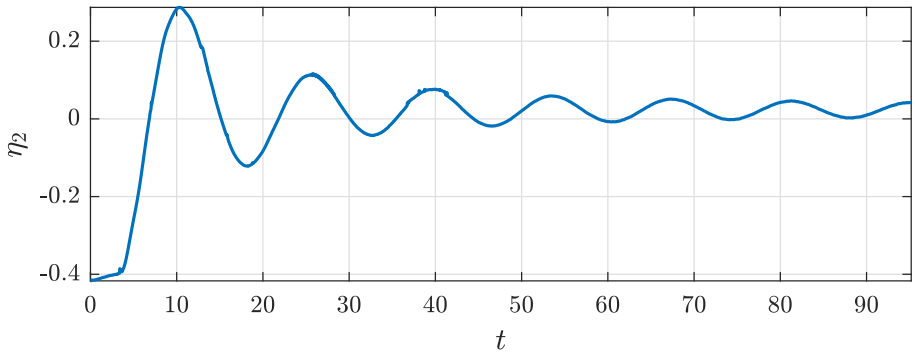

(d) Sway (MP3)

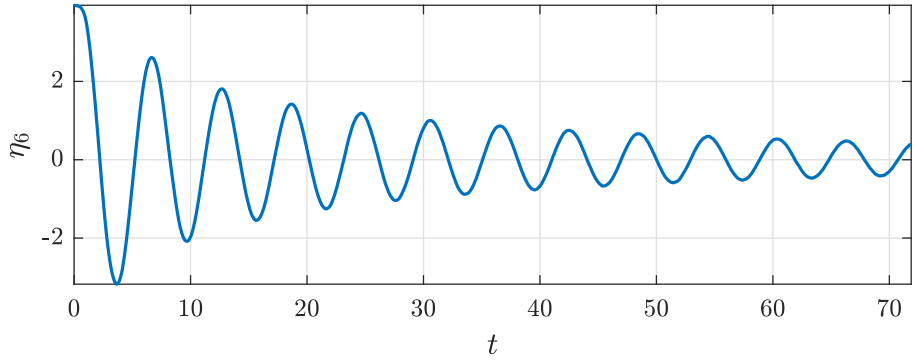

(e) Yaw (MP1)

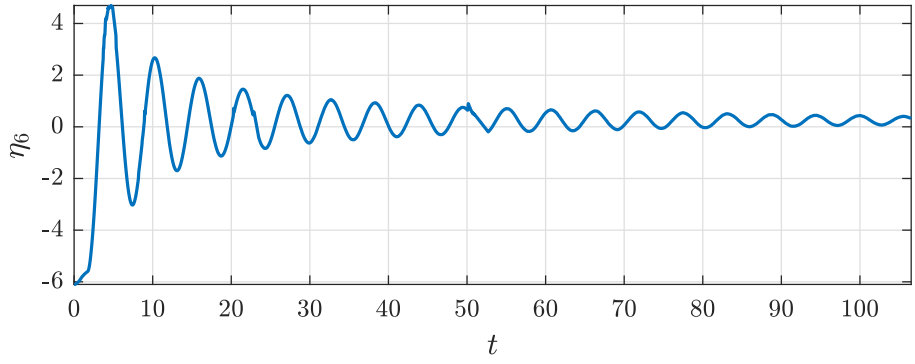

(f) Yaw (MP3)

Figure A.4: Free decay tests from model tests in the Ocean Basin. Free decay in heave and pitch are not included since these tests failed.

Appendix B

Numerical simulations

B.1 Modified VBEM in freely floating conditions

The presented moonpool and heave RAOs in §8.2 suggested that the equation of motion in heave must be modified to improve the responses in freely floating conditions. The modifications are presented in the following.

The acceleration in heave, $\ddot{\eta}_3$, is determined as

$$\ddot{\eta}_3^{n+1} = \frac{F_3 - \frac{1}{4\gamma^2}\rho\frac{K}{\mathrm{Sn}}\overline{w}|\overline{w}|A - C_{33}\eta_3^n - C_{35}\eta_5^n + \tilde{A}_{33}\ddot{\eta}_3^n}{m + \tilde{A}_{33}}, \tag{B.1}$$

where $A = \int_{S_b} n_3 dS$. S_b and n_3 are the wetted body surface and normal vector pointing into the fluid, respectively. n is the time step number. $\overline{w}$ is the averaged fluid velocity at the moonpool entrance. Sn and K are the solidity ratio and the pressure drop coefficient, respectively. K/Sn is equivalent to the drag coefficient for a slat screen, C_D (Tait et al. 2005). Including (B.1) in VBEM, in addition to (6.11), improves the estimates considerably.

B.2 Meshes in PVC3D

The details of the meshes used in the PVC3D simulations for MP1-3 are discussed in the following. The meshes used in the PVC3D simulations for the 3DQ configurations are discussed in Appendix B.3.

The mesh is generated by specifying the size of the computational domain, and the mesh sizes, using the BlockMesh module. SnappyHexMesh is then used to refine the mesh sizes with a factor of two within prescribed boxes, as illustrated in

Figure B.1. The yellow region is the mesh size as generated from the BlockMesh module. The red region indicates the first box, where the mesh sizes are reduced by a factor of two. This is process is repeated three times. The finest mesh region is indicated with purple color. Example of the meshes used in the present simulations are presented in Figure B.2. The extent of the refinement regions for MP1-3 are presented in Table B.1.

We use three boxes to refine the mesh. This yields four regions with different mesh sizes, as illustrated in Figure B.2. The extent of the refinement boxes depend on the wavelength, λ. The computational time increases with decreasing T. Although we could have adopted an alternative approach to reduce the number of cells for small oscillation periods, we did not choose to do so since the simulations were carried out on an external computer and computational time was not a major issue in the present simulations.

Table B.1: Dimensions of the mesh refinement boxes in the present simulations with PVC3D for MP1-3. The origin is located at the center of the ship at the calm free-surface, as illustrated in Figure B.1. Figure B.1 explains the color codes presented below.

Box number (color)	x-direction	y-direction	z-direction
1 (red)	$2\lambda + 4.1$ m	$2\lambda + 0.5$ m	1.0 m
2 (blue)	$\lambda + 4.1$ m	$\lambda + 0.5$ m	0.55 m
3 (purple)	4.1 m	0.5 m	0.4 m

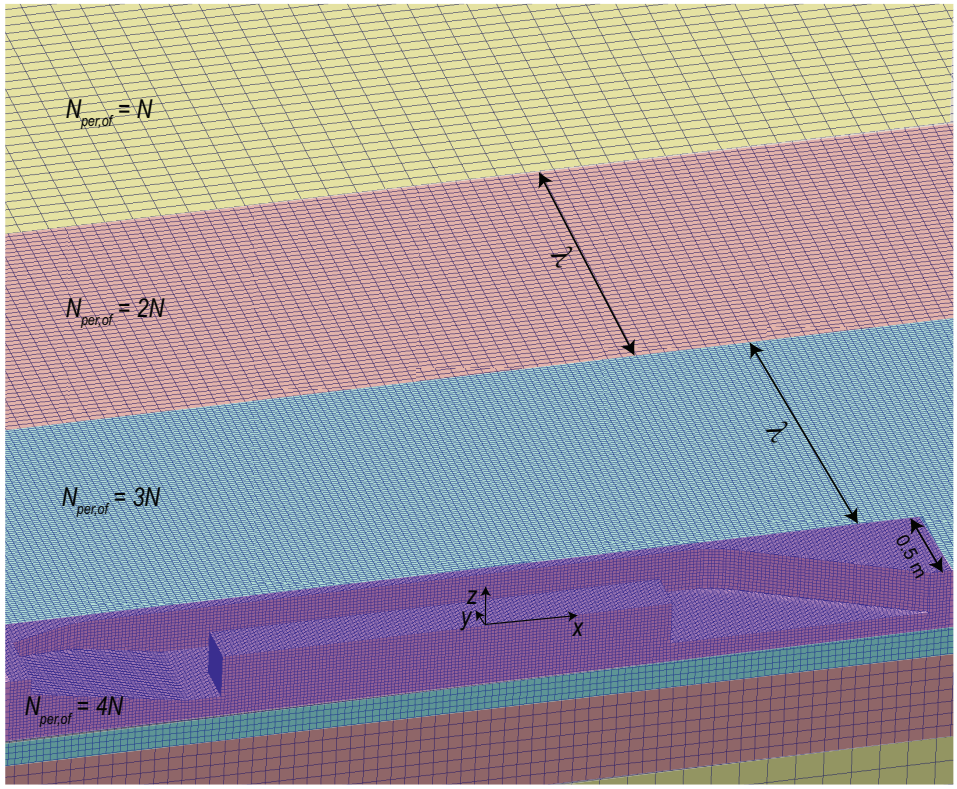

Figure B.1: An example mesh, indicating how the mesh sizes are refined towards the ship. Yellow indicates the coarsest mesh region, generated by the BlockMesh module. The mesh is then refined stepwise. λ is the wavelength. $N_{per,of}$ is the number of cells per wavelength. In the present simulations, we use $N = 15$.

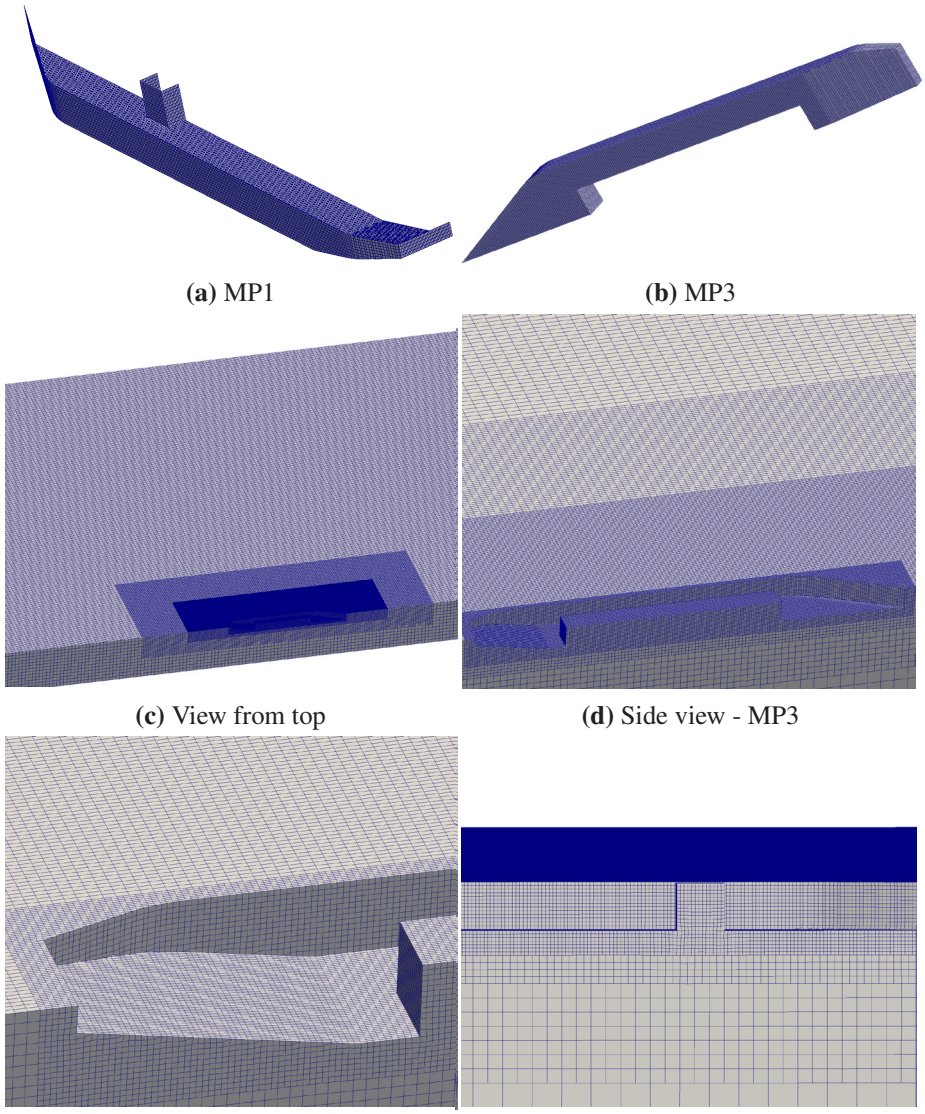

(a) MP1 **(b)** MP3

(c) View from top **(d)** Side view - MP3

(e) Zoomed around to the aft **(f)** Side view - MP1

Figure B.2: Example of meshes used in the present PVC3D simulations.

B.3 PVC3D simulations for 3DQ configurations

The simulations with PVC3D for the 3DQ configurations are slightly different from those for MP1-3. Since the model is symmetric about the yz- and xz-planes at $x = 0$ and $y = 0$, respectively, only 1/4 of the computational domain is meshed. The boundary conditions are illustrated in Figure 6.11. The small gaps between the model and the glass walls, as evident in the model tests in the wave flume, are not meshed in the present simulations. Otherwise, the mesh is generated as discussed in Appendix B.2. An example mesh is presented in Figure B.4.

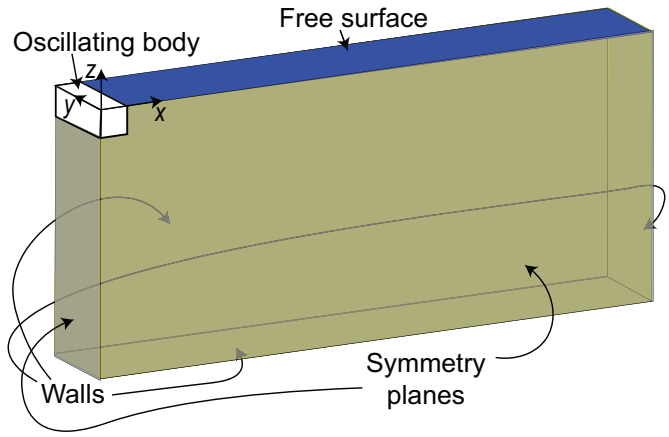

Figure B.3: Sketch illustrating the boundary conditions applied in the present simulations with PVC3D. The walls, symmetry planes and free-surface are indicated.

The regular forced heave simulations are carried out as discussed in §6.6. In addition, irregular forced heave simulations are carried out for the 3DQ simulations. The irregular forced heave motion is defined as discussed in §4.1.2, i.e. with pink noise spectra. The mesh is created such that $N_{per,of} = 15$ is obtained for the lowest forced heave period in the pink noise spectra. The length of the computational domain is chosen such that re-reflected waves do not affect the results, since numerical beaches are not implemented.

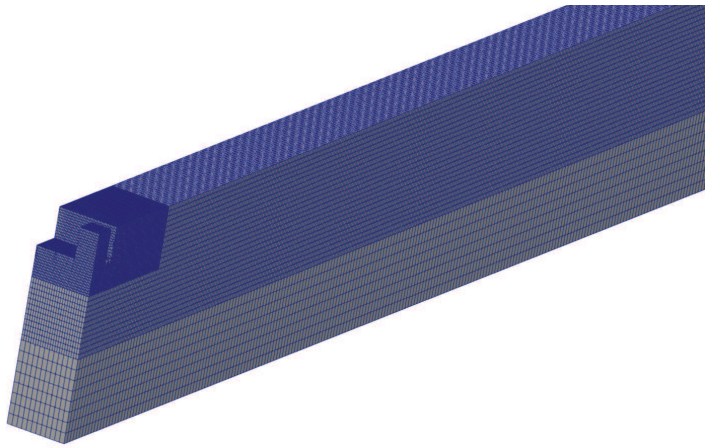

Figure B.4: Example mesh for Case 1, cf. Table 4.1. The gaps between the model and glass walls in the wave flume are not meshed.

B.4 Snapshots of flow fields from the forced motion simulations with PVC3D

Snapshots of flow fields from the present simulations with PVC3D are presented in this section. The dynamic pressure field is indicated with colors, ranging from blue (minimum pressure) to red (maximum pressure). In addition, the velocity vectors at $y = 0$ m are presented as white arrows. The simulation type are indicated in parentheses in the figure caption, i.e. whether the plots are from forced heave or forced surge simulations. The simulations were carried out for visualization purposes only, and they were carried out with $N_{per,of} = 10$ (cf. §6.6). The refinement regions in the plots below were also somewhat smaller.

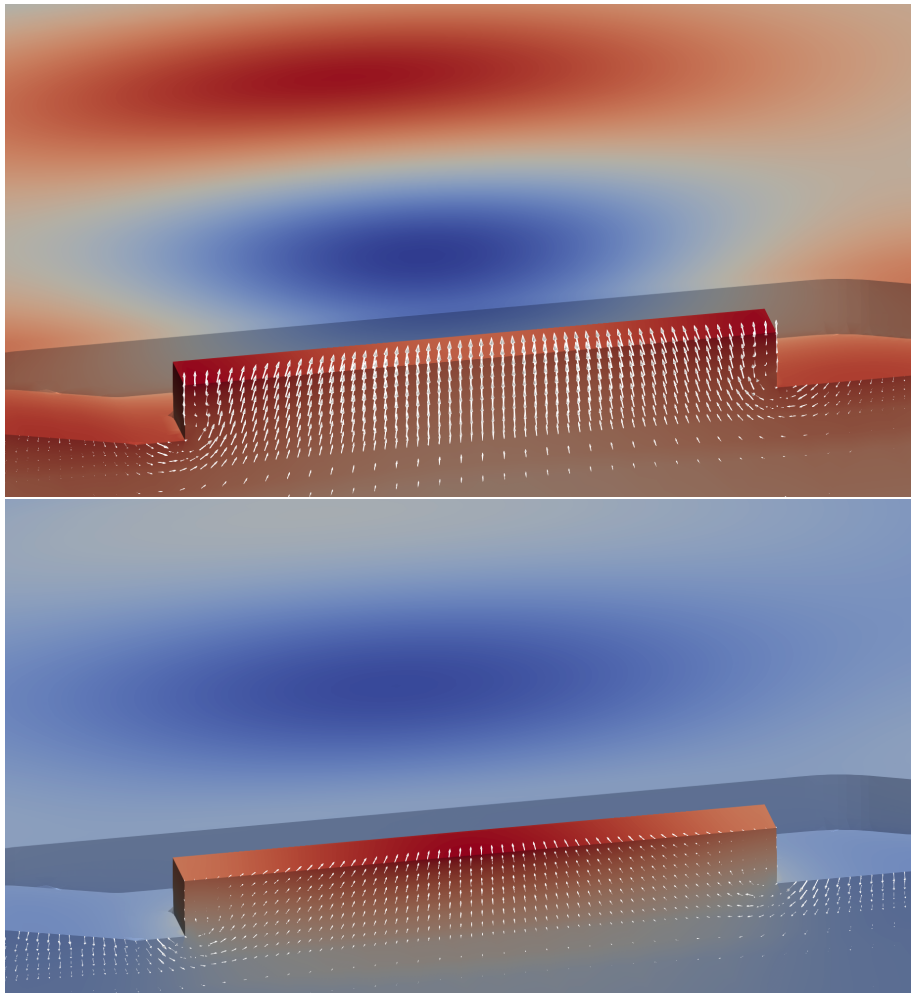

Figure B.5: Piston mode - MP3 (forced heave)

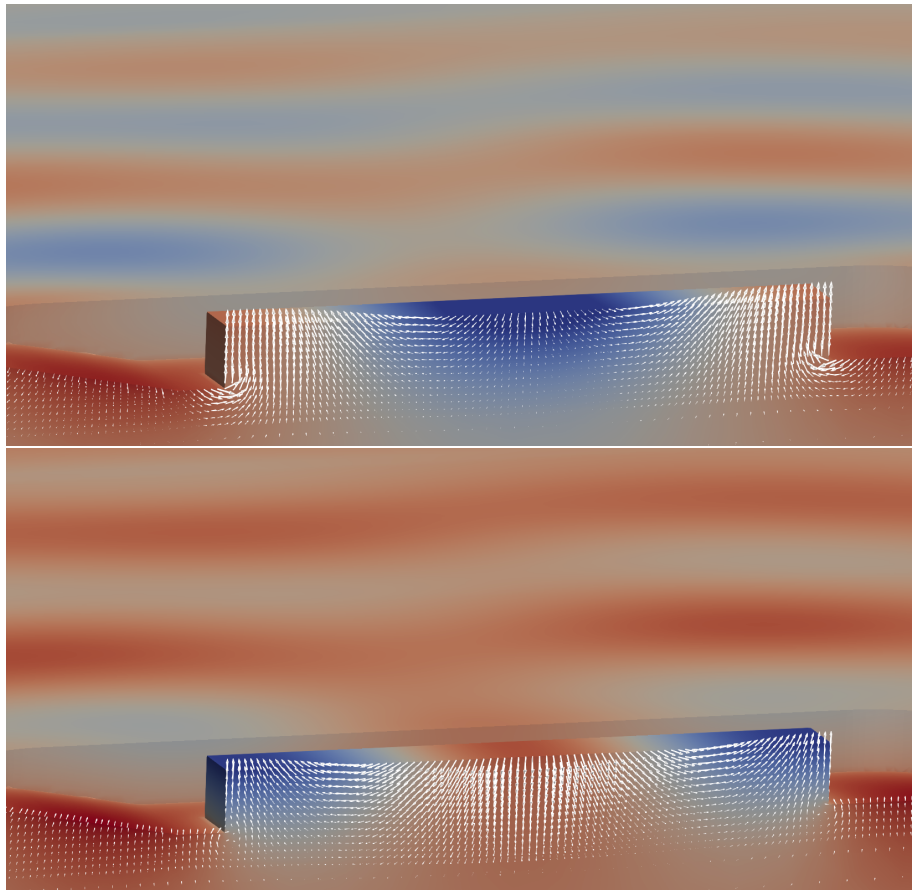

Figure B.6: Second sloshing mode - MP3 (forced heave)

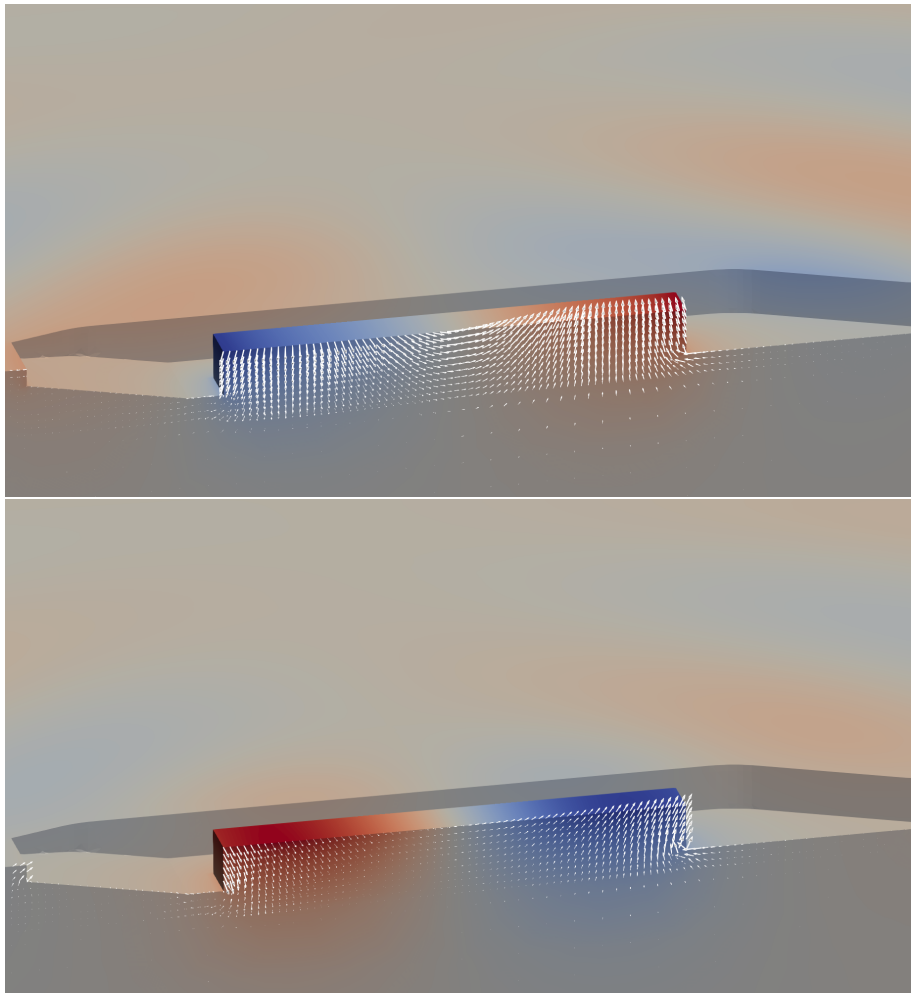

Figure B.7: First sloshing mode - MP3 (forced surge)

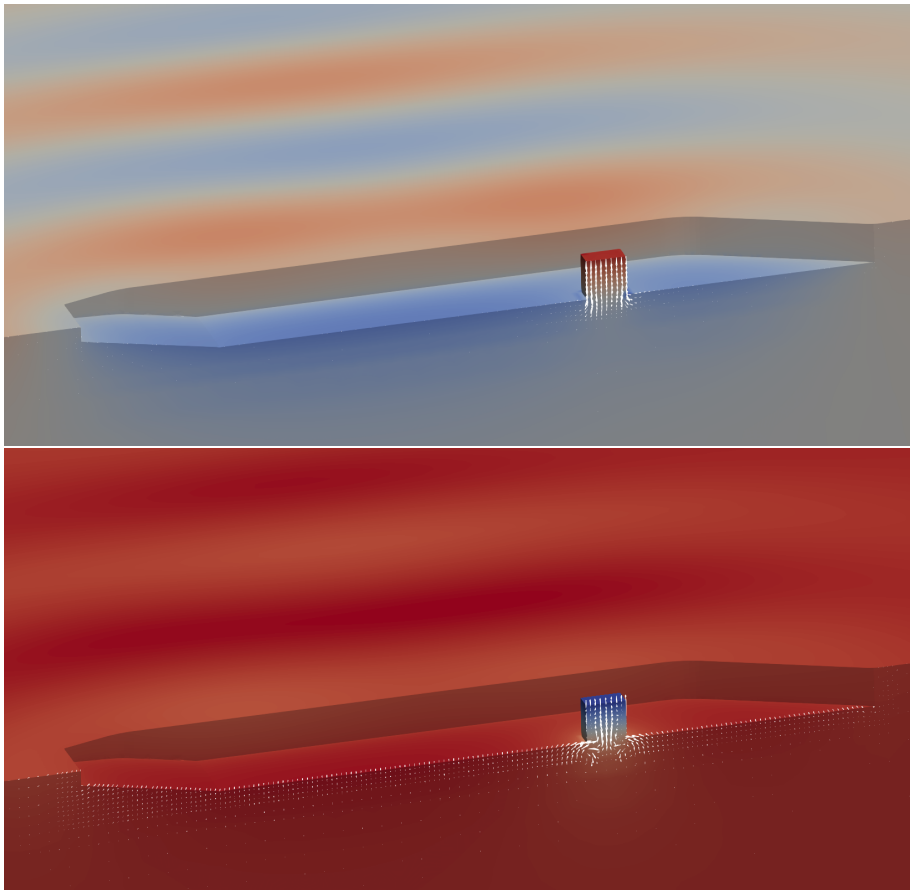

Figure B.8: Piston mode - MP1 (forced heave)

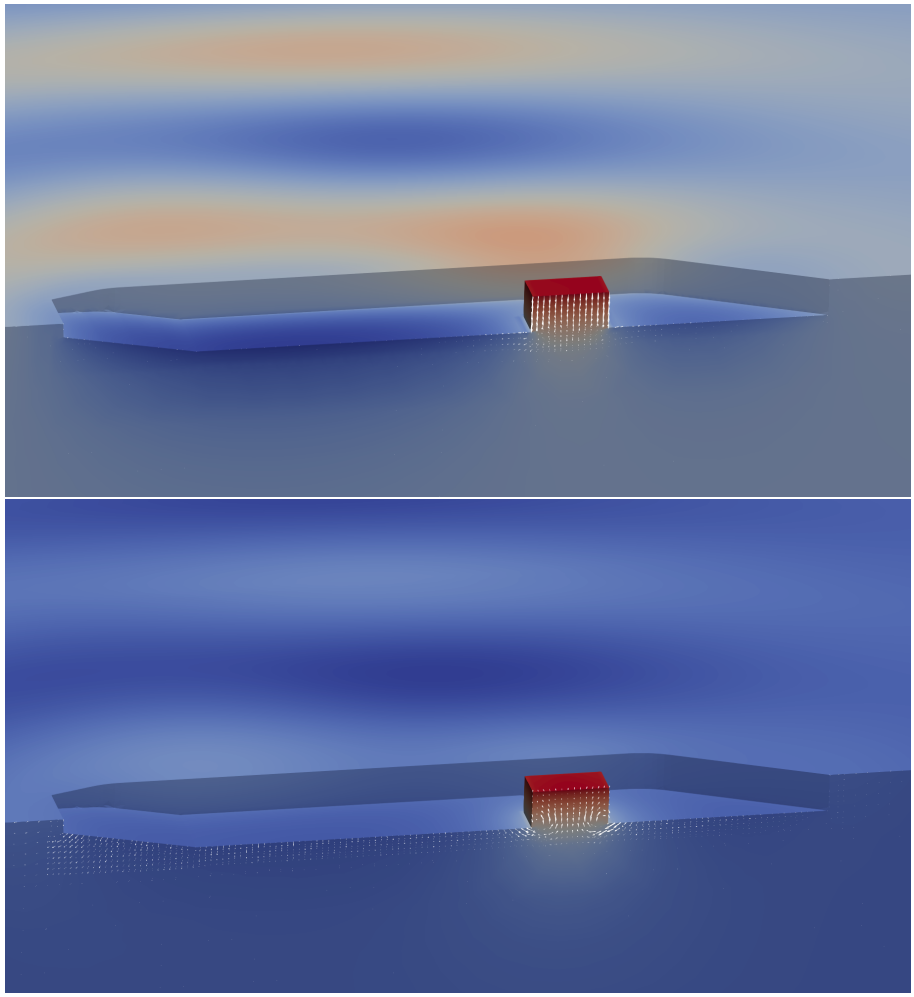

Figure B.9: Piston mode - MP2 (forced heave)

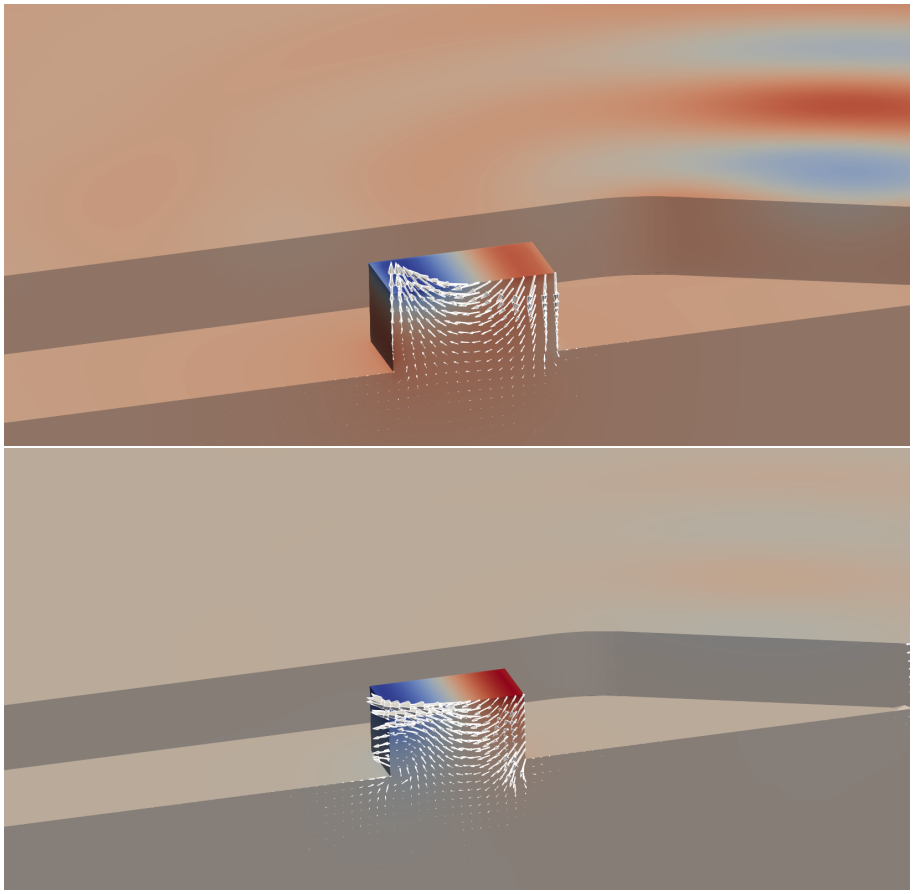

Figure B.10: First longitudinal sloshing mode - MP2 (forced surge)

B.5 Snapshots of vorticity from the forced motion simulations with PVC3D

Snapshots of flow fields, similar to those presented in Appendix B.4. The difference is that the colors indicate the magnitude of the vorticity, ranging from zero (blue) to maximum vorticity (red). The snapshots are approximately $T/2$ apart, where T is the forced heave/surge period.

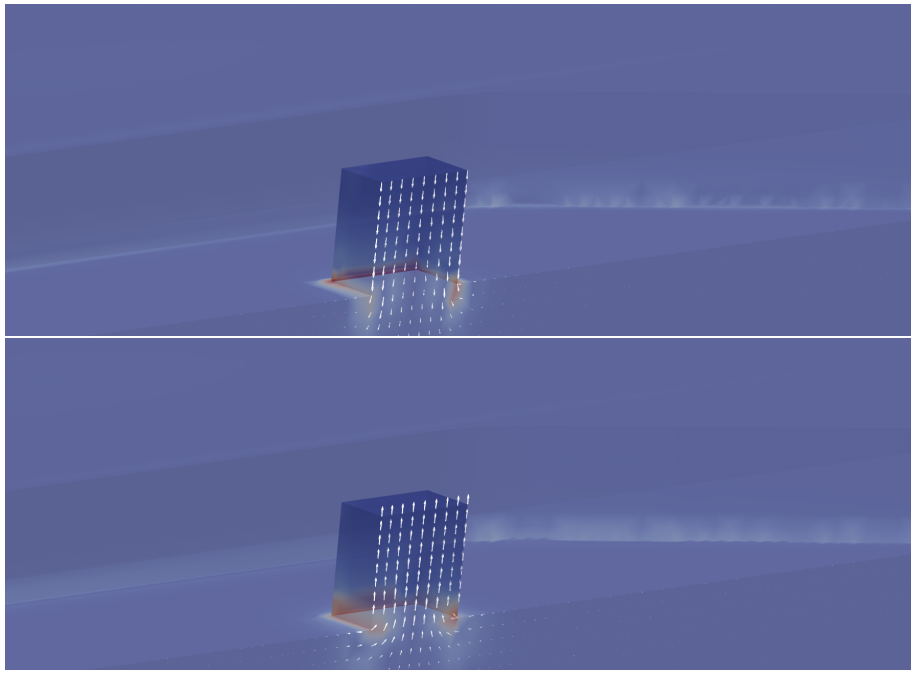

Figure B.11: Piston mode - MP1 (forced heave)

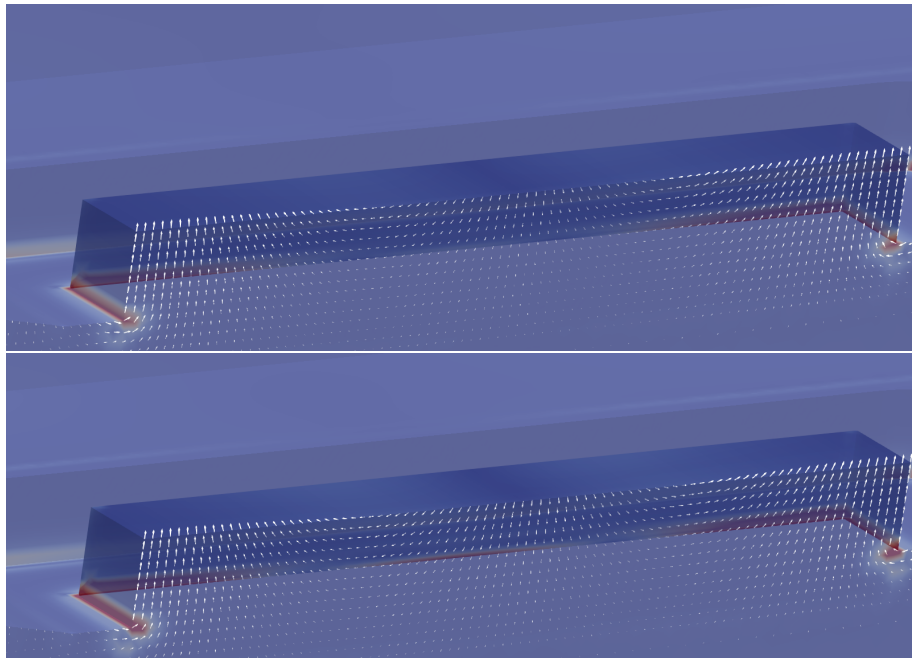

Figure B.12: Second longitudinal sloshing mode - MP3 (forced heave)

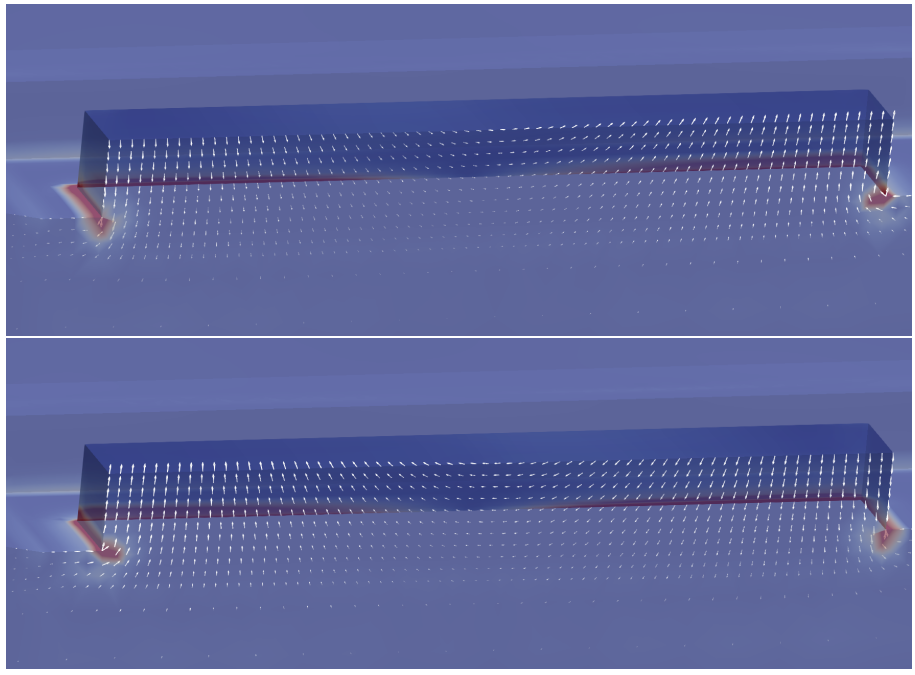

Figure B.13: First longitudinal sloshing mode - MP3 (forced surge)

Appendix C

Additional results

C.1 Experimental and numerical studies with the 2DMR configurations

C.1.1 Convergence of the domain decomposition method

The presently developed DD method was discussed in §2.1.2. The convergence of the DD method is presented in Figure C.1, where N is varied from $N = 1$ to $N = 500$. The natural periods (cf. Table 7.1) are predicted with a precision of four significant digits with $N = 25$ for Cases 1-3 (cf. Table 4.1).

With $N = 1$, the predicted piston mode periods, as illustrated in Figure C.1(a), are approximately 40 % different from those predicted with $N = 500$. For clean moonpools, as discussed by Molin (2001), the piston mode periods can be predicted with a single mode approximation, which provides good estimates. For moonpools with recess, the single mode approximation will under-estimate the piston mode periods. For the sloshing modes, a single mode approximation approach would yield fairly accurate results.

Figure C.2 illustrates how the piston and first sloshing mode periods vary as a function of the recess floor length, L_r, and recess floor height, H_r.

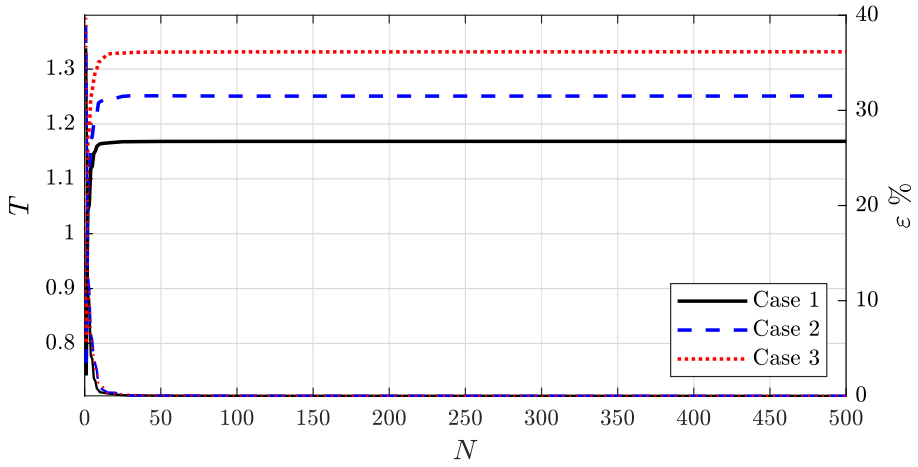

(a) Piston mode

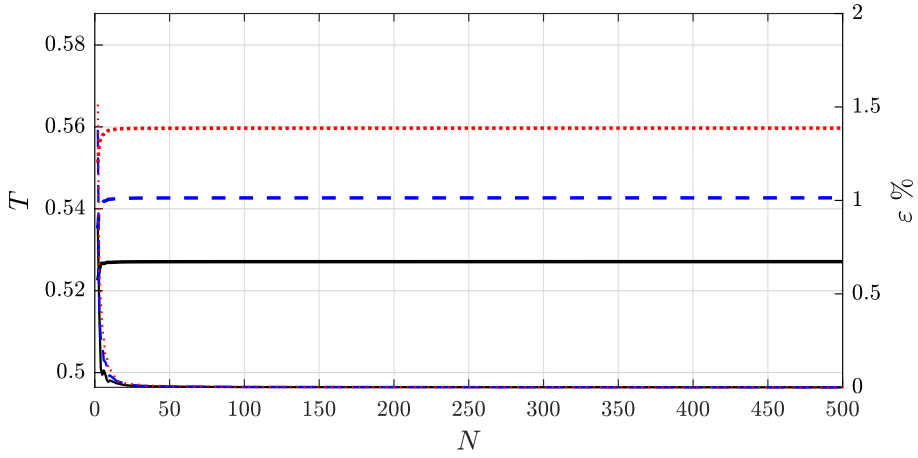

(b) First sloshing mode

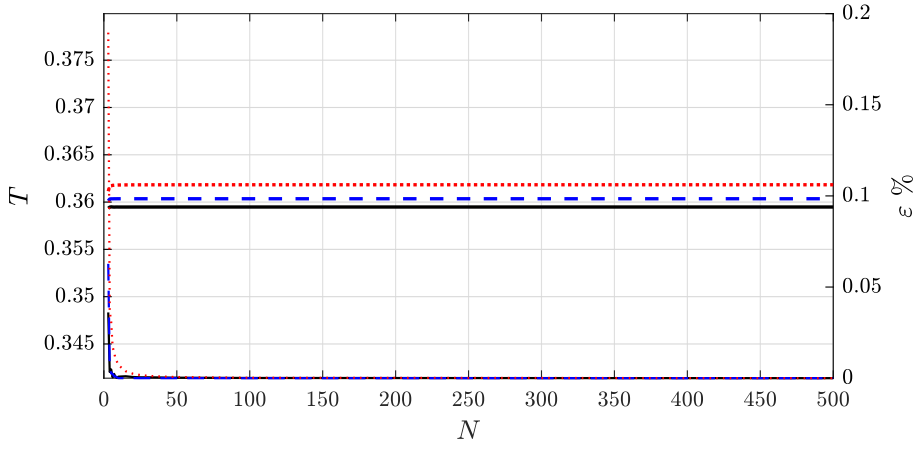

(c) Third sloshing mode

Figure C.1: Convergence of natural periods as predicted with the present DD method (cf. (2.10)). ε is the difference in the predicted natural period relative to the natural period predicted with $N = 500$.

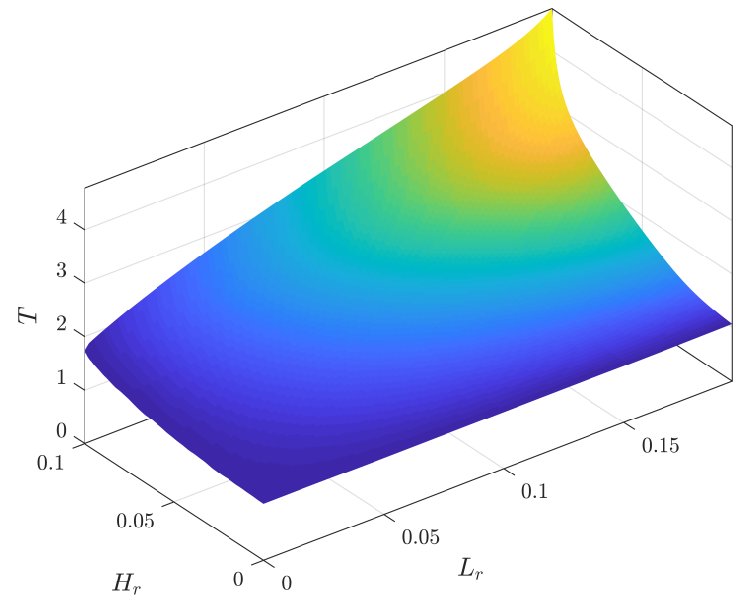

(a) Piston mode

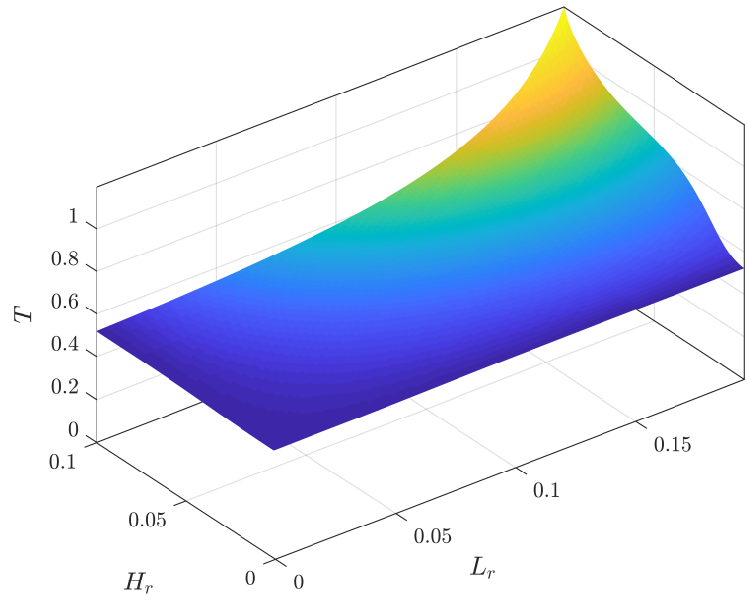

(b) First sloshing mode

Figure C.2: Natural periods as predicted with the present DD method. L_r and H_r are varied, while L_m = 0.2 m, $D = 0.11$ m and $L = 1.0$ m.

C.1.2 Beats in experiments

Beating was observed in the experiments, as in discussed for the BEM simulations in §2.4. This is illustrated for Case 3 in the proximity of the first sloshing mode in Figure C.3 for the forced heave period where beating persisted for the longest time. The dashed lines indicate where the steady-state responses are extracted.

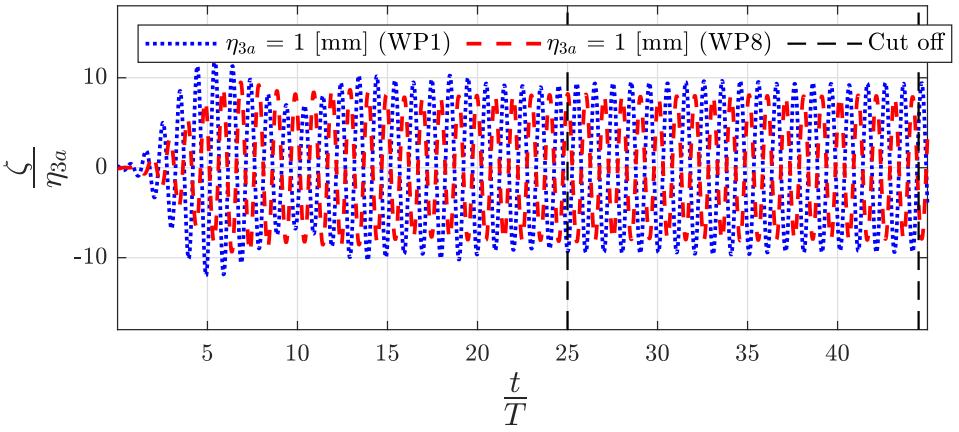

Figure C.3: Time series from model tests for Case 3. Beating was observed in the proximity of the first sloshing mode. The dashed lines indicate where the steady-state responses are extracted. $T = 0.5$ s is the forced heave period.

C.1.3 Quadratic-type damping

The following was presented by Ravinthrakumar et al. (2019a), where the quadratic-type damping due to flow separation at the piston and first sloshing modes for the presently investigated 2DMR cases was discussed. First sloshing mode RAOs for the 2DMR cases at WP1 are presented in §7.1.3. The measured sloshing RAOs are significant; up to 35 in the tested range. The BEM simulations over-predicted the moonpool responses at first sloshing mode, much more than for the piston mode. The reason is limited wave radiation caused by the sloshing for the present configurations. The predicted moonpool RAO at the sloshing natural frequency predicted by the BEM is approximately 300-400. Evidence of that the damping is quadratic is provided in Figure C.4. Here the maximum moonpool RAOs at resonance as predicted with the present CFD are presented as a function of η_{3a}. With quadratic damping, the maximum responses decrease as ${\eta_{3a}}^{-1/2}$, when presented as ζ_{mp}/η_{3a}.

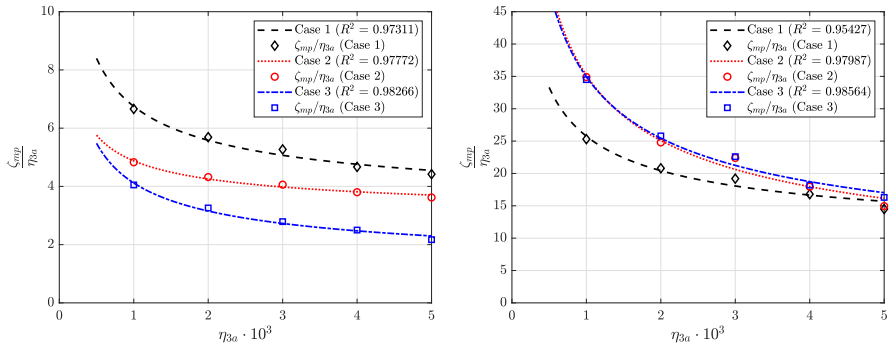

(a) Piston mode **(b)** First sloshing mode

Figure C.4: Regression of the maximum responses at resonance as predicted by forced heave motion simulations with the present CFD for the five forcing amplitudes studied. Damping at resonance is dominated by viscous effects, mainly quadratic with the relative motion between the flow and body motions. The maximum responses are fitted to a curve on the form $\zeta_{mp}/\eta_{3a} = c_0 + a_0 {\eta_{3a}}^{-1/2}$.

C.2 Forced heave with 2DMR configuration (failed tests)

Forced heave experiments with twice the moonpool length at the mean waterline relative to those presented in §4.5 were conducted, but the model tests were not successful since the wave probe measurements failed. However, video recordings at selected forced heave periods and forced heave amplitudes were stored. Snapshots from the video recordings are presented in Figures C.5 and C.6.

The video recordings suggest that nonlinear free-surface effects are dominant at the sloshing modes, although this statement is not supported by measured experimental data. We observed nonlinear effects such as wave breaking and wave run-up along the recess end wall. In fact, the run-up along the recess wall end for the configuration in Figure C.6 was so significant that water splashed out of the wave flume! The distance above the mean waterline to the top of the wave flume was 30 cm, and the forced heave amplitude was $\eta_{3a} = 5$ mm. Since we do not have measurements of the free-surface elevation in the moonpool, we cannot comment on whether the higher harmonic moonpool responses were significant, although the video recordings suggest that they were.

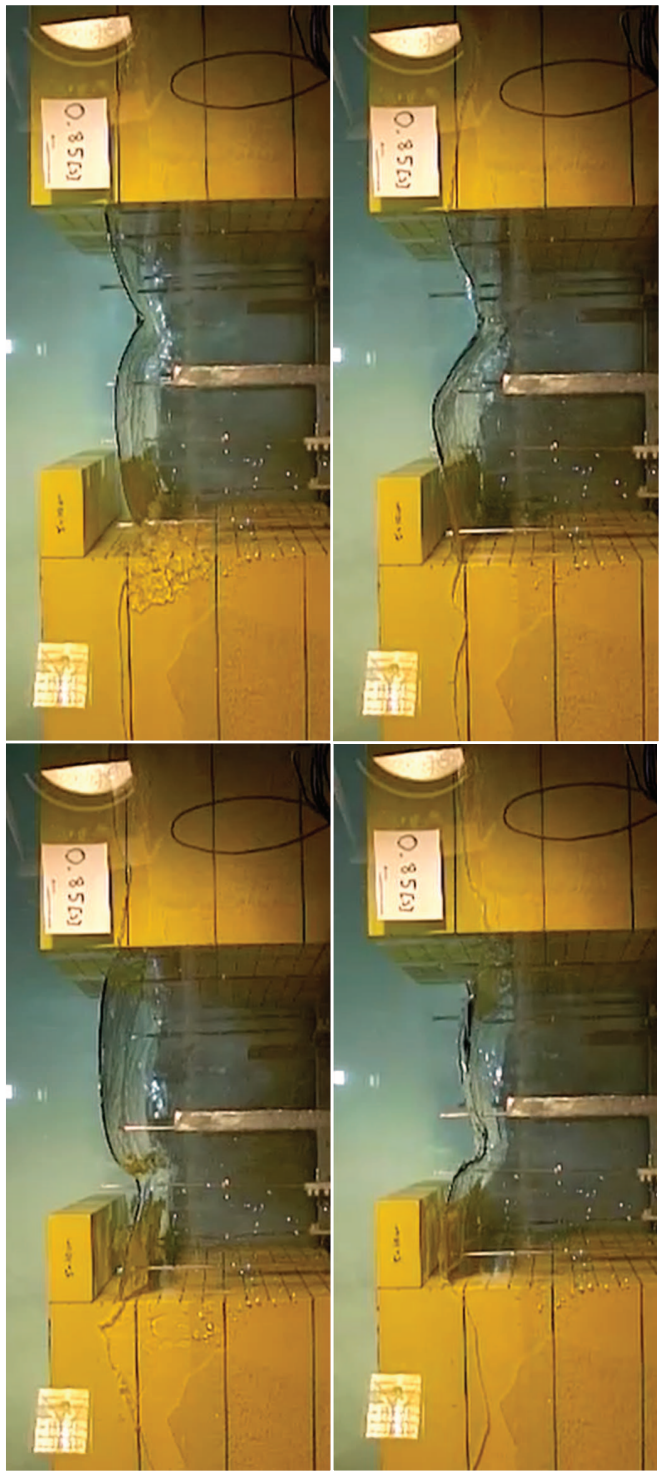

Figure C.5: 2DMR configuration with moonpool length $L_m = 40$ cm at the calm waterline. $L_r = 10$ cm, $H_r = 5$ cm, $D = 0.10$ cm, $\eta_{3a} = 3$ mm and $T = 0.85$ s.

Figure C.6: 2DMR configuration with moonpool length $L_m = 40$ cm at the calm waterline. $L_r = 20$ cm, $H_r = 5$ cm, $D = 0.10$ cm, $\eta_{3a} = 3$ mm and $T = 0.85$ s.

C.3 Ocean Basin tests

C.3.1 Heave RAOs from irregular wave tests

Heave RAOs in head sea from the irregular wave tests are presented in Figure C.7. The first three minutes of the time-series are used. Wave reflection from the side walls takes time to build up. We present heave responses before re-reflection occurs by reducing the time-window in the time-series. For $T > 1.2$ s, the heave RAOs suggest that re-reflection has not occurred, which strengthens the discussion in §9.3. For small wave periods, that is $T \lessapprox 1.2$ s, the wave components have still not fully reached the model, hence the differences between the heave RAOs in Figure C.7 and those presented in Chapter 9. The purpose of presenting the results in this manner is to illustrate that re-reflection affects the heave responses in irregular waves. In regular waves, we use a time-window prior to re-reflection.

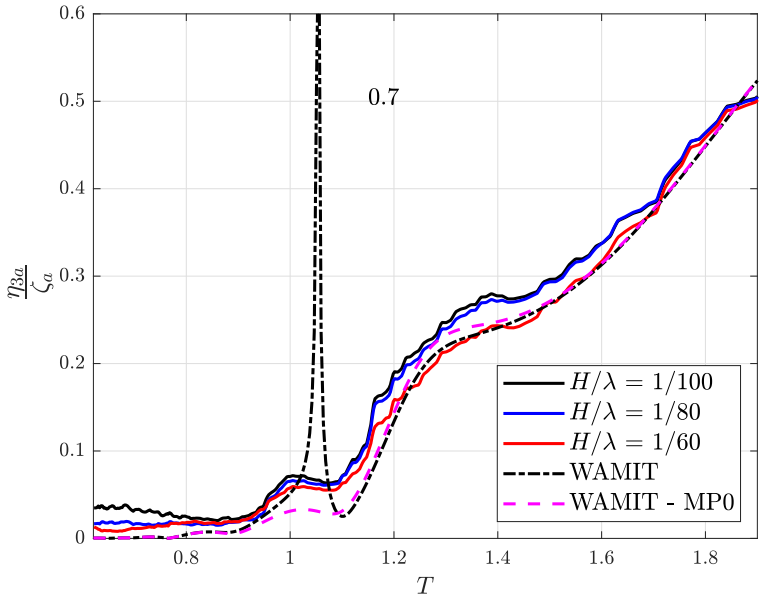

(a) MP1

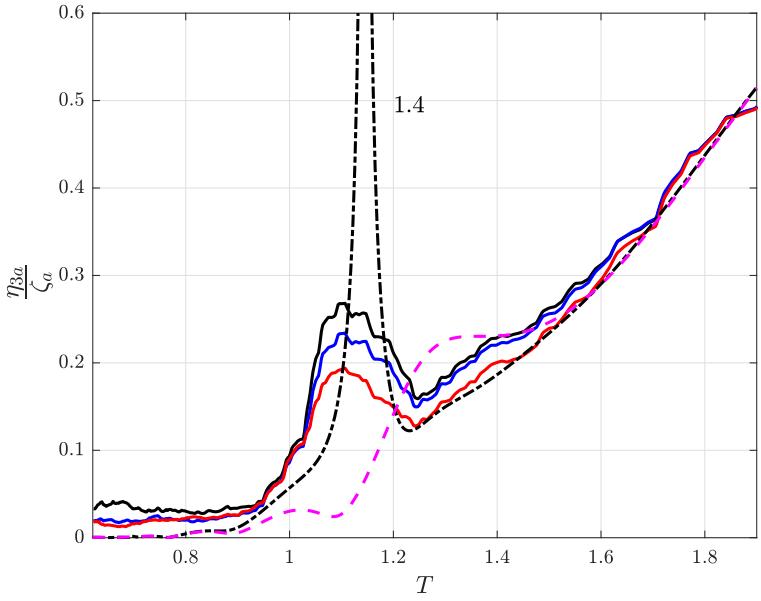

(b) MP2

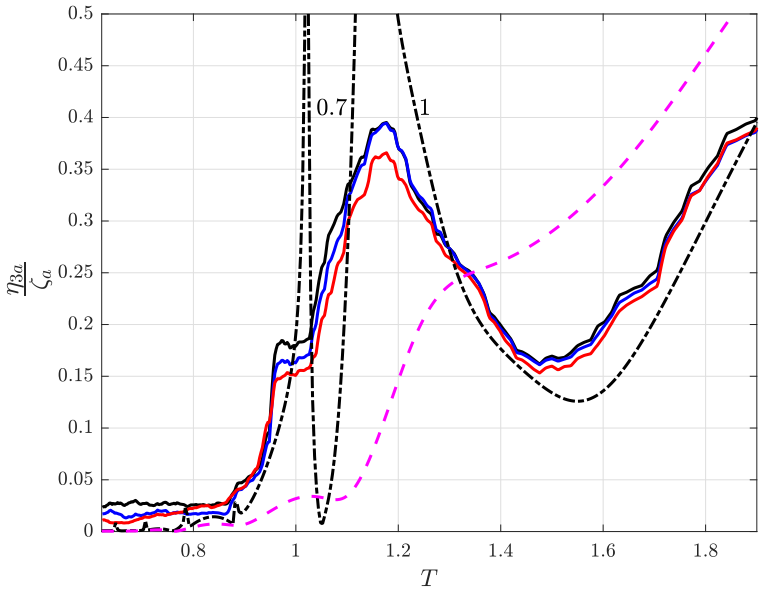

(c) MP3

Figure C.7: Heave RAOs in head sea from irregular wave tests. Only the first three minutes of the time-series are used, where the first 30 seconds are cut-off.

C.3.2 Selected time series

Selected time series of the nth harmonic moonpool responses from the model tests in the Ocean Basin are presented in Figure C.8. The measured responses are band pass filtered, such that the contribution from each harmonic component is illustrated.

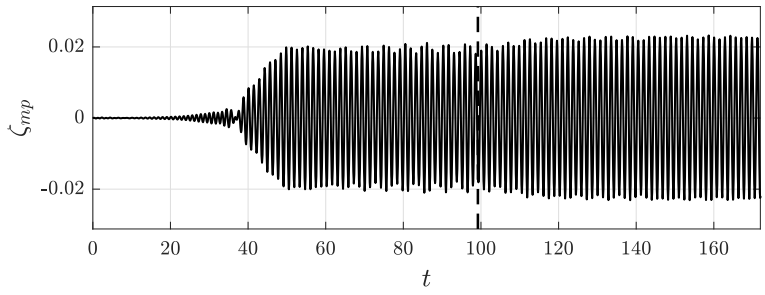

(a) First harmonic responses for MP2 at $T = 1.4$ s in beam sea.

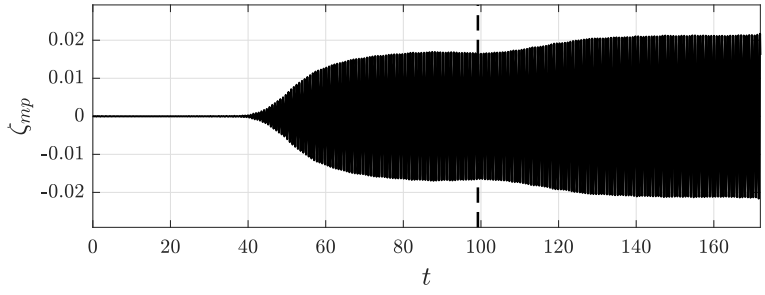

(b) Second harmonic responses for MP2 at $T = 1.4$ s in beam sea.

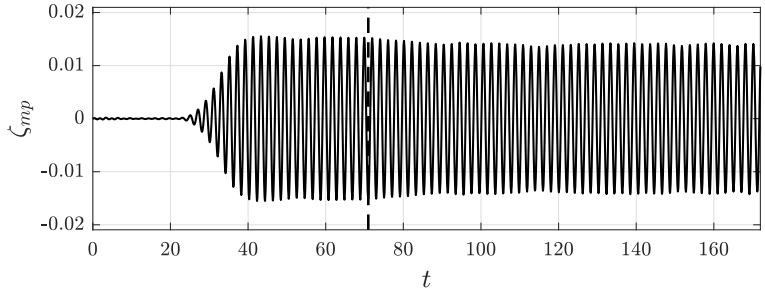

(c) First harmonic responses for MP3 at $T = 2.05$ s in head sea.

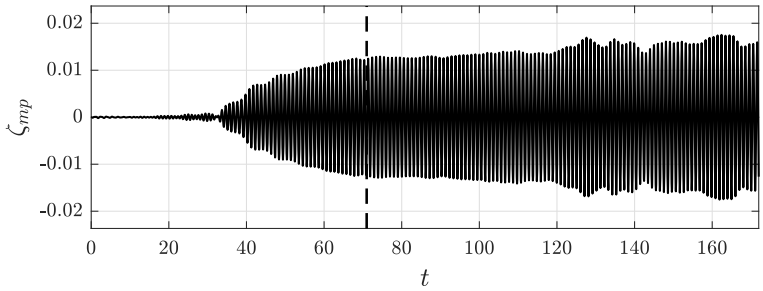

(d) Second harmonic responses for MP3 at $T = 2.05$ s in head sea.

Figure C.8: Selected time series of the nth harmonic moonpool responses from the model tests in regular waves in the Ocean Basin with wave steepness $H/\lambda = 1/60$. Measurements at WP1 are presented (cf. Figure 5.3). The dashed lines indicate the time until re-reflected waves affect the measurements, as predicted by linear wave theory.

C.4 Responses for MP1, MP2 and MP3

The moonpool, surge, sway and pitch responses for MP1, MP2 and MP3 are compared in Figure C.9. The results from the irregular wave tests with the PNWW spectra with $H/\lambda = 1/80$ are presented with WAMIT simulations.

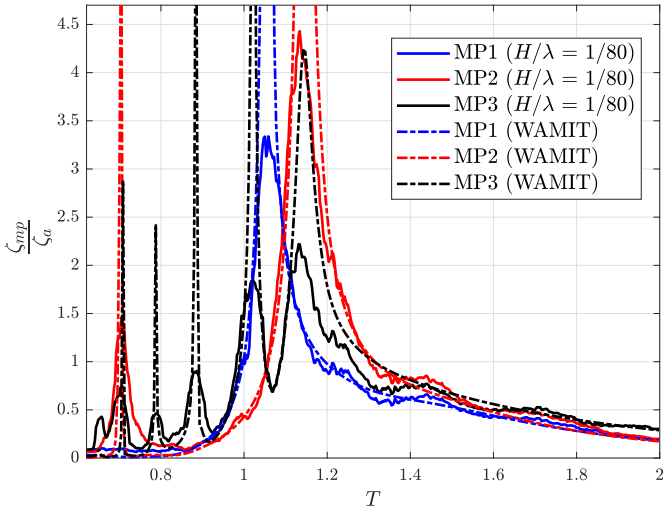

(a) Moonpool responses at WP1 in head sea

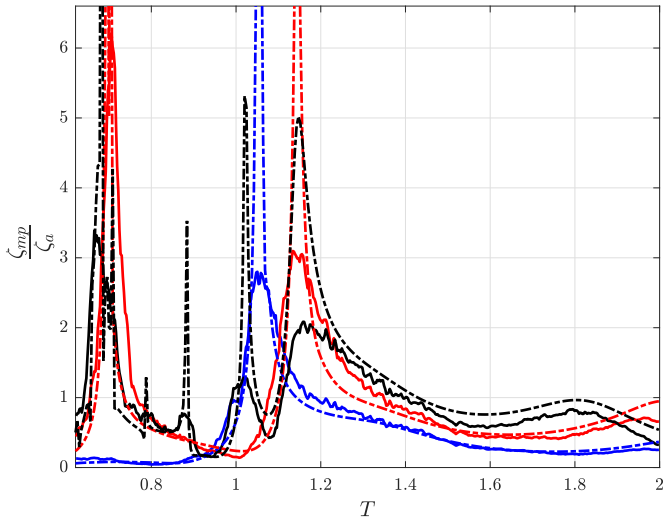

(b) Moonpool responses at WP1 in beam sea

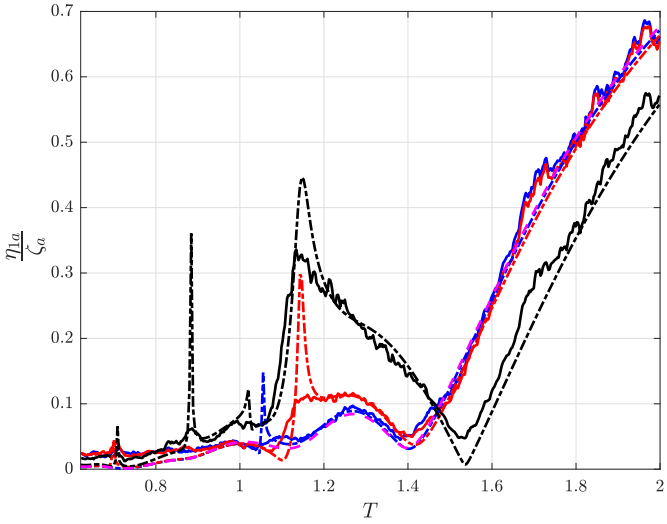

(c) Surge responses in head sea

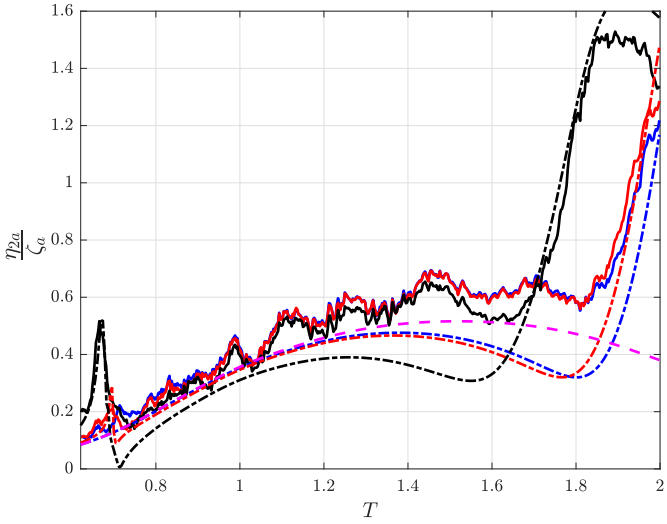

(d) Sway responses in beam sea

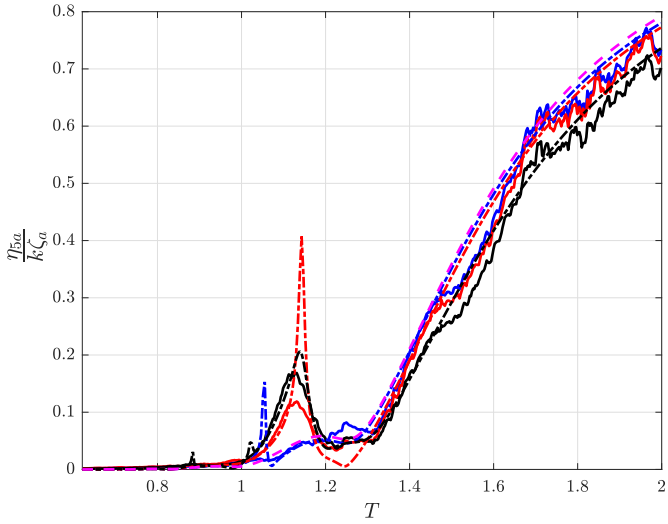

(e) Pitch responses in head sea

Figure C.9: Moonpool, surge, sway and pitch responses for MP1-3. The RAOs from the irregular wave tests with PNWW spectra and $H/\lambda = 1/80$ are presented with WAMIT simulations.

C.5 Higher harmonic moonpool responses for MP2 and MP3

The higher harmonic moonpool responses, as presented and discussed in §9.8, are presented in an alternative form in Figure C.10. The higher harmonic moonpool responses are made non-dimensional with respect to the incident wave amplitude, ζ_a. We present the RAOs in manner such that it is easier to relate the higher harmonic moonpool responses to the first harmonic moonpool responses, as presented in §9.4 and §9.5.

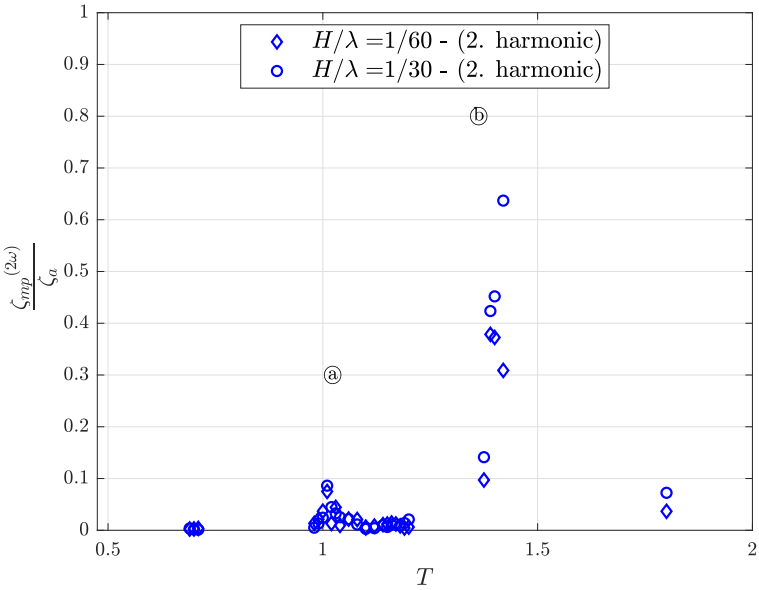

(a) Second harmonic - MP2 in head sea. ⓐ: Second longitudinal sloshing mode. ⓑ: First longitudinal sloshing mode.

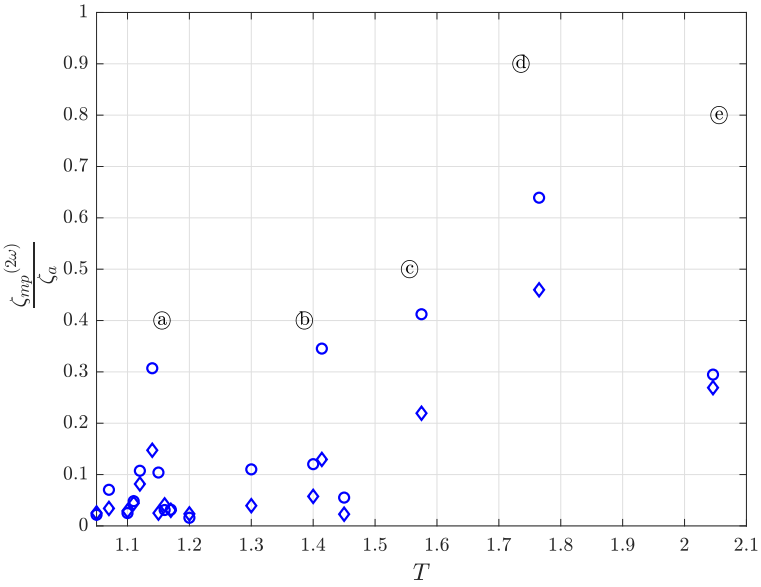

(b) Second harmonic - MP3 in head sea. ⓐ: Seventh longitudinal sloshing mode. ⓑ: Fifth longitudinal sloshing mode. ⓒ: Fourth longitudinal sloshing mode. ⓓ: Third longitudinal sloshing mode. ⓔ: Second longitudinal sloshing mode.

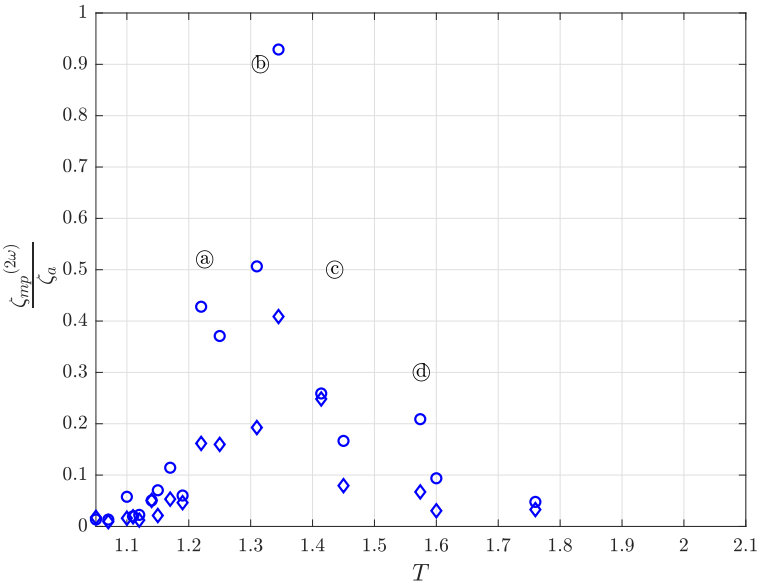

(c) Second harmonic - MP3 in beam sea. ⓐ: Second transverse sloshing mode. ⓑ: Sixth longitudinal sloshing mode. ⓒ: First transverse sloshing mode. ⓓ: Second longitudinal sloshing mode.

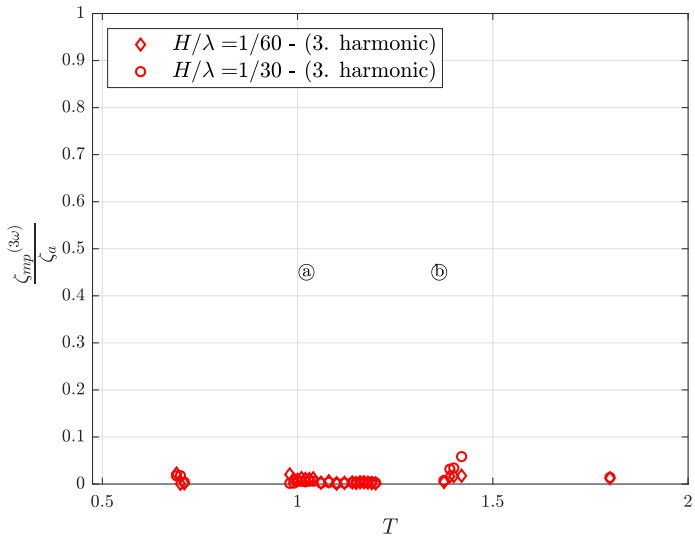

(d) Third harmonic - MP2 in head sea. ⓐ: Second longitudinal sloshing mode. ⓑ: First longitudinal sloshing mode.

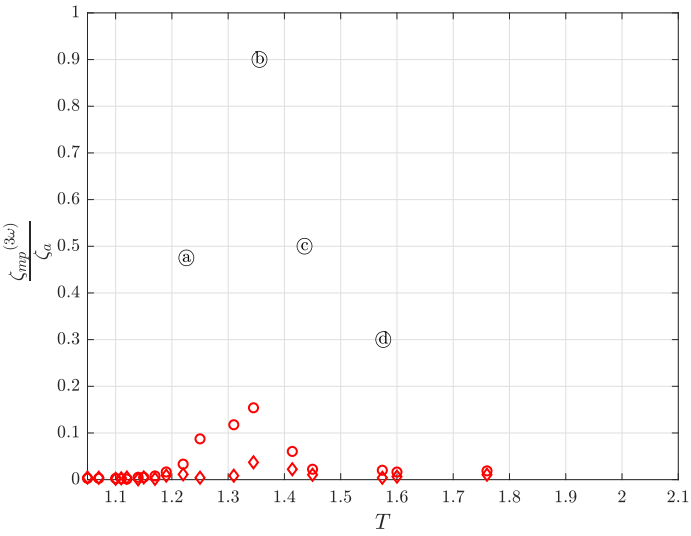

(e) Third harmonic - MP3 in beam sea. ⓐ: Second transverse sloshing mode. ⓑ: Sixth longitudinal sloshing mode. ⓒ: First transverse sloshing mode. ⓓ: Second longitudinal sloshing mode.

Figure C.10: Higher harmonic moonpool RAOs at WP1 (cf. Figure 5.3). The nth harmonic moonpool responses are made non-dimensional with respect to the incident wave amplitude, ζ_a, instead of $k^{n-1}\zeta_a^n$, as done in Figure 9.35.

Previous PhD theses published at the Department of Marine Technology (earlier: Faculty of Marine Technology) NORWEGIAN UNIVERSITY OF SCIENCE AND TECHNOLOGY

Report No.	Author	Title
	Kavlie, Dag	Optimization of Plane Elastic Grillages, 1967
	Hansen, Hans R.	Man-Machine Communication and Data-Storage Methods in Ship Structural Design, 1971
	Gisvold, Kaare M.	A Method for non-linear mixed -integer programming and its Application to Design Problems, 1971
	Lund, Sverre	Tanker Frame Optimalization by means of SUMT-Transformation and Behaviour Models, 1971
	Vinje, Tor	On Vibration of Spherical Shells Interacting with Fluid, 1972
	Lorentz, Jan D.	Tank Arrangement for Crude Oil Carriers in Accordance with the new Anti-Pollution Regulations, 1975
	Carlsen, Carl A.	Computer-Aided Design of Tanker Structures, 1975
	Larsen, Carl M.	Static and Dynamic Analysis of Offshore Pipelines during Installation, 1976
UR-79-01	Brigt Hatlestad, MK	The finite element method used in a fatigue evaluation of fixed offshore platforms. (Dr.Ing. Thesis)
UR-79-02	Erik Pettersen, MK	Analysis and design of cellular structures. (Dr.Ing. Thesis)
UR-79-03	Sverre Valsgård, MK	Finite difference and finite element methods applied to nonlinear analysis of plated structures. (Dr.Ing. Thesis)
UR-79-04	Nils T. Nordsve, MK	Finite element collapse analysis of structural members considering imperfections and stresses due to fabrication. (Dr.Ing. Thesis)
UR-79-05	Ivar J. Fylling, MK	Analysis of towline forces in ocean towing systems. (Dr.Ing. Thesis)
UR-80-06	Nils Sandsmark, MM	Analysis of Stationary and Transient Heat Conduction by the Use of the Finite Element Method. (Dr.Ing. Thesis)
UR-80-09	Sverre Haver, MK	Analysis of uncertainties related to the stochastic modeling of ocean waves. (Dr.Ing. Thesis)
UR-81-15	Odland, Jonas	On the Strength of welded Ring stiffened cylindrical Shells primarily subjected to axial Compression
UR-82-17	Engesvik, Knut	Analysis of Uncertainties in the fatigue Capacity of

		Welded Joints
UR-82-18	Rye, Henrik	Ocean wave groups
UR-83-30	Eide, Oddvar Inge	On Cumulative Fatigue Damage in Steel Welded Joints
UR-83-33	Mo, Olav	Stochastic Time Domain Analysis of Slender Offshore Structures
UR-83-34	Amdahl, Jørgen	Energy absorption in Ship-platform impacts
UR-84-37	Mørch, Morten	Motions and mooring forces of semi submersibles as determined by full-scale measurements and theoretical analysis
UR-84-38	Soares, C. Guedes	Probabilistic models for load effects in ship structures
UR-84-39	Aarsnes, Jan V.	Current forces on ships
UR-84-40	Czujko, Jerzy	Collapse Analysis of Plates subjected to Biaxial Compression and Lateral Load
UR-85-46	Alf G. Engseth, MK	Finite element collapse analysis of tubular steel offshore structures. (Dr.Ing. Thesis)
UR-86-47	Dengody Sheshappa, MP	A Computer Design Model for Optimizing Fishing Vessel Designs Based on Techno-Economic Analysis. (Dr.Ing. Thesis)
UR-86-48	Vidar Aanesland, MH	A Theoretical and Numerical Study of Ship Wave Resistance. (Dr.Ing. Thesis)
UR-86-49	Heinz-Joachim Wessel, MK	Fracture Mechanics Analysis of Crack Growth in Plate Girders. (Dr.Ing. Thesis)
UR-86-50	Jon Taby, MK	Ultimate and Post-ultimate Strength of Dented Tubular Members. (Dr.Ing. Thesis)
UR-86-51	Walter Lian, MH	A Numerical Study of Two-Dimensional Separated Flow Past Bluff Bodies at Moderate KC-Numbers. (Dr.Ing. Thesis)
UR-86-52	Bjørn Sortland, MH	Force Measurements in Oscillating Flow on Ship Sections and Circular Cylinders in a U-Tube Water Tank. (Dr.Ing. Thesis)
UR-86-53	Kurt Strand, MM	A System Dynamic Approach to One-dimensional Fluid Flow. (Dr.Ing. Thesis)
UR-86-54	Arne Edvin Løken, MH	Three Dimensional Second Order Hydrodynamic Effects on Ocean Structures in Waves. (Dr.Ing. Thesis)
UR-86-55	Sigurd Falch, MH	A Numerical Study of Slamming of Two-Dimensional Bodies. (Dr.Ing. Thesis)
UR-87-56	Arne Braathen, MH	Application of a Vortex Tracking Method to the Prediction of Roll Damping of a Two-Dimension Floating Body. (Dr.Ing. Thesis)

UR-87-57	Bernt Leira, MK	Gaussian Vector Processes for Reliability Analysis involving Wave-Induced Load Effects. (Dr.Ing. Thesis)
UR-87-58	Magnus Småvik, MM	Thermal Load and Process Characteristics in a Two-Stroke Diesel Engine with Thermal Barriers (in Norwegian). (Dr.Ing. Thesis)
MTA-88-59	Bernt Arild Bremdal, MP	An Investigation of Marine Installation Processes – A Knowledge - Based Planning Approach. (Dr.Ing. Thesis)
MTA-88-60	Xu Jun, MK	Non-linear Dynamic Analysis of Space-framed Offshore Structures. (Dr.Ing. Thesis)
MTA-89-61	Gang Miao, MH	Hydrodynamic Forces and Dynamic Responses of Circular Cylinders in Wave Zones. (Dr.Ing. Thesis)
MTA-89-62	Martin Greenhow, MH	Linear and Non-Linear Studies of Waves and Floating Bodies. Part I and Part II. (Dr.Techn. Thesis)
MTA-89-63	Chang Li, MH	Force Coefficients of Spheres and Cubes in Oscillatory Flow with and without Current. (Dr.Ing. Thesis
MTA-89-64	Hu Ying, MP	A Study of Marketing and Design in Development of Marine Transport Systems. (Dr.Ing. Thesis)
MTA-89-65	Arild Jæger, MH	Seakeeping, Dynamic Stability and Performance of a Wedge Shaped Planing Hull. (Dr.Ing. Thesis)
MTA-89-66	Chan Siu Hung, MM	The dynamic characteristics of tilting-pad bearings
MTA-89-67	Kim Wikstrøm, MP	Analysis av projekteringen for ett offshore projekt. (Licenciat-avhandling)
MTA-89-68	Jiao Guoyang, MK	Reliability Analysis of Crack Growth under Random Loading, considering Model Updating. (Dr.Ing. Thesis)
MTA-89-69	Arnt Olufsen, MK	Uncertainty and Reliability Analysis of Fixed Offshore Structures. (Dr.Ing. Thesis)
MTA-89-70	Wu Yu-Lin, MR	System Reliability Analyses of Offshore Structures using improved Truss and Beam Models. (Dr.Ing. Thesis)
MTA-90-71	Jan Roger Hoff, MH	Three-dimensional Green function of a vessel with forward speed in waves. (Dr.Ing. Thesis)
MTA-90-72	Rong Zhao, MH	Slow-Drift Motions of a Moored Two-Dimensional Body in Irregular Waves. (Dr.Ing. Thesis)
MTA-90-73	Atle Minsaas, MP	Economical Risk Analysis. (Dr.Ing. Thesis)
MTA-90-74	Knut-Aril Farnes, MK	Long-term Statistics of Response in Non-linear Marine Structures. (Dr.Ing. Thesis)
MTA-90-75	Torbjørn Sotberg, MK	Application of Reliability Methods for Safety Assessment of Submarine Pipelines. (Dr.Ing.

		Thesis)
MTA-90-76	Zeuthen, Steffen, MP	SEAMAID. A computational model of the design process in a constraint-based logic programming environment. An example from the offshore domain. (Dr.Ing. Thesis)
MTA-91-77	Haagensen, Sven, MM	Fuel Dependant Cyclic Variability in a Spark Ignition Engine - An Optical Approach. (Dr.Ing. Thesis)
MTA-91-78	Løland, Geir, MH	Current forces on and flow through fish farms. (Dr.Ing. Thesis)
MTA-91-79	Hoen, Christopher, MK	System Identification of Structures Excited by Stochastic Load Processes. (Dr.Ing. Thesis)
MTA-91-80	Haugen, Stein, MK	Probabilistic Evaluation of Frequency of Collision between Ships and Offshore Platforms. (Dr.Ing. Thesis)
MTA-91-81	Sødahl, Nils, MK	Methods for Design and Analysis of Flexible Risers. (Dr.Ing. Thesis)
MTA-91-82	Ormberg, Harald, MK	Non-linear Response Analysis of Floating Fish Farm Systems. (Dr.Ing. Thesis)
MTA-91-83	Marley, Mark J., MK	Time Variant Reliability under Fatigue Degradation. (Dr.Ing. Thesis)
MTA-91-84	Krokstad, Jørgen R., MH	Second-order Loads in Multidirectional Seas. (Dr.Ing. Thesis)
MTA-91-85	Molteberg, Gunnar A., MM	The Application of System Identification Techniques to Performance Monitoring of Four Stroke Turbocharged Diesel Engines. (Dr.Ing. Thesis)
MTA-92-86	Mørch, Hans Jørgen Bjelke, MH	Aspects of Hydrofoil Design: with Emphasis on Hydrofoil Interaction in Calm Water. (Dr.Ing. Thesis)
MTA-92-87	Chan Siu Hung, MM	Nonlinear Analysis of Rotordynamic Instabilities in Highspeed Turbomachinery. (Dr.Ing. Thesis)
MTA-92-88	Bessason, Bjarni, MK	Assessment of Earthquake Loading and Response of Seismically Isolated Bridges. (Dr.Ing. Thesis)
MTA-92-89	Langli, Geir, MP	Improving Operational Safety through exploitation of Design Knowledge - an investigation of offshore platform safety. (Dr.Ing. Thesis)
MTA-92-90	Sævik, Svein, MK	On Stresses and Fatigue in Flexible Pipes. (Dr.Ing. Thesis)
MTA-92-91	Ask, Tor Ø., MM	Ignition and Flame Growth in Lean Gas-Air Mixtures. An Experimental Study with a Schlieren System. (Dr.Ing. Thesis)
MTA-86-92	Hessen, Gunnar, MK	Fracture Mechanics Analysis of Stiffened Tubular Members. (Dr.Ing. Thesis)

MTA-93-93	Steinebach, Christian, MM	Knowledge Based Systems for Diagnosis of Rotating Machinery. (Dr.Ing. Thesis)
MTA-93-94	Dalane, Jan Inge, MK	System Reliability in Design and Maintenance of Fixed Offshore Structures. (Dr.Ing. Thesis)
MTA-93-95	Steen, Sverre, MH	Cobblestone Effect on SES. (Dr.Ing. Thesis)
MTA-93-96	Karunakaran, Daniel, MK	Nonlinear Dynamic Response and Reliability Analysis of Drag-dominated Offshore Platforms. (Dr.Ing. Thesis)
MTA-93-97	Hagen, Arnulf, MP	The Framework of a Design Process Language. (Dr.Ing. Thesis)
MTA-93-98	Nordrik, Rune, MM	Investigation of Spark Ignition and Autoignition in Methane and Air Using Computational Fluid Dynamics and Chemical Reaction Kinetics. A Numerical Study of Ignition Processes in Internal Combustion Engines. (Dr.Ing. Thesis)
MTA-94-99	Passano, Elizabeth, MK	Efficient Analysis of Nonlinear Slender Marine Structures. (Dr.Ing. Thesis)
MTA-94-100	Kvålsvold, Jan, MH	Hydroelastic Modelling of Wetdeck Slamming on Multihull Vessels. (Dr.Ing. Thesis)
MTA-94-102	Bech, Sidsel M., MK	Experimental and Numerical Determination of Stiffness and Strength of GRP/PVC Sandwich Structures. (Dr.Ing. Thesis)
MTA-95-103	Paulsen, Hallvard, MM	A Study of Transient Jet and Spray using a Schlieren Method and Digital Image Processing. (Dr.Ing. Thesis)
MTA-95-104	Hovde, Geir Olav, MK	Fatigue and Overload Reliability of Offshore Structural Systems, Considering the Effect of Inspection and Repair. (Dr.Ing. Thesis)
MTA-95-105	Wang, Xiaozhi, MK	Reliability Analysis of Production Ships with Emphasis on Load Combination and Ultimate Strength. (Dr.Ing. Thesis)
MTA-95-106	Ulstein, Tore, MH	Nonlinear Effects of a Flexible Stern Seal Bag on Cobblestone Oscillations of an SES. (Dr.Ing. Thesis)
MTA-95-107	Solaas, Frøydis, MH	Analytical and Numerical Studies of Sloshing in Tanks. (Dr.Ing. Thesis)
MTA-95-108	Hellan, Øyvind, MK	Nonlinear Pushover and Cyclic Analyses in Ultimate Limit State Design and Reassessment of Tubular Steel Offshore Structures. (Dr.Ing. Thesis)
MTA-95-109	Hermundstad, Ole A., MK	Theoretical and Experimental Hydroelastic Analysis of High Speed Vessels. (Dr.Ing. Thesis)
MTA-96-110	Bratland, Anne K., MH	Wave-Current Interaction Effects on Large-Volume Bodies in Water of Finite Depth. (Dr.Ing. Thesis)
MTA-96-111	Herfjord, Kjell, MH	A Study of Two-dimensional Separated Flow by a Combination of the Finite Element Method and

		Navier-Stokes Equations. (Dr.Ing. Thesis)
MTA-96-112	Æsøy, Vilmar, MM	Hot Surface Assisted Compression Ignition in a Direct Injection Natural Gas Engine. (Dr.Ing. Thesis)
MTA-96-113	Eknes, Monika L., MK	Escalation Scenarios Initiated by Gas Explosions on Offshore Installations. (Dr.Ing. Thesis)
MTA-96-114	Erikstad, Stein O., MP	A Decision Support Model for Preliminary Ship Design. (Dr.Ing. Thesis)
MTA-96-115	Pedersen, Egil, MH	A Nautical Study of Towed Marine Seismic Streamer Cable Configurations. (Dr.Ing. Thesis)
MTA-97-116	Moksnes, Paul O., MM	Modelling Two-Phase Thermo-Fluid Systems Using Bond Graphs. (Dr.Ing. Thesis)
MTA-97-117	Halse, Karl H., MK	On Vortex Shedding and Prediction of Vortex-Induced Vibrations of Circular Cylinders. (Dr.Ing. Thesis)
MTA-97-118	Igland, Ragnar T., MK	Reliability Analysis of Pipelines during Laying, considering Ultimate Strength under Combined Loads. (Dr.Ing. Thesis)
MTA-97-119	Pedersen, Hans-P., MP	Levendefiskteknologi for fiskefartøy. (Dr.Ing. Thesis)
MTA-98-120	Vikestad, Kyrre, MK	Multi-Frequency Response of a Cylinder Subjected to Vortex Shedding and Support Motions. (Dr.Ing. Thesis)
MTA-98-121	Azadi, Mohammad R. E., MK	Analysis of Static and Dynamic Pile-Soil-Jacket Behaviour. (Dr.Ing. Thesis)
MTA-98-122	Ulltang, Terje, MP	A Communication Model for Product Information. (Dr.Ing. Thesis)
MTA-98-123	Torbergsen, Erik, MM	Impeller/Diffuser Interaction Forces in Centrifugal Pumps. (Dr.Ing. Thesis)
MTA-98-124	Hansen, Edmond, MH	A Discrete Element Model to Study Marginal Ice Zone Dynamics and the Behaviour of Vessels Moored in Broken Ice. (Dr.Ing. Thesis)
MTA-98-125	Videiro, Paulo M., MK	Reliability Based Design of Marine Structures. (Dr.Ing. Thesis)
MTA-99-126	Mainçon, Philippe, MK	Fatigue Reliability of Long Welds Application to Titanium Risers. (Dr.Ing. Thesis)
MTA-99-127	Haugen, Elin M., MH	Hydroelastic Analysis of Slamming on Stiffened Plates with Application to Catamaran Wetdecks. (Dr.Ing. Thesis)
MTA-99-128	Langhelle, Nina K., MK	Experimental Validation and Calibration of Nonlinear Finite Element Models for Use in Design of Aluminium Structures Exposed to Fire. (Dr.Ing. Thesis)
MTA-99-	Berstad, Are J., MK	Calculation of Fatigue Damage in Ship Structures.

129		(Dr.Ing. Thesis)
MTA-99-130	Andersen, Trond M., MM	Short Term Maintenance Planning. (Dr.Ing. Thesis)
MTA-99-131	Tveiten, Bård Wathne, MK	Fatigue Assessment of Welded Aluminium Ship Details. (Dr.Ing. Thesis)
MTA-99-132	Søreide, Fredrik, MP	Applications of underwater technology in deep water archaeology. Principles and practice. (Dr.Ing. Thesis)
MTA-99-133	Tønnessen, Rune, MH	A Finite Element Method Applied to Unsteady Viscous Flow Around 2D Blunt Bodies With Sharp Corners. (Dr.Ing. Thesis)
MTA-99-134	Elvekrok, Dag R., MP	Engineering Integration in Field Development Projects in the Norwegian Oil and Gas Industry. The Supplier Management of Norne. (Dr.Ing. Thesis)
MTA-99-135	Fagerholt, Kjetil, MP	Optimeringsbaserte Metoder for Ruteplanlegging innen skipsfart. (Dr.Ing. Thesis)
MTA-99-136	Bysveen, Marie, MM	Visualization in Two Directions on a Dynamic Combustion Rig for Studies of Fuel Quality. (Dr.Ing. Thesis)
MTA-2000-137	Storteig, Eskild, MM	Dynamic characteristics and leakage performance of liquid annular seals in centrifugal pumps. (Dr.Ing. Thesis)
MTA-2000-138	Sagli, Gro, MK	Model uncertainty and simplified estimates of long term extremes of hull girder loads in ships. (Dr.Ing. Thesis)
MTA-2000-139	Tronstad, Harald, MK	Nonlinear analysis and design of cable net structures like fishing gear based on the finite element method. (Dr.Ing. Thesis)
MTA-2000-140	Kroneberg, André, MP	Innovation in shipping by using scenarios. (Dr.Ing. Thesis)
MTA-2000-141	Haslum, Herbjørn Alf, MH	Simplified methods applied to nonlinear motion of spar platforms. (Dr.Ing. Thesis)
MTA-2001-142	Samdal, Ole Johan, MM	Modelling of Degradation Mechanisms and Stressor Interaction on Static Mechanical Equipment Residual Lifetime. (Dr.Ing. Thesis)
MTA-2001-143	Baarholm, Rolf Jarle, MH	Theoretical and experimental studies of wave impact underneath decks of offshore platforms. (Dr.Ing. Thesis)
MTA-2001-144	Wang, Lihua, MK	Probabilistic Analysis of Nonlinear Wave-induced Loads on Ships. (Dr.Ing. Thesis)
MTA-2001-145	Kristensen, Odd H. Holt, MK	Ultimate Capacity of Aluminium Plates under Multiple Loads, Considering HAZ Properties. (Dr.Ing. Thesis)
MTA-2001-146	Greco, Marilena, MH	A Two-Dimensional Study of Green-Water

		Loading. (Dr.Ing. Thesis)
MTA-2001-147	Heggelund, Svein E., MK	Calculation of Global Design Loads and Load Effects in Large High Speed Catamarans. (Dr.Ing. Thesis)
MTA-2001-148	Babalola, Olusegun T., MK	Fatigue Strength of Titanium Risers – Defect Sensitivity. (Dr.Ing. Thesis)
MTA-2001-149	Mohammed, Abuu K., MK	Nonlinear Shell Finite Elements for Ultimate Strength and Collapse Analysis of Ship Structures. (Dr.Ing. Thesis)
MTA-2002-150	Holmedal, Lars E., MH	Wave-current interactions in the vicinity of the sea bed. (Dr.Ing. Thesis)
MTA-2002-151	Rognebakke, Olav F., MH	Sloshing in rectangular tanks and interaction with ship motions. (Dr.Ing. Thesis)
MTA-2002-152	Lader, Pål Furset, MH	Geometry and Kinematics of Breaking Waves. (Dr.Ing. Thesis)
MTA-2002-153	Yang, Qinzheng, MH	Wash and wave resistance of ships in finite water depth. (Dr.Ing. Thesis)
MTA-2002-154	Melhus, Øyvin, MM	Utilization of VOC in Diesel Engines. Ignition and combustion of VOC released by crude oil tankers. (Dr.Ing. Thesis)
MTA-2002-155	Ronæss, Marit, MH	Wave Induced Motions of Two Ships Advancing on Parallel Course. (Dr.Ing. Thesis)
MTA-2002-156	Økland, Ole D., MK	Numerical and experimental investigation of whipping in twin hull vessels exposed to severe wet deck slamming. (Dr.Ing. Thesis)
MTA-2002-157	Ge, Chunhua, MK	Global Hydroelastic Response of Catamarans due to Wet Deck Slamming. (Dr.Ing. Thesis)
MTA-2002-158	Byklum, Eirik, MK	Nonlinear Shell Finite Elements for Ultimate Strength and Collapse Analysis of Ship Structures. (Dr.Ing. Thesis)
IMT-2003-1	Chen, Haibo, MK	Probabilistic Evaluation of FPSO-Tanker Collision in Tandem Offloading Operation. (Dr.Ing. Thesis)
IMT-2003-2	Skaugset, Kjetil Bjørn, MK	On the Suppression of Vortex Induced Vibrations of Circular Cylinders by Radial Water Jets. (Dr.Ing. Thesis)
IMT-2003-3	Chezhian, Muthu	Three-Dimensional Analysis of Slamming. (Dr.Ing. Thesis)
IMT-2003-4	Buhaug, Øyvind	Deposit Formation on Cylinder Liner Surfaces in Medium Speed Engines. (Dr.Ing. Thesis)
IMT-2003-5	Tregde, Vidar	Aspects of Ship Design: Optimization of Aft Hull with Inverse Geometry Design. (Dr.Ing. Thesis)
IMT-	Wist, Hanne Therese	Statistical Properties of Successive Ocean Wave

2003-6		Parameters. (Dr.Ing. Thesis)
IMT-2004-7	Ransau, Samuel	Numerical Methods for Flows with Evolving Interfaces. (Dr.Ing. Thesis)
IMT-2004-8	Soma, Torkel	Blue-Chip or Sub-Standard. A data interrogation approach of identity safety characteristics of shipping organization. (Dr.Ing. Thesis)
IMT-2004-9	Ersdal, Svein	An experimental study of hydrodynamic forces on cylinders and cables in near axial flow. (Dr.Ing. Thesis)
IMT-2005-10	Brodtkorb, Per Andreas	The Probability of Occurrence of Dangerous Wave Situations at Sea. (Dr.Ing. Thesis)
IMT-2005-11	Yttervik, Rune	Ocean current variability in relation to offshore engineering. (Dr.Ing. Thesis)
IMT-2005-12	Fredheim, Arne	Current Forces on Net-Structures. (Dr.Ing. Thesis)
IMT-2005-13	Heggernes, Kjetil	Flow around marine structures. (Dr.Ing. Thesis
IMT-2005-14	Fouques, Sebastien	Lagrangian Modelling of Ocean Surface Waves and Synthetic Aperture Radar Wave Measurements. (Dr.Ing. Thesis)
IMT-2006-15	Holm, Håvard	Numerical calculation of viscous free surface flow around marine structures. (Dr.Ing. Thesis)
IMT-2006-16	Bjørheim, Lars G.	Failure Assessment of Long Through Thickness Fatigue Cracks in Ship Hulls. (Dr.Ing. Thesis)
IMT-2006-17	Hansson, Lisbeth	Safety Management for Prevention of Occupational Accidents. (Dr.Ing. Thesis)
IMT-2006-18	Zhu, Xinying	Application of the CIP Method to Strongly Nonlinear Wave-Body Interaction Problems. (Dr.Ing. Thesis)
IMT-2006-19	Reite, Karl Johan	Modelling and Control of Trawl Systems. (Dr.Ing. Thesis)
IMT-2006-20	Smogeli, Øyvind Notland	Control of Marine Propellers. From Normal to Extreme Conditions. (Dr.Ing. Thesis)
IMT-2007-21	Storhaug, Gaute	Experimental Investigation of Wave Induced Vibrations and Their Effect on the Fatigue Loading of Ships. (Dr.Ing. Thesis)
IMT-2007-22	Sun, Hui	A Boundary Element Method Applied to Strongly Nonlinear Wave-Body Interaction Problems. (PhD Thesis, CeSOS)
IMT-2007-23	Rustad, Anne Marthine	Modelling and Control of Top Tensioned Risers. (PhD Thesis, CeSOS)
IMT-2007-24	Johansen, Vegar	Modelling flexible slender system for real-time simulations and control applications
IMT-2007-25	Wroldsen, Anders Sunde	Modelling and control of tensegrity structures.

		(PhD Thesis, CeSOS)
IMT-2007-26	Aronsen, Kristoffer Høye	An experimental investigation of in-line and combined inline and cross flow vortex induced vibrations. (Dr. avhandling, IMT)
IMT-2007-27	Gao, Zhen	Stochastic Response Analysis of Mooring Systems with Emphasis on Frequency-domain Analysis of Fatigue due to Wide-band Response Processes (PhD Thesis, CeSOS)
IMT-2007-28	Thorstensen, Tom Anders	Lifetime Profit Modelling of Ageing Systems Utilizing Information about Technical Condition. (Dr.ing. thesis, IMT)
IMT-2008-29	Refsnes, Jon Erling Gorset	Nonlinear Model-Based Control of Slender Body AUVs (PhD Thesis, IMT)
IMT-2008-30	Berntsen, Per Ivar B.	Structural Reliability Based Position Mooring. (PhD-Thesis, IMT)
IMT-2008-31	Ye, Naiquan	Fatigue Assessment of Aluminium Welded Box-stiffener Joints in Ships (Dr.ing. thesis, IMT)
IMT-2008-32	Radan, Damir	Integrated Control of Marine Electrical Power Systems. (PhD-Thesis, IMT)
IMT-2008-33	Thomassen, Paul	Methods for Dynamic Response Analysis and Fatigue Life Estimation of Floating Fish Cages. (Dr.ing. thesis, IMT)
IMT-2008-34	Pákozdi, Csaba	A Smoothed Particle Hydrodynamics Study of Two-dimensional Nonlinear Sloshing in Rectangular Tanks. (Dr.ing.thesis, IMT/ CeSOS)
IMT-2007-35	Grytøyr, Guttorm	A Higher-Order Boundary Element Method and Applications to Marine Hydrodynamics. (Dr.ing.thesis, IMT)
IMT-2008-36	Drummen, Ingo	Experimental and Numerical Investigation of Nonlinear Wave-Induced Load Effects in Containerships considering Hydroelasticity. (PhD thesis, CeSOS)
IMT-2008-37	Skejic, Renato	Maneuvering and Seakeeping of a Singel Ship and of Two Ships in Interaction. (PhD-Thesis, CeSOS)
IMT-2008-38	Harlem, Alf	An Age-Based Replacement Model for Repairable Systems with Attention to High-Speed Marine Diesel Engines. (PhD-Thesis, IMT)
IMT-2008-39	Alsos, Hagbart S.	Ship Grounding. Analysis of Ductile Fracture, Bottom Damage and Hull Girder Response. (PhD-thesis, IMT)
IMT-2008-40	Graczyk, Mateusz	Experimental Investigation of Sloshing Loading and Load Effects in Membrane LNG Tanks Subjected to Random Excitation. (PhD-thesis, CeSOS)
IMT-2008-41	Taghipour, Reza	Efficient Prediction of Dynamic Response for Flexible amd Multi-body Marine Structures. (PhD-

		thesis, CeSOS)
IMT-2008-42	Ruth, Eivind	Propulsion control and thrust allocation on marine vessels. (PhD thesis, CeSOS)
IMT-2008-43	Nystad, Bent Helge	Technical Condition Indexes and Remaining Useful Life of Aggregated Systems. PhD thesis, IMT
IMT-2008-44	Soni, Prashant Kumar	Hydrodynamic Coefficients for Vortex Induced Vibrations of Flexible Beams, PhD thesis, CeSOS
IMT-2009-45	Amlashi, Hadi K.K.	Ultimate Strength and Reliability-based Design of Ship Hulls with Emphasis on Combined Global and Local Loads. PhD Thesis, IMT
IMT-2009-46	Pedersen, Tom Arne	Bond Graph Modelling of Marine Power Systems. PhD Thesis, IMT
IMT-2009-47	Kristiansen, Trygve	Two-Dimensional Numerical and Experimental Studies of Piston-Mode Resonance. PhD-Thesis, CeSOS
IMT-2009-48	Ong, Muk Chen	Applications of a Standard High Reynolds Number Model and a Stochastic Scour Prediction Model for Marine Structures. PhD-thesis, IMT
IMT-2009-49	Hong, Lin	Simplified Analysis and Design of Ships subjected to Collision and Grounding. PhD-thesis, IMT
IMT-2009-50	Koushan, Kamran	Vortex Induced Vibrations of Free Span Pipelines, PhD thesis, IMT
IMT-2009-51	Korsvik, Jarl Eirik	Heuristic Methods for Ship Routing and Scheduling. PhD-thesis, IMT
IMT-2009-52	Lee, Jihoon	Experimental Investigation and Numerical in Analyzing the Ocean Current Displacement of Longlines. Ph.d.-Thesis, IMT.
IMT-2009-53	Vestbøstad, Tone Gran	A Numerical Study of Wave-in-Deck Impact usin a Two-Dimensional Constrained Interpolation Profile Method, Ph.d.thesis, CeSOS.
IMT-2009-54	Bruun, Kristine	Bond Graph Modelling of Fuel Cells for Marine Power Plants. Ph.d.-thesis, IMT
IMT 2009-55	Holstad, Anders	Numerical Investigation of Turbulence in a Sekwed Three-Dimensional Channel Flow, Ph.d.-thesis, IMT.
IMT 2009-56	Ayala-Uraga, Efren	Reliability-Based Assessment of Deteriorating Ship-shaped Offshore Structures, Ph.d.-thesis, IMT
IMT 2009-57	Kong, Xiangjun	A Numerical Study of a Damaged Ship in Beam Sea Waves. Ph.d.-thesis, IMT/CeSOS.
IMT 2010-58	Kristiansen, David	Wave Induced Effects on Floaters of Aquaculture Plants, Ph.d.-thesis, CeSOS.

IMT 2010-59	Ludvigsen, Martin	An ROV-Toolbox for Optical and Acoustic Scientific Seabed Investigation. Ph.d.-thesis IMT.
IMT 2010-60	Hals, Jørgen	Modelling and Phase Control of Wave-Energy Converters. Ph.d.thesis, CeSOS.
IMT 2010- 61	Shu, Zhi	Uncertainty Assessment of Wave Loads and Ultimate Strength of Tankers and Bulk Carriers in a Reliability Framework. Ph.d. Thesis, IMT/ CeSOS
IMT 2010-62	Shao, Yanlin	Numerical Potential-Flow Studies on Weakly-Nonlinear Wave-Body Interactions with/without Small Forward Speed, Ph.d.thesis,CeSOS.
IMT 2010-63	Califano, Andrea	Dynamic Loads on Marine Propellers due to Intermittent Ventilation. Ph.d.thesis, IMT.
IMT 2010-64	El Khoury, George	Numerical Simulations of Massively Separated Turbulent Flows, Ph.d.-thesis, IMT
IMT 2010-65	Seim, Knut Sponheim	Mixing Process in Dense Overflows with Emphasis on the Faroe Bank Channel Overflow. Ph.d.thesis, IMT
IMT 2010-66	Jia, Huirong	Structural Analysis of Intect and Damaged Ships in a Collission Risk Analysis Perspective. Ph.d.thesis CeSoS.
IMT 2010-67	Jiao, Linlin	Wave-Induced Effects on a Pontoon-type Very Large Floating Structures (VLFS). Ph.D.-thesis, CeSOS.
IMT 2010-68	Abrahamsen, Bjørn Christian	Sloshing Induced Tank Roof with Entrapped Air Pocket. Ph.d.thesis, CeSOS.
IMT 2011-69	Karimirad, Madjid	Stochastic Dynamic Response Analysis of Spar-Type Wind Turbines with Catenary or Taut Mooring Systems. Ph.d.-thesis, CeSOS.
IMT - 2011-70	Erlend Meland	Condition Monitoring of Safety Critical Valves. Ph.d.-thesis, IMT.
IMT – 2011-71	Yang, Limin	Stochastic Dynamic System Analysis of Wave Energy Converter with Hydraulic Power Take-Off, with Particular Reference to Wear Damage Analysis, Ph.d. Thesis, CeSOS.
IMT – 2011-72	Visscher, Jan	Application of Particla Image Velocimetry on Turbulent Marine Flows, Ph.d.Thesis, IMT.
IMT – 2011-73	Su, Biao	Numerical Predictions of Global and Local Ice Loads on Ships. Ph.d.Thesis, CeSOS.
IMT – 2011-74	Liu, Zhenhui	Analytical and Numerical Analysis of Iceberg Collision with Ship Structures. Ph.d.Thesis, IMT.
IMT – 2011-75	Aarsæther, Karl Gunnar	Modeling and Analysis of Ship Traffic by Observation and Numerical Simulation. Ph.d.Thesis, IMT.

Imt – 2011-76	Wu, Jie	Hydrodynamic Force Identification from Stochastic Vortex Induced Vibration Experiments with Slender Beams. Ph.d.Thesis, IMT.
Imt – 2011-77	Amini, Hamid	Azimuth Propulsors in Off-design Conditions. Ph.d.Thesis, IMT.
IMT – 2011-78	Nguyen, Tan-Hoi	Toward a System of Real-Time Prediction and Monitoring of Bottom Damage Conditions During Ship Grounding. Ph.d.thesis, IMT.
IMT- 2011-79	Tavakoli, Mohammad T.	Assessment of Oil Spill in Ship Collision and Grounding, Ph.d.thesis, IMT.
IMT- 2011-80	Guo, Bingjie	Numerical and Experimental Investigation of Added Resistance in Waves. Ph.d.Thesis, IMT.
IMT- 2011-81	Chen, Qiaofeng	Ultimate Strength of Aluminium Panels, considering HAZ Effects, IMT
IMT- 2012-82	Kota, Ravikiran S.	Wave Loads on Decks of Offshore Structures in Random Seas, CeSOS.
IMT- 2012-83	Sten, Ronny	Dynamic Simulation of Deep Water Drilling Risers with Heave Compensating System, IMT.
IMT- 2012-84	Berle, Øyvind	Risk and resilience in global maritime supply chains, IMT.
IMT- 2012-85	Fang, Shaoji	Fault Tolerant Position Mooring Control Based on Structural Reliability, CeSOS.
IMT- 2012-86	You, Jikun	Numerical studies on wave forces and moored ship motions in intermediate and shallow water, CeSOS.
IMT- 2012-87	Xiang ,Xu	Maneuvering of two interacting ships in waves, CeSOS
IMT- 2012-88	Dong, Wenbin	Time-domain fatigue response and reliability analysis of offshore wind turbines with emphasis on welded tubular joints and gear components, CeSOS
IMT- 2012-89	Zhu, Suji	Investigation of Wave-Induced Nonlinear Load Effects in Open Ships considering Hull Girder Vibrations in Bending and Torsion, CeSOS
IMT- 2012-90	Zhou, Li	Numerical and Experimental Investigation of Station-keeping in Level Ice, CeSOS
IMT- 2012-91	Ushakov, Sergey	Particulate matter emission characteristics from diesel enignes operating on conventional and alternative marine fuels, IMT
IMT- 2013-1	Yin, Decao	Experimental and Numerical Analysis of Combined In-line and Cross-flow Vortex Induced Vibrations, CeSOS

IMT-2013-2	Kurniawan, Adi	Modelling and geometry optimisation of wave energy converters, CeSOS
IMT-2013-3	Al Ryati, Nabil	Technical condition indexes doe auxiliary marine diesel engines, IMT
IMT-2013-4	Firoozkoohi, Reza	Experimental, numerical and analytical investigation of the effect of screens on sloshing, CeSOS
IMT-2013-5	Ommani, Babak	Potential-Flow Predictions of a Semi-Displacement Vessel Including Applications to Calm Water Broaching, CeSOS
IMT-2013-6	Xing, Yihan	Modelling and analysis of the gearbox in a floating spar-type wind turbine, CeSOS
IMT-7-2013	Balland, Océane	Optimization models for reducing air emissions from ships, IMT
IMT-8-2013	Yang, Dan	Transitional wake flow behind an inclined flat plate-----Computation and analysis, IMT
IMT-9-2013	Abdillah, Suyuthi	Prediction of Extreme Loads and Fatigue Damage for a Ship Hull due to Ice Action, IMT
IMT-10-2013	Ramìrez, Pedro Agustìn Pèrez	Ageing management and life extension of technical systems- Concepts and methods applied to oil and gas facilities, IMT
IMT-11-2013	Chuang, Zhenju	Experimental and Numerical Investigation of Speed Loss due to Seakeeping and Maneuvering. IMT
IMT-12-2013	Etemaddar, Mahmoud	Load and Response Analysis of Wind Turbines under Atmospheric Icing and Controller System Faults with Emphasis on Spar Type Floating Wind Turbines, IMT
IMT-13-2013	Lindstad, Haakon	Strategies and measures for reducing maritime CO2 emissons, IMT
IMT-14-2013	Haris, Sabril	Damage interaction analysis of ship collisions, IMT
IMT-15-2013	Shainee, Mohamed	Conceptual Design, Numerical and Experimental Investigation of a SPM Cage Concept for Offshore Mariculture, IMT
IMT-16-2013	Gansel, Lars	Flow past porous cylinders and effects of biofouling and fish behavior on the flow in and around Atlantic salmon net cages, IMT
IMT-17-2013	Gaspar, Henrique	Handling Aspects of Complexity in Conceptual Ship Design, IMT
IMT-18-2013	Thys, Maxime	Theoretical and Experimental Investigation of a Free Running Fishing Vessel at Small Frequency of Encounter, CeSOS
IMT-19-2013	Aglen, Ida	VIV in Free Spanning Pipelines, CeSOS

IMT-1-2014	Song, An	Theoretical and experimental studies of wave diffraction and radiation loads on a horizontally submerged perforated plate, CeSOS
IMT-2-2014	Rogne, Øyvind Ygre	Numerical and Experimental Investigation of a Hinged 5-body Wave Energy Converter, CeSOS
IMT-3-2014	Dai, Lijuan	Safe and efficient operation and maintenance of offshore wind farms ,IMT
IMT-4-2014	Bachynski, Erin Elizabeth	Design and Dynamic Analysis of Tension Leg Platform Wind Turbines, CeSOS
IMT-5-2014	Wang, Jingbo	Water Entry of Freefall Wedged – Wedge motions and Cavity Dynamics, CeSOS
IMT-6-2014	Kim, Ekaterina	Experimental and numerical studies related to the coupled behavior of ice mass and steel structures during accidental collisions, IMT
IMT-7-2014	Tan, Xiang	Numerical investigation of ship's continuous- mode icebreaking in leverl ice, CeSOS
IMT-8-2014	Muliawan, Made Jaya	Design and Analysis of Combined Floating Wave and Wind Power Facilities, with Emphasis on Extreme Load Effects of the Mooring System, CeSOS
IMT-9-2014	Jiang, Zhiyu	Long-term response analysis of wind turbines with an emphasis on fault and shutdown conditions, IMT
IMT-10-2014	Dukan, Fredrik	ROV Motion Control Systems, IMT
IMT-11-2014	Grimsmo, Nils I.	Dynamic simulations of hydraulic cylinder for heave compensation of deep water drilling risers, IMT
IMT-12-2014	Kvittem, Marit I.	Modelling and response analysis for fatigue design of a semisubmersible wind turbine, CeSOS
IMT-13-2014	Akhtar, Juned	The Effects of Human Fatigue on Risk at Sea, IMT
IMT-14-2014	Syahroni, Nur	Fatigue Assessment of Welded Joints Taking into Account Effects of Residual Stress, IMT
IMT-1-2015	Bøckmann, Eirik	Wave Propulsion of ships, IMT
IMT-2-2015	Wang, Kai	Modelling and dynamic analysis of a semi-submersible floating vertical axis wind turbine, CeSOS
IMT-3-2015	Fredriksen, Arnt Gunvald	A numerical and experimental study of a two-dimensional body with moonpool in waves and current, CeSOS
IMT-4-2015	Jose Patricio Gallardo Canabes	Numerical studies of viscous flow around bluff bodies, IMT

IMT-5-2015	Vegard Longva	Formulation and application of finite element techniques for slender marine structures subjected to contact interactions, IMT
IMT-6-2015	Jacobus De Vaal	Aerodynamic modelling of floating wind turbines, CeSOS
IMT-7-2015	Fachri Nasution	Fatigue Performance of Copper Power Conductors, IMT
IMT-8-2015	Oleh I Karpa	Development of bivariate extreme value distributions for applications in marine technology,CeSOS
IMT-9-2015	Daniel de Almeida Fernandes	An output feedback motion control system for ROVs, AMOS
IMT-10-2015	Bo Zhao	Particle Filter for Fault Diagnosis: Application to Dynamic Positioning Vessel and Underwater Robotics, CeSOS
IMT-11-2015	Wenting Zhu	Impact of emission allocation in maritime transportation, IMT
IMT-12-2015	Amir Rasekhi Nejad	Dynamic Analysis and Design of Gearboxes in Offshore Wind Turbines in a Structural Reliability Perspective, CeSOS
IMT-13-2015	Arturo Jesùs Ortega Malca	Dynamic Response of Flexibles Risers due to Unsteady Slug Flow, CeSOS
IMT-14-2015	Dagfinn Husjord	Guidance and decision-support system for safe navigation of ships operating in close proximity, IMT
IMT-15-2015	Anirban Bhattacharyya	Ducted Propellers: Behaviour in Waves and Scale Effects, IMT
IMT-16-2015	Qin Zhang	Image Processing for Ice Parameter Identification in Ice Management, IMT
IMT-1-2016	Vincentius Rumawas	Human Factors in Ship Design and Operation: An Experiential Learning, IMT
IMT-2-2016	Martin Storheim	Structural response in ship-platform and ship-ice collisions, IMT
IMT-3-2016	Mia Abrahamsen Prsic	Numerical Simulations of the Flow around single and Tandem Circular Cylinders Close to a Plane Wall, IMT
IMT-4-2016	Tufan Arslan	Large-eddy simulations of cross-flow around ship sections, IMT

IMT-5-2016	Pierre Yves-Henry	Parametrisation of aquatic vegetation in hydraulic and coastal research,IMT
IMT-6-2016	Lin Li	Dynamic Analysis of the Instalation of Monopiles for Offshore Wind Turbines, CeSOS
IMT-7-2016	Øivind Kåre Kjerstad	Dynamic Positioning of Marine Vessels in Ice, IMT
IMT-8-2016	Xiaopeng Wu	Numerical Analysis of Anchor Handling and Fish Trawling Operations in a Safety Perspective, CeSOS
IMT-9-2016	Zhengshun Cheng	Integrated Dynamic Analysis of Floating Vertical Axis Wind Turbines, CeSOS
IMT-10-2016	Ling Wan	Experimental and Numerical Study of a Combined Offshore Wind and Wave Energy Converter Concept
IMT-11-2016	Wei Chai	Stochastic dynamic analysis and reliability evaluation of the roll motion for ships in random seas, CeSOS
IMT-12-2016	Øyvind Selnes Patricksson	Decision support for conceptual ship design with focus on a changing life cycle and future uncertainty, IMT
IMT-13-2016	Mats Jørgen Thorsen	Time domain analysis of vortex-induced vibrations, IMT
IMT-14-2016	Edgar McGuinness	Safety in the Norwegian Fishing Fleet – Analysis and measures for improvement, IMT
IMT-15-2016	Sepideh Jafarzadeh	Energy effiency and emission abatement in the fishing fleet, IMT
IMT-16-2016	Wilson Ivan Guachamin Acero	Assessment of marine operations for offshore wind turbine installation with emphasis on response-based operational limits, IMT
IMT-17-2016	Mauro Candeloro	Tools and Methods for Autonomous Operations on Seabed and Water Coumn using Underwater Vehicles, IMT
IMT-18-2016	Valentin Chabaud	Real-Time Hybrid Model Testing of Floating Wind Tubines, IMT
IMT-1-2017	Mohammad Saud Afzal	Three-dimensional streaming in a sea bed boundary layer
IMT-2-2017	Peng Li	A Theoretical and Experimental Study of Wave-induced Hydroelastic Response of a Circular Floating Collar
IMT-3-2017	Martin Bergström	A simulation-based design method for arctic maritime transport systems

IMT-4-2017	Bhushan Taskar	The effect of waves on marine propellers and propulsion
IMT-5-2017	Mohsen Bardestani	A two-dimensional numerical and experimental study of a floater with net and sinker tube in waves and current
IMT-6-2017	Fatemeh Hoseini Dadmarzi	Direct Numerical Simualtion of turbulent wakes behind different plate configurations
IMT-7-2017	Michel R. Miyazaki	Modeling and control of hybrid marine power plants
IMT-8-2017	Giri Rajasekhar Gunnu	Safety and effiency enhancement of anchor handling operations with particular emphasis on the stability of anchor handling vessels
IMT-9-2017	Kevin Koosup Yum	Transient Performance and Emissions of a Turbocharged Diesel Engine for Marine Power Plants
IMT-10-2017	Zhaolong Yu	Hydrodynamic and structural aspects of ship collisions
IMT-11-2017	Martin Hassel	Risk Analysis and Modelling of Allisions between Passing Vessels and Offshore Installations
IMT-12-2017	Astrid H. Brodtkorb	Hybrid Control of Marine Vessels – Dynamic Positioning in Varying Conditions
IMT-13-2017	Kjersti Bruserud	Simultaneous stochastic model of waves and current for prediction of structural design loads
IMT-14-2017	Finn-Idar Grøtta Giske	Long-Term Extreme Response Analysis of Marine Structures Using Inverse Reliability Methods
IMT-15-2017	Stian Skjong	Modeling and Simulation of Maritime Systems and Operations for Virtual Prototyping using co-Simulations
IMT-1-2018	Yingguang Chu	Virtual Prototyping for Marine Crane Design and Operations
IMT-2-2018	Sergey Gavrilin	Validation of ship manoeuvring simulation models
IMT-3-2018	Jeevith Hegde	Tools and methods to manage risk in autonomous subsea inspection,maintenance and repair operations
IMT-4-2018	Ida M. Strand	Sea Loads on Closed Flexible Fish Cages
IMT-5-2018	Erlend Kvinge Jørgensen	Navigation and Control of Underwater Robotic Vehicles

IMT-6-2018	Bård Stovner	Aided Intertial Navigation of Underwater Vehicles
IMT-7-2018	Erlend Liavåg Grotle	Thermodynamic Response Enhanced by Sloshing in Marine LNG Fuel Tanks
IMT-8-2018	Børge Rokseth	Safety and Verification of Advanced Maritime Vessels
IMT-9-2018	Jan Vidar Ulveseter	Advances in Semi-Empirical Time Domain Modelling of Vortex-Induced Vibrations
IMT-10-2018	Chenyu Luan	Design and analysis for a steel braceless semi-submersible hull for supporting a 5-MW horizontal axis wind turbine
IMT-11-2018	Carl Fredrik Rehn	Ship Design under Uncertainty
IMT-12-2018	Øyvind Ødegård	Towards Autonomous Operations and Systems in Marine Archaeology
IMT-13-2018	Stein Melvær Nornes	Guidance and Control of Marine Robotics for Ocean Mapping and Monitoring
IMT-14-2018	Petter Norgren	Autonomous Underwater Vehicles in Arctic Marine Operations: Arctic marine research and ice monitoring
IMT-15-2018	Minjoo Choi	Modular Adaptable Ship Design for Handling Uncertainty in the Future Operating Context
MT-16-2018	Ole Alexander Eidsvik	Dynamics of Remotely Operated Underwater Vehicle Systems
IMT-17-2018	Mahdi Ghane	Fault Diagnosis of Floating Wind Turbine Drivetrain- Methodologies and Applications
IMT-18-2018	Christoph Alexander Thieme	Risk Analysis and Modelling of Autonomous Marine Systems
IMT-19-2018	Yugao Shen	Operational limits for floating-collar fish farms in waves and current, without and with well-boat presence
IMT-20-2018	Tianjiao Dai	Investigations of Shear Interaction and Stresses in Flexible Pipes and Umbilicals
IMT-21-2018	Sigurd Solheim Pettersen	Resilience by Latent Capabilities in Marine Systems
IMT-22-2018	Thomas Sauder	Fidelity of Cyber-physical Empirical Methods. Application to the Active Truncation of Slender Marine Structures
IMT-23-2018	Jan-Tore Horn	Statistical and Modelling Uncertainties in the Design of Offshore Wind Turbines

IMT-24-2018	Anna Swider	Data Mining Methods for the Analysis of Power Systems of Vessels
IMT-1-2019	Zhao He	Hydrodynamic study of a moored fish farming cage with fish influence
IMT-2-2019	Isar Ghamari	Numerical and Experimental Study on the Ship Parametric Roll Resonance and the Effect of Anti-Roll Tank
IMT-3-2019	Håkon Strandenes	Turbulent Flow Simulations at Higher Reynolds Numbers
IMT-4-2019	Siri Mariane Holen	Safety in Norwegian Fish Farming – Concepts and Methods for Improvement
IMT-5-2019	Ping Fu	Reliability Analysis of Wake-Induced Riser Collision
IMT-6-2019	Vladimir Krivopolianskii	Experimental Investigation of Injection and Combustion Processes in Marine Gas Engines using Constant Volume Rig
IMT-7-2019	Anna Maria Kozlowska	Hydrodynamic Loads on Marine Propellers Subject to Ventilation and out of Water Condition.
IMT-8-2019	Hans-Martin Heyn	Motion Sensing on Vessels Operating in Sea Ice: A Local Ice Monitoring System for Transit and Stationkeeping Operations under the Influence of Sea Ice
IMT-9-2019	Stefan Vilsen	Method for Real-Time Hybrid Model Testing of Ocean Structures – Case on Slender Marine Systems
IMT-10-2019	Finn-Christian W. Hanssen	Non-Linear Wave-Body Interaction in Severe Waves
IMT-11-2019	Trygve Olav Fossum	Adaptive Sampling for Marine Robotics
IMT-12-2019	Jørgen Bremnes Nielsen	Modeling and Simulation for Design Evaluation
IMT-13-2019	Yuna Zhao	Numerical modelling and dyncamic analysis of offshore wind turbine blade installation
IMT-14-2019	Daniela Myland	Experimental and Theoretical Investigations on the Ship Resistance in Level Ice
IMT-15-2019	Zhengru Ren	Advanced control algorithms to support automated offshore wind turbine installation
IMT-16-2019	Drazen Polic	Ice-propeller impact analysis using an inverse propulsion machinery simulation approach
IMT-17-2019	Endre Sandvik	Sea passage scenario simulation for ship system performance evaluation

IMT-18-2019	Loup Suja-Thauvin	Response of Monopile Wind Turbines to Higher Order Wave Loads
IMT-19-20119	Emil Smilden	Structural control of offshore wind turbines – Increasing the role of control design in offshore wind farm development
IMT-20-2019	Aleksandar-Sasa Milakovic	On equivalent ice thickness and machine learning in ship ice transit simulations
IMT-1-2020	Amrit Shankar Verma	Modelling, Analysis and Response-based Operability Assessment of Offshore Wind Turbine Blade Installation with Emphasis on Impact Damages
IMT-2-2020	Bent Oddvar Arnesen Haugaløkken	Autonomous Technology for Inspection, Maintenance and Repair Operations in the Norwegian Aquaculture
IMT-3-2020	Seongpil Cho	Model-based fault detection and diagnosis of a blade pitch system in floating wind turbines
IMT-4-2020	Jose Jorge Garcia Agis	Effectiveness in Decision-Making in Ship Design under Uncertainty
IMT-5-2020	Thomas H. Viuff	Uncertainty assessment of wave-and current-induced global response of floating bridges
IMT-6-2020	Fredrik Mentzoni	Hydrodynamic Loads on Complex Structures in the Wave Zone
IMT-7-2020	Senthuran Ravinthrakumar	Numerical and Experimental Studies of Resonant Flow in Moonpools in Operational Conditions

ISBN 978-82-326-4653-1 (printed version)
ISBN 978-82-326-4652-4 (electronic version)
ISSN 1503-8181

Doctoral theses at NTNU, 2020:152

Senthuran Ravinthrakumar

Numerical and Experimental Studies of Resonant Flow in Moonpools in Operational Conditions

NTNU
Norwegian University of
Science and Technology
Faculty of Engineering
Department of MarineTechnology

NTNU
Norwegian University of
Science and Technology

Doctoral Thesis

Senthuran Ravinthrakumar

Doctoral theses at NTNU, 2020:152

NTNU

NTNU
Norwegian University of
Science and Technology